

ISSN 2071-4726
2071-0305

Инженерно-строительный журнал

НАУЧНОЕ ИЗДАНИЕ

№8(92) 2019





ПОЛИТЕХ
Санкт-Петербургский
политехнический университет
Петра Великого

Инженерно-строительный институт
Центр дополнительных профессиональных программ
195251, г. Санкт-Петербург, Политехническая ул., 29,
тел/факс: 552-94-60, www.stroikursi.spbstu.ru,
stroikursi@mail.ru

**Приглашает специалистов организаций, вступающих в СРО,
на курсы повышения квалификации (72 часа)**

Код	Наименование программы	Виды работ*
Курсы по строительству		
БС-01-04	«Безопасность и качество выполнения общестроительных работ»	п.1,2, 3, 5, 6, 7, 9, 10, 11, 12, 13, 14
БС-01	«Безопасность и качество выполнения геодезических, подготовительных и земляных работ, устройства оснований и фундаментов»	1,2,3,5
БС-02	«Безопасность и качество возведения бетонных и железобетонных конструкций»	6,7
БС-03	«Безопасность и качество возведения металлических, каменных и деревянных конструкций»	9,10,11
БС-04	«Безопасность и качество выполнения фасадных работ, устройства кровель, защиты строительных конструкций, трубопроводов и оборудования»	12,13,14
БС-05	«Безопасность и качество устройства инженерных сетей и систем»	15,16,17,18,19
БС-06	«Безопасность и качество устройства электрических сетей и линий связи»	20,21
БС-08	«Безопасность и качество выполнения монтажных и пусконаладочных работ»	23,24
БС-12	«Безопасность и качество устройства мостов, эстакад и путепроводов»	29
БС-13	«Безопасность и качество выполнения гидротехнических, водолазных работ»	30
БС-14	«Безопасность и качество устройства промышленных печей и дымовых труб»	31
БС-15	«Осуществление строительного контроля»	32
БС-16	«Организация строительства, реконструкции и капитального ремонта. Выполнение функций технического заказчика и генерального подрядчика»	33
Курсы по проектированию		
БП-01	«Разработка схемы планировочной организации земельного участка, архитектурных решений, мероприятий по обеспечению доступа маломобильных групп населения»	1,2,11
БП-02	«Разработка конструктивных и объемно-планировочных решений зданий и сооружений»	3
БП-03	«Проектирование внутренних сетей инженерно-технического обеспечения»	4
БП-04	«Проектирование наружных сетей инженерно-технического обеспечения»	5
БП-05	«Разработка технологических решений при проектировании зданий и сооружений»	6
БП-06	«Разработка специальных разделов проектной документации»	7
БП-07	«Разработка проектов организации строительства»	8
БП-08	«Проектные решения по охране окружающей среды»	9
БП-09	«Проектные решения по обеспечению пожарной безопасности»	10
БП-10	«Обследование строительных конструкций и грунтов основания зданий и сооружений»	12
БП-11	«Организация проектных работ. Выполнение функций генерального проектировщика»	13
Э-01	«Проведение энергетических обследований с целью повышения энергетической эффективности и энергосбережения»	
Курсы по инженерным изысканиям		
И-01	«Инженерно-геодезические изыскания в строительстве»	1
И-02	«Инженерно-геологические изыскания в строительстве»	2,5
И-03	«Инженерно-гидрометеорологические изыскания в строительстве»	3
И-04	«Инженерно-экологические изыскания в строительстве»	4
И-05	«Организация работ по инженерным изысканиям»	7

*(согласно приказам Минрегионразвития РФ N 624 от 30 декабря 2009 г.)

**По окончании курса слушателю выдается удостоверение о краткосрочном повышении
квалификации установленного образца (72 ак. часа)**

Для регистрации на курс необходимо выслать заявку на участие, и копию диплома об образовании по телефону/факсу: 8(812) 552-94-60, 535-79-92, , e-mail: stroikursi@mail.ru.

Инженерно-строительный журнал

НАУЧНОЕ ИЗДАНИЕ

ISSN 2071-4726, 2071-0305

Свидетельство о государственной регистрации: ПИ №ФС77-38070, выдано Роскомнадзором

Специализированный научный журнал. Выходит с 09.2008.

Включен в Перечень ведущих периодических изданий ВАК РФ

Периодичность: 8 раз в год

Учредитель и издатель:

Санкт-Петербургский политехнический университет Петра Великого

Адрес редакции:

195251, СПб, ул. Политехническая, д. 29, Гидрокорпус-2, ауд. 245

Главный редактор:

Екатерина Александровна Линник

Научный редактор:

Николай Иванович Ватин

Выпускающий редактор:

Анастасия Крупина

Редакционная коллегия:

д.ф.-м.н., доцент Р.А. Абдикаримов;
 д.т.н., проф. В.В. Бабков;
 к.т.н., проф. А.И. Боровков;
 д.т.н., проф. А. Бородинец;
 д.т.н., проф. Н.И. Ватин;
 PhD, проф. М. Вельжкович;
 к.т.н., М.Р. Гарифуллин;
 д.т.н., проф. Э.К. Завадскас;
 д.ф.-м.н., проф. М.Н. Кирсанов;
 D.Sc., проф. М. Кнежевич;
 д.т.н., проф. В.В. Лалин;
 д.т.н., проф. Б.Е. Мельников;
 д.т.н., академик М.М. Мирсаидов;
 д.т.н., проф. Р.Б. Орлович;
 Dr. Sc. Ing., professor
 Л. Пакрастиньш;
 Dr.-Ing. Habil., professor
 Х. Пастернак;
 д.т.н., проф. А.В. Перельмутер;
 д.т.н., проф. М.Р. Петриченко;
 д.т.н., проф. В.В. Сергеев;
 д.ф.-м.н., проф. М.Х. Стрелец;
 д.т.н., проф. О.В. Тараканов;
 д.т.н., проф. Б.Б. Телтаев;
 д.т.н., проф. В.И. Травуш;
 д.т.н., проф. Д. Унгерман;
 д.т.н., проф. С.В. Федосов

Дата выхода: 30.12.2019

Содержание

Юрченко В. Алгоритм определения потоков касательных усилий для произвольных сечений тонкостенных стержней	3
Никоноров В.В., Никонорова Д.О., Пикус Г.А. Теплофизические свойства массива грунта	27
Адевуми А.А., Исмаил М., Ариффин М.А.М., Юсуф М.О., Маслехуддин М., Мохамед Х.Д. Прочность и микроструктура щелочно-активированного пуццоланового и известнякового раствора	36
Аль-Рушан Р., Або-Мсамх И. Поведение при изгибе и кручении железобетонных балок, усиленных композитным углеволокном	48
Левцев А.П., Лапин Е.С., Чжан Ц. Повышение эффективности теплопередачи секционных радиаторов в системах теплоснабжения зданий	63
Петриченко М.Р., Сергеев В.В., Немова Д.В., Котов Е.В., Андреева Д.С. CFD-моделирование конвективных течений в вертикальных кавернах	76
Белаш Т.А., Иванова Ж.В. Деревянные здания каркасного типа с эффективными конструкциями узловых соединений для сейсмически активных районов	84
Славчева Г.С., Байджанов Д.О., Хан М.А., Шведова М.А., Иманов Е.К. Бесклинкерное шлако-кремнеземистое вяжущее: параметры структурообразования и кинетика твердения	96
Рахмани Х., Монтазер Гейб М. Насыщение CO ₂ гидратированного известью модифицированного проницаемого бетона	106
Ильина О.Н., Ильин И.Б. Дорожные органоминеральные смеси на основе нефтяного шлама	115
Герасимова Е.Н., Галямичев А.В., Михайлова М.К., Догру С. Напряженно-деформированное состояние панели из стекла с точечным клеевым креплением	127
Душимимана А., Ньонсенга А.А., Декаджеви, Г.Дж., Катумби Л.К. Влияние модельно-ориентированного проектирования и нагрузки на отклики конструкции с изолированным фундаментом	142
Колчунов В.И., Федорова Н.В., Савин С.Ю., Ковалев В.В., Ильющенко Т.А. Моделирование разрушения железобетонного каркаса многоэтажного здания с предварительно напряженными ригелями	155
Урханова Л.А., Буянтуев С.Л., Урханова А.А., Лхасаранов С.А., Ардашова Г.Р., Федюк Р.С., Свинцов А.П., Иванов И.А. Механические и электрические свойства бетона, модифицированного углеродными наночастицами	163

© ФГАОУ ВО СПбГУ, 2019

© Иллюстрация на обложке: Илья Смагин

Контакты:

E-mail: mce@spbstu.ru

Web: <http://www.engstroy.spbstu.ru>

Magazine of Civil Engineering

SCHOLAR JOURNAL

ISSN 2071-4726, 2071-0305

Peer-reviewed scientific journal

Start date: 2008/09

8 issues per year

Publisher:Peter the Great St. Petersburg
Polytechnic University**Indexing:**Scopus, Russian Science Citation
Index (WoS), Compendex, DOAJ,
EBSCO, Google Academia, Index
Copernicus, ProQuest, Ulrich's Serials
Analysis System, CNKI**Corresponding address:**245 Hydro Building, 29
Polytechnicheskaya st., Saint-
Petersburg, 195251, Russia**Editor-in-chief:**

Ekaterina A. Linnik

Science editor:

Nikolay I. Vatin

Technical editor:

Anastasia Krupina

Editorial board:R.A. Abdikarimov, D.Sc., associate
professor

V.V. Babkov, D.Sc., professor

A.I. Borovkov, PhD, professor

A. Borodinecs, Dr.Sc.Ing., professor

M. Veljkovic, PhD, professor

M. Garifullin, PhD, postdoctorant

E.K. Zavadskas, D.Sc., professor

M.N. Kirsanov, D.Sc., professor

M. Knezevic, D.Sc., professor

V.V. Lalin, D.Sc., professor

B.E. Melnikov, D.Sc., professor

M.M. Mirsaidov, D.Sc., professor

R.B. Orlovich, D.Sc., professor

L. Pakrastinsh, Dr.Sc.Ing., professor

H. Pasternak, Dr.-Ing.habil.,
professor

A.V. Perelmuter, D.Sc., professor

M.R. Petrichenko, D.Sc., professor

V.V. Sergeev, D.Sc., professor

M.Kh. Strelets, D.Sc., professor

O.V. Tarakanov, D.Sc., professor

B.B. Teltayev, D.Sc., professor

V.I. Travush, D.Sc., professor

S.V. Fedosov, D.Sc., professor

Date of issue: 30.12.2019

Contents

Yurchenko, V. Algorithm for shear flows in arbitrary cross-sections of thin-walled bars	3
Nikonorov, V.V., Nikonorova, D.O., Pikus, G.A. Thermophysical properties of the soil massif	27
Adewumi, A.A., Ismail, M., Ariffin, M.A.M., Yusuf, M.O., Maslehuddin, M., Mohamed, H.D. Strength and microstructure of alkali-activated natural pozzolan and limestone powder mortar	36
Al-Rousan, R., Abo-Msamh, I. Bending and torsion behaviour of CFRP strengthened RC beams	48
Levsev, A.P., Lapin, E.S., Zhang, Q. Increasing the heat transfer efficiency of sectional radiators in building heating systems	63
Petrichenko, M.R., Sergeev, V.V., Nemova, D., Kotov, E.V., Andreeva, D.S. CFD simulation of the convective flows in the vertical caverns	76
Belash, T.A., Ivanova, Zh.V. Timber frame buildings with efficient junction designs for earthquake-prone areas	84
Slavcheva, G.S., Baidzhanov, D.O., Khan, M.A., Shvedova, M.A., Imanov, Y.K. Clinkerless slag-silica binder: hydration process and hardening kinetics	96
Rahmani, H., Montazer Gheib, M. CO ₂ curing of hydrated lime modified pervious concretes.	106
Ilina, O.N., Ilin, I.B. Road organo-mineral mixtures based on oil sludge	115
Gerasimova, E.N., Galyamichev, A.V., Mikhaylova, M.K., Dogru, S. Stress-strain state of a glass panel with adhesive point fixings	127
Dushimimana, A., Niyonsenga, A.A., Decadjevi, G.J., Kathumbi, L.K. Effects of model-based design and loading on responses of base-isolated structures	142
Kolchunov, V.I., Fedorova, N.V., Savin, S.Yu., Kovalev, V.V., Iliushchenko, T.A. Failure simulation of a RC multi-storey building frame with prestressed girders	155
Urkanova, L.A., Buyantuev, S.L., Urkanova, A.A., Lkhasaranov, S.A., Ardashova, G.R., Fediuk, R.S., Svintsov, A.P., Ivanov, I.A. Mechanical and electrical properties of concrete modified by carbon nanoparticles	163

© Peter the Great St. Petersburg Polytechnic University. All rights reserved.

© Coverpicture – Ilya Smagin

E-mail: mce@spbstu.ruWeb: <https://engstroy.spbstu.ru/en/>



DOI: 10.18720/MCE.92.1

Algorithm for shear flows in arbitrary cross-sections of thin-walled bars

V. Yurchenko*

Kyiv National University of Construction and Architecture, Kyiv, Ukraine

* E-mail: vitalinay@rambler.ru

Keywords: thin-walled bar, arbitrary cross-section, shear forces flow, closed contour, graph theory, numerical algorithm, numerical examples, software implementation

Abstract. Development of a general computer program for the design and verification of thin-walled bar structural members remains an actual task. Despite the prevailing influence of normal stresses on the stress-strain state of thin-walled bars design and verification of thin-walled structural members should be performed taking into account not only normal stresses, but also shear stresses. Therefore, in the paper a thin-walled bar of an arbitrary cross-section which is undergone to the general load case is considered as investigated object. The main research question is development of mathematical support and knoware for numerical solution for the shear stresses problem with orientation on software implementation in a computer-aided design system for thin-walled bar structures. The problem of shear stresses outside longitudinal edges of an arbitrary cross-section (including open-closed multi-contour cross-sections) of a thin-walled bar subjected to the general load case has been considered in the paper. The formulated problem has been reduced to the searching problem for unknown shear forces flows that have the least value of the Castigliano's functional. Besides, constraints-equalities of shear forces flows equilibrium formulated for cross-section branch points, as well as equilibrium equation formulated for the whole cross-section relating to longitudinal axes of the thin-walled bar have been taken into account. A detailed numerical algorithm intended to solve the formulated problem has been proposed by the paper. The algorithm is oriented on software implementation in systems of computer-aided design of thin-walled bar structures. Developed algorithm has been implemented in SCAD Office environment by the program TONUS. Numerical examples for calculation of thin-walled bars with open and open-closed multi-contour cross-sections have been considered in order to validate developed algorithm and verify calculation accuracy for sectorial cross-section geometrical properties and shear stresses caused by warping torque and shear forces. Validity of the calculation results obtained using developed software has been proven by considered examples.

1. Introduction

To provide desired stiffness and strength in torsion, bridge superstructures are often constructed with a cross-section consisting of multiple cells (Figure 1) which have thin walls relative to their overall dimensions. When the cross-section contains multiple cells, they all provide resistance to applied torsion and for elastic continuity each cell must twist the same amount. With these considerations, equilibrium and compatibility conditions allow simultaneous equations to be formed and solved to determine the shear flow for each cell [1].

The behavior of single-box multi-cell box-girders with corrugated steel webs under pure torsion has been considered by Kongjian Shen et al. [2]. Experimental and numerical studies for considered structures have been also performed [3].

Dowell and Johnson proposed a relaxation method that distributes incremental shear flows back and forth between cells, reducing errors with each distribution cycle, until the final shear flows for all cells approximate the correct values. A closed-form approach has been introduced to determine, exactly, both the torsional constant and all shear flows for multi-cell cross-sections under torsion in the paper [1].

The problem of shear stresses determination for thin-walled bars has been also studied by Slivker in [4, 5] for the general loading case. His semi-sheared theory has been applied by Lalin et al. [6, 7] and Dyakov [8]

Yurchenko, V. Algorithm for shear flows in arbitrary cross-sections of thin-walled bars. Magazine of Civil Engineering. 2019. 92(8). Pp. 3–26. DOI: 10.18720/MCE.92.1

Юрченко В. Алгоритм определения потоков касательных усилий для произвольных сечений тонкостенных стержней // Инженерно-строительный журнал. 2019. № 8(92). С. 3–26. DOI: 10.18720/MCE.92.1



This work is licensed under a [CC BY-NC 4.0](https://creativecommons.org/licenses/by-nc/4.0/)

for the stability problems of thin-walled bars.

Further investigations in this area require the development of a detailed algorithm intended to software implementation in a computer-aided design system for thin-walled structures [9]. Such algorithm can be validated against benchmark examples as well as finite element results [10, 11]. It is reasonable to construct this algorithm using the mathematical apparatus of the graph theory as it is convenient to describe the topological properties of multi-cellular cross-section [12].

The graph algorithm used in this paper is given first by Tarjan [13]. Its application in analysis of thin-walled multi-cellular section is described by Alfano et al. [14], but the distribution of torsion stresses due to a change in normal stresses has not been considered. The graph theory has been also applied in [15, 16] to calculate the geometrical cross-sectional properties of thin-walled bars with hybrid (open-closed) types of cross-sections.

A simple computer program has been developed by Chai H. Yoo et al. [17] to evaluate the bending shear flow of any multiply-connected cellular sections. Prokić has developed a computer program for the determination of the torsional and flexural properties of thin-walled beams with arbitrary open-closed cross-section. In his paper [18] graph theory has been also applied to establish the topological properties of multi-cellular cross-section. Gurujee and Shah [19] presented a general purpose computer program capable of analyzing any planar frame made up of thin-walled structural members. Choudhary and Doshi proposed an algorithm for shear stress evaluation in ship hull girders [20].

Although many papers are published on the behavior of thin-walled bars, the development of a general computer program for the design and verification of thin-walled structural members remains an actual task. Despite the prevailing influence of normal stresses on the stress-strain state of thin-walled bars, the design and verification of thin-walled structural members should be performed taking into account not only normal stresses, but also shear stresses. Therefore, in this paper, a thin-walled bar of an arbitrary cross-section under the general load case is considered as *investigated object*. The main *research question* is the development of mathematical support and software for numerical solution for the shear stresses problem with orientation on software implementation in a computer-aided design system for the thin-walled structures.

2. Methods

2.1. Problem formulation

Let us consider the problem of shear stresses on longitudinal edges of an arbitrary section of a thin-walled bar that consists of several closed (connected and/or disconnected) contours and/or also open parts. Let us introduce in the plane of thin-walled cross-section a Cartesian coordinate system $y_c O z_c$ with the origin in the center of mass C of the section, the direction of the coordinate system axes $y_c O z_c$ coincides with the direction of principle axes of inertia. Let us also introduce in the plane of thin-walled cross-section a Cartesian coordinate system $y_s O z_s$ with the origin in the shear center S of the section, the direction of the coordinate system axes $y_s O z_s$ coincides with the direction of principle axes of inertia.

Let us introduce in further consideration the system of angular position coordinate with the origin in a certain (generally randomly selected) sectional point. Each considered sectional point can be associated with the angular position ζ . The value ζ should be calculated as the geometrical length of the curve constructed from the origin to the considered sectional point taken along the sectional contour. We also assume that the increment of the angular position ζ corresponds to the positive direction of section path tracing.

We assume that the integral geometrical properties of the section are known: A is the cross-sectional area, I_y and I_z are the second moments of area relative to the main axes of inertia which coincide with axes of global Cartesian coordinate system $y_c O z_c$; I_ω is the sectorial moment of inertia; I_t is the second moment of area for pure torsion. We also assume that Young's modulus E and shear modulus G are constant for the whole cross-section of the thin-walled bar.

Generally, the thin-walled bar is subjected to the action of eight force factors. Axial force N , bending moments M_y and M_z relative to the principle axes of inertia and warping bimoment B are applied at the center of mass C (see Figure 2) of the section and cause normal stresses in the cross-section $\sigma_i(x, \zeta)$:

$$\sigma_i(x, \zeta) = \frac{N(x)}{A} + \frac{M_y(x)}{I_y} z_i(\zeta) + \frac{M_z(x)}{I_z} y_i(\zeta) + \frac{B(x)}{I_\omega} \varpi_i(\zeta), \quad (1.1)$$

where $y_i(\zeta)$, $z_i(\zeta)$, $\varpi_i(\zeta)$ are the coordinates and sectorial coordinate of the considered point in cross-section of a thin-walled bar.



Figure 1. Box-girder bridge multi-cell cross-section [23].

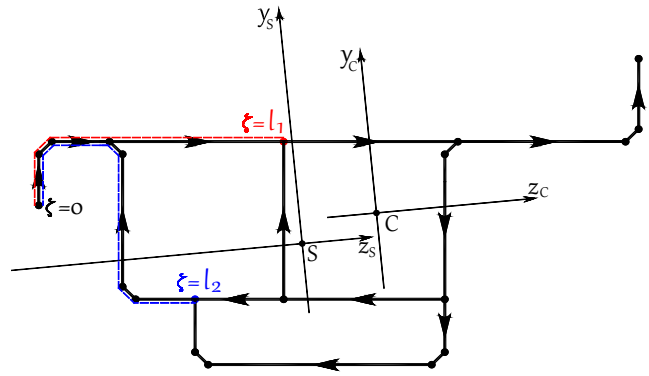


Figure 2. Cross-section of a thin-walled bar with representation of different angular positions as examples.

Shear forces Q_y and Q_z , total torque M_x and warping torque M_ω are applied at the shear center S (see Figure 2) of the cross-section and cause shear stresses in the cross-section, which can be written in terms of shear forces flows $T_j(x, \zeta)$ as presented below:

$$\tau_j(x, \zeta) = \frac{T_j(x, \zeta)}{\delta_j(\zeta)}, \quad (1.2)$$

where $\delta_j(\zeta)$ is the thickness of j^{th} section element.

An arbitrary section of the thin-walled bar can be described by the set of sectional points $\mathbf{P} = \{\bar{p}_p = \{y_p, z_p\} \mid p = \overline{1, n_p}\}$ (y_p and z_p are the coordinates of p^{th} sectional point in the global Cartesian coordinate system yOz) and by the set of sectional segments $\mathbf{S} = \{\bar{s}_s = \{p_s^{st}, p_s^{end}\} \mid s = \overline{1, n_s}\}$, which connect some two adjacent sectional points (Figure 3), where n_p and n_s are the numbers of the sectional points and segments, respectively.

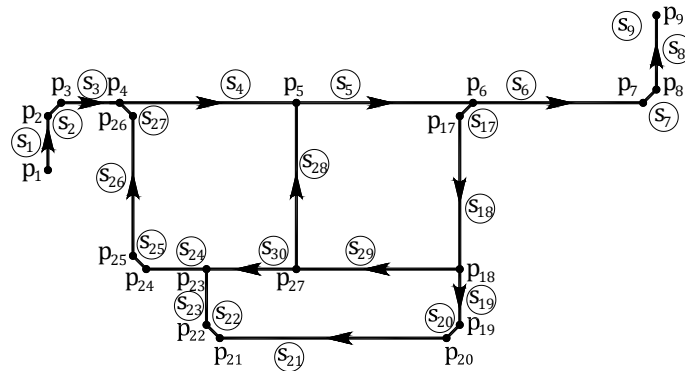


Figure 3. Arbitrary cross-section of a thin-walled bar determined on the set of sectional points \mathbf{P} and set of sectional segments \mathbf{S} .

The specified segment thickness $\delta = \{\delta_s \mid s = \overline{1, n_s}\}$ corresponds to each sectional segment. The set of sectorial coordinates $\omega = \{\omega_p \mid p = \overline{1, n_p}\}$ and the set of normalized sectorial coordinates $\varpi = \{\varpi_p \mid p = \overline{1, n_p}\}$ of the section correspond to the set of the sectional points \mathbf{P} , assuming that the values of the sectorial coordinates and normalized sectorial coordinates in each cross-sectional point are known.

The set of angular positions $\zeta = \{\zeta_\kappa = \{\zeta_\kappa^{start}, \zeta_\kappa^{end}\} \mid \kappa = \overline{1, n_\zeta - 1}\}$ is actually intended to implement a numerical integration taken along the thin-walled section contour (e.g., when calculating geometrical properties of the cross-section, values of shear forces flows, etc.), where κ is the number of a segment, $n_\zeta - 1$ is the number of the sectional segments. It should be noted that the angular positions are attributes of the ends of the sectional segments.

The initial data about the thin-walled section should be mapped onto the set of the angular positions ζ , $\kappa = \overline{1, n_\zeta - 1}$ by means of corresponding sets of sectional segments $\mathbf{S}^\zeta = \{\bar{s}_\kappa^\zeta = \{\zeta_\kappa^{start}, \zeta_\kappa^{end}\} : \zeta_\kappa^{start}, \zeta_\kappa^{end} \subseteq \zeta\}$, set of sectorial coordinates $\omega^\zeta = \{\bar{\omega}_\kappa^\zeta = \{\omega_\kappa^{start}, \omega_\kappa^{end}\} : \omega_\kappa^{start}, \omega_\kappa^{end} \subseteq \omega\}$ for the ends of sectional segments as well as the set of thicknesses $\delta^\zeta = \{\bar{\delta}_\kappa^\zeta \subseteq \delta\}$ for the segments, $\kappa = \overline{1, n_\zeta - 1}$.

2.2. Distribution of shear forces flows along closed contours of an arbitrary cross-section of thin-walled bar

2.2.1. Construction of connected graph \mathbf{G} associated with a section of a thin-walled bar

An arbitrary cross-section of a thin-walled bar can be associated with a planar connected non-oriented graph \mathbf{G} determined on the sets of $\mathbf{G} = \{\mathbf{V}, \mathbf{R}\}$, where \mathbf{V} is the finite set of the graph vertices, \mathbf{R} is the set of the graph edges or the set of unordered pairs on \mathbf{V} (Figure 4) [21, 22]. Herewith, for each graph edge $\mathbf{r} = \{u, v\} \in \mathbf{R}$ we assume that $u \neq v$.

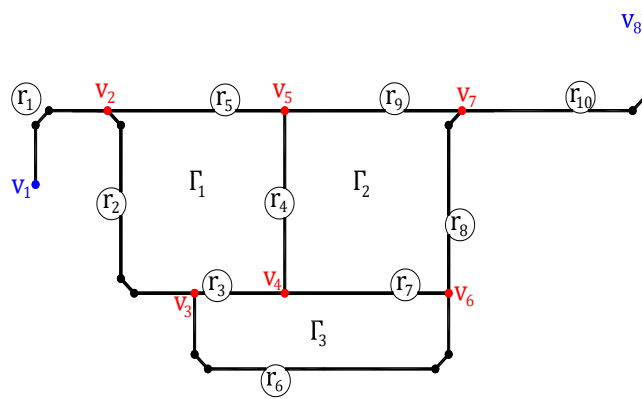


Figure 4. Graph \mathbf{G} associated with cross-section of thin-walled bar (the branch points are highlighted in red, while the end points are highlighted in blue).

The vertices of the graph \mathbf{G} are associated with *characteristic sectional points* only, which can be either:

1) *branch points*, i.e. sectional points connected with more than two sectional segments,

$$\mathbf{v}^p = \{\bar{p}_v \mid v = \overline{1, n_v}\}, \text{ here } n_v \text{ is the number of these points;}$$

2) *end points*, i.e. sectional points connected with only one sectional segment $\mathbf{v}^p_{end} = \{\bar{p}_g \mid g = \overline{1, n_g}\}$,

here n_g is the number of these points.

The edges of the graph \mathbf{G} are associated with sectional parts located between characteristic sectional points (with *unbranched sectional parts*). An edge of the graph \mathbf{G} , as a rule, may contain several sectional segments, so the full information about edge \mathbf{R}_j^ζ of the graph can be described by the set of sectional segments \bar{s}_r^ζ , $r = \overline{1, n_{\zeta rj}}$, from the array $\mathbf{S}^\zeta = \{\bar{s}_\kappa^\zeta = \{\zeta_\kappa^{start}, \zeta_\kappa^{end}\} \mid \kappa = \overline{1, n_\zeta - 1}\}$, $\bar{s}_r^\zeta \in \mathbf{S}^\zeta$, belonging to considered graph edge, $\bar{s}_r^\zeta \in \mathbf{R}_j : \mathbf{R}_j^\zeta = \{\bar{s}_r^\zeta : \bar{s}_r^\zeta \in \mathbf{S}^\zeta \wedge \bar{s}_r^\zeta \in \mathbf{R}_j \mid r = \overline{1, n_{\zeta rj}}\}$, here $n_{\zeta rj}$ is the number of segments for j^{th} graph edge. The set of all the graph edges defined on the set of segments \mathbf{S}^ζ can be expressed as $\mathbf{R}^\zeta = \{\mathbf{R}_j^\zeta \mid j = \overline{1, n_r}\}$.

We also assume that the arbitrary section of the thin-walled bar may contain some quantity of closed contours. Each closed contour is associated with a cycle of the graph \mathbf{G} or with a vertices sequence $v_0^k, v_1^k, v_2^k, \dots, v_n^k$, such that $v_i^k \mapsto v_{i+1}^k \forall i \Leftrightarrow \exists v_{i+1}^k$, where n_k is the number of closed contours in the section (the number of the graph \mathbf{G} cycles).

Some closed contour of a section $\Gamma_k^{r\zeta}$ (a basic cycle of the graph \mathbf{G}) can be definitely determined by the set of the graph edges $\mathbf{R}_j^\zeta \in \mathbf{R}^\zeta$ belonging to the considered contour $\Gamma_k^{r\zeta} = \{\mathbf{R}_j^\zeta \mid j = \overline{1, n_{r\zeta\Gamma_k}}\}$, where $n_{r\zeta\Gamma_k}$ is the number of the graph edges belonging to k^{th} closed contour. Besides, it is convenient to have the mapping of the closed contour $\Gamma_k^{r\zeta}$ onto the set of sectional segments $\vec{s}_m^\zeta, \vec{s}_m^\zeta \in \mathbf{S}^\zeta$, belonging to the considered closed contour, $\forall m = \overline{1, n_{\zeta\Gamma_k}} : \Gamma_k^\zeta = \{\vec{s}_m^\zeta : \vec{s}_m^\zeta \in \mathbf{S}^\zeta, \exists \mathbf{R}_\alpha^\zeta \subseteq \mathbf{R}^\zeta : \vec{s}_m^\zeta \subseteq \mathbf{R}_\alpha^\zeta \wedge \mathbf{R}_\alpha^\zeta \subseteq \Gamma_k^{r\zeta}\}$, here $n_{\zeta\Gamma_k}$ is the number of the sectional segments belonging to k^{th} closed contour.

The closed contours (basic cycles of the graph \mathbf{G}) defined on the set of graph edges \mathbf{R}^ζ and on the set of section segments \mathbf{S}^ζ can be described as $\Phi^{r\zeta} = \{\Gamma_k^{r\zeta} \mid k = \overline{1, n_k}\}$ and $\Phi^\zeta = \{\Gamma_k^\zeta \mid k = \overline{1, n_k}\}$, respectively. It should be noted that the identification of closed contours in the section $\Phi^{r\zeta}$ and Φ^ζ can be easily implemented using depth-first search algorithms on the graph.

Let us compose an incidence matrix \mathbf{I} for the graph \mathbf{G} with dimensions $n_v \times n_r$, $\mathbf{I} = \{g_{ij} \mid i = \overline{1, n_v}, j = \overline{1, n_r}\}$. The components of the matrix take the following values: $g_{ij} = 1$, if i^{th} graph vertex is a start vertex for j^{th} edge; $g_{ij} = -1$, if i^{th} graph vertex is an end vertex for j^{th} edge; $g_{ij} = 0$, otherwise. Let us also introduce a matrix $|\mathbf{I}| = \{|g_{ij}| \mid i = \overline{1, n_v}, j = \overline{1, n_r}\}$ composed of the modulus of elements g_{ij} of the matrix \mathbf{I} .

Next, we can compose a matrix of basic graph cycles \mathbf{F} with dimensions $n_k \times n_k$, $\mathbf{F} = \{f_{kj}\}$, $k = \overline{1, n_k}$, $j = \overline{1, n_r}$. The components of the matrix take the following values: $f_{kj} = 1$, if j^{th} graph edge belongs to k^{th} basic graph cycle ($\mathbf{R}_j^\zeta \subseteq \Gamma_k^\zeta$) and the edge direction coincides with the positive direction of path tracing; $f_{kj} = -1$, if j^{th} graph edge belongs to k^{th} basic graph cycle ($\mathbf{R}_j^\zeta \subseteq \Gamma_k^\zeta$) and the edge direction does not coincide with the positive direction of path tracing; $f_{kj} = 0$, if j^{th} graph edge does not belong to k^{th} basic graph cycle ($\mathbf{R}_j^\zeta \cap \Gamma_k^\zeta = \emptyset$).

2.2.2. Resolving equations relating to distribution of shear forces flows taken along closed contours for an arbitrary section of a thin-walled bar

Each j^{th} edge \mathbf{R}_j^ζ , $j = \overline{1, n_r}$ of the graph \mathbf{G} corresponds to a constant – edge weight, $\forall \kappa : \vec{s}_\kappa^\zeta \in \mathbf{R}_j^\zeta \wedge \vec{s}_\kappa^\zeta \in \mathbf{S}^\zeta :$

$$p_j = \int_{\ell_{rj}} \frac{d\zeta}{\delta(\zeta)} = \sum_{r=1}^{n_{\zeta rj}} \int_{\ell_\zeta \in \mathbf{R}_j^\zeta} \frac{d\zeta}{\delta(\zeta)} = \sum_{r=1}^{n_{\zeta rj}} \frac{1}{\delta_\kappa^\zeta} \int_{\zeta_\kappa}^{\zeta_{\kappa+1}} d\zeta = \sum_{r=1}^{n_{\zeta rj}} \frac{l_\kappa^\zeta}{\delta_\kappa^\zeta}. \quad (2.1)$$

Let us also compose the weighting matrix of unbranched sectional parts (edges of graph \mathbf{G}) – a square matrix \mathbf{W} with dimensions $n_r \times n_r$ and diagonal elements p_j , $j = \overline{1, n_r}$:

$$\mathbf{W} = \begin{bmatrix} p_1 & 0 & \dots & 0 \\ 0 & p_2 & \dots & 0 \\ \vdots & \vdots & \ddots & \vdots \\ 0 & 0 & 0 & p_{n_r} \end{bmatrix}. \quad (2.2)$$

Besides, each j^{th} graph edge \mathbf{R}_j^ζ corresponds to the increment of the sectorial coordinate $\Delta\omega_r^\zeta = \{\Delta\omega_{r,j}^\zeta \mid j = \overline{1, n_r}\}^T$, $\forall \kappa : \vec{s}_\kappa^\zeta \in \mathbf{R}_j^\zeta \wedge \vec{s}_\kappa^\zeta \in \mathbf{S}^\zeta :$

$$\Delta\omega_{r,j}^\zeta = \int_{\ell_{rj}} \rho d\zeta = \int_{\ell_{rj}} d\omega = \sum_{r=1}^{n_{\zeta rj}} \int_{\ell_\zeta \in \mathbf{R}_j^\zeta} d\omega = \sum_{r=1}^{n_{\zeta rj}} \int_{\zeta_\kappa}^{\zeta_{\kappa+1}} d\omega = \sum_{r=1}^{n_{\zeta rj}} \Delta\omega_\kappa^\zeta. \quad (2.3)$$

Each closed contour of the section Γ_k^r , $k = \overline{1, n_k}$, corresponds to the following constant – *contour weight*, $f_{kj} \in \mathbf{F}$, $\forall j: \mathbf{R}_j^r \subseteq \Gamma_k^r$:

$$\tilde{p}_k = \oint_{\Gamma_k^r} \frac{d\zeta}{\delta(\zeta)} = \int_{\mathbf{R}_j^r \subseteq \Gamma_k^r} \frac{d\zeta}{\delta(\zeta)} = \sum_{j=1}^{n_r \Gamma_k} |f_{kj}| p_j. \quad (2.4)$$

Let us also introduce the *weighting matrix of sectional contours* – a square matrix \mathbf{K} with dimensions $n_k \times n_k$:

$$\mathbf{K} = \begin{bmatrix} \tilde{p}_{11} & -p_{12} & \cdots & -p_{1k} & \cdots & -p_{1n_k} \\ -p_{21} & \tilde{p}_{22} & \cdots & -p_{2k} & \cdots & -p_{2n_k} \\ \vdots & \vdots & \ddots & \vdots & \vdots & \vdots \\ -p_{k1} & -p_{k2} & \cdots & \tilde{p}_{kk} & \cdots & -p_{kn_k} \\ \vdots & \vdots & \vdots & \vdots & \ddots & \vdots \\ -p_{n_k 1} & -p_{n_k 2} & \cdots & -p_{n_k k} & \cdots & \tilde{p}_{n_k n_k} \end{bmatrix}, \quad (2.5)$$

where the diagonal elements of the matrix are the weights of k^{th} closed contour, $\tilde{p}_{kk} = \tilde{p}_k$, $k = \overline{1, n_k}$; other elements of the matrix $p_{\alpha\beta}$ take zero value $p_{\alpha\beta} = p_{\beta\alpha} = 0$ when corresponded closed contours have no common edges: $\Gamma_\alpha^r \cap \Gamma_\beta^r = \emptyset$, and the sum of the weights for all common edges: $p_{\alpha\beta} = p_{\beta\alpha} = \sum_r p_r$, $\forall r: \mathbf{R}_r^r \subseteq \Gamma_\alpha^r \wedge \mathbf{R}_r^r \subseteq \Gamma_\beta^r$.

Let us consider the problem of torsion for an arbitrary thin-walled section subjected to total torque M_x only. When the cross-section consists of a certain number of closed (connected and/or disconnected) contours, as well as open parts, the torsion problem for the cross-section of the thin-walled bar is statically indeterminate. Therefore, not only static equations but also strain compatibility conditions must be introduced to consideration.

Let us formulate the strain compatibility conditions considering Castigliano's functional. The latter can be identified with an expression for strain energy formulated in terms of stresses for an isotropic material [5]:

$$\mathbf{C} = \frac{1}{2G} \left(\sum_{j=1}^{n_r} \left(\int_{\ell_j} \frac{(\sigma(\zeta))^2}{2(1+\nu)} \delta(\zeta) d\zeta + \int_{\ell_j} (\tau(\zeta))^2 \delta(\zeta) d\zeta \right) \right). \quad (2.6)$$

Besides, normal stresses $\sigma(\zeta)$ can be omitted, as total torque acts only:

$$\mathbf{C} = \frac{1}{2G} \left(\sum_{j=1}^{n_r} \int_{\ell_j} (\tau(\zeta))^2 \delta(\zeta) d\zeta \right). \quad (2.7)$$

Let us rewrite Castigliano's functional \mathbf{C} Equation (2.7) substituting shear stresses $\tau(\zeta)$ by their representation in terms of contour flows $\vec{\tilde{T}} = \{\tilde{T}_k\}^T$, $k = \overline{1, n_k}$:

$$\tilde{\tau}_k(\zeta) = \frac{\tilde{T}_k(\zeta)}{\delta_k(\zeta)}. \quad (2.8)$$

In this case we obtain the following expression for Castigliano's functional:

$$\begin{aligned} \mathbf{C} = & \frac{\tilde{T}_1^2}{2G} \oint_{\Gamma_1} \frac{d\zeta}{\delta(\zeta)} + \frac{\tilde{T}_2^2}{2G} \oint_{\Gamma_2} \frac{d\zeta}{\delta(\zeta)} + \dots + \frac{\tilde{T}_k^2}{2G} \oint_{\Gamma_k} \frac{d\zeta}{\delta(\zeta)} - \frac{\tilde{T}_1 \tilde{T}_2}{G} \int_{\Gamma_{12}} \frac{d\zeta}{\delta(\zeta)} - \frac{\tilde{T}_1 \tilde{T}_3}{G} \int_{\Gamma_{13}} \frac{d\zeta}{\delta(\zeta)} - \dots \\ & \dots - \frac{\tilde{T}_1 \tilde{T}_k}{G} \int_{\Gamma_{1k}} \frac{d\zeta}{\delta(\zeta)} - \frac{\tilde{T}_2 \tilde{T}_3}{G} \int_{\Gamma_{23}} \frac{d\zeta}{\delta(\zeta)} - \frac{\tilde{T}_2 \tilde{T}_4}{G} \int_{\Gamma_{24}} \frac{d\zeta}{\delta(\zeta)} - \dots - \frac{\tilde{T}_2 \tilde{T}_k}{G} \int_{\Gamma_{2k}} \frac{d\zeta}{\delta(\zeta)} - \dots - \frac{\tilde{T}_{k-1} \tilde{T}_k}{G} \int_{\Gamma_{k-1,k}} \frac{d\zeta}{\delta(\zeta)}. \end{aligned} \quad (2.9)$$

Negative summands $\frac{\tilde{T}_{k-1}\tilde{T}_k}{G} \int_{\Gamma_{k-1,k}} \frac{d\zeta}{\delta(\zeta)}$ in Equation (2.9) take into account the mutual work of the counter flows of shear stresses on the common parts of the thin-walled bar cross-section.

It is evident that the resulting torsional moment in the section caused by all contour flows of shear stresses $\tilde{T} = \{\tilde{T}_k\}^T$, $k = \overline{1, n_k}$ equals to the sum of the torsional moments caused by each of these flows [5]:

$$M_x = \sum_{k=1}^{n_k} \tilde{T}_k \Omega_k, \quad (2.10)$$

where Ω_k is the double area embraced by k^{th} closed contour Γ_k^ζ of the section.

Let us present the formulated problem in the form of a mathematical programming task, namely as a problem for unknown contour shear forces flows $\tilde{T} = \{\tilde{T}_k\}^T$, $k = \overline{1, n_k}$ that ensure the least value of the optimum criterion, i.e. Castigliano's functional **C** Equation (2.9) subject to equilibrium condition Equation (2.10).

Let us present the solution of the formulated problem as follow:

$$\tilde{T}_k = \tilde{a}_k \frac{M_x}{\Omega_0}, \quad (2.11)$$

where Ω_0 is the double area for all closed contours of the section Φ^ζ , $\Omega_0 = \sum_{k=1}^{n_k} \Omega_k$; \tilde{a}_k is the factor for the distribution of shear forces flows along k^{th} closed contour. Then Castigliano's functional Equation (2.9) can be rewritten as presented below:

$$\begin{aligned} C = \frac{M_x^2}{2G\Omega_0^2} & \left(\tilde{a}_1^2 \oint_{\Gamma_1} \frac{d\zeta}{\delta(\zeta)} + \tilde{a}_2^2 \oint_{\Gamma_2} \frac{d\zeta}{\delta(\zeta)} + \dots + \tilde{a}_k^2 \oint_{\Gamma_k} \frac{d\zeta}{\delta(\zeta)} - 2\tilde{a}_1\tilde{a}_2 \int_{\Gamma_{12}} \frac{d\zeta}{\delta(\zeta)} - 2\tilde{a}_1\tilde{a}_2 \int_{\Gamma_{12}} \frac{d\zeta}{\delta(\zeta)} - \right. \\ & - 2\tilde{a}_1\tilde{a}_3 \int_{\Gamma_{13}} \frac{d\zeta}{\delta(\zeta)} - \dots - 2\tilde{a}_1\tilde{a}_k \int_{\Gamma_{1k}} \frac{d\zeta}{\delta(\zeta)} - 2\tilde{a}_2\tilde{a}_3 \int_{\Gamma_{23}} \frac{d\zeta}{\delta(\zeta)} - \dots \\ & \left. \dots - 2\tilde{a}_2\tilde{a}_4 \int_{\Gamma_{24}} \frac{d\zeta}{\delta(\zeta)} - 2\tilde{a}_2\tilde{a}_k \int_{\Gamma_{2k}} \frac{d\zeta}{\delta(\zeta)} - \dots - 2\tilde{a}_{k-1}\tilde{a}_k \int_{\Gamma_{k-1,k}} \frac{d\zeta}{\delta(\zeta)} \right), \end{aligned} \quad (2.11)$$

and the equilibrium equation Equation (2.10) can be presented by the following:

$$M_x = \sum_{k=1}^{n_k} \tilde{a}_k \frac{M_x}{\Omega_0} \Omega_k = \frac{M_x}{\Omega_0} \sum_{k=1}^{n_k} \tilde{a}_k \Omega_k$$

or

$$\Omega_0 = \sum_{k=1}^{n_k} \tilde{a}_k \Omega_k. \quad (2.12)$$

So, the formulated problem can be presented as a searching problem for unknown distribution factors $\tilde{a} = \{\tilde{a}_k\}^T$, $k = \overline{1, n_k}$ of shear forces flows taken along closed contours of section that ensure the least value of Castigliano's functional **C** Equation (2.11) subject to equilibrium condition Equation (2.12).

The method of Lagrange multipliers can be used to reduce the problem Equations (2.11)–(2.12) to the searching for a stationary point of the following modified functional $\Lambda(\tilde{a}, \lambda_a)$, where λ_a is the Lagrange multiplier. Besides, the stationary conditions for the modified functional $\Lambda(\tilde{a}, \lambda_a)$ can be transformed to a system of linear algebraic equations with an order of $n_k + 1$ presented below in the vector-matrix form:

$$\begin{bmatrix} \mathbf{K} & \vec{\Omega} \\ (\vec{\Omega})^T & 0 \end{bmatrix} \times \begin{bmatrix} \tilde{a} \\ \lambda_a \end{bmatrix} = \begin{bmatrix} 0_k \\ \Omega_0 \end{bmatrix}, \quad (2.13)$$

where $\bar{\Omega} = \{\Omega_k\}^T$, $k = \overline{1, n_k}$ is the column vector of double areas embraced by the closed contours of the thin-walled bar. The resolving system of equations Equation (2.13) to calculate distribution factors $\tilde{a}_k = \{\tilde{a}_k\}^T$, $k = \overline{1, n_k}$ of shear forces flows along the closed contours of the section is presented below:

$$\begin{bmatrix} \tilde{p}_{11} & -p_{12} & \cdots & -p_{1k} & \cdots & -p_{1n_k} & \Omega_1 \\ -p_{21} & \tilde{p}_{22} & \cdots & -p_{2k} & \cdots & -p_{2n_k} & \Omega_2 \\ \vdots & \vdots & \ddots & \vdots & \vdots & \vdots & \vdots \\ -p_{k1} & -p_{k2} & \cdots & \tilde{p}_{kk} & \cdots & -p_{kn_k} & \Omega_k \\ \vdots & \vdots & \vdots & \vdots & \ddots & \vdots & \vdots \\ -p_{n_k1} & -p_{n_k2} & \cdots & -p_{n_kk} & \cdots & \tilde{p}_{n_k n_k} & \Omega_{n_k} \\ \Omega_1 & \Omega_2 & \cdots & \Omega_k & \cdots & \Omega_{n_k} & 0 \end{bmatrix} \times \begin{bmatrix} \tilde{a}_1 \\ \tilde{a}_2 \\ \vdots \\ \tilde{a}_k \\ \vdots \\ \tilde{a}_{n_k} \\ \lambda_a \end{bmatrix} = \begin{bmatrix} 0 \\ 0 \\ \vdots \\ 0 \\ \vdots \\ 0 \\ \Omega_0 \end{bmatrix}, \quad (2.14)$$

where the diagonal elements of the matrix are the weights of k^{th} closed contour,

$$\tilde{p}_{kk} = \tilde{p}_k, \quad k = \overline{1, n_k}; \quad \Omega_k \text{ is double area embraced by } k^{\text{th}} \text{ closed contour } \Gamma_k^\zeta, \quad \Omega_0 = \sum_{k=1}^{n_k} \Omega_k;$$

λ_a is the Lagrange multiplier. Other elements of the matrix $p_{\alpha\beta}$ take zero value $p_{\alpha\beta} = p_{\beta\alpha} = 0$ when corresponded closed contours have no common edges: $\Gamma_\alpha^\zeta \cap \Gamma_\beta^\zeta = \emptyset$, and the sum of weights for all common edges [5] is $p_{\alpha\beta} = p_{\beta\alpha} = \sum_r p_r, \forall r : \mathbf{R}_r^\zeta \subseteq \Gamma_\alpha^\zeta \wedge \mathbf{R}_r^\zeta \subseteq \Gamma_\beta^\zeta$.

The solution of the system of algebraic equations Equation (2.14) returns the column vector of factors $\tilde{a}_k = \{\tilde{a}_k | k = \overline{1, n_k}\}$ for the distribution of shear forces flows along the closed contours of the section. Based on \tilde{a}_k , we can generate the column vector of factors for the distribution of shear forces flows along the graph \mathbf{G} edges: $\mathbf{A}_r = \{a_j | j = \overline{1, n_r}\}$, where each element should be determined as:

$$a_j = \sum_{k=1}^{n_k} f_{kj} \tilde{a}_k, \quad f_{kj} \in \mathbf{F} \quad \forall j = \overline{1, n_r}, \quad (2.15)$$

Since every graph edge \mathbf{R}_j^ζ , $j = \overline{1, n_r}$, is described by the set of sectional segments $\vec{s}_r^\zeta \in \mathbf{S}^\zeta$ as: $\mathbf{R}_j^\zeta = \{\vec{s}_r^\zeta : \vec{s}_r^\zeta \in \mathbf{S}^\zeta \wedge \vec{s}_r^\zeta \in \mathbf{R}_j | r = \overline{1, n_{\zeta r j}}\}$, then it is possible to determine for each sectional segment $\vec{s}_\kappa^\zeta \in \mathbf{S}^\zeta$ the value of piecewise constant *distribution function for shear flows taken along section* $a^\zeta(\zeta)$ as the set of $a^\zeta = \{a_\kappa^\zeta | \kappa = \overline{1, n_\zeta - 1}\}$ as follows: $a_\kappa^\zeta = a_j, \forall \kappa : \vec{s}_\kappa^\zeta \cap \mathbf{R}_j^\zeta \neq \emptyset$, and $a_\kappa^\zeta = 0$, otherwise.

2.3. Resolving equations for an arbitrary cross-section of a thin-walled bar

The search problem of shear forces flows for an arbitrary cross-section of a thin-walled bar (including open-closed multi-contour cross-sections) can be transformed into a minimization problem of Castiglano's functional \mathbf{C} subject to constraints-equalities of shear forces flows equilibrium formulated for cross-section branch points, as well as subject to equilibrium equation for the whole cross-section relating to longitudinal axes of the thin-walled bar [5].

Let us present the formulated problem as a mathematical programming task, namely as searching for unknown values of shear forces flows at the start points of unbranched parts of a section:

$$\vec{T}_S = \{T_{S,j}\}^T, \quad j = \overline{1, n_r}, \quad (3.1)$$

which ensure the least value of the optimum criterion – Castiglano's functional \mathbf{C} :

$$\mathbf{C}^* = \mathbf{C}(\vec{T}_S^*) = \min_{\vec{T}_S \in \mathfrak{S}_T} \mathbf{C}(\vec{T}_S) \quad (3.2)$$

on a hyperplane of feasible decisions \mathfrak{S}_T described by the following system of constraints-equalities:

$$\begin{cases} f(\vec{T}_S) = \{f_v(\vec{T}_S) = 0 \mid v = \overline{1, n_v - 1}\}; \\ f_x(\vec{T}_S) = 0, \end{cases} \quad (3.3)$$

where \vec{T}_S is the vector of design variables (searched shear flows);

n_r is the number of unknown shear flows;

\vec{T}_S^* is the optimum decision of the problem;

C^* is the minimum value of Castigliano's functional;

f_v is the function of the vector argument \vec{T}_S ;

n_v is the general number of constraints-equalities $f_v(\vec{T}_S)$ and $f_x(\vec{T}_S)$ which define the hyperplane of feasible decisions \mathfrak{S}_T in the sought space.

For Castigliano's functional C we will consider only those Euler's equations that define the strain compatibility conditions and are expressed depending on shear forces flows $\vec{T}_S = \{T_{S,j}\}^T$, $j = \overline{1, n_r}$. Let us rewrite Castigliano's functional C Equation (2.6) replacing normal stresses $\sigma(\zeta)$ by Equation (1.1), and shear stresses $\tau(\zeta)$ – by the dependence on shear forces flows Equation (1.2) as presented below:

$$\tau_j(\zeta) = \frac{1}{\delta_j(\zeta)} \left(T_{S,j} - \frac{Q_z}{I_y} S_{oy,j}(\zeta) - \frac{Q_y}{I_z} S_{oz,j}(\zeta) - \frac{M_\varpi}{I_\varpi} S_{o\varpi,j}(\zeta) \right); \quad (3.4)$$

$$\begin{aligned} C = & \frac{1}{2G} \left(\sum_{j=1}^{n_r} \int_{\ell_j} \frac{1}{2(1+\nu)} \left(\frac{N}{A} + \frac{M_y}{I_y} z_j + \frac{M_z}{I_z} y_j + \frac{B}{I_\varpi} \varpi_j \right)^2 \delta_j d\zeta + \right. \\ & \left. + \int_{\ell_j} \left(T_{S,j}^2 - 2T_{S,j} \frac{Q_z}{I_y} S_{oy,j} - 2T_{S,j} \frac{Q_y}{I_z} S_{oz,j} - 2T_{S,j} \frac{M_\varpi}{I_\varpi} S_{o\varpi,j} \right) \frac{d\zeta}{\delta_j} + \right. \\ & \left. + \int_{\ell_j} \left(\frac{Q_z}{I_y} S_{oy,j} + \frac{Q_y}{I_z} S_{oz,j} + \frac{M_\varpi}{I_\varpi} S_{o\varpi,j} \right)^2 \frac{d\zeta}{\delta_j} \right), \end{aligned} \quad (3.5)$$

where the functional dependence on the angular position ζ is omitted to simplify the presented formulas.

Let us leave in Equation (3.5) those summands that depend on shear forces flows values $\vec{T}_S = \{T_{S,j}\}^T$, $j = \overline{1, n_r}$, and also denote by the symbol ... all other summands that do not depend on the vector \vec{T}_S . In this way we can obtain Castigliano's functional C in terms of shear forces flows $\vec{T}_S = \{T_{S,j}\}^T$ [5] as presented below:

$$C = \sum_{j=1}^{n_r} \left(\int_{\ell_j} \left(\frac{T_{S,j}^2}{2G} - T_{S,j} \frac{Q_z}{GI_y} S_{oy,j} - T_{S,j} \frac{Q_y}{GI_z} S_{oz,j} - T_{S,j} \frac{M_\varpi}{GI_\varpi} S_{o\varpi,j} \right) \frac{d\zeta}{\delta_j} + \dots \right); \quad (3.6)$$

$$C = \sum_{j=1}^{n_r} \left(\frac{T_{S,j}^2}{2G} \int_{\ell_j} \frac{d\zeta}{\delta_j} - T_{S,j} \frac{Q_z}{GI_y} \int_{\ell_j} S_{oy,j} \frac{d\zeta}{\delta_j} - T_{S,j} \frac{Q_y}{GI_z} \int_{\ell_j} S_{oz,j} \frac{d\zeta}{\delta_j} - T_{S,j} \frac{M_\varpi}{GI_\varpi} \int_{\ell_j} S_{o\varpi,j} \frac{d\zeta}{\delta_j} + \dots \right), \quad (3.7)$$

where the integral $\int_{\ell_j} \frac{d\zeta}{\delta_j}$ can be calculated according to Equation (2.1), and the integrals $\int_{\ell_j} S_{oy,j} \frac{d\zeta}{\delta_j}$, $\int_{\ell_j} S_{oz,j} \frac{d\zeta}{\delta_j}$ and $\int_{\ell_j} S_{o\varpi,j} \frac{d\zeta}{\delta_j}$ – using following Equations (3.8)–(3.10), respectively, $\forall \kappa: \vec{s}_\kappa^\zeta \in \mathbb{R}_j^\zeta \wedge \vec{s}_\kappa^\zeta \in \mathbb{S}^\zeta$;

$$S_{hz,j} = \int_{\ell_{rj}} \frac{S_{oz,j}^\zeta(\zeta) d\zeta}{\delta(\zeta)} = \sum_{\kappa=1}^{n_{\zeta rj}} \left(\frac{l_\kappa^\zeta}{6\delta_\kappa^\zeta} (S_{oz,\kappa}^{\zeta, start} + 4S_{oz,\kappa}^{\zeta, mid} + S_{oz,\kappa}^{\zeta, end}) \right); \tag{3.8}$$

$$S_{hy,j} = \int_{\ell_{rj}} \frac{S_{oy,j}^\zeta(\zeta) d\zeta}{\delta(\zeta)} = \sum_{\kappa=1}^{n_{\zeta rj}} \left(\frac{l_\kappa^\zeta}{6\delta_\kappa^\zeta} (S_{oy,\kappa}^{\zeta, start} + 4S_{oy,\kappa}^{\zeta, mid} + S_{oy,\kappa}^{\zeta, end}) \right); \tag{3.9}$$

$$S_{h\varpi,j} = \int_{\ell_{rj}} \frac{S_{o\varpi,j}^\zeta(\zeta) d\zeta}{\delta(\zeta)} = \sum_{\kappa=1}^{n_{\zeta rj}} \left(\frac{l_\kappa^\zeta}{6\delta_\kappa^\zeta} (S_{o\varpi,\kappa}^{\zeta, start} + 4S_{o\varpi,\kappa}^{\zeta, mid} + S_{o\varpi,\kappa}^{\zeta, end}) \right). \tag{3.10}$$

Let us define the following column vectors consisting of n_r elements, $\forall j = \overline{1, n_r}$ (according to the number of edges of the graph \mathbf{G}):

$$\vec{S}_{hz} = \begin{bmatrix} S_{hz,1} \\ S_{hz,2} \\ \vdots \\ S_{hz,n_r} \end{bmatrix}; \quad \vec{S}_{hy} = \begin{bmatrix} S_{hy,1} \\ S_{hy,2} \\ \vdots \\ S_{hy,n_r} \end{bmatrix}; \quad \vec{S}_{h\varpi} = \begin{bmatrix} S_{h\varpi,1} \\ S_{h\varpi,2} \\ \vdots \\ S_{h\varpi,n_r} \end{bmatrix}. \tag{3.11}$$

Using the weighting matrix of unbranched sectional parts \mathbf{W} , Equation (2.2), as well as column vectors \vec{S}_{hz} , \vec{S}_{hy} and $\vec{S}_{h\varpi}$, Equation (3.11), we can rewrite Castigliano’s functional, Equation (3.7), as the following vector-matrix equation:

$$C = \frac{1}{2G} \vec{T}_S^T \mathbf{W} \vec{T}_S - \vec{T}_S^T \frac{Q_y}{GI_z} \vec{S}_{hz} - \vec{T}_S^T \frac{Q_z}{GI_y} \vec{S}_{hy} - \vec{T}_S^T \frac{M_\varpi}{GI_\varpi} \vec{S}_{h\varpi} + \dots \tag{3.12}$$

Next, for each section branch point we can develop an equation of shear forces flows equilibrium in terms of projections on the longitudinal axis of the thin-walled bar. In order to obtain the general view for these equations (the system of equations by the number of branch points in the section), we can use the incidence matrices $\mathbf{\dot{I}}$ and $|\mathbf{\dot{I}}|$ introduced above, which reflect the topological structure of the considered cross-section of the thin-walled bar. In this case we obtain the following system of equations presented below in the matrix-vector form:

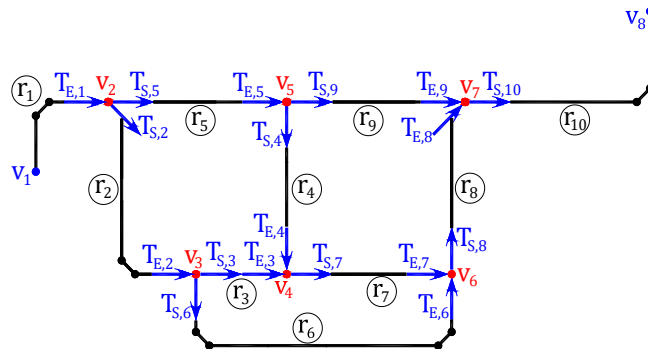


Figure 5. Relating to formulate equilibrium equations for shear stresses flows in branch points of a thin-walled bar.

$$\left(|\mathbf{\dot{I}}| + \mathbf{\dot{I}} \right) \vec{T}_S - \left(|\mathbf{\dot{I}}| - \mathbf{\dot{I}} \right) \vec{T}_E = \mathbf{0}, \tag{3.13}$$

where $\vec{T}_S = \{T_{S,j}\}^T$, $j = \overline{1, n_r}$ is the vector of shear forces flows at the start points of unbranched sectional parts;

$\vec{T}_E = \{T_{E,j}\}^T$, $j = \overline{1, n_r}$ is the vector of shear forces flows at the end points of unbranched sectional parts:

$$\vec{T}_E = \vec{T}_S - \Delta\vec{T}, \quad (3.14)$$

where $\Delta\vec{T} = \{\Delta T_j\}^T$, $j = \overline{1, n_r}$ is the vector of shear forces flows increments for each unbranched sectional part:

$$\Delta\vec{T}_j = \frac{Q_y}{I_z} \vec{S}_{z,j} + \frac{Q_z}{I_y} \vec{S}_{y,j} + \frac{M_\varpi}{I_\varpi} \vec{S}_{\varpi,j}; \quad (3.15)$$

where the vectors $\vec{S}_{z,j}$, $\vec{S}_{y,j}$, $\vec{S}_{\varpi,j}$ are presented below:

$$\vec{S}_z = \begin{bmatrix} S_{z,1} \\ S_{z,2} \\ \vdots \\ S_{z,n_r} \end{bmatrix}; \quad \vec{S}_y = \begin{bmatrix} S_{y,1} \\ S_{y,2} \\ \vdots \\ S_{y,n_r} \end{bmatrix}; \quad \vec{S}_\varpi = \begin{bmatrix} S_{\varpi,1} \\ S_{\varpi,2} \\ \vdots \\ S_{\varpi,n_r} \end{bmatrix}; \quad (3.16)$$

and the components of vectors $\vec{S}_{z,j}$, $\vec{S}_{y,j}$, $\vec{S}_{\varpi,j}$ can be calculated as follow, $\forall \kappa: \delta_\kappa^\zeta \in \mathbf{R}_j^\zeta \wedge \delta_\kappa^\zeta \in \mathbf{S}^\zeta$:

$$S_{z,j} = \int_{\ell_{rj}} y^\zeta(\zeta) \delta(\zeta) d\zeta = \sum_{\kappa=1}^{n_{\zeta rj}} \left(\delta_\kappa^\zeta I_\kappa^\zeta \left(y_\kappa^{\zeta, start} + \frac{1}{2} \Delta y_\kappa^\zeta \right) \right); \quad (3.17)$$

$$S_{y,j} = \int_{\ell_{rj}} z^\zeta(\zeta) \delta(\zeta) d\zeta = \sum_{\kappa=1}^{n_{\zeta rj}} \left(\delta_\kappa^\zeta I_\kappa^\zeta \left(z_\kappa^{\zeta, start} + \frac{1}{2} \Delta z_\kappa^\zeta \right) \right); \quad (3.18)$$

$$S_{\varpi,j} = \int_{\ell_{rj}} \varpi^\zeta(\zeta) \delta(\zeta) d\zeta = \sum_{\kappa=1}^{n_{\zeta rj}} \left(\delta_\kappa^\zeta I_\kappa^\zeta \left(\varpi_\kappa^{\zeta, start} + \frac{1}{2} \Delta \varpi_\kappa^\zeta \right) \right). \quad (3.19)$$

Let us rewrite the system of equations Equation (3.13) substituting \vec{T}_E according to Equation (3.14). We obtain the following system of equations:

$$\left(|\mathbf{i}| + \mathbf{i} \right) \vec{T}_S - \left(|\mathbf{i}| - \mathbf{i} \right) \times \left(\vec{T}_S - \Delta\vec{T} \right) = \mathbf{0}; \quad (3.20)$$

$$\left(|\mathbf{i}| - \mathbf{i} \right) \vec{T}_S - \left(|\mathbf{i}| - \mathbf{i} \right) \vec{T}_S + \left(|\mathbf{i}| - \mathbf{i} \right) \Delta\vec{T} = \mathbf{0}; \quad (3.21)$$

$$2\mathbf{i} \vec{T}_S + \left(|\mathbf{i}| - \mathbf{i} \right) \Delta\vec{T} = \mathbf{0}; \quad (3.22)$$

and taking into account Equation (3.15):

$$2\mathbf{i} \vec{T}_S + \left(|\mathbf{i}| - \mathbf{i} \right) \times \left(\frac{Q_y}{I_z} \vec{S}_{z,j} + \frac{Q_z}{I_y} \vec{S}_{y,j} + \frac{M_\varpi}{I_\varpi} \vec{S}_{\varpi,j} \right) = \mathbf{0}. \quad (3.23)$$

The system of equations in Equation (3.23) in the matrix-vector form has n_v equilibrium equations. The last equation is linear-dependent or a linear combination from the previous $n_v - 1$ equations. Let us rewrite Equation (3.23) excluding the last equilibrium equation:

$$2\mathbf{i}' \vec{T}_S + \left(|\mathbf{i}'| - \mathbf{i}' \right) \times \left(\frac{Q_y}{I_z} \vec{S}_{z,j} + \frac{Q_z}{I_y} \vec{S}_{y,j} + \frac{M_\varpi}{I_\varpi} \vec{S}_{\varpi,j} \right) = \mathbf{0}; \quad (3.24)$$

where \mathbf{i}' is the incidence matrix of the graph \mathbf{G} truncated by the last row with dimensions $(n_v - 1) \times n_r$,

$$\mathbf{i}' = \{g_{ij} \mid i = \overline{1, n_v - 1}, j = \overline{1, n_r}\};$$

$|\dot{\mathbf{I}}'|$ is the matrix composed using the modulus of elements g_{ij} of the truncated matrix $\dot{\mathbf{I}}'$ as $|\dot{\mathbf{I}}'| = \left\{ \left| g_{ij} \right| \mid i = \overline{1, n_v - 1}, j = \overline{1, n_r} \right\}$.

It is possible to derive the last equilibrium equation relating to the longitudinal axis $x - x$ of the thin-walled bar as a condition of the static equivalence of the torsion moment caused by the shear forces flows to the total torque M_x acting in the cross-section of the thin-walled bar:

$$M_x - \sum_{j=1}^{n_r} \int_{\ell_j} T_j(\zeta) d\omega = 0; \tag{3.25}$$

where $T_j(\zeta)$ is the shear forces flow at some point of the cross-section, which can be expressed depending on shear forces flow $T_{S,j}(\zeta)$ at the start point of the corresponded unbranched part of the section as follow:

$$T_j = T_{S,j} - \frac{Q_y}{I_z} S_{oz,j} - \frac{Q_z}{I_y} S_{oy,j} - \frac{M_{\varpi}}{I_{\varpi}} S_{o\varpi,j}, \tag{3.26}$$

where we omitted the functional dependence from the angular position ζ (to simplify presented formulas).

Then:

$$M_x - \sum_{j=1}^{n_r} \int_{\ell_j} \left(T_{S,j} - \frac{Q_y}{I_z} S_{oz,j} - \frac{Q_z}{I_y} S_{oy,j} - \frac{M_{\varpi}}{I_{\varpi}} S_{o\varpi,j} \right) \rho d\zeta = 0;$$

$$M_x - \sum_{j=1}^{n_r} \left(T_{S,j} \int_{\ell_j} \rho d\zeta - \frac{Q_y}{I_z} \int_{\ell_j} S_{oz,j} \rho d\zeta - \frac{Q_z}{I_y} \int_{\ell_j} S_{oy,j} \rho d\zeta - \frac{M_{\varpi}}{I_{\varpi}} \int_{\ell_j} S_{o\varpi,j} \rho d\zeta \right) = 0.$$

Finally, we obtain [5]:

$$\sum_{j=1}^{n_r} T_{S,j} \int_{\ell_j} \rho d\zeta - \frac{Q_y}{I_z} \sum_{j=1}^{n_r} \int_{\ell_j} S_{oz,j} \rho d\zeta - \frac{Q_z}{I_y} \sum_{j=1}^{n_r} \int_{\ell_j} S_{oy,j} \rho d\zeta - \frac{M_{\varpi}}{I_{\varpi}} \sum_{j=1}^{n_r} \int_{\ell_j} S_{o\varpi,j} \rho d\zeta - M_x = 0; \tag{3.27}$$

where integrals $\sum_{j=1}^{n_r} \int_{\ell_j} S_{oz,j} \rho d\zeta$, $\sum_{j=1}^{n_r} \int_{\ell_j} S_{oy,j} \rho d\zeta$ and $\sum_{j=1}^{n_r} \int_{\ell_j} S_{o\varpi,j} \rho d\zeta$ can be calculated using

Equations (3.28)–(3.30), respectively, $\forall \kappa : \vec{s}_{\kappa}^{\zeta} \in \mathbb{R}_j^{\zeta} \wedge \vec{s}_{\kappa}^{\zeta} \in \mathbb{S}^{\zeta}$:

$$S_{\rho z} = \sum_{j=1}^{n_r} \int_{\ell_{rj}} S_{oz,j}^{\zeta}(\omega) \rho d\zeta = \sum_{j=1}^{n_r} \left(\sum_{\kappa=1}^{n_{\zeta rj}} \frac{\Delta \omega_{\kappa}^{\zeta}}{6} (S_{oz,\kappa}^{\zeta, start} + 4S_{oz,\kappa}^{\zeta, mid} + S_{oz,\kappa}^{\zeta, end}) \right); \tag{3.28}$$

$$S_{\rho y} = \sum_{j=1}^{n_r} \int_{\ell_{rj}} S_{oy,j}^{\zeta}(\omega) \rho d\zeta = \sum_{j=1}^{n_r} \left(\sum_{\kappa=1}^{n_{\zeta rj}} \frac{\Delta \omega_{\kappa}^{\zeta}}{6} (S_{oy,\kappa}^{\zeta, start} + 4S_{oy,\kappa}^{\zeta, mid} + S_{oy,\kappa}^{\zeta, end}) \right); \tag{3.29}$$

$$S_{\rho \varpi} = \sum_{j=1}^{n_r} \int_{\ell_{rj}} S_{o\varpi,j}^{\zeta}(\omega) \rho d\zeta = \sum_{j=1}^{n_r} \left(\sum_{\kappa=1}^{n_{\zeta rj}} \frac{\Delta \omega_{\kappa}^{\zeta}}{6} (S_{o\varpi,\kappa}^{\zeta, start} + 4S_{o\varpi,\kappa}^{\zeta, mid} + S_{o\varpi,\kappa}^{\zeta, end}) \right). \tag{3.30}$$

Let us rewrite the constraints-equality Equation (3.27) using vector representation taking into account Equations (3.28)–(3.30) as presented below:

$$\vec{\omega}^T \vec{T}_S - \frac{Q_y}{I_z} S_{\rho z} - \frac{Q_z}{I_y} S_{\rho y} - \frac{M_{\varpi}}{I_{\varpi}} S_{\rho \varpi} - M_x = 0. \tag{3.31}$$

Thus, the formulated problem is presented as a mathematical programming task of searching for the unknown values of shear forces flows at the start points of the unbranched parts of the section:

$$\vec{T}_S = \{ T_{S,j} \}^T, \quad j = \overline{1, n_r}, \tag{3.32}$$

which ensure the least value of the following Castigliano's functional **C** Equation (3.12):

$$\mathbf{C} = \frac{1}{2G} \bar{\mathbf{T}}_S^T \mathbf{W} \bar{\mathbf{T}}_S - \bar{\mathbf{T}}_S^T \frac{Q_y}{GI_z} \bar{\mathbf{S}}_{hz} - \bar{\mathbf{T}}_S^T \frac{Q_z}{GI_y} \bar{\mathbf{S}}_{hy} - \bar{\mathbf{T}}_S^T \frac{M_\varpi}{GI_\varpi} \bar{\mathbf{S}}_{h\varpi} + \dots \rightarrow \min, \quad (3.33)$$

subject to the following equilibrium conditions Equations (3.24) and (3.31):

$$\begin{cases} 2\dot{\mathbf{i}}' \bar{\mathbf{T}}_S + (|\dot{\mathbf{i}}'| - \dot{\mathbf{i}}') \left(\frac{Q_y}{I_z} \bar{\mathbf{S}}_{z,j} + \frac{Q_z}{I_y} \bar{\mathbf{S}}_{y,j} + \frac{M_\varpi}{I_\varpi} \bar{\mathbf{S}}_{\varpi,j} \right) = \mathbf{0}; \\ \bar{\omega}^T \bar{\mathbf{T}}_S - \frac{Q_y}{I_z} S_{\rho z} - \frac{Q_z}{I_y} S_{\rho y} - \frac{M_\varpi}{I_\varpi} S_{\rho\varpi} - M_x = 0. \end{cases} \quad (3.34)$$

The method of Lagrange multipliers can be used to reduce the mathematical programming task Equations (3.32)–(3.34) to the searching for the stationary point of the following modified functional $\Lambda(\bar{\mathbf{T}}_S, \bar{\lambda}^T, \lambda_{n_v})$:

$$\begin{aligned} \Lambda(\bar{\mathbf{T}}_S, \bar{\lambda}^T, \lambda_{n_v}) = & \frac{1}{2G} \bar{\mathbf{T}}_S^T \mathbf{W} \bar{\mathbf{T}}_S - \bar{\mathbf{T}}_S^T \frac{Q_y}{GI_z} \bar{\mathbf{S}}_{hz} - \bar{\mathbf{T}}_S^T \frac{Q_z}{GI_y} \bar{\mathbf{S}}_{hy} - \bar{\mathbf{T}}_S^T \frac{M_\varpi}{GI_\varpi} \bar{\mathbf{S}}_{h\varpi} + \\ & + \bar{\lambda}^T \left[2\dot{\mathbf{i}}' \bar{\mathbf{T}}_S + (|\dot{\mathbf{i}}'| - \dot{\mathbf{i}}') \left(\frac{Q_y}{I_z} \bar{\mathbf{S}}_{z,j} + \frac{Q_z}{I_y} \bar{\mathbf{S}}_{y,j} + \frac{M_\varpi}{I_\varpi} \bar{\mathbf{S}}_{\varpi,j} \right) \right] + \\ & + \lambda_{n_v} \left[\bar{\omega}^T \bar{\mathbf{T}}_S - \frac{Q_y}{I_z} S_{\rho z} - \frac{Q_z}{I_y} S_{\rho y} - \frac{M_\varpi}{I_\varpi} S_{\rho\varpi} - M_x \right] \rightarrow \min, \end{aligned} \quad (3.35)$$

where $\bar{\lambda} = \{\lambda_f\}$, $f = \overline{1, n_v - 1}$ is the vector of Lagrange multipliers consisting of $n_v - 1$ elements;

λ_{n_v} is an additional Lagrange multiplier.

The stationary conditions of the modified functional $\Lambda(\bar{\mathbf{T}}_S, \bar{\lambda}^T, \lambda_{n_v})$, Equation (3.35), can be transformed into a system of $n_r + n_v$ linear algebraic equations and presented in vector-matrix form as follow [5]:

$$\begin{aligned} \begin{bmatrix} \frac{1}{G} \mathbf{W} & 2\dot{\mathbf{i}}'^T & \Delta\omega_r^\xi \\ 2\dot{\mathbf{i}}' & \Theta_{n_v-1, n_v-1} & \mathbf{0}_{n_v-1} \\ (\Delta\omega_r^\xi)^T & \mathbf{0}_{n_v-1}^T & 0 \end{bmatrix} \times \begin{bmatrix} \bar{\mathbf{T}}_S \\ \bar{\lambda} \\ \lambda_{n_v} \end{bmatrix} = M_x \times \begin{bmatrix} \mathbf{0}_{n_r} \\ \mathbf{0}_{n_v-1} \\ 1 \end{bmatrix} + \frac{Q_y}{I_z} \times \begin{bmatrix} \frac{\bar{\mathbf{S}}_{hz}}{G} \\ (\dot{\mathbf{i}}' - |\dot{\mathbf{i}}'|) \bar{\mathbf{S}}_z \\ S_{\rho z} \end{bmatrix} + \\ + \frac{Q_z}{I_y} \times \begin{bmatrix} \frac{\bar{\mathbf{S}}_{hy}}{G} \\ (\dot{\mathbf{i}}' - |\dot{\mathbf{i}}'|) \bar{\mathbf{S}}_y \\ S_{\rho y} \end{bmatrix} + \frac{M_\varpi}{I_\varpi} \times \begin{bmatrix} \frac{\bar{\mathbf{S}}_{h\varpi}}{G} \\ (\dot{\mathbf{i}}' - |\dot{\mathbf{i}}'|) \bar{\mathbf{S}}_\varpi \\ S_{\rho\varpi} \end{bmatrix} \end{aligned} \quad (3.36)$$

where

$$\mathbf{M} = \begin{bmatrix} \frac{1}{G} \mathbf{W} & 2\dot{\mathbf{i}}'^T & \Delta\omega_r^\xi \\ 2\dot{\mathbf{i}}' & \Theta_{n_v-1, n_v-1} & \mathbf{0}_{n_v-1} \\ (\Delta\omega_r^\xi)^T & \mathbf{0}_{n_v-1}^T & 0 \end{bmatrix};$$

\mathbf{M} is a square matrix with dimensions $(n_r + n_v) \times (n_r + n_v)$, where n_r and n_v are the numbers of edges

and vertices of the graph \mathbf{G}^r , respectively; $\Delta\omega_r^\zeta$ is the column vector of sectorial coordinates increments $\Delta\omega_r^\zeta = \left\{ \Delta\omega_{r,j}^\zeta \mid j = \overline{1, n_r} \right\}^T$ consisting of n_r components calculated according to Equation (2.3); $\vec{S}_y, \vec{S}_z, \vec{S}_\omega$ are the column vectors Equation (3.16) with n_r components calculated according to Equations (3.17)–(3.19) respectively; $\vec{S}_{hy}, \vec{S}_{hz}, \vec{S}_{h\omega}$ are the column vectors Equation (3.11) with n_r components calculated according to Equations (3.8)–(3.10), respectively; $S_{\rho y}, S_{\rho z}, S_{\rho\omega}$ are the integral section properties calculated according to Equations (3.28)–(3.30), respectively.

The solution of the system of equations in Equation (3.36) determines the column vector of shear forces flows $\vec{T}_S = \left\{ T_{S,j} \right\}^T, j = \overline{1, n_r}$, at the start points of unbranched cross-section parts. The vector \vec{T}_S can be also presented as follow:

$$\vec{T}_S = M_x \vec{b}_x + \frac{Q_y}{I_z} \vec{b}_z + \frac{Q_z}{I_y} \vec{b}_y + \frac{M_\omega}{I_\omega} \vec{b}_\omega. \tag{3.37}$$

In this case, the system of algebraic equations, Equation (3.36), disintegrates and transforms into four systems of $n_r + n_v$ algebraic equations relating to the column vectors $\vec{b}_x, \vec{b}_y, \vec{b}_z$ and \vec{b}_ω consisting of n_r elements [5] as presented below:

$$\mathbf{M} \times \begin{bmatrix} \vec{b}_x \\ \vec{\lambda}_x \\ \lambda_{n_v,x} \end{bmatrix} = \begin{bmatrix} \mathbf{0}_{n_r} \\ \mathbf{0}_{n_v-1} \\ 1 \end{bmatrix}; \quad \mathbf{M} \times \begin{bmatrix} \vec{b}_y \\ \vec{\lambda}_y \\ \lambda_{n_v,y} \end{bmatrix} = \begin{bmatrix} \frac{\vec{S}_{hy}}{G} \\ (\mathbf{i}' - |\mathbf{i}'|) \times \vec{S}_y \\ S_{\rho y} \end{bmatrix}; \tag{3.38}$$

$$\mathbf{M} \times \begin{bmatrix} \vec{b}_z \\ \vec{\lambda}_z \\ \lambda_{n_v,z} \end{bmatrix} = \begin{bmatrix} \frac{\vec{S}_{hz}}{G} \\ (\mathbf{i}' - |\mathbf{i}'|) \times \vec{S}_z \\ S_{\rho z} \end{bmatrix}; \quad \mathbf{M} \times \begin{bmatrix} \vec{b}_\omega \\ \vec{\lambda}_\omega \\ \lambda_{n_v,\omega} \end{bmatrix} = \begin{bmatrix} \frac{\vec{S}_{h\omega}}{G} \\ (\mathbf{i}' - |\mathbf{i}'|) \times \vec{S}_\omega \\ S_{\rho\omega} \end{bmatrix},$$

where $\vec{\lambda}_x = \left\{ \lambda_{x,f} \right\}^T, \vec{\lambda}_y = \left\{ \lambda_{y,f} \right\}^T, \vec{\lambda}_z = \left\{ \lambda_{z,f} \right\}^T, \vec{\lambda}_\omega = \left\{ \lambda_{\omega,f} \right\}^T, f = \overline{1, n_v - 1}$ are the unknown column vectors of Lagrange multipliers consisting of $n_v - 1$ elements;

$\lambda_{n_v,x}, \lambda_{n_v,y}, \lambda_{n_v,z}, \lambda_{n_v,\omega}$ are the additional Lagrange multipliers.

The projection of the vector $\vec{b}_x = \left\{ b_{x,j} \mid j = \overline{1, n_r} \right\}$ defined of the set of n_r unbranched sectional parts into the set of sectional segments $\vec{b}_x^\zeta = \left\{ b_{x,\kappa}^\zeta \mid \kappa = \overline{1, n_\zeta - 1} \right\}$ can be written as: $b_{x,\kappa}^\zeta = b_{x,j} \forall \kappa: \vec{s}_\kappa^\zeta \subseteq \mathbf{R}_j^\zeta$; and $b_{x,\kappa}^\zeta = 0 \forall \kappa: \vec{s}_\kappa^\zeta \cap \mathbf{R}_j^\zeta = \emptyset$. Similarly, the column vectors $\vec{b}_y = \left\{ b_{y,j} \mid j = \overline{1, n_r} \right\}, \vec{b}_z = \left\{ b_{z,j} \mid j = \overline{1, n_r} \right\}$ and $\vec{b}_\omega = \left\{ b_{\omega,j} \mid j = \overline{1, n_r} \right\}$ can be also projected into the set of sectional segments obtaining corresponded column vectors $\vec{b}_y^\zeta = \left\{ b_{y,\kappa}^\zeta \mid \kappa = \overline{1, n_\zeta - 1} \right\}, \vec{b}_z^\zeta = \left\{ b_{z,\kappa}^\zeta \mid \kappa = \overline{1, n_\zeta - 1} \right\}$ and $\vec{b}_\omega^\zeta = \left\{ b_{\omega,\kappa}^\zeta \mid \kappa = \overline{1, n_\zeta - 1} \right\}$.

The following transformations for the first moments of inertia and for the sectorial moment of inertia should be performed, $\forall \kappa = \overline{1, n_\zeta - 1}$:

$$\vec{S}_{oz,\kappa}^\zeta \leftarrow \left\{ S_{oz,\kappa}^\zeta - b_{z,\kappa}^\zeta \right\}; \quad \vec{S}_{oy,\kappa}^\zeta \leftarrow \left\{ S_{oy,\kappa}^\zeta - b_{y,\kappa}^\zeta \right\} \tag{3.39}$$

$$\vec{S}_{o\omega,\kappa}^\zeta \leftarrow \left\{ S_{o\omega,\kappa}^\zeta - b_{\omega,\kappa}^\zeta \right\}; \quad \vec{S}_{o\omega,\kappa}^\zeta \leftarrow \left\{ \vec{S}_{o\omega,\kappa}^\zeta - a_\kappa^\zeta \frac{I_\omega}{\Omega_0} \right\}. \tag{3.40}$$

Let us define the sets of shear forces flows values for the start, middle and end points at the middle line of the sectional segments $\mathbf{T}^{\zeta, \text{st}} = \{T_{\kappa}^{\zeta, \text{st}}\}$, $\mathbf{T}^{\zeta, \text{mid}} = \{T_{\kappa}^{\zeta, \text{mid}}\}$, $\mathbf{T}^{\zeta, \text{end}} = \{T_{\kappa}^{\zeta, \text{end}}\}$, $\kappa = \overline{1, n_{\zeta} - 1}$, consisting of $n_{\zeta} - 1$ elements (by the number of sectional segments) as presented below [22]:

$$T_{\kappa}^{\zeta, \text{start}} = \frac{\wp H}{\Omega_0} a_{\kappa}^{\zeta} - \frac{Q_y}{I_z} \bar{S}_{oz, \kappa}^{\zeta, \text{start}} - \frac{Q_z}{I_y} \bar{S}_{oy, \kappa}^{\zeta, \text{start}} - \frac{M_{\varpi}}{I_{\varpi}} \tilde{S}_{o\varpi, \kappa}^{\zeta, \text{start}}, \quad (3.41)$$

$$T_{\kappa}^{\zeta, \text{mid}} = \frac{\wp H}{\Omega_0} a_{\kappa}^{\zeta} - \frac{Q_y}{I_z} \bar{S}_{oz, \kappa}^{\zeta, \text{mid}} - \frac{Q_z}{I_y} \bar{S}_{oy, \kappa}^{\zeta, \text{mid}} - \frac{M_{\varpi}}{I_{\varpi}} \tilde{S}_{o\varpi, \kappa}^{\zeta, \text{mid}}, \quad (3.42)$$

$$T_{\kappa}^{\zeta, \text{end}} = \frac{\wp H}{\Omega_0} a_{\kappa}^{\zeta} - \frac{Q_y}{I_z} \bar{S}_{oz, \kappa}^{\zeta, \text{end}} - \frac{Q_z}{I_y} \bar{S}_{oy, \kappa}^{\zeta, \text{end}} - \frac{M_{\varpi}}{I_{\varpi}} \tilde{S}_{o\varpi, \kappa}^{\zeta, \text{end}}, \quad (3.43)$$

where the first moments of inertia $\bar{S}_{oz, \kappa}^{\zeta}$, $\bar{S}_{oy, \kappa}^{\zeta}$ and the sectorial moment of inertia $\tilde{S}_{o\varpi, \kappa}^{\zeta}$ are calculated using transformations in Equations (3.39) and (3.40), respectively.

The shear stresses for each κ^{th} sectional segment $\tau^{\zeta} = \{\bar{\tau}_{\kappa}^{\zeta} = \{\tau_{\kappa}^{\zeta, \text{start}}, \tau_{\kappa}^{\zeta, \text{mid}}, \tau_{\kappa}^{\zeta, \text{end}}\}\}$, $\kappa = \overline{1, n_{\zeta} - 1}$, can be calculated as presented below:

$$\tau_{\kappa}^{\zeta} = \left\{ \begin{array}{l} \tau_{\kappa}^{\zeta, \text{start}} = \frac{T_{\kappa}^{\zeta, \text{start}}}{\delta_{\kappa}^{\zeta}} \pm \frac{(1 - \wp) H \delta_{\kappa}^{\zeta}}{I_k} \\ \tau_{\kappa}^{\zeta, \text{mid}} = \frac{T_{\kappa}^{\zeta, \text{mid}}}{\delta_{\kappa}^{\zeta}} \pm \frac{(1 - \wp) H \delta_{\kappa}^{\zeta}}{I_k} \\ \tau_{\kappa}^{\zeta, \text{end}} = \frac{T_{\kappa}^{\zeta, \text{end}}}{\delta_{\kappa}^{\zeta}} \pm \frac{(1 - \wp) H \delta_{\kappa}^{\zeta}}{I_k} \end{array} \right\}, \quad (3.44)$$

where the torsion moment of inertia I_x and the parameter \wp are calculated as:

$$I_x = I_k + I_{\Gamma} = \frac{1}{3} \sum_{\kappa=1}^{n_{\zeta}-1} I_{\kappa}^{\zeta} (\delta_{\kappa}^{\zeta})^3 + I_{\Gamma}; \quad (3.45)$$

$$\wp = 1 - \frac{I_k}{I_x}. \quad (3.46)$$

The components $\left| \frac{T_{\kappa}^{\zeta, \text{start}}}{\delta_{\kappa}^{\zeta}} \right|$, $\left| \frac{T_{\kappa}^{\zeta, \text{mid}}}{\delta_{\kappa}^{\zeta}} \right|$ and $\left| \frac{T_{\kappa}^{\zeta, \text{end}}}{\delta_{\kappa}^{\zeta}} \right|$ in Equation (3.44) define shear stresses values for the

start, middle and end points at the middle line of κ^{th} sectional segment, accordingly. Besides, transition from the shear stresses related to the middle line of κ^{th} segment to the shear stresses at the outside longitudinal edges of this segment can be performed by addition or subtraction of the member $\frac{(1 - \wp)}{I_k} H \delta_{\kappa}^{\zeta}$.

3. Results and Discussion

3.1. Software implementation

The numerical algorithm developed and presented above has been implemented to the TONUS software (hereinafter – TONUS), which is a satellite of the SCAD Office environment [24], as shown in Figure 6. TONUS is intended to create cross-sections of thin-walled bars, to calculate their geometrical properties as well as to calculate normal, shear and equivalent stresses in these cross-sections [9]. TONUS allows to consider arbitrary (including open-closed) cross-sections of thin-walled bars. The cross-section of a thin-walled bar is constructed from the set of segments (stripes) by specifying node coordinates that define the position of segment ends as well as by specifying thicknesses for all segments.

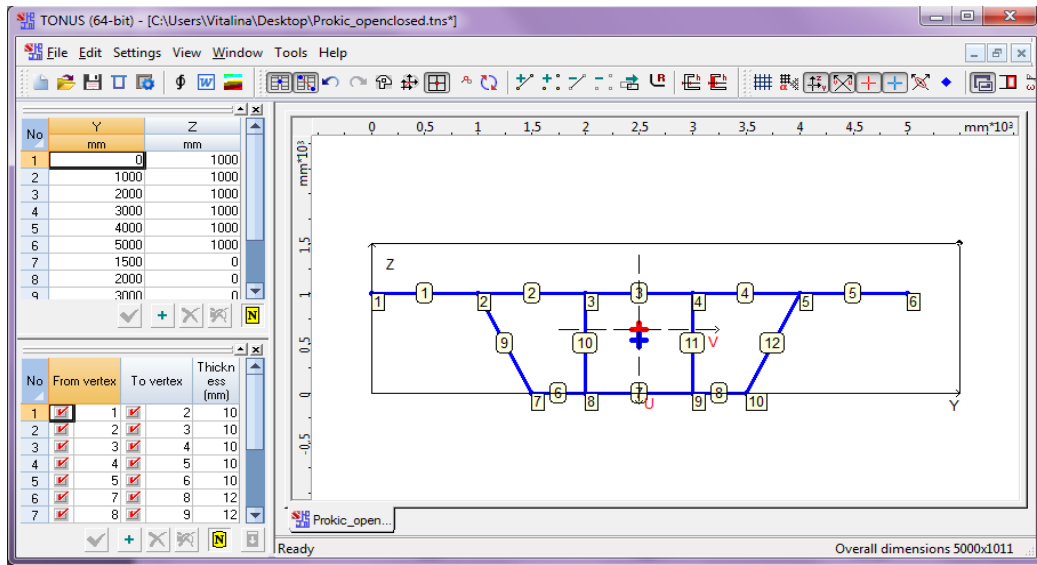


Figure 6. TONUS main window.

In addition to the calculation of geometrical properties for the cross-sections of thin-walled bars, TONUS also presents a sectorial coordinates diagram as well as static moment diagrams S_u , S_v and a first sectorial moment S_ω diagram.

To present normal, shear and equivalent stresses diagrams in the section of a thin-walled bar, the user should specify internal forces acting in the section. Initial data to construct normal stresses diagram include bending moments M_u and M_v relating to the main axis of inertia of the thin-walled bar cross-section, axial force N applied at the center of mass of the section, as well as warping bimoment B . Initial data to construct shear stresses diagram are shear forces Q_u and Q_v applied at the center of mass of the cross-section as well as total torque M_x and warping torque M_ω . In order to represent equivalent stresses diagram user should also specify a strength theory.

3.2. Example 1: open thin-walled cross-section

Let us consider an example of calculation of a thin-walled bar with open profile in order to validate the developed algorithm and verify the accuracy of the calculated sectorial cross-section properties and shear stresses caused by warping torsion.

Initial data for calculation are presented in Figure 7. The results of calculation, namely sectorial coordinates diagram ω [cm²], and shear stresses diagram related to the value of warping torque $\tau_\omega M_\omega^{-1} \times 10^7$ [cm⁻³], have been obtained in [18] and presented in Figure 8.

The results of calculation, namely sectorial coordinates ω , sectorial moment of inertia S_ω and shear stresses τ_ω caused by the warping torque $M_\omega = 10^7$ kN cm, have been also obtained using TONUS and presented in Figures 10–12.

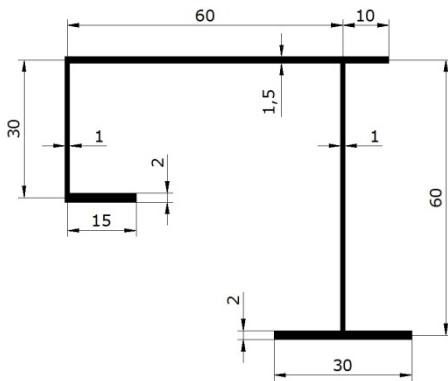


Figure 7. Dimensions [cm] of the open thin-walled section.

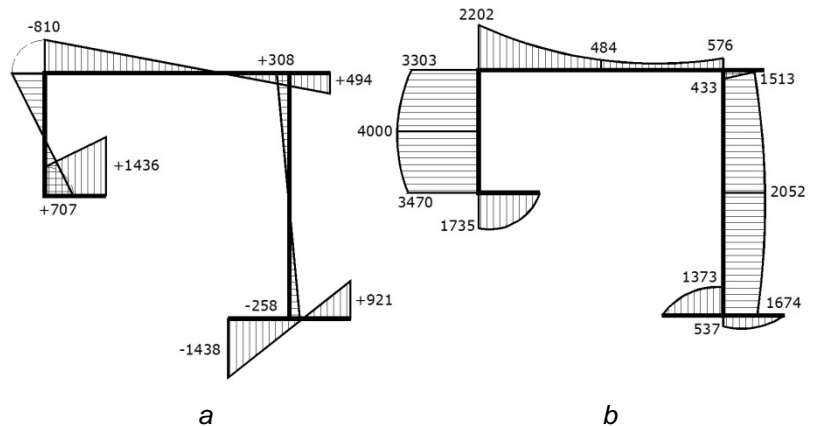


Figure 8. Results of calculation according to [18]: a – sectorial coordinate ω [cm²]; b – shear stresses related to the warping torque $\tau_\omega M_\omega^{-1} \times 10^7$ [cm⁻³].

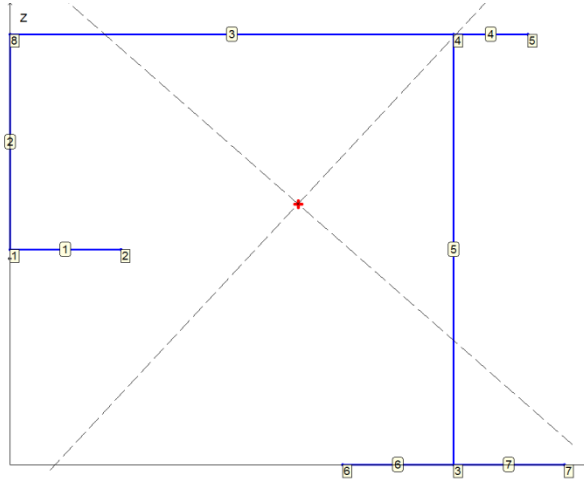


Figure 9. Considered cross-section with segments and points numbers.

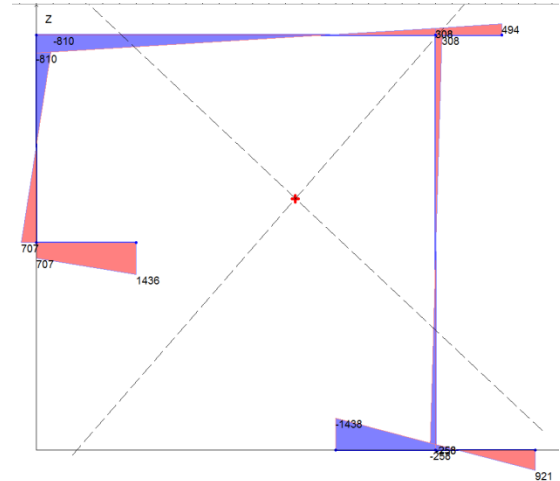


Figure 10. Results obtained using TONUS: sectorial coordinate ω [cm²].

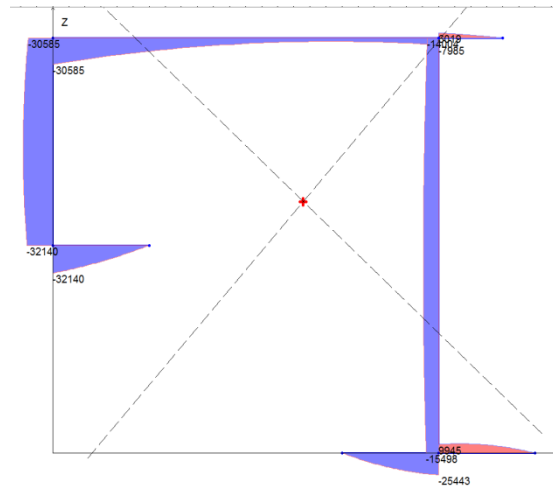


Figure 11. Results obtained using TONUS: sectorial moment of inertia S_ω [cm⁴].

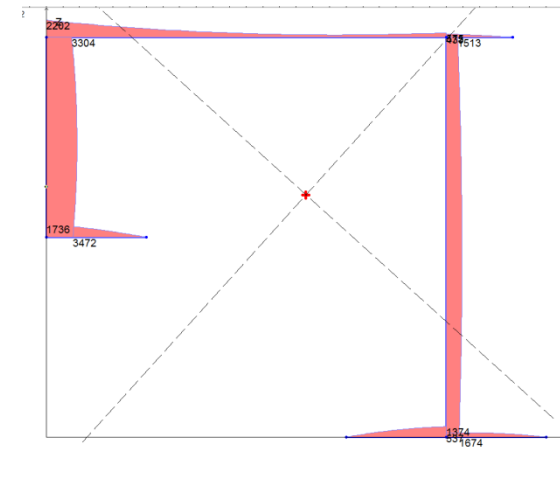


Figure 12. Results obtained using TONUS: modulus of shear stresses τ_ω [kN/cm²] caused by warping torsion for the value of warping torque $M_\omega = 10^7$ kN cm.

Table 1. Comparison of the first sectorial moment and shear stresses caused by the warping torque for the considered cross-section.

Section segment number (Figure 9)	Section point number (Figure 9)	First sectorial moment S_ω [cm ⁴]			Shear stresses τ_ω [kN/cm ²] (when $M_\omega = 10^7$ kN cm)		
		[18]	TONUS	Deviation,%	[18]	TONUS	Deviation,%
1	1	32126	32140	0.04	1735	1736	0.06
1	2	0	0	0	0	0	0
2	1	32126	32140	0.04	3470	3472	0.06
2	8	30580	30585	0.02	3303	3304	0.06
3	8	30580	30585	0.02	2202	2202	0
3	4	7999	7985	0.18	576	575	0.17
4	4	6013	6019	0.1	433	432	0.23
4	5	0	0	0	0	0	0
5	4	14008	14004	0.03	1513	1513	0
5	3	15498	15498	0	1674	1674	0
6	6	0	0	0	0	0	0
6	3	25423	25443	0.08	1373	1374	0.07
7	3	9943	9945	0.02	537	537	0
7	7	0	0	0	0	0	0

Table 2. Comparison of sectorial coordinates for the considered cross-section.

Section point number (Figure 9)	Sectorial coordinate ω [cm ²]		
	[18]	TONUS	Deviation, %
1	707	707	0
2	1436	1436	0
3	-258	-258	0
4	308	308	0
5	494	494	0
6	-1438	-1438	0
7	921	921	0
8	-810	-810	0

Sectorial first moment of inertia and shear stresses caused by warping torsion, as well as sectorial coordinates for considered thin-walled bar cross-section are presented in Tables 1 and 2. The comparisons have been made with some results presented in [18], which represent exact results for the considered example. As it can be seen, the deviations do not exceed 0.25 % in all cases. It proves the validity of the results obtained using the developed software.

3.3. Example 2: open-closed multi-contour thin-walled cross-section

Let us consider an example of calculation of a thin-walled bar with open-closed multi-contour profile in order to validate developed algorithm and verify calculation accuracy for geometrical cross-section properties and shear stresses caused by warping torsion, as well as shear force. The initial data for calculation are presented in Figure 13.

The calculation results, namely sectorial coordinates diagram ω [cm²], diagram of shear stresses caused by warping torsion related to the value of warping torque $\tau_{\omega} M_{\omega}^{-1} \times 10^7$ [cm⁻³], as well as diagram of shear stresses caused by acting of shear force related to the value of shear force $\tau_u Q_u^{-1} \times 10^5$ [cm⁻²] have been obtained by Prokić [18] and presented in Figure 14.

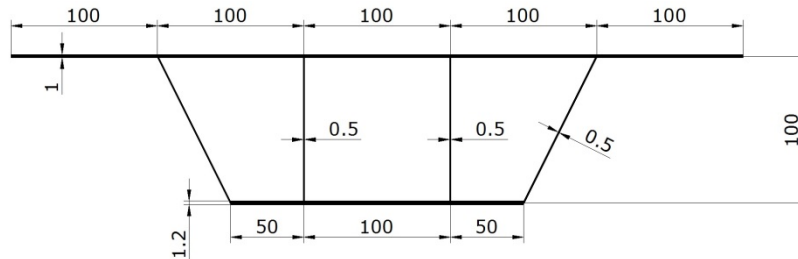


Figure 13. Dimensions [cm] of the open-closed multi-contour section of the thin-walled bar.

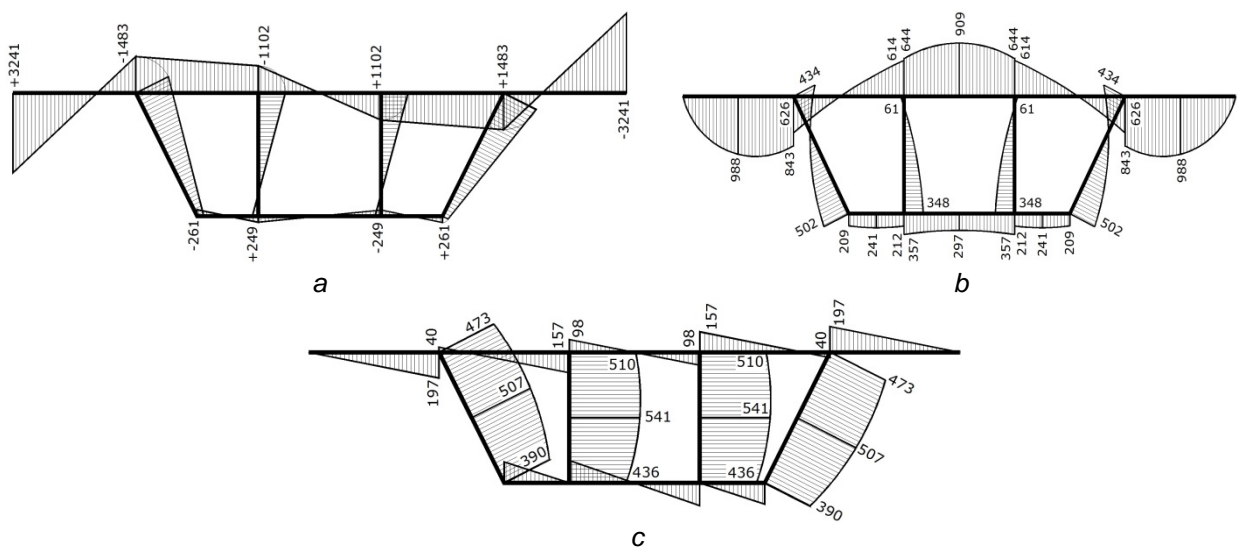


Figure 14. Results of calculations according to [18]: a – sectorial coordinates diagram ω [cm²]; b – shear stresses diagram caused by warping torsion related to the value of the warping torque $\tau_{\omega} M_{\omega}^{-1} \times 10^7$ [cm⁻³]; c – shear stresses diagram caused by shear force related to the value of shear force $\tau_u M_u^{-1} \times 10^5$ [cm⁻²].

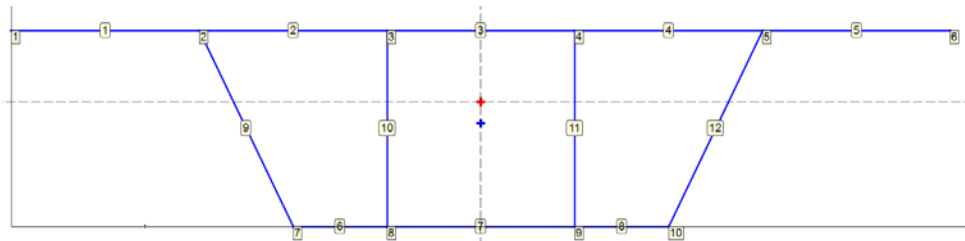


Figure 15. Cross-section with segments and points numbers.

The calculation results, namely sectorial coordinates ϖ , static moment S_v relating to the main axes of inertia $\nu - \nu$, first sectorial moment S_ϖ , shear stresses τ_u caused by shear force $Q_u = 10^5$ kN, as well as shear stresses τ_ϖ caused by warping torque $M_\varpi = 10^7$ kN cm for the considered cross-section section have been obtained using TONUS and presented in Figure 16.

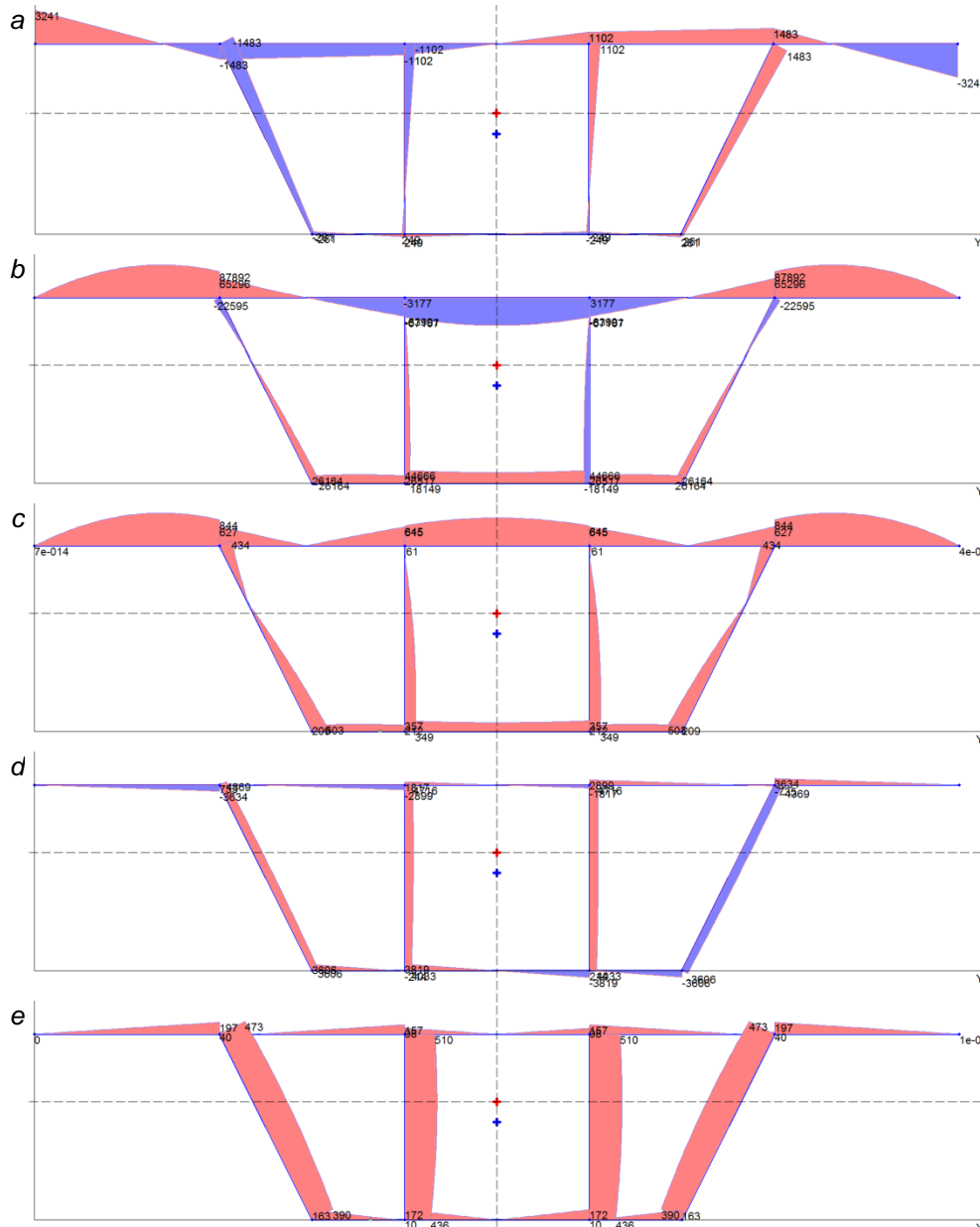


Figure 16. Results obtained using TONUS: a – distribution diagram of normalized sectorial coordinates ϖ [cm²]; b – distribution diagram of first sectorial moment S_ϖ [cm⁴]; c – distribution diagram of modulus of shear stresses τ_ϖ [kN/cm²], constructed depending on the value of the warping torque $M_\varpi = 10^7$ kN cm; d – distribution diagram for the first moment S_v [cm³] relating to the principle axis $\nu - \nu$; e – distribution diagram of modulus of shear stresses τ_u [kN/cm²], constructed depending on the value of shear force $Q_u = 10^5$ kN.

First moment S_v and first sectorial moment S_{ϖ} , shear stresses τ_u and τ_{ϖ} caused by shear force Q_u and warping torque M_{ϖ} , respectively, as well as sectorial coordinates ϖ for the considered cross-section are presented in Tables 3–5. The comparisons have been made with some results presented in [18], which represent exact results for the considered example. The deviations are no more than 0.3 % in all design cases. It proves the validity of the results obtained using the developed software.

Table 3. Comparison of first moments for considered cross-section.

Section segment number (Figure 15)	Section point number (Figure 15)	First sectorial moment S_{ϖ} [cm ⁴]			First moment S_v [cm ³]		
		[18]	TONUS	Deviation,%	[18]	TONUS	Deviation,%
1	1	0	0	0	0	0	0
1	2	87776	87892	0.13	3643	3634	0.25
2	2	65181	65296	0.18	740	741	0.14
2	3	63932	64036	0.16	2903	2899	0.14
3	3	67055	67159	0.16	1812	1817	0.28
6	7	26114	26164	0.19	3595	3606	0.3
6	8	26489	26517	0.11	–	10	–
7	8	44606	44666	0.13	3816	3819	0.08
9	2	22595	22595	0	4373	4369	0.09
9	7	26135	26164	0.11	3606	3606	0
10	3	3176	3177	0.03	4715	4716	0.02
10	8	18117	18149	0.15	4031	4033	0.05

Table 4. Comparison of shear stresses caused by the warping torque, as well as by the shear force for the considered cross-section.

Section segment number (Figure 15)	Section point number (Figure 15)	Shear stresses τ_{ϖ} [kN/cm ²] (when $M_{\varpi} = 10^7$ kN cm)			Shear stresses τ_u [kN/cm ²] (when $Q_u = 10^5$ kN)		
		[18]	TONUS	Deviation, %	[18]	TONUS	Deviation, %
1	1	0	0	0	0	0	0
1	2	843	844	0.12	197	197	0
2	2	626	627	0.16	40	40	0
2	3	614	615	0.16	157	157	0
3	3	644	645	0.16	98	98	0
6	7	209	209	0	162	163	0.6
6	8	212	212	0	–	10	0
7	8	357	357	0	172	172	0
9	2	434	434	0	473	473	0
9	7	502	503	0.20	390	390	0
10	3	61	61	0	510	510	0
10	8	348	349	0.29	436	436	0

Table 5. Comparison of normalized sectorial coordinate for the considered cross-section.

Section point number (Figure 15)	Sectorial coordinate ϖ [cm ²]		
	[18]	TONUS	Deviation, %
1	+3241	+3241	0
2	–1483	–1483	0
3	–1102	–1102	0
7	–261	–261	0
8	+249	+249	0

4. Conclusions

The results of the presented study can be formulated as follow:

1. The searching problem of shear stresses outside longitudinal edges of an arbitrary cross-section (including open-closed multi-contour cross-sections) of a thin-walled bar subjected to the general load case has been considered in the paper.
2. The formulated problem has been transformed into a minimization problem of Castigliano's functional subject to constraints-equalities of shear forces flows equilibrium formulated for cross-section branch points as well as subject to an equilibrium equation for the whole cross-section relating to longitudinal axes of the thin-walled bar.
3. A detailed numerical algorithm intended to solve the searching problem of shear forces flows for an arbitrary cross-section of a thin-walled bar subjected to the general loading case using the mathematical apparatus of the graph theory has been developed. The algorithm is oriented on software implementation in systems of computer-aided design of the thin-walled structures.
4. The developed algorithm has been implemented to the TONUS software, which is a satellite of the SCAD Office environment.
5. Numerical examples for calculation of the thin-walled bars with open and open-closed multi-contour cross-sections have been considered in order to validate developed algorithm and verify calculation accuracy for sectorial cross-section geometrical properties and shear stresses caused by warping torque and shear forces.
6. Validity of the calculation results obtained using the developed software has been proven by considered examples.

References

1. Dowell, R.K., Johnson, T.P. Closed-form shear flow solution for box-girder bridges under torsion [Online]. *Engineering Structures*. 2012. No. 34. Pp. 383–390. URL: <https://doi.org/10.1016/j.engstruct.2011.09.023>
2. Shen, K., Wan, S., Mo, Y.L., Jiang, Z., Li, X. Behavior of single-box multi-cell box-girders with corrugated steel webs under pure torsion. Part II: Theoretical model and analysis [Online]. *Thin-Walled Structures*. 2018. No. 129. Pp. 558–572. URL: <https://doi.org/10.1016/j.tws.2017.12.023>
3. Shen, K., Wan, S., Mo, Y.L., Jiang, Z., Li, X. Behavior of single-box multi-cell box-girders with corrugated steel webs under pure torsion. Part I: Experimental and numerical studies [Online]. *Thin-Walled Structures*. 2018. No. 129. Pp. 542–557. URL: <https://doi.org/10.1016/j.tws.2017.10.038>
4. Perelmuter, A.V., Slivker, V.I. *Numerical structural analysis: models, methods and pitfalls*. Springer-Verlag Berlin Heidelberg, 2003. 600 p.
5. Slivker, V.I. *Mechanics of structural elements. Theory and applications*. Springer-Verlag Berlin Heidelberg, 2007. 786 p.
6. Lalin, V., Rybakov, V., Sergey, A. The finite elements for design of frame of thin-walled beams. *Applied Mechanics and materials*. 2014. Vol. 578–579. Pp. 858–863. DOI: 10.4028/www.scientific.net/AMM.578-579.858
7. Lalin, V.V., Rybakov, V.A., Diakov, S.F., Kudinov, V.V., Orlova, E.S. The semi-shear theory of V.I. Slivker for the stability problems of thin-walled bars. *Magazine of Civil Engineering*. 2019. Vol. 87. Is. 3. Pp. 66–79.
8. Dyakov, S.F. Comparing the results of the thin-walled bar torsion problem according to Vlasov and Slivker theories [Online]. *Structural mechanics of engineering constructions and buildings*. 2013. No. 1. Pp. 24–31. URL: <http://journals.rudn.ru/structural-mechanics/article/view/11128> (rus)
9. Yurchenko, V.V. *Proyektirovaniye karkasov zdaniy iz tonkostennykh kholodnognutnykh profiley v srede SCAD Office [Designing of steel frameworks from thin-walled cold-formed profiles in SCAD Office]* [Online]. *Magazine of Civil Engineering*. 2010. No. 8. Pp. 38–46. URL: http://engstroy.spbstu.ru/index_2010_08/yurchenko_LSTK.pdf (rus)
10. Ádány, S., Schafer, B.W. Generalized constrained finite strip method for thin-walled members with arbitrary cross-section: Primary modes [Online]. *Thin-Walled Structures*. 2014. No. 84. Pp. 150–169. URL: <https://doi.org/10.1016/j.tws.2014.06.001>
11. Jönsson, J. Determination of shear stresses, warping functions and section properties of thin-walled beams using finite elements. *Computer and Structures*. 1998. No. 68. Pp. 393–410.
12. Sharafi, P., Teh, L.H., Hadi, M.N.S. Shape optimization of thin-walled steel sections using graph theory and ACO algorithm. *Journal of Constructional Steel Research*. 2014. No. 101. Pp. 331–341.
13. Tarjan, R. Depth-first search and linear graph algorithms. *SIAM Journal Computing*. 1972. No. 1. Pp. 146–60.
14. Alfano, G., Marotti de Sciarra, F., Rosati, L. Automatic analysis of multicell thin-walled sections. *Computer and Structures*. 1996. No. 59. Pp. 641–655.
15. Waldron, P. Sectorial properties of straight thin-walled beams. *Computers and Structures*. 1986. Vol. 24. Is. 1. Pp. 147–156.
16. Yoo, C.H. Cross-sectional properties of thin-walled multi-cellular section. *Computer and Structures*. 1986. No. 22. Pp. 53–61.
17. Yoo, C.H., Kang, J., Kim, K., Lee, K.C. Shear flow in thin-walled cellular sections [Online]. *Thin-Walled Structures*. 2011. 49(11). Pp. 1341–1347. URL: <https://doi.org/10.1016/j.tws.2011.02.014>
18. Prokić, A. Computer program for determination of geometrical properties of thin-walled beams with open-closed section. *Computers and Structures*. 2000. No. 74. Pp. 705–715.
19. Gurujee, C.S., Shah, K.R. A computer program for thin-walled frame analysis. *Advances in Engineering Software*. 1989. No. 11. Pp. 58–70.
20. Choudhary, G.K., Doshi, K.M. An algorithm for shear stress evaluation in ship hull girders [Online]. *Ocean Engineering*. 2015. 108(1). Pp. 678–691. URL: <https://doi.org/10.1016/j.oceaneng.2015.08.048>

21. Perelmuter, A., Yurchenko, V. Shear stresses in hybrid thin-walled section: development of detail numerical algorithm based on the graph theory. Proceedings of 3rd Polish Congress of Mechanics and 21st International Conference on Computer Methods in Mechanics. Short Papers. 2015. Vol. 2. Pp. 943–944.
22. Yurchenko, V. Searching shear forces flows for an arbitrary cross-section of a thin-walled bar: development of numerical algorithm based on the graph theory. International journal for computational civil and structural engineering. 2019. No. 15(1). Pp. 153–170.
23. San Francisco-Oakland Bay Bridge New East Span Skyway – San Francisco and Oakland, California. American Segmental Bridge Institute [Online]. URL: <http://www.asbi-assoc.org/projects>
24. URL: www.scadsoft.com

Contacts:

Vitalina Yurchenko, +38(063)8926491; vitalinay@rambler.ru

© Yurchenko, V., 2019



DOI: 10.18720/MCE.92.1

Алгоритм определения потоков касательных усилий для произвольных сечений тонкостенных стержней

В. Юрченко*

Киевский национальный университет строительства и архитектуры, г. Киев, Украина

* E-mail: vitalinay@rambler.ru

Ключевые слова: тонкостенный стержень, произвольное сечение, потоки касательных усилий, замкнутый контур, теория графов, численный алгоритм, численные примеры, программная реализация

Аннотация. Разработка универсального программного комплекса для расчета и проектирования тонкостенных стержневых элементов конструкций остается актуальной задачей. Несмотря на преобладающее влияние нормальных напряжений на напряженно-деформированное состояние тонкостенных стержней, проверка несущей способности таких элементов должна выполняться, принимая во внимание также и значения касательных напряжений. В связи с этим рассмотрена задача поиска значений потоков касательных усилий для произвольного сечения (открыто-замкнутого многоконтурного сечения) тонкостенного стержня для общего случая нагружения. Сформулированная задача приведена к задаче математического программирования, а именно к задаче поиска значений неизвестных потоков касательных напряжений, обеспечивающих наименьшее значение функционала Кастильяно при удовлетворении ограничений равновесия потоков в точках ветвления сечения, а также при удовлетворении уравнения равновесия всего сечения тонкостенного стержня относительно продольной оси. Разработан детальный алгоритм численного решения сформулированной задачи с использованием математического аппарата теории графов, ориентированный на программную реализацию в системах автоматизированного проектирования тонкостенных стержневых систем. Выполнена программная реализация разработанного алгоритма в среде вычислительного комплекса SCAD Office в программе ТОНУС. С целью верификации разработанного алгоритма и проверки точности вычислений геометрических характеристик и касательных напряжений рассмотрены примеры расчета тонкостенных стержневых элементов открытого и открыто-замкнутого многоконтурного сечений. На рассмотренных примерах доказана достоверность результатов, получаемых при использовании разработанного программного обеспечения.

Литература

1. Dowell R.K., Johnson T.P. Closed-form shear flow solution for box-girder bridges under torsion [Электронный ресурс] // Engineering Structures. 2012. No. 34. Pp. 383–390. URL: <https://doi.org/10.1016/j.engstruct.2011.09.023>
2. Shen K., Wan S., Mo Y.L., Jiang Z., Li X. Behavior of single-box multi-cell box-girders with corrugated steel webs under pure torsion. Part II: Theoretical model and analysis [Электронный ресурс] // Thin-Walled Structures. 2018. No. 129. Pp. 558–572. URL: <https://doi.org/10.1016/j.tws.2017.12.023>
3. Shen K., Wan S., Mo Y.L., Jiang Z., Li X. Behavior of single-box multi-cell box-girders with corrugated steel webs under pure torsion. Part I: Experimental and numerical studies [Электронный ресурс] // Thin-Walled Structures. 2018. No. 129. Pp. 542–557. URL: <https://doi.org/10.1016/j.tws.2017.10.038>
4. Perelmuter A.V., Slivker V.I. Numerical structural analysis: models, methods and pitfalls. Springer-Verlag Berlin Heidelberg, 2003. 600 p.
5. Slivker V.I. Mechanics of structural elements. Theory and applications. Springer-Verlag Berlin Heidelberg, 2007. 786 p.
6. Lalin V., Rybakov V., Sergey A. The finite elements for design of frame of thin-walled beams [Электронный ресурс] // Applied Mechanics and materials. 2014. Vol. 578–579. Pp. 858–863. URL: [10.4028/www.scientific.net/AMM.578-579.858](http://www.scientific.net/AMM.578-579.858)
7. Лалин В.В., Рыбаков В.А., Дьяков С.Ф., Кудинов В.В., Орлова Е.С. Полусдвиговая теория В.И. Сливкера в задачах устойчивости тонкостенных стержней // Инженерно-строительный журнал. 2019. № 3(87). С. 66–79. DOI: 10.18720/MCE.87.6
8. Дьяков С.Ф. Сравнительный анализ задачи кручения тонкостенного стержня по моделям Власова и Сливкера [Электронный ресурс] // Строительная механика инженерных конструкций и сооружений. Обзорно-аналитический и научно-технический журнал. 2013. № 1. С. 24–31. URL: <http://journals.rudn.ru/structural-mechanics/article/view/11128>
9. Юрченко В.В. Проектирование каркасов зданий из тонкостенных холодногнутых профилей в среде SCAD Office // Инженерно-строительный журнал. 2010. № 8(18). С. 38–4. DOI: 10.18720/MCE.18.7.
10. Ádány S., Schafer B.W. Generalized constrained finite strip method for thin-walled members with arbitrary cross-section: Primary modes [Электронный ресурс] // Thin-Walled Structures. 2014. No. 84. Pp. 150–169. URL: <https://doi.org/10.1016/j.tws.2014.06.001>

11. Jönsson J. Determination of shear stresses, warping functions and section properties of thin-walled beams using finite elements // Computer and Structures. 1998. No. 68. Pp. 393–410.
12. Sharafi P., Teh L.H., Hadi M.N.S. Shape optimization of thin-walled steel sections using graph theory and ACO algorithm // Journal of Constructional Steel Research. 2014. No. 101. Pp. 331–341.
13. Tarjan R. Depth-first search and linear graph algorithms // SIAM Journal Computing. 1972. Np. 1. Pp. 146–60.
14. Alfano G., Marotti de Sciarra F., Rosati L. Automatic analysis of multicell thin-walled sections // Computer and Structures. 1996. No. 59. Pp. 641–55.
15. Waldron P. Sectorial properties of straight thin-walled beams // Computers and Structures. 1986. Vol. 24. Is. 1. Pp. 147–156.
16. Yoo C.H. Cross-sectional properties of thin-walled multi-cellular section // Computer and Structures. 1986. No. 22. Pp. 53–61.
17. Yoo C.H., Kang J., Kim K., Lee K.C. Shear flow in thin-walled cellular sections [Электронный ресурс] // Thin-Walled Structures. 2011. No. 49(11). Pp. 1341–1347. URL: <https://doi.org/10.1016/j.tws.2011.02.014>
18. Prokić A. Computer program for determination of geometrical properties of thin-walled beams with open-closed section // Computers and Structures. 2000. No. 74. Pp. 705–715.
19. Gurujee C.S., Shah K.R. A computer program for thin-walled frame analysis // Advances in Engineering Software. 1989. No. 11. Pp. 58–70.
20. Choudhary G.K., Doshi K.M. An algorithm for shear stress evaluation in ship hull girders [Электронный ресурс] // Ocean Engineering. 2015. No. 108(1). Pp. 678–691. URL: <https://doi.org/10.1016/j.oceaneng.2015.08.048>
21. Perelmuter A., Yurchenko V. Shear stresses in hybrid thin-walled section: development of detail numerical algorithm based on the graph theory // Proceedings of 3rd Polish Congress of Mechanics and 21st International Conference on Computer Methods in Mechanics. Short Papers. 2015. Vol. 2. Pp. 943–944.
22. Yurchenko V. Searching shear forces flows for an arbitrary cross-section of a thin-walled bar: development of numerical algorithm based on the graph theory // International journal for computational civil and structural engineering. 2019. No. 15(1). Pp. 153–170.
23. San Francisco-Oakland Bay Bridge New East Span Skyway – San Francisco and Oakland, California [Электронный ресурс]. American Segmental Bridge Institute. URL: <http://www.asbi-assoc.org/projects>.
24. URL: www.scadsoft.com

Контактные данные:

Виталина Юрченко, +38(063)8926491; Эл. почта: vitalinay@rambler.ru

© Юрченко В., 2019



DOI: 10.18720/MCE.92.2

Thermophysical properties of the soil massif

V.V. Nikonorov, D.O. Nikonorova, G.A. Pikus*

South Ural State University, Chelyabinsk, Russia

** E-mail: pikusga@susu.ru*

Keywords: heat transfer, heat flow, soil property, temperature, mathematical modeling

Abstract. Calculations show that a significant percent of the heat losses of monolithic foundations consists of heat loss to the ground from concrete during construction. Therefore, ignoring heat losses to the ground (i.e., taking into account only the formwork and thermal insulation) leads to significant deviations between calculated and actual technological parameters. The existing methods for calculating the coefficient of heat transfer of enclosures are not suitable when calculating this same parameter for soil massifs. While finite thicknesses are used in this calculation for enclosures, thickness is infinite for soil massifs. To create a method for calculating heat losses to the ground, we solved a differential equation of heat conduction using integral transform methods. In the classical theory of heat transfer, for any material of finite thickness, the heat transfer coefficient is constant over time. However, for an array of soil, this parameter varies depending on period of time during which concrete loses heat to the soil. At the same time, the heat transfer coefficient increases with increasing soil density, which is explained by the growing contact area between particles in a unit volume of soil. Thus, the surface area through which the heat flux moves also increases. The article presents the results of the finite element calculation in the simulation software ELCUT, confirming the reliability of the obtained analytical dependencies.

1. Introduction

When calculating the technological parameters of curing foundation structures, especially massive structures or those cured at negative temperatures, it is often necessary to estimate heat losses from concrete to the soil massif and to the surrounding air [1–4]. The calculation of heat losses to the air through the formwork and thermal insulation does not cause any difficulties since the process of heat distribution is described by the classical theory of heat transfer from a more heated medium to a less heated one through a separating wall of a given thickness [5–10]. Moreover, the entire calculation concerns the heat transfer coefficient of the concrete enclosure, which is influenced by the properties of the enclosure and the environment.

When calculating heat losses to the ground, it is impossible to specify the thickness of the soil massif in light of its near infinite size. Consequently, the standard methods for calculating the soil heat transfer coefficient are not suitable here. To this end, designers often ignore heat losses into the soil massif, focusing on the formwork and thermal insulation. At the same time, the reduced heat transfer coefficient of a concrete enclosure used in the calculations does not only take into account the ratio of heat transfer coefficients of different enclosures of the same design, but also the ratio of their areas. Thus, ignoring heat losses in the soil massif in the calculations can lead to significant errors.

It should be noted that these errors can affect not only the estimated time of concrete curing, but also its structural properties, since heat losses through a concrete enclosure play a major role in the formation of its thermally-stressed state [11–14]. It has already been shown [15] that the thermal characteristics of enclosures lead to uneven distribution of temperatures along the cross section of a monolithic structure, which can cause (if the temperature gradients exceed the limit values) unacceptable temperature stresses in concrete and, as a result, cracking.

Nikonorov, V.V., Nikonorova, D.O., Pikus, G.A. Thermophysical properties of the soil massif. Magazine of Civil Engineering. 2019. 92(8). Pp. 27–35. DOI: 10.18720/MCE.92.2

Никоноров В.В., Никонорова Д.О., Пикус Г.А. Теплофизические свойства массива грунта // Инженерно-строительный журнал. 2019. № 8(92). С. 27–35. DOI: 10.18720/MCE.92.2



This work is licensed under a CC BY-NC 4.0

In the norms of the Republic of Belarus [16], a different approach was taken to account for the thermophysical characteristics of the substrates while maintaining concrete structures. Here, the calculation principle is based on the heat balance equation, and the concrete temperature is estimated after the concrete loses some of its heat to the reinforcement, embedded parts, formwork, and soil foundation.

A book by Finnish authors [17] indicates that the average temperature of concrete in the hardening process depends on the coefficient of heat permeability of the surface at the time of the calculation (Wm^2C , which corresponds to the heat transfer coefficient of the enclosure considered in this article). However, methods for calculating this coefficient are not given in the book. At the same time, the authors indicate that it is the formwork that affects heat loss, without mentioning the soil base.

The American standard [18] provides tables that indicate the minimum permissible outdoor temperatures when concreting slabs of different thicknesses with an insulated enclosure with a certain thermal resistance (m^2C/W , i.e. the reciprocal of the value considered in this article for fence heat transfer coefficient). However, it is also implied here that only formwork and insulation can be a fence, ignoring the soil base.

A publication by Canadian scientists [19] considers temperature changes at various points of the soil mass when exposed to coolant. The soil heat transfer coefficient appears in the study, but its values are not determined analytically - they are set from the results of the experiment. Moreover, the values are given as constant, although the heat transfer coefficient of the soil varies over time for objective reasons, as will be discussed below.

The overwhelming majority of literature published in recent years on the thermophysical properties of soil masses only provide data on measured temperatures in the soil column under the influence of an external heat source [20–22]. That is, the values of soil temperature themselves are not determined analytically - they are only recorded during experiments. This approach makes it possible to effectively and accurately to determine the actual temperature change of a particular soil over time. However, at the same time, the issue of predicting temperature changes at the project stage under external conditions which differ from the experimental conditions is not being addressed. In addition, the use of such experimental data does not allow one to quickly switch to solving similar problems with other soils nor to change their thermophysical characteristics.

In a number of works [23, 24], in addition to experimental data (or instead of them), the authors provide computer calculations of changes in the temperature of specific soils under given conditions under the action of an external heat source. Scientific works in which only computer calculations are presented a priori have significantly less accurate results and are not confirmed experimentally. The use of computer programs operating on the basis of the finite element method for solving thermotechnical problems does not allow for performing on-line calculations of heat losses of concrete in the soil on construction sites without preliminary development of the design scheme. Moreover, the degree of accuracy of the calculations is determined by the degree of detail of this calculation scheme.

Thus, the aim of the study is to obtain a fairly simple mathematical dependence, based on an analytical conclusion, to calculate the heat transfer coefficient of the soil mass.

To achieve this goal it is necessary to solve the following tasks:

- solve the differential heat equation for given boundary conditions;
- analyze the result of the decision;
- perform a sample calculation based on the obtained mathematical dependence and compare the obtained data with the calculation in the ELCUT software package.

2. Methods

To estimate heat losses to the ground, let us use Fourier's differential equation of heat conduction

$$\frac{\partial T(x, \tau)}{\partial \tau} = \alpha \frac{\partial^2 T(x, \tau)}{\partial x^2}, \quad (1)$$

specifying a soil foundation in the form of a semi-infinite body. In this case, due to the concrete laid on the soil, at the initial moment of time ($\tau = 0$), the surface temperature of the semi-infinite body is T_c and does not change during the entire time of its curing, τ_v . In addition, at the initial moment of time, the temperature at all points of the soil massif is constant and equal to T_{0o} , and there is no temperature drop at an infinitely distant point of the soil massif.

To solve equation (1), let us use the Laplace integral transform method and obtain:

$$L\left[\frac{\partial T(x, \tau)}{\partial \tau}\right] = L\left[\frac{\partial^2 T(x, \tau)}{\partial x^2}\right]. \quad (2)$$

If we apply the Laplace transform to the function of temperature distribution inside the body of the soil massif in time and in depth $T(x, \tau)$ and to the left side of equation (2), we obtain an ordinary differential equation for the image $T_L(x, s)$ (since $T_L(x, s)$ does not depend on time τ):

$$T_L''(x, s) - \frac{s}{\alpha} T_L(x, s) + \frac{T_0}{\alpha} = 0 \quad (3)$$

To solve equation (3), let us use the method of variation of constants [22] and obtain:

$$T_L(x, s) - \frac{T_0}{s} = A_1 e^{\sqrt{\frac{s}{\alpha}} x} + B_1 e^{-\sqrt{\frac{s}{\alpha}} x} \quad (4)$$

where A_1 and B_1 are the constants determined from the boundary conditions.

If we apply the Laplace transform to the boundary conditions and substitute the results in (4), we find that the constants are equal to:

$$A_1 = 0; \quad B_1 = -\frac{T_0 - T_c}{s}.$$

Then, (4) can be written as follows:

$$\frac{T_0}{s} - T_L(x, s) = (T_0 - T_c) \cdot \frac{1}{s} \cdot e^{-\sqrt{\frac{s}{\alpha}} x}.$$

Restore the original function from its modified state (image):

$$T_0 - T(x, \tau) = (T_0 - T_c) \left[1 - \operatorname{erf}\left(\frac{x}{2\sqrt{\alpha\tau}}\right) \right].$$

After the transform, we obtain the solution of the heat transfer equation (1):

$$\frac{T(x, \tau) - T_c}{T_0 - T_c} = \operatorname{erf}\left(\frac{x}{2\sqrt{\alpha\tau}}\right).$$

Now, according to Fourier's basic law of heat conduction, we determine the heat losses over time $d\tau$ through a unit of area:

$$dQ_s = -\lambda \left(\frac{\partial T}{\partial x} \right)_{x=0} d\tau = -\lambda (T_0 - T_c) \left\{ \frac{\partial}{\partial x} \left[\operatorname{erf}\left(\frac{x}{2\sqrt{\alpha\tau}}\right) \right] \right\}_{x=0}.$$

According to the main property of the error function ($\operatorname{erf}x$), its derivative:

$$\frac{\partial}{\partial x} \left[\operatorname{erf}\left(\frac{x}{2\sqrt{\alpha\tau}}\right) \right] = \frac{1}{\sqrt{\pi\alpha\tau}} e^{-\left(\frac{x^2}{4\alpha\tau}\right)}.$$

Wherein at $x = 0$ the value of the exponential function is 1.

Thus, we obtained a very important intermediate result - an expression for determining the density of the heat flux (W/m^2) into the soil massif of the foundation from the concrete mixture cured at a specific moment of time:

$$q = \frac{dQ_s}{d\tau} = -\frac{\lambda \cdot (T_0 - T_c)}{\sqrt{\pi\alpha\tau}} = -\sqrt{\frac{\lambda c \gamma}{\pi \tau}} (T_0 - T_c). \quad (5)$$

The total amount of heat Q given by the cured concrete to the soil massif over a certain period of time (τ_v) is found by the integration from 0 to τ_v :

$$Q = \int_0^{\tau_v} \sqrt{\frac{\lambda c \gamma}{\pi \tau}} (T_0 - T_c) d\tau = 2 \sqrt{\frac{\lambda c \gamma}{\pi}} (T_0 - T_c) s \sqrt{\tau_v}. \quad (6)$$

Then, we transform expression (6) so that to isolate the part acting as a heat transfer coefficient:

$$Q = \left[2 \sqrt{\frac{\lambda c \gamma}{\pi \tau_v}} \right] (T_0 - T_c) \cdot s \cdot \tau_v. \quad (7)$$

Thus, it can be seen that in (7) the parenthesized expression determines the average heat transfer coefficient (α_m) during the concrete curing time. Therefore, the desired value is determined by the following analytical dependence:

$$\alpha_m = 2 \sqrt{\frac{\lambda c \gamma}{\pi \tau_v}} = 1,13 \sqrt{\frac{\lambda c \gamma}{\tau_v}}, \quad (8)$$

where λ , c , γ are the coefficient of thermal conduction, the coefficient of specific heat and soil density, respectively.

In the classical theory of heat transfer, the heat transfer coefficient is constant over time for any material of finite thickness. However, for an array of soil, this parameter varies depending on the period of time during which concrete gives off heat to the soil. This fully complies with the method proposed by Arbeniev [25] for calculating the decreased temperature of concrete mixtures laid on a frozen base and indicates the non-stationary nature of heat transfer processes.

At the same time, it can be seen from (8) that the heat transfer coefficient increases with increasing soil density, which is explained by the growing contact area between particles in a unit volume of soil. Thus, the surface area through which the heat flux moves also increases. This correlates well with the works [20, 21].

Thus, for a typical monolithic reinforced concrete structure, we can write a formula for determining the reduced heat transfer coefficient of its enclosure, which allows us to take into account heat loss through all surfaces of the monolithic structure:

$$\alpha_r = \frac{\alpha_f A_f + \alpha_c A_c + \alpha_m A_m}{A_f + A_c + A_m},$$

where α_f , α_c , α_m are the heat transfer coefficients of the formwork and covering material of undecked surfaces, respectively;

and A_f , A_c , A_m are the area of formwork surfaces, undecked surfaces and surfaces in contact with the soil, respectively.

3. Results and Discussion

The obtained results were verified using finite element modeling in the ELCUT software suite and then analyzing of the results.

Figure 1 shows the calculation results in ELCUT as an image of the temperature distribution in a soil block when concrete of a monolithic free-standing foundation is cured on its surface (the size of the slab of the foundation contacting the foundation soil is 1.5×1.5 m; the initial temperature of the concrete mixture and concrete curing temperature is +30 °C; the initial soil temperature is +3 °C; the outdoor air temperature is -7 °C, the curing time is 7 days). The soil itself is represented by loam from solid to semi-solid consistency, weakly eruptive, with the density of 2030 kg/m³, the humidity of 15%, the thermal conduction coefficient of 2.1 W/m·°C and specific heat capacity of 1530 J/kg·°C.

Due to the impossibility of obtaining the heat transfer coefficient of one or another body in ELCUT, we will verify using the heat flux values F_{elc} [W] generated by the software by the contact area of the slab part of the foundation and the soil foundation at certain points in time (Table 1).

Let us compare our formula (5) with the classical formula of the theory of thermal conduction, which determines heat flux density,

$$q = \alpha \cdot (T_0 - T_c).$$

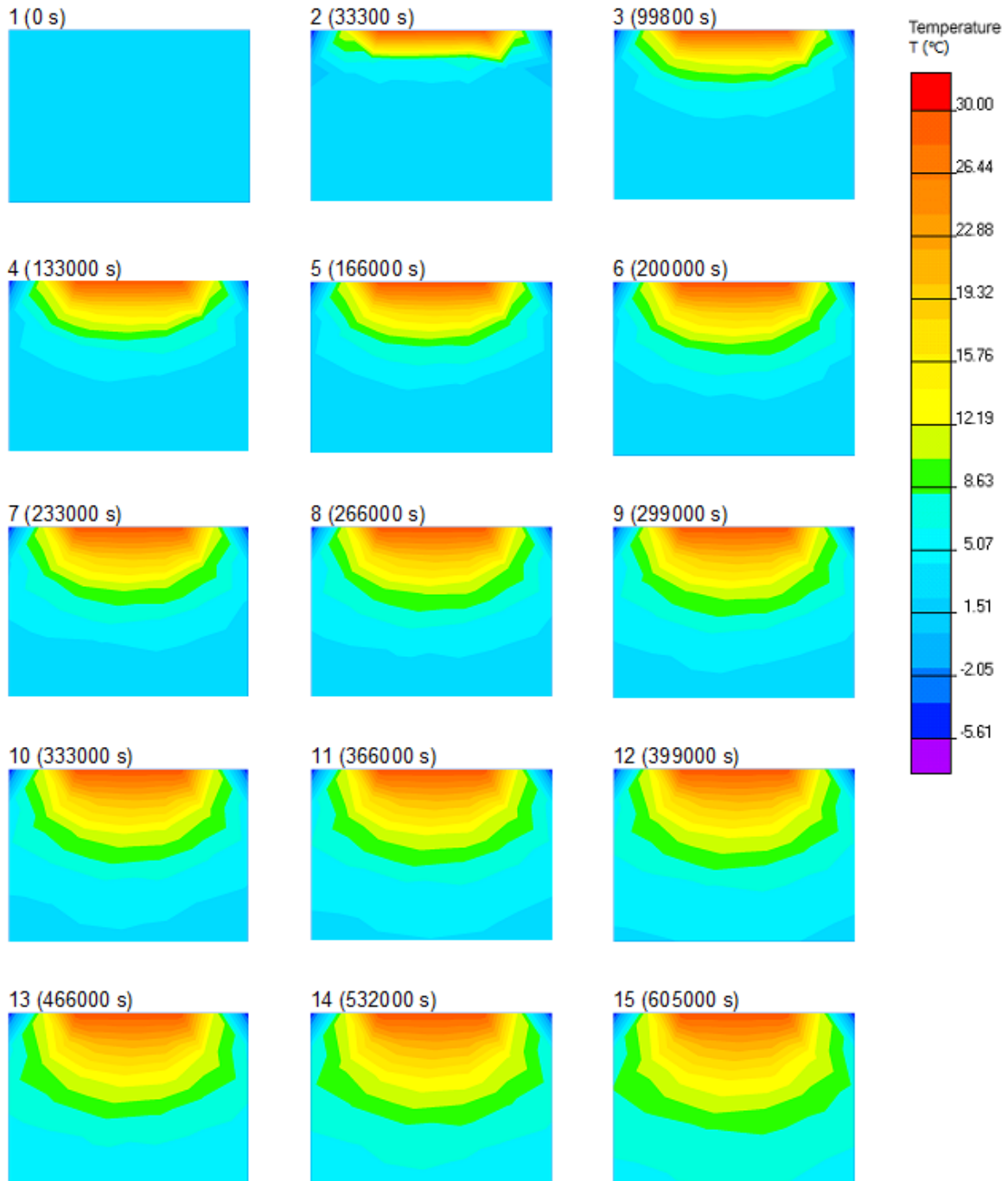


Figure 1. Temperature distribution in the soil block.

As the formula shows, heat flux density is determined by the instantaneous value of the heat transfer coefficient and the temperature difference at the interface between the bodies that are heat exchange participants. In turn, (8) determines the average value of the heat transfer coefficient of the soil massif over the whole curing time of concrete on a soil foundation.

Given that heat flux density is determined by the value of the heat transfer coefficient at a certain moment of time, and knowing the area of the slab portion of the foundation $s = 1.5 \times 1.5 = 2.25 \text{ m}^2$, we can analytically determine heat flux density $F_{an} [\text{W}]$ for the considered example,

$$F_{an} = -\sqrt{\frac{\lambda c \gamma}{\pi \tau_i}} (T_0 - T_c) \cdot s. \quad (9)$$

The most important condition for applying the method of mathematical modeling of complex physical processes is the proof of the reliability of the mathematical model. Table 1 and Figure 2 show a comparison of the heat flux values determined in ELCUT and according to the derived analytical dependencies over the concrete curing time of 7 days.

Table 1. Heat flux values.

# of item	Moment of time, s	F_{elc} (W)	F_{an} (W)	Divergence (%)
1	33 300	366.41	479.93	-23.6
2	99 800	262.63	273.38	-5.26
3	133 000	232.61	239.96	-3.04
4	166 000	213.07	215.06	-0.85
5	200 000	199.22	195.62	1.86
6	233 000	188.80	182.25	3.67
7	266 000	180.60	169.49	6.45
8	299 000	173.94	160.38	8.33
9	333 000	168.39	151.88	10.8
10	366 000	163.67	144.59	13.03
11	399 000	159.58	138.51	15.35
12	466 000	153.07	128.18	19.43
13	532 000	147.67	120.29	22.73
14	605 000	142.71	120.59	27.0

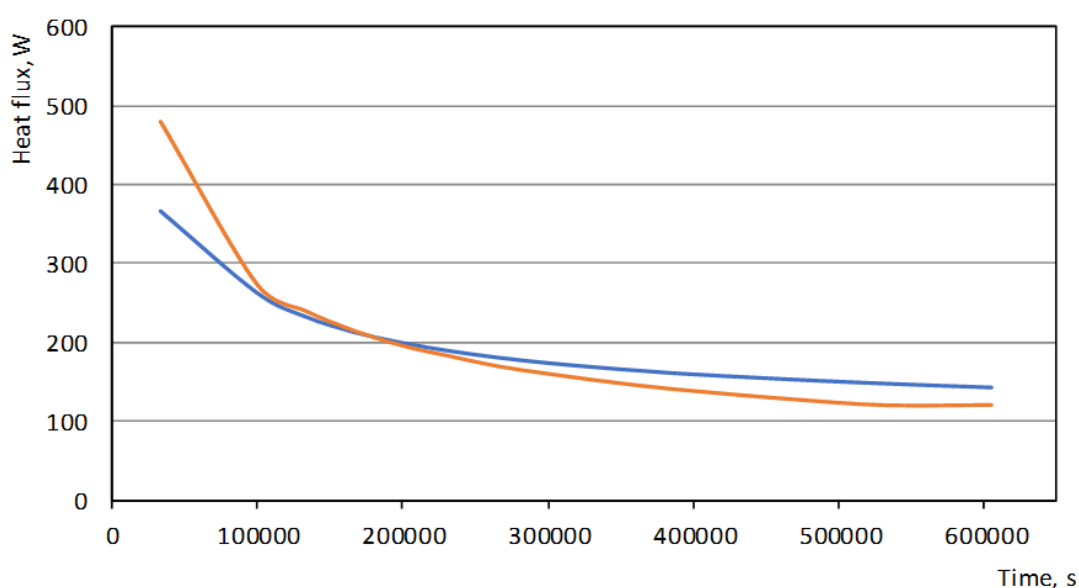


Figure 2. A comparison of heat flux values using ELCUT and analytical dependencies. The orange curve is calculated by formula (9), the blue curve represents the results from ELCUT.

As the data shows, divergence between the calculation results based on finite-element modeling and based on analytical dependence derived in this article for heat losses of concrete cured in the soil mass of the foundation is insignificant (on average +6.85%). At the same time, higher values of the heat flux at the initial moment of concrete curing can be explained by the accumulation of heat in the soil, which has a temperature much lower than the temperature of the concrete mix [22]. It is clear that for different types of soils with a variety of thermophysical characteristics (thermal conductivity, specific heat, density), the amount of accumulated heat will be different. We compare our obtained graph of changes in the values of heat fluxes over time with the results obtained in [19] based on laboratory tests.

When the monolithic construction is 300 mm high, Our calculations for the above problem show that heat losses into the soil mass are responsible for 54.6 % of the total heat losses (i.e., 45.4 % of losses occur at all other surfaces contacting the vertical formwork and horizontal thermal insulation). This value is significant, and ignoring it leads to considerable deviations between the calculated and actual technological parameters. Thus, the specific heat capacities needed to ensure isothermal heating of concrete of this design at a temperature of 30 °C, without and without taking into account heat losses to the ground, differ by almost 2 times.

4. Conclusions

Based on the solution of the Fourier differential heat equation, the research objective was realized - the assessment of the heat loss of concrete in the ground. The following results were obtained:

1. We obtained analytical dependencies that are convenient for calculations which allow us to determine heat losses of concrete structures into the soil foundation and to determine the heat transfer coefficient of the soil mass.

2. The results of calculations for the derived analytical dependencies and calculations using finite element modeling in ELCUT were compared. In the considered example, the calculation accuracy of heat losses according to the derived dependence and the results of computer modeling in ELCUT averaged +6.85 %.

3. The necessity of accounting for heat losses to the soil while maintaining monolithic concrete is proved. In the considered example, heat loss to the soil mass was 54.6 % of the total heat loss.

References

1. SP 70.13330.2012, Nesushchiye i ogradhdayushchiye konstruksii [Load-bearing and separating constructions]. Moscow: Gosstroy, 2012. 203 p. (rus)
2. Pikus, G., Mozgalev, K. Kontrol' parametrov betona, vyderzhivayemogo v zimnikh usloviyakh [Controlling the parameters of concrete cured in winter conditions]. Bulletin of SUSU. Series Building and Architecture. 2015. 15(1). Pp. 1, 6–9. (rus)
3. Murgul, V. Investigation of heat losses through ground supported floors of historical buildings. IOP Conference Series: Materials Science and Engineering. 2018. 365. Pp. 022066. DOI: 10.1088/1757-899X/365/2/022066.
4. Sobota, T., Taler, J. Determination of heat losses through building partitions. MATEC Web of Conferences. 2018. 240. Pp. 05030. DOI: 10.1051/mateconf/201824005030.
5. Golovnev, S.G. Tekhnologiya zimnego betonirovaniya. Optimizatsiya parametrov i vybor metodov [The winter concreting technology. The parameters optimization and choice of ways]. Chelyabinsk: SUSU, 1999. 156 p. (rus)
6. Rukovodstvo po progrevu betona v monolitnykh konstruksiyakh [A guide to concrete heating in monolithic structures] / Ed. by B.A. Krylov, S.A. Ambartsumyan, A.I. Svezdov. Moscow: RAASN, NIIZHB, 2005. 275 p. (rus)
7. Dudin, M.O., Vatin, N.I., Barabanshchikov, Yu.G. Modeling a set of concrete strength in the program ELCUT at warming of monolithic structures by wire. Magazine of Civil Engineering. 2015. 2. Pp. 33–45. DOI: 10.5862/MCE.54.4. (rus)
8. Pukhkal, V.A., Mottaeva, A.B. FEM modeling of external walls made of autoclaved aerated concrete blocks. Magazine of Civil Engineering. 2018. 81(5). Pp. 202–211. DOI: 10.18720/MCE.81.20.
9. Bushmanova, A.V., Barabanshchikov, Yu.G., Semenov, K.V., Struchkova, A.Y., Manovitsky, S.S. Thermal cracking resistance in massive foundation slabs in the building period. Magazine of Civil Engineering. 2017. 8. Pp. 193–200. DOI: 10.18720/MCE.76.17.
10. Bonivento Bruges, J.C., Vieira, G., Revelo Orellana, D.P., Togo, I. Parameter of thermal resistance of bamboo multilayer wall. Magazine of Civil Engineering. 2018. 83(7). Pp. 92–101. DOI: 10.18720/MCE.83.9.
11. Kuchin, V.N., Shilonosova, N.V. Features of peripheral heating of monolithic reinforced concrete structures. IOP Conference Series: Materials Science and Engineering. 2018. 451. Pp. 012088. DOI: 10.1088/1742-6596/451/1/012088.
12. Akbarnezhad, A., Ong, K.C.G. Thermal stress and pore pressure development in microwave heated concrete. Computers and Concrete. 2011. 8(4). Pp. 425–443. DOI: 10.12989/cac.2011.8.4.425.
13. Gnyrya, A.I., Abzaev, Y.A., Korobkov, S. V., Gauss, K.S. Mechanical properties of cement paste curing at different isothermal conditions. IOP Conference Series: Earth and Environmental Science. 2018. 193. Pp. 012010. DOI: 10.1088/1755-1315/193/1/012010.
14. Korotchenko, I.A., Ivanov, E.N., Manovitsky, S.S., Borisova, V.A., Semenov, K.V., Barabanshchikov, Yu.G. Deformation of concrete creep in the thermal stress state calculation of massive concrete and reinforced concrete structures. Magazine of Civil Engineering. 2017. 69(1). Pp. 56–63. DOI: 10.18720/MCE.69.5.
15. Pikus, G.A., Lebed, A.R. Warming of Monolithic Structures in Winter. IOP Conference Series: Materials Science and Engineering. 2017. 262. Pp. 012064. DOI: 10.1088/1757-899X/262/1/012064.
16. TKP 45-5.03-21-2006, Betonnyye raboty pri otritsatel'nykh temperaturakh vozdukh. Pravila pro-izvodstva [Concrete work at subzero air temperatures. Rules of works]. Ministry of Architecture and Construction of the Republic of Belarus, 2006. 103 p. (rus)
17. Kokki, P. Mäkelä, H. Construction in winter conditions: Heat protection and energy saving / Translation from Finnish V.P. Kalinin. Edited by S.A. Mironova. Moscow: Stroyizdat, 1986. 84 p. (rus)
18. ACI 306R, Guide to Cold Weather Concreting. American Concrete Institute, 2010. 30 p.
19. Svec, O.J., Goodrich, L.E., Palmer, J.H.L. Heat transfer characteristics of inground heat exchangers. International Journal of Energy Research. 1983. 7. Pp. 265-278. DOI: 10.1002/er.4440070307.
20. Kumar Agrawal, K., Yadav, T., Misra, R., Das Agrawal, G. Effect of soil moisture contents on thermal performance of earth-air-pipe heat exchanger for winter heating in arid climate: In situ measurement. Geothermics. 2019. 77. Pp. 12–23. DOI: 10.1016/j.geothermics.2018.08.004.
21. Elminshawy, N.A.S., Siddiqui, F.R., Farooq, Q.U., Addas, M.F. Experimental investigation on the performance of earth-air pipe heat exchanger for different soil compaction levels. Applied Thermal Engineering. 2017. 124. Pp. 1319–1327. DOI: 10.1016/j.applthermaleng.2017.06.119.
22. Zhang, Z., Wu, Q., Liu, Y., Zhang, Z., Wu, G. Thermal accumulation mechanism of asphalt pavement in permafrost regions of the Qinghai–Tibet Plateau. Applied Thermal Engineering. 2018. 129. Pp. 345–353. DOI: 10.1016/j.applthermaleng.2017.10.065.
23. Sudisman, R.A., Osada, M., Yamabe, T. Experimental Investigation on Effects of Water Flow to Freezing Sand around Vertically Buried Freezing Pipe. Journal of Cold Regions Engineering. 2019. 33(3). Pp. 04019004. DOI: 10.1061/(ASCE)CR.1943-5495.0000187.
24. Alimonti, C., Soldo, E., Minniti, S., Speetjens, M.F.M. Sustainability assessment and performance evaluation of a Ground Coupled Heat Pump system: Coupling a model based on COMSOL Multiphysics and a MATLAB heat pump model. Journal of Physics: Conference Series. 2019. 1224. Pp. 012023. DOI: 10.1088/1742-6596/1224/1/012023.
25. Arbenev, A.S. Ot elektrotermosa k sinergobetonirovaniyu [From electrothermos to synergistic concrete]. Vladimir: VSTU, 1996. 272 p. (rus)

Contacts:

Vladislav Nikonorov, +7(982)3024318; vladislav50595@yandex.ru

Daria Nikonorova, +7(912)7997325; evs95@inbox.ru

Grigorii Pikus, +7(905)8390956; pikusga@susu.ru



DOI: 10.18720/MCE.92.2

Теплофизические свойства массива грунта

В.В. Никоноров, Д.О. Никонорова, Г.А. Пикус*

Южно-Уральский государственный университет, г. Челябинск, Россия

Ключевые слова: теплопередача, тепловой поток, свойства грунта, температура, математическое моделирование

Аннотация. Расчеты показывают, что тепловые потери в грунт бетона монолитных фундаментов в процессе их возведения занимают значительную долю в общем объеме тепловых потерь таких конструкций. Поэтому игнорирование тепловых потерь в грунт (т.е. учет только опалубки и утеплителя) приводит к значительным отклонениям рассчитываемых технологических параметров от фактических. Существующие методы расчета коэффициента теплопередачи ограждения не подходят для использования при расчете данного параметра грунтовых массивов. Это объясняется тем, что в таких расчетах используются конечные толщины ограждений, а у грунтовых массивов она бесконечна. Для создания методики расчета тепловых потерь в грунт было решено дифференциальное уравнение теплопроводности с использованием методов интегрального преобразования. Получено, что в отличие от классической теории теплопередачи, когда для любого материала конечной толщины коэффициент теплопередачи является величиной постоянной во времени, для массива грунта этот параметр меняется в зависимости от времени, в течение которого бетон отдает тепло грунту. При этом коэффициент теплопередачи увеличивается при увеличении плотности грунта, что объясняется растущей площадью контакта между частицами в единице объема грунта. Таким образом, увеличивается и площадь поверхности, через которую движется тепловой поток. Приведены результаты конечно-элементного расчёта в программном комплексе ELCUT подтверждающие достоверность полученных аналитических зависимостей.

Литература

1. СП 70.13330.2012 Несущие и ограждающие конструкции. М.: Госстрой, 2012. 203 с.
2. Пикус Г., Мозгалёв К. Контроль параметров бетона, выдерживаемого в зимних условиях // Вестник Южно-Уральского государственного университета. Серия: Строительство и архитектура. 2015. 1(15). С. 6–9.
3. Murgul V. Investigation of heat losses through ground supported floors of historical buildings // IOP Conference Series: Materials Science and Engineering. 2018. No. 365. 022066. DOI: 10.1088/1757-899X/365/2/022066
4. Sobota T., Taler J. Determination of heat losses through building partitions // MATEC Web of Conferences. 2018. No. 240. 05030. DOI: 10.1051/mateconf/201824005030
5. Головнев С.Г. Технология зимнего бетонирования. Оптимизация параметров и выбор методов. Челябинск: ЮУрГУ, 1999. 156 с.
6. Руководство по прогреву бетона в монолитных конструкциях / Под ред. Б.А. Крылов, С.А. Амбарцумян, А.И. Звездов. М.: РААСН, НИИЖБ, 2005. 275 с.
7. Дудин М.О., Ватин Н.И., Барабанщиков Ю.Г. Моделирование набора прочности бетона в программе ELCUT при прогреве монолитных конструкций проводом // Инженерно-строительный журнал. 2015. № 2. С. 33–45. DOI: 10.5862/MCE.54.4.
8. Пухгал В.А., Моттаева А.Б. МКЭ-моделирование ограждающих стен, выполненных из автоклавного газобетона // Инженерно-строительный журнал. 2018. № 5(81). С. 202–211. doi: 10.18720/MCE.81.20
9. Бушманова А.В., Барабанщиков Ю.Г., Семенов К.В., Стручкова А.Я., Мановицкий С.С. Термическая трещиностойкость массивных фундаментных плит в строительный период // Инженерно-строительный журнал. 2017. № 8(76). С. 193–200. doi: 10.18720/MCE.76.17
10. Бонивенто Брюгес Х., Виейра Г.Б., Ревело Орельяна Д., Того И. Показатели теплотехнического сопротивления бамбуковой стены // Инженерно-строительный журнал. 2018. № 7(83). С. 92–101. doi: 10.18720/MCE.83.9
11. Kuchin V.N., Shilonosova N.V. Features of peripheral heating of monolithic reinforced concrete structures // IOP Conference Series: Materials Science and Engineering. 2018. No. 451. 012088. DOI: 10.1088/1742-6596/451/1/012088.
12. Akbarnezhad A., Ong K.C.G. Thermal stress and pore pressure development in microwave heated concrete // Computers and Concrete. 2011. 4(8). Pp. 425–443. DOI: 10.12989/cac.2011.8.4.425.
13. Gnurya A.I., Abzaev Y.A., Korobkov S. V., Gauss K.S. Mechanical properties of cement paste curing at different isothermal conditions // IOP Conference Series: Earth and Environmental Science. 2018. No. 193. 012010. DOI: 10.1088/1755-1315/193/1/012010.
14. Коротченко И.А., Иванов Э.Н., Мановицкий С.С., Борисова В.А., Семенов К.В., Барабанщиков Ю.Г. Деформации ползучести бетона в расчетах термонапряженного состояния массивных бетонных и железобетонных конструкций // Инженерно-строительный журнал. 2017. № 1(69). С. 56–63. doi: 10.18720/MCE.69.5

15. Pikus G.A., Lebed A.R. Warming of Monolithic Structures in Winter // IOP Conference Series: Materials Science and Engineering. 2017. No. 262. 012064. DOI: 10.1088/1757-899X/262/1/012064.
16. ТКП 45-5.03-21-2006 Бетонные работы при отрицательных температурах воздуха. Правила производства. Министерство архитектуры и строительства Республики Беларусь, 2006. 103 с.
17. Кокки П., Мякеля Х. Строительство в зимних условиях: Теплозащита и экономия энергии : пер. с фин. В.П. Калинина / под ред. С.А. Миронова. М.: Стройиздат, 1986. 84 с.
18. ACI 306R. Guide to Cold Weather Concreting. American Concrete Institute, 2010. 30 p.
19. Svec O.J., Goodrich L.E., Palmer J.H.L. Heat transfer characteristics of inground heat exchangers // International Journal of Energy Research. 1983. № 7. Pp. 265–278. DOI: 10.1002/er.4440070307.
20. Kumar Agrawal K., Yadav T., Misra R., Das Agrawal G. Effect of soil moisture contents on thermal performance of earth-air-pipe heat exchanger for winter heating in arid climate: In situ measurement // Geothermics. 2019. 77. Pp. 12–23. DOI: 10.1016/j.geothermics.2018.08.004.
21. Elminshawy N.A.S., Siddiqui F.R., Farooq Q.U., Addas M.F. Experimental investigation on the performance of earth-air pipe heat exchanger for different soil compaction levels // Applied Thermal Engineering. 2017. 124. Pp. 1319–1327. DOI: 10.1016/j.applthermaleng.2017.06.119.
22. Zhang Z., Wu Q., Liu Y., Zhang Z., Wu G. Thermal accumulation mechanism of asphalt pavement in permafrost regions of the Qinghai–Tibet Plateau // Applied Thermal Engineering. 2018. 129. Pp. 345–353. DOI: 10.1016/j.applthermaleng.2017.10.065.
23. Sudisman R.A., Osada M., Yamabe T. Experimental Investigation on Effects of Water Flow to Freezing Sand around Vertically Buried Freezing Pipe // Journal of Cold Regions Engineering. 2019. No. 3(33). 04019004. DOI: 10.1061/(ASCE)CR.1943-5495.0000187.
24. Alimonti C., Soldo E., Minniti S., Speetjens M.F.M. Sustainability assessment and performance evaluation of a Ground Coupled Heat Pump system: Coupling a model based on COMSOL Multiphysics and a MATLAB heat pump model // Journal of Physics: Conference Series. 2019. No. 1224. 012023. DOI: 10.1088/1742-6596/1224/1/012023.
25. Арбеньев А.С. От электротермоса к синергобетонированию. Владимир: ВГТУ, 1996. 272 с.

Контактные данные:

Владислав Вячеславович Никоноров, +7(982)3024318; эл. почта: vladislav50595@yandex.ru
Дарья Олеговна Никонорова, +7(912)7997325; почта: evs95@inbox.ru
Григорий Александрович Пикус, +7(905)8390956; почта: pikusga@susu.ru

© Никоноров В.В., Никонорова Д.О., Пикус Г.А., 2019



DOI: 10.18720/MCE.92.3

Strength and microstructure of alkali-activated natural pozzolan and limestone powder mortar

A.A. Adewumi^a, M. Ismail^{a*}, M.A.M. Ariffin^a, M.O. Yusuf^b, M. Maslehuddin^c, H.D. Mohamed^c

^a Universiti Teknologi Malaysia, Johor Bahru, Malaysia

^b Univeristy of Hafr Albatin, Hafr Al-Batin, Saudi Arabia

^c King Fahd University of Petroleum and Minerals, Dhahran, Saudi Arabia

* E-mail: mohammad@utm.my

Keywords: alkali-activated mortar, natural pozzolan, limestone powder, microstructure, aluminosilicate, compressive strength

Abstract. In this study, the synergistic effects of natural pozzolan (NP) and limestone powder waste (LSPW) alkaline activated mortar has been investigated using compressive strength and microstructure analysis. LSPW was added in varying percentages to alkaline activated NP such that the combined ratio (LSPW/(LSPW + NP)) varied from (0 to 1) at the interval of 0.2. The activators used were sodium silicate ($\text{Na}_2\text{SiO}_3(\text{aq})$) and sodium hydroxide ($10\text{M NaOH}(\text{aq})$) combined as 1:1. The findings revealed that the synergistic effect of NP with LSPW emanated from silica and alumina required for the formation of aluminosilicate framework which required cation sourced from LSPW (Ca^{2+}) for charge balancing in the formed skeletal framework. The products formed were mainly anorthite ($\text{CaAl}_2\text{Si}_2\text{O}_8$) and gehlenite ($\text{CaO} \cdot \text{Al}_2\text{O}_3 \cdot \text{SiO}_2$). Besides, about 77 % of 28-days compressive strength (27 MPa) could be achieved in 24 h using heat curing. Microstructural analysis revealed that the rough texture of activated NP characterized with high porosity turned to be filled up by the presence of LSPW thereby improving the microstructural density.

1. Introduction

Ordinary Portland cement (OPC), the main hydraulic binder in concrete is the largest manufactured binder globally [1]. OPC world production was estimated to be 4.6 billion tonnes in the year 2015 with a projection of four-fold increase by 2050 [2]. One of the negative sides of OPC is its contribution of CO_2 to the environment and the fuel consumption during its manufacturing process. OPC calcination process significantly leads to the emission of 5–8 % of global CO_2 into the atmosphere which has greatly contributed to the depletion of the ozone layer [3, 4]. Climate change is mainly due to greenhouse gas (GHG) emissions, of which CO_2 is a major contributor, it accounts for 82 % of the total GHG [3].

Alkali-activated material (AAM) has been identified as an eco-efficient and economically viable alternative for replacing OPC due to its excellent strength, thermal and low permeability [5, 6]. AAM is a system formed by the reaction of soluble alkali activator and aluminosilicate precursors [5]. AAM is classified into low calcium (fly ash, metakaolin and natural pozzolans) and high calcium (blast furnace slag) binders. The main products in low binder AAM could be mainly potassium/sodium aluminosilicate hydrate with impregnation of alumina (NASH and KASH) within the formation. In high calcium binder such as blast furnace slag that is synthesized with a mild alkali, the main product is calcium alumina silicate hydrate [7].

Many researchers have successfully synthesized alkali-activated mortars and concretes from volcanic materials such as natural pozzolan (NP) [7–9], agricultural waste materials such as, rice husk ash [10], palm oil fuel ash (POFA) [10–14] or industrial waste such as silico-manganese slag (SiMn) [15], ground granulated blast furnace

Adewumi, A.A., Ismail, M., Ariffin, M.A.M., Yusuf, M.O., Maslehuddin, M., Mohamed, H.D. Strength and microstructure of alkali-activated natural pozzolan and limestone powder mortar. Magazine of Civil Engineering. 2019. 92(8). Pp. 36–47. DOI: 10.18720/MCE.92.3

Адеуми А.А., Исмаил М., Ариффин М.А.М., Юсуф М.О., Маслехуддин М., Мохамед Х.Д. Прочность и микроструктура щелочно-активированного пуццоланового и известнякового раствора // Инженерно-строительный журнал. 2019. № 8(92). С. 36–47. DOI: 10.18720/MCE.92.3



slag (GGBFS) [15–17], fly ash (FA) [18], silica fume (SF) [18, 19], coal bottom ash [20], paper sludge ash [21] and mine tails [5] with aluminosilicate components. Fly ash (class F), silica fume, and slag have been shown to be a good precursor for alkali-activated concrete, however, the proliferation of environmental wastes and the need to improve public health have called for utilization of other solid wastes for alkali-activated binders.

This research has identified natural pozzolan (NP) and limestone powder wastes (LSPW) in the synthesis of alkali-activated binder. NP is formed from a volcanic eruption with very high silica and moderate alumina contents. The world reserve of NP has been estimated to be 7 billion tons [22] while 180,000 km² of NP is also available in the western region of Saudi-Arabia [23]. Furthermore, significant deposits of NP have been reported in China, Turkey, Greece, Iran and the USA [24]. Due to NP chemical compositions and its plethora availability across the volcanic regions, it has gained global acceptance for the synthesis of geopolymer concrete [25]. The production of limestone tiles by diamond cutting of limestone rock generates millions of tonnage of limestone powder wastes (LSPW). Limestone quarry generates around 20 % to 25 % powder waste [26]. About 21.2 million tons of LSPW is generated in the UK, while in Greece, 18 million tons are generated and Turkey generates 30 million tons per annum [26]. LSPW are deposited in landfills, the dust particles from the landfills contaminate the air as a result of wind blow, these have resulted in environmental, air and water pollution leading to severe health hazards such as cancer and asthma [27]. LSPW has been used as filler in concrete to enhance the compressive strength of concrete [27, 28].

In some of the previous studies on NP, Ghafoori et al. [29] studied the effect of alkali activators parameter on alkali-activated NP mortar. However, the influence of alkaline-activator on microstructure of the resulted products was not explored. In another study, Ibrahim et al. [30] studied similar effects under continuous heat curing condition at 60 °C for 28 days. Furthermore, the binary effect of blast furnace slag (BFS) and NP on the strength development of mortars cured at room temperature has been investigated and it was found that the CaO in slag contributed to the improved strength as a result of the formation of Ca-Al-Si gel in the matrix [7]. Silva et al. [25] synthesized geopolymer concrete using fired clay brick waste and NP, also under continuous oven curing for 7 days. Oven curing for long days will result in high consumption of energy. Cwirzen et al. [31] investigated the blends of metakaolin and limestone alkali-activated paste using NaOH only, which show relatively low strength of 7MPa. Yuan et al. [32] found that 30 % of limestone powder could improve the strength of sodium carbonate activated slag.

Several environmental friendly waste materials have been studied by researchers, however, despite these numerous works on the performance of alkali-activated binders, none of these studies has addressed the engineering properties of activated mortar using a blend of limestone powder and natural pozzolan. So far, the effects of LSPW on the reaction products, strength development, bond characteristics and the microstructure of LSPW/NP alkali-activated mortar are yet to be investigated. Therefore, the present research aims at studying the synergistic effect of LSPW/NP on the reaction products, strength development, bond characteristics and the microstructure of the product matrix. The outcomes of this study will contribute to waste valorization, dumpsite land reclamation, low CO₂ footprint, energy consumption reduction, reduction in environmental pollution and addition to more sustainable alternative binders for structural purposes.

2. Materials and Methods

2.1. Materials and reagents

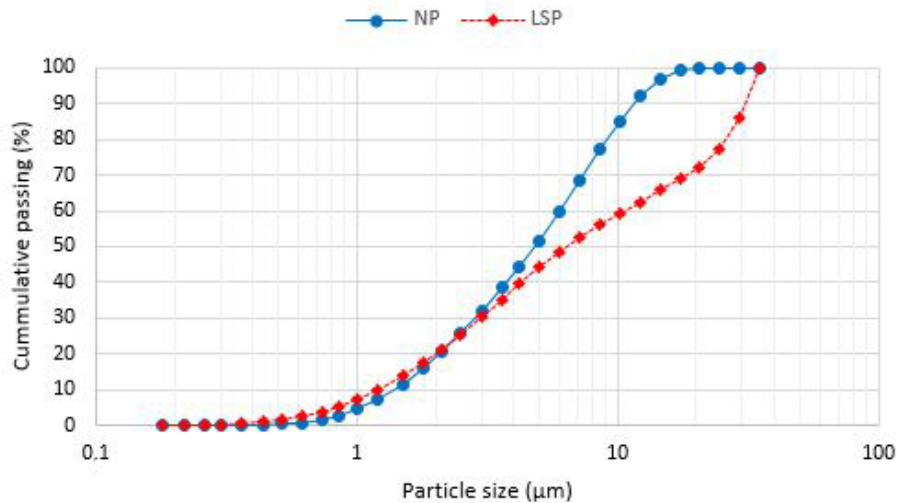
2.1.1. Natural pozzolan and limestone powder waste

Natural pozzolan (NP) was provided by Imerys minerals Arabia and the limestone powder waste (LSPW) was obtained from tiles cutting factory. The LSPW was oven-dried at 105 °C ± 5 °C for 24 hrs to remove the moistures. The LSPW was sieved through sieve 200 µm sieve to remove stones and debris. The particle size distributions (PSDs) of precursors were determined with the aid of HELOS (H3533) & QUIXEL particle size analyzer using sedimentation method and X-ray absorption, while the specific surface areas (BET) of the precursors were determined with Micromeritics ASAP2020 by using nitrogen gas adsorption, the results are presented in Table 1 and Figure. 1. The oxide compositions of these two materials as revealed in Table 2 were determined by using X-ray fluorescence (XRF) machine.

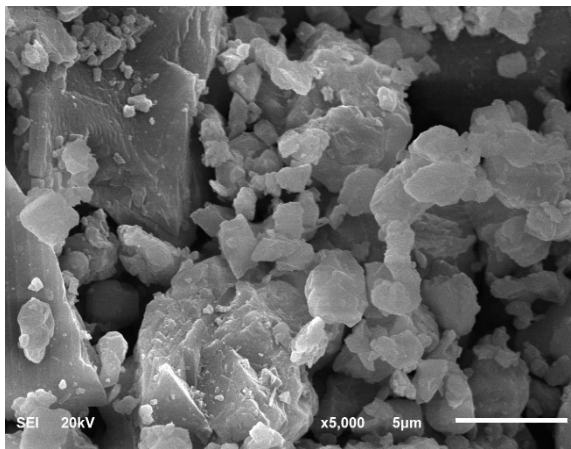
The morphology of the powdered LSPW and NP was evaluated using a JSM-5800LV scanning electron microscope (SEM). As revealed in Figure. 2, LSPW has a round edge polycrystal-like shape, while NP has an angular particle shape coupled with elongated flakiness. The mineralogical composition and amorphous or crystalline nature of the raw materials were explored using X-ray diffraction (XRD) analysis. The crystalline phases were identified from the COD database (2019 edition) in conjunction with the MATCH XRD software. According to the XRD result shown in Figure. 3, NP contains mainly quartz (SiO₂), plagioclase (Ca, Na)Al₂Si₂O₈) and microcline (KAl₂Si₂O₈), it revealed that NP is an amorphous compound with very low crystallinity while the LSPW contains mainly calcite (CaCO₃) and quartz ((SiO₂) and it is of high crystallinity.

Table 1. Physical properties of NP and LSPW.

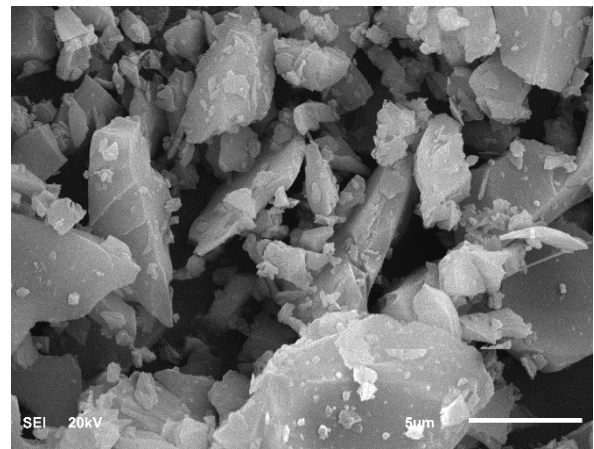
Materials	Specific gravity	Average particle size, d_{50} (μm)	Specific surface area (cm^2/g)
NP	2.3	4.84	3.1
LSPW	2.7	6.43	0.6

**Figure 1. Particle size distribution of LSP and NP.****Table 2. Chemical compositions of NP and LSPW obtained from XRF.**

Oxides	SiO ₂	CaO	Al ₂ O ₃	Fe ₂ O ₃	MgO	Na ₂ O	K ₂ O	S ₂ O ₃	L.O.I
LSPW (%)	2.5	94.1	0.8	1.2	0.6	-	0.3	0.5	44
NP (%)	74	2	13	1.5	0.5	4	5	-	5



(a)



(b)

Figure 2. SEM micrographs of raw materials: (a) LSPW and (b) NP.

2.1.2. Synthesis of alkali activator

Sodium silicate (SS) and sodium hydroxide (NH) that are commercially available were used as activators in this study. The initial silica modulus ($M_s = \text{SiO}_2/\text{Na}_2\text{O}$) was 3.3 while the molarity of $\text{NaOH}_{(\text{aq})}$ (NH) was 10 M. The percentage composition of SS is as follows: H_2O : 62.11 %, SiO_2 : 29.13 % and Na_2O : 8.76 %. The 10 M- $\text{NaOH}_{(\text{aq})}$ was prepared by dissolving 404.4 g of NaOH pellet (99 % assays) into distilled water to form 1 L of an alkali solution (10 M- $\text{NaOH}_{(\text{aq})}$).

2.1.3. Aggregates

Dune desert sand passing the gradation size requirement of ASTM C33 was used as fine aggregate (FA). The fineness modulus of FA was 1.82 and the specific gravity in saturated surface dry (SSD) condition was 2.63.

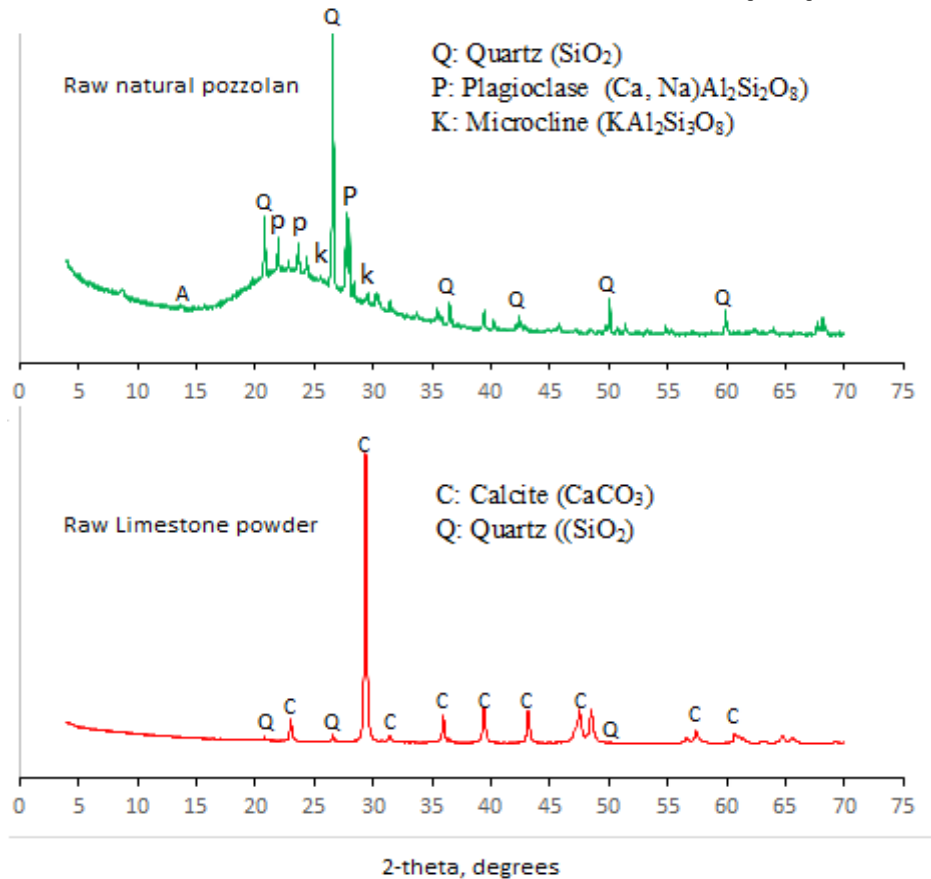


Figure 3. X-ray diffractograms: (a) Raw natural pozzolan and (b) Raw limestone powder.

2.2. Experimental program

2.2.1. Mix design

The mixture proportions of alkali-activated mortar were designed with LSPW content of 0 %, 20 %, 40 %, 60 % 80 % and 100 % (natural pozzolan contents of 100 %, 80 %, 60 %, 40 %, 20 % and 0 %, respectively). The samples were designated as AANL_x (alkali-activated NP/LSPW mortar), where x is the $\frac{L}{L+N}$ ratios. A total of six AANL_x (where $x = 0, 0.2, 0.4, 0.6, 0.8$ and 1) mixtures were prepared. AANL₀ and AANL₁ served as the control. Table 3 summarizes the proportion of the constituent materials in the alkali-activated mortar mixtures. A constant fine aggregate -to-the binder ratio of 2 was used. This was the optimum value from our preliminary trial mix. All the mixtures were prepared using Na₂SiO₃(aq)/ NaOH_{aq} (NS/NH) ratio of 1.0 and alkali activator to binder ratio of 0.5 for the mortar and 0.25 for the paste. In all the mixtures, The free water to precursor ratio was maintained 10 %.

Table 3. Mixture proportion of alkali-activated natural pozzolan/limestone powder waste mortar.

Mix #	Mix ID.	NP kg/m ³	LSPW kg/m ³	Na ₂ SiO ₃ (aq) (NS) kg/m ³	NaOH _(aq) (NH) kg/m ³	Water kg/m ³	Sand kg/m ³
M1	AANL ₀	605	0	151.5	151.5	60.5	1210
M2	AANL _{0.2}	484	121	151.5	151.5	60.5	1210
M3	AANL _{0.4}	363	242	151.5	151.5	60.5	1210
M4	AANL _{0.6}	242	363	151.5	151.5	60.5	1210
M5	AANL _{0.8}	121	484	151.5	151.5	60.5	1210
M6	AANL ₁	0	605	151.5	151.5	60.5	1210

2.2.2. Sample preparation, mixing, placing and curing

The required quantities of constituent materials were measured and mixed in batches in 5.0 L capacity Hobart planetary bench mixer, the mixing of the materials was in two stages. First, the NP and LSPW powder and sand were mixed in a dry condition for 3 mins. Secondly, the alkali solution (NaOH_(aq) + Na₂SiO₃(aq)) and water were added for the wet mixing stage which involves low speed mixing for 2mins and another 4 mins for

fast or higher speed mixing until a homogeneous mixture was achieved, the total mixing time was about 9 to 10 min. It should also be noted that 10M NaOH(aq) was prepared a day prior to mixing to allow cooling of the solution due to the exothermic nature of the solution. Thereafter, the mortar was placed in the oil-smear steel moulds of 50×50×50 mm in two layers and each layer was vibrated on the vibrating table for 30 s to remove any entrapped air from the mixture. Follow by surface smoothing of the specimen with a hand trowel. The specimens were then covered with a plastic sheet to prevent moisture loss. Afterwards, the specimens were kept in the laboratory at 20 ± 5 °C for 24 hrs. The cubes were de-moulded after 24 hrs. This was followed by placing the samples in zip plastic bags to avoid loss of moisture to the environment. The samples were then subjected to temperature curing in an oven maintained at 75 °C for 24 hrs. After that, the specimens were cured under a normal condition of 20 ± 5 °C until the age of testing (1, 3, 7, 14 and 28 days). The mineralogical and morphological analysis in this study was conducted by using a paste of the alkali-activated material.

2.3. Evaluation methods

2.3.1. Setting time and workability

The initial and final setting times of the AANL paste were determined in accordance with ASTM C191 [33] and the workability of AANL mortar was measured in accordance with ASTM C1437 [34].

2.3.2. Compressive strength

Compressive strength of the AANL mortar was determined in accordance with ASTM C 150 [35] on cube specimens measuring 50×50×50 mm using a digital compression testing machine. The compressive strength of the specimens was determined after 1, 3, 7, 14 and 28 days of curing. Three specimens were tested at each age and the average compressive strength value is reported.

2.3.3. Microstructural characterization of the specimens

X-ray diffractometer (XRD), scanning electron microscopy coupled with energy dispersive X-ray spectroscopic analysis (SEM + EDS) and Fourier transform spectroscopy (FTIR) were used to characterize the microstructure of the products and to determine the contribution of LSPW to the nature of the alkali-activated product, AANL₀, AANL₁ were compared with AANL_{0.6}, AANL₀, and AANL₁ served as the control specimens. The bond vibrations of the fine powder product obtained from 25 mm cube of AAP specimen after 14 days of curing were observed by using a Perking Elmer 880 spectrometer FTIR machine. The morphological study of the middle portions of the 25 mm cube of AAP specimens was done with the aid of the JEOL SEM + EDS model 5800 LV at accelerating voltage of 20 kV. The phases of the product were explored using XRD Bruker instrument model d2-Phaser with Cu Ka radiation (40 kV, 40 mA) by continuous scanning within angle 2-theta range of 4–80° and at a scan speed of 2.5°/min.

3. Results and Discussion

3.1. Effect of LSPW on workability alkaline-activated NP

The slump flow of the fresh AANL_x ($x = \text{LSPW}/(\text{LSPW} + \text{NP})$) varies from 0 to 1) mixture is presented in Figure 4. The flow of the AANL₀ is the lowest in the mix, this phenomenon can be due to higher water demand of NP caused by high silica content (74 %). NP also has an angular particle shape coupled with elongated flakiness [Figure 2b] and larger specific surface area [Table 1] compared to LSPW. However, upon addition of LSPW to the alkali-activated NP mortar, it leads to an increase in the flowability of the mixture. There were 40 %, 90 %, 105 %, 120 % and 125 % increment in AANL_{0.2}, AANL_{0.4}, AANL_{0.6}, AANL_{0.8} and AANL₁, respectively, when compared with AANL₀. This observation is due to high dissolution rate of LSPW in alkali activator compared to NP. This resulted in the micro-filling effect of the finer particle of LSPW within the matrix. The micro-filling effect positively enhanced the early strength in the synergized AANL as shown in Figure 5. This is in agreement with previous studies that showed that finer particle size distribution could contribute to better flowability [36, 37]. Equation 1 shows the correlation between the experimental values.

$$y = -14.063x^2 + 26.634x + 9.939. \quad (1)$$

3.2. Effect of LSPW on setting time of alkaline-activated NP

As shown in Figure 6, the incorporation of LSPW to AANL_x ($x = \text{LSPW}/(\text{LSPW} + \text{NP})$) varies from 0 to 1) mixture generally leads to a reduction in setting time of the mixtures. The AANL₀ with 100 % NP has very high initial and final setting time as shown in Figure 2, however, when 20 % of LSPW was added to the mix, its initial setting time and final setting time reduced by 41 % and 64 % respectively, Further addition of 20 % LSPW (AANL_{0.4}) to the mix leads to a reduction of 76 % and 79 % of the initial setting time and final setting time, respectively in reference to AANL₀. Similar trends were observed upon total addition of 60 %, 80 % and 100 % of LSPW to the mixture. It should be noted that with 100 % LSPW, false setting was observed due to high reactivity of LSPW in alkali activators. The model equations predicting the results for the initial and final setting time in terms of x ($x = \text{LSPW}/(\text{LSPW} + \text{NP})$) is shown in Figure 6.

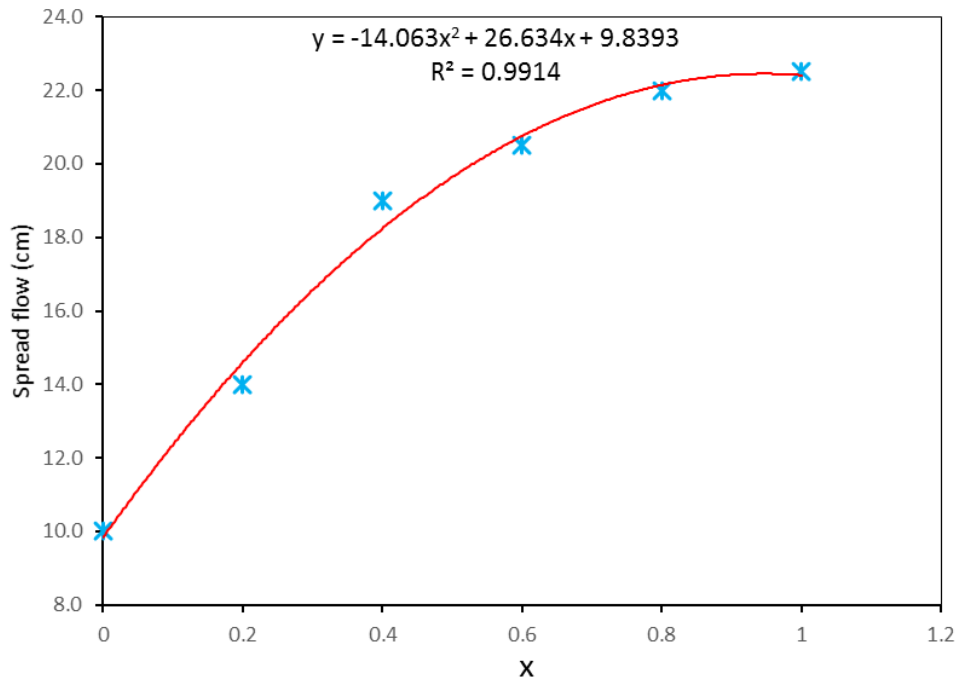


Figure 4. Flowability of the AANL.

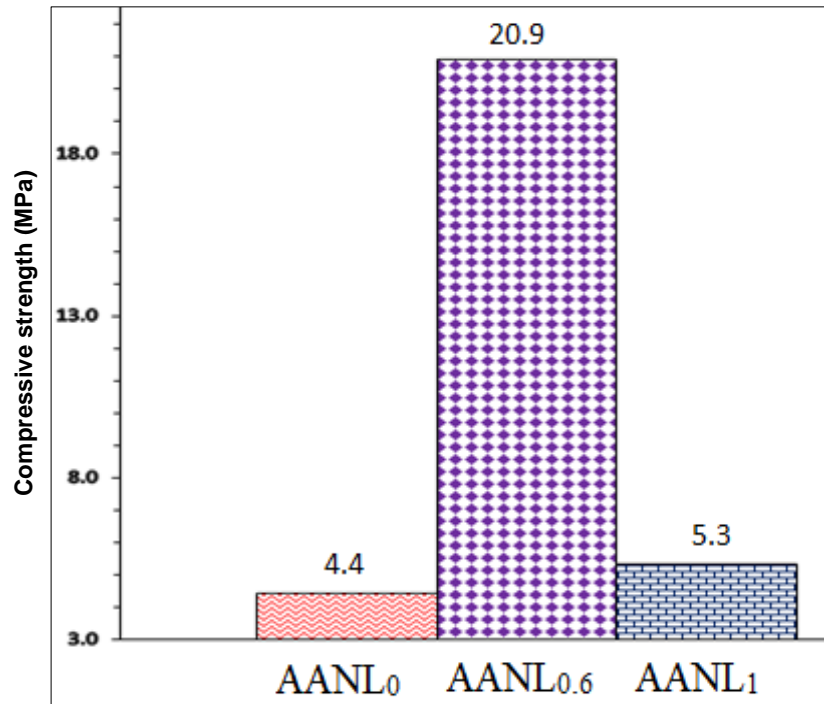


Figure 5. 1-day compressive strength of alkali-activated mortar.

3.3. Effect of LSPW on compressive strength of alkaline-activated NP

The synergistic effect of LSPW and NP on the compressive strength of synthesized alkali-activated mortar is shown in Figure 7. Generally, the compressive strength for all the mixes increases with age. The 1-day compressive strength of 4.4 MPa was obtained in AANL₀ which was 21.3 % of the strength obtained upon substituting NP with 20 % LSPW. The increase in strength continued as the substitution level increases as shown in Figure 7. The strength increased by 370.45 %, 322.7 %, 375 %, 193 % when 20 %, 40 %, 60 % and 80 % of LSPW were added to the mix proportion in AANL_{0.2}, AANL_{0.4}, AANL_{0.6}, AANL_{0.8}, respectively. The compressive strength of the mortar increase with LSPW content up to 60 % (AANL_{0.2}, AANL_{0.4} and AANL_{0.6}) and then drastically decline upon 80 % LSPW (AANL_{0.8}) addition. While the 1-day compressive strength of 5.3 MPa was obtained in AANL₁. At 28days, 102.27 % of strength was gained in AANL₀. while 18.87 % was gained in AANL₁. The maximum strength of 27 MPa was obtained in AANL_{0.6} after 28 days. It is remarkable that the combination of LSPW and NP in the synthesis of the AAM enhanced early strength development of the mixed than individual usage of the primary material.

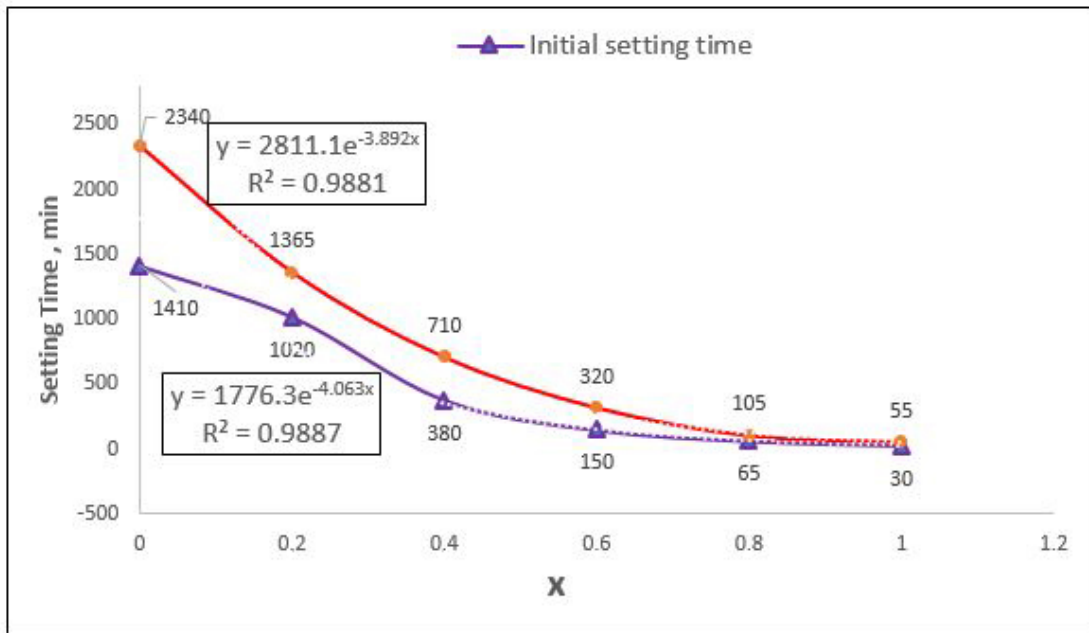


Figure 6. Setting time of AANL.

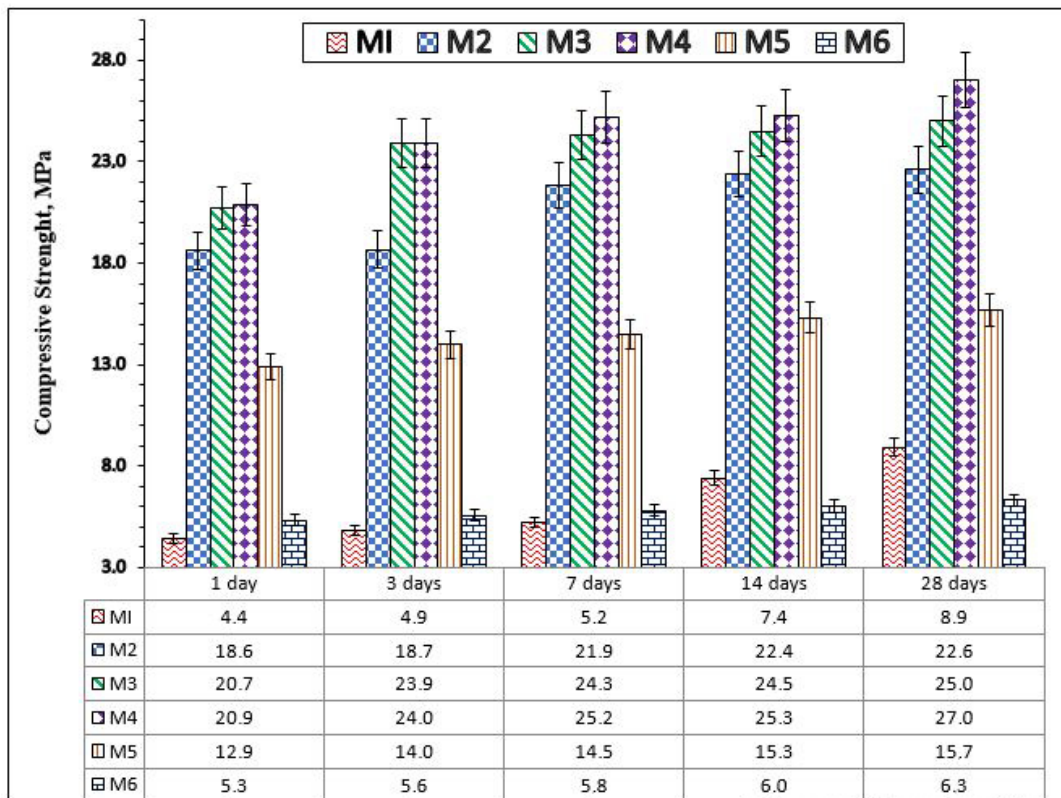


Figure 7. Compressive strength of AANL mixes

(M1 = AANL₀, M2 = AANL_{0.2}, M3 = AANL_{0.4}, M4 = AANL_{0.6}, M5 = AANL_{0.8}, M6 = AANL₁)

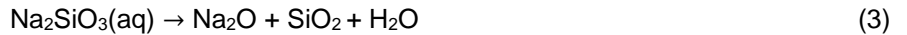
3.4. Effect of limestone powder on microstructures and bonds of alkali-activated mortar

Limestone powder waste (LSPW) contains mainly CaO (94.1 %) and SiO₂ (2.5 %) with a little percentage of Al₂O₃ (0.8 %) as shown in Table 2, this can be expressed empirically as Ca₁₁₈AS₃. The XRD results in Figure 3 also confirmed the presence of high crystalline calcite (CaCO₃) and quartz (SiO₂). Alkali activation of LSPW starts by the breaking down of the LSPW bonds which mainly comprises calcite that breaks down into lime and carbon dioxide as shown in Equation 2 thereby making CaO available to play the charge balancing role in the stability of the oligomer formed from the condensation process of the transported silicate dominated monomers.



Alkali activators most specifically, NaOH_(aq) caused the dissolution of complex aluminosilicate, most especially during the early reactions thereby releasing the monomers such as Ca-O, Si-O-Si, Al-O-Al and

Al-O-Si together with that obtained from sodium silicate activators (Si-O-Si). $\text{Na}_2\text{SiO}_3(\text{aq})$ and $\text{NaOH}(\text{aq})$ dissociate according to Equations 3 and 4



The SiO_2 from $\text{Na}_2\text{SiO}_3(\text{aq})$ supplies the soluble Si ions while $\text{NaOH}(\text{aq})$ provides the OH^- for bond cleaving [38]. There is an exchange of H^+ for Ca^{2+} and Na^+ when the PH of the medium is between 7–10 during the early stage of the reaction, followed by the hydrolysis of Si-O-Si, Al-O-Al, or Al-O-Si to form Si-O-CaOH monomers [37]. The monomers polymerized to form CaSiO_3 (wollastonite), albite ($\text{NaAlSi}_3\text{O}_8$), and chains of SiO_2 as revealed in Figure 8b (AANL₁). The Ca^{2+} could also have reacted with OH^- to form portlandite ($\text{Ca}(\text{OH})_2$), FTIR in Figure 9c confirms the precipitation of portlandite due to the increase in the intensity of OH^- , vibrating at wavenumber 3450 cm^{-1} which is not present in the raw LSPW as shown in Figure 8a. A very low 28-day compressive strength of 6.3 MPa was obtained in AANL₁, this was due to the formation portlandite ($\text{Ca}(\text{OH})_2$) as explained previously.

In addition to this, FTIR in Figure 9c shows that there is an asymmetric stretching of H-O-H formed due to hydrogen bonding at a wavenumber of 2359 cm^{-1} coupled with bending of an unbound water molecule at 1645 cm^{-1} . Furthermore, Figure 10 shows the SEM image and the EDS result of AANL₁ which has an interconnected porous microstructure, that is responsible for the low compressive strength recorded. The EDS results also show very low content of Si (0.8 %) and Al (0.2 %) in spectrum 1 alongside with Si (1.4 %) and Al (0.2 %) in spectrum 3. Spectrum 2 reveals the presence of CaO in the matrix which can mix with entrapped water in the matrix as earlier stated to form ($\text{Ca}(\text{OH})_2$). All these could contribute to the negative strength development in the AANL₁

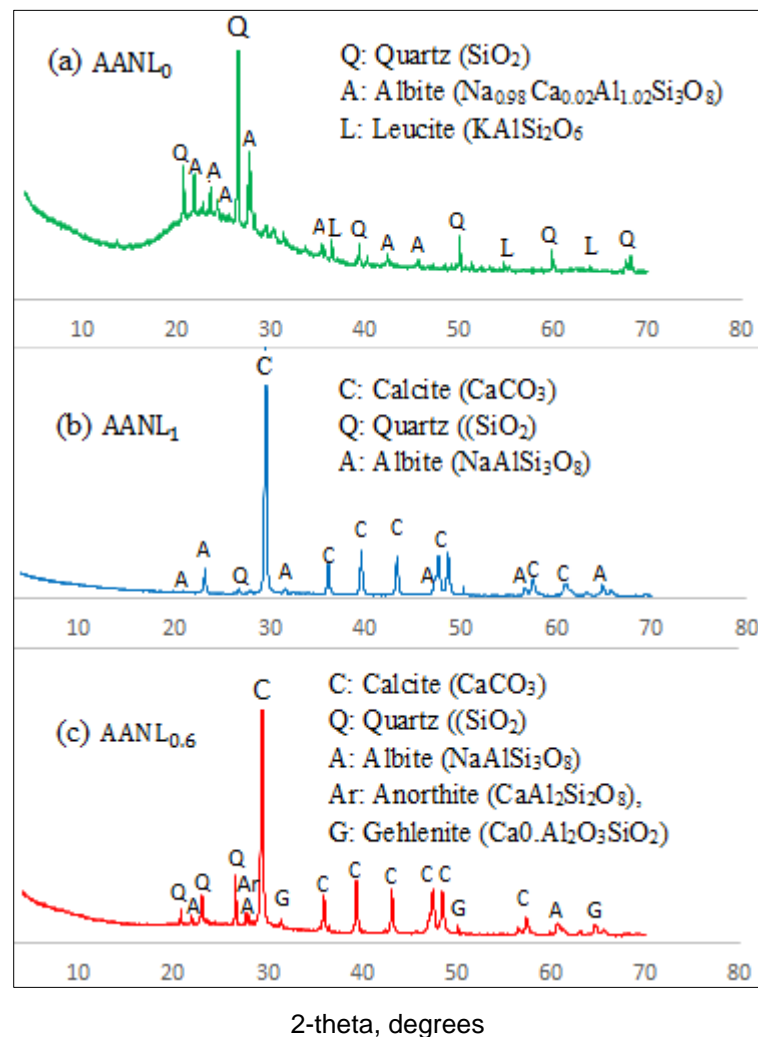


Figure 8. X-ray diffractograms of the activated product of (a) NP (b) LSPW (c) combined NP and LSPW.

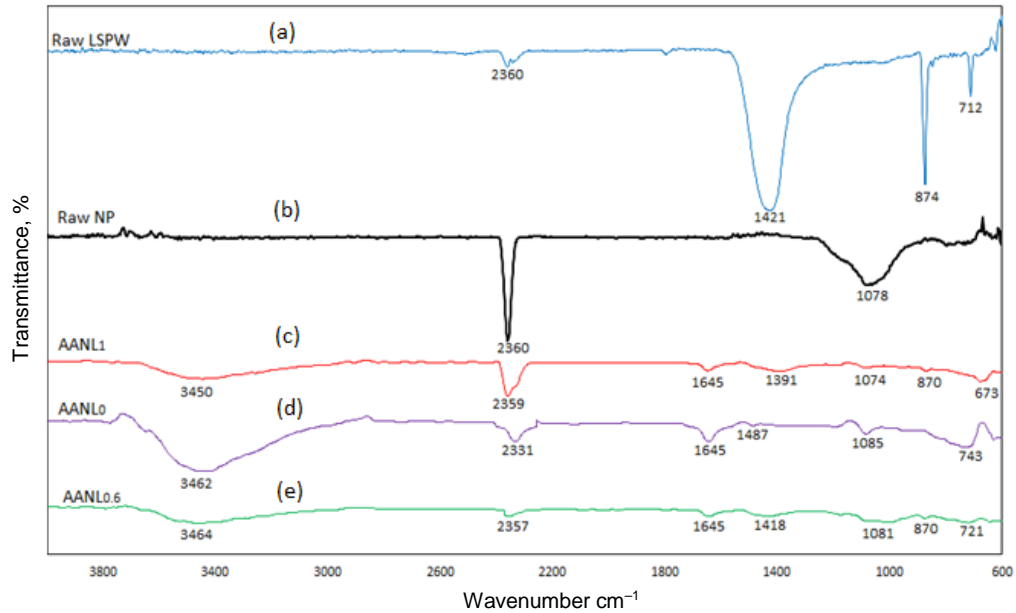


Figure 9. FTIR spectra of (a) unactivated limestone powder (b) unactivated natural pozzolan (c) activated limestone powder waste (d) activated natural pozzolan (e) activated limestone powder wastes and natural pozzolan.

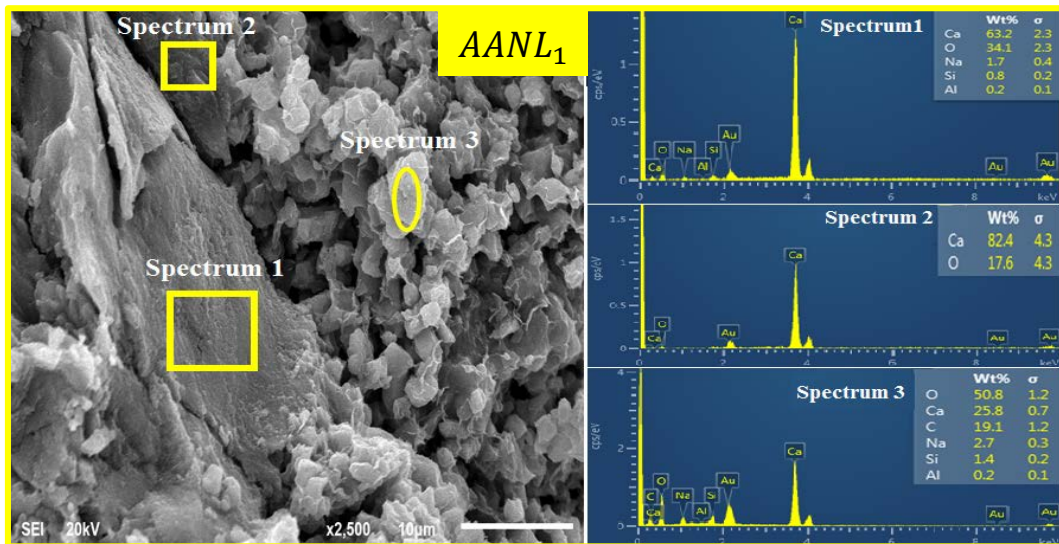


Figure 10. SEM/EDS of alkali-activated limestone powder wastes (AANL₁).

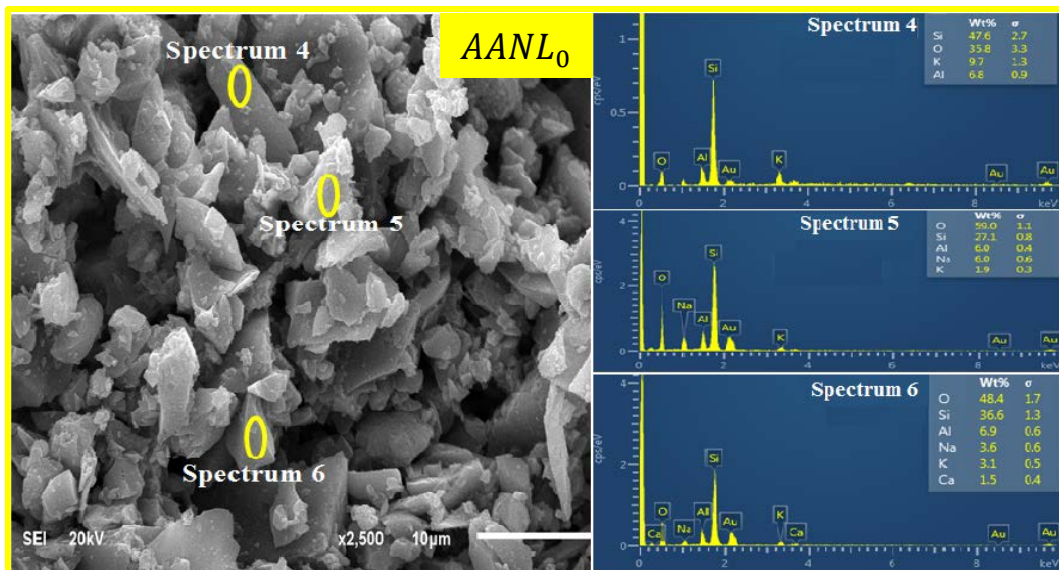


Figure 11. SEM/EDS of alkali-activated natural pozzolan (AANL₀).

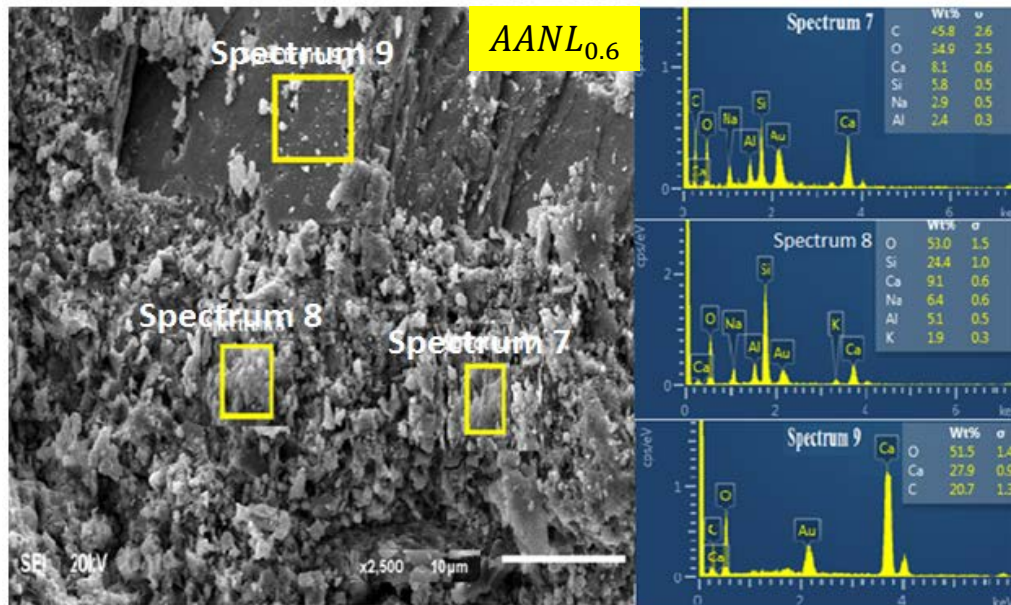


Figure 12. SEM/EDS of binary blended alkali-activated natural pozzolan and limestone powder (AANL_{0.6}).

3.5. Effect of NP on microstructures and bonds of alkali-activated mortar

The XRF results in Table 2 show that NP contains SiO₂ (74 %), Al₂O₃ (13 %), K₂O (5 %), Na₂O (4 %) and CaO (2 %), which can also be expressed as C(N₂)A₇S₃₇ and K₃A₇S₃₇. The XRD results in Figure 3 also confirmed the presence of the amorphous phase of NP as indicated by the diffuse halo diffraction peaks between 15° and 40°. The peaks in the NP diffractogram include the plagioclase (albite/Anorthite (Ca, Na)Al₂Si₂O₈), microcline (KAl₂Si₃O₈) and quartz (SiO₂). Alkali activation of NP structures resulted in the dissolution of the C(N₂)A₇S₃₇ and K₃A₇S₃₇ bonds and the formation of potassium-aluminosilicate hydrate (KASH), sodium-aluminosilicate hydrate (NASH) and calcium-aluminosilicate hydrate (CASH). The SiO₂ from Na₂SiO₃(aq) supplies the soluble Si ions while NaOH(aq) provides the OH⁻ for bond cleaving. Al and Si in NP became pentavalent as a result of OH⁻ attachment, hence severing the Si-O-Si, Al-O-Al, or Al-O-Si bond.

The 5- and 6- coordinated Al in complex form is converted to 4-coordination upon dissolution, The Al-O-Al being the weakest bond ruptured first to form Al-O that reacts with SiO₂ from Na₂SiO₃(aq) to form aluminosilicate oligomer. The Al-O⁻ (negative) is charged balanced by the positive charged (K, Ca or Na). The next stage is the agglomeration of these monomers -Al-O-KOH, -Al-O-NaOH, and -Al-O-CaOH together with -Si-O-Si to form KASH, NASH and CASH, respectively. The XRD results in Figure 8a also revealed the formation albite (Na_{0.98}Ca_{0.02}Al_{1.02}Si₃O₈) similar to (C, NASH), Leucite (KAlSi₂O₆) similar in form to KASH with quartz.

A very low 28-day compressive strength of 8.9 MPa was obtained in AANL₀, this is attributed to the formation portlandite (Ca(OH)₂) as a result of the presence OH⁻ vibration of a broad peak centered at wavenumber 3462 cm⁻¹ (FTIR in Figure 9d) which is absent in the raw NP as shown in Figure 9b. In addition, FTIR in Figure 9d shows that there is an asymmetric stretching of H-O-H formed due to hydrogen bonding at a wavenumber of 2331 cm⁻¹ coupled with bending of an unbound water molecule at 1645 cm⁻¹ and this could constitute to weak microstructure. Furthermore, Figure 10 shows the SEM image and the EDS result of AANL₀, AANL₀ SEM image appeared to be non-homogenous, flaky and non-dense structure due to the presence of air voids. This is responsible for the low compressive strength recorded in AANL₀. The EDS results also show high Si/Al (4.5~7) and low Ca/Si (0.04) (spectrum 3). The low Ca/Si could also have contributed to the negative strength development in the AANL₀.

3.6. Effect of NP/LSPW on reaction product, bond characteristic and microstructures of alkali-activation AANL mortar

The alkali activation of the combined precursors (NP/LSPW) gives the maximum 28-day compressive strength of 27 MPa with 60 % LSPW combination with 40 % NP (ANNL_{0.6}). The reaction products are calcite (CaCO₃), quartz ((SiO₂), albite (NaAlSi₃O₈), anorthite (CaAl₂Si₂O₈), gehlenite (Ca_{0.4}Al₂O₃SiO₂) as revealed in the XRD in Figure 8c. Anorthite (CaAl₂Si₂O₈) and gehlenite (Ca_{0.4}Al₂O₃SiO₂) are present in ANNL_{0.6} but absent in ANNL₀ and ANNL₁ as depicted in Figure. 8. These two compounds contributed positively to the compressive strength development of ANNL_{0.6}. Furthermore, Figure 12 shows the SEM image and the EDS result of ANNL_{0.6}, ANNL_{0.6} SEM image appeared to be homogenous and dense in the microstructure. There are two distinct regions on the image. Spectrum 7 showing a dense microstructure is the reactive products while spectrum 9 shows the reactive CaCO₃. The calcite has pores filling effect on the microstructure, which also favours the compressive strength development. The EDS of ANNL_{0.6} also, show the lowest Si/Al (2.4~4.9) in comparison with ANNL₁

(Si/Al (4~7) and ANNL₀ (Si/Al) (4.5~7). When the Ca/Si is 1.4 (spectrum 7), this value is 34 % greater than Ca/Si in ANNL₀. The Ca/Si was higher in ANNL_{0.6} due to soluble Ca²⁺ contribution from LSPW. The Ca²⁺ contributes to the strength development by both pores filling and bonding with O-Si-O and O-Al-O and the OH⁻¹ to form CaOH-Si-O-AlCaOH.

FTIR spectrum in Figure 9e validate the presence of hydroxylation of a widespread peak vibration centered at wavenumber 3464 cm⁻¹ in ANNL_{0.6} which is weaker if compared to that of ANNL₀ and ANNL₁ (Figure 8c/8d). Besides, there is asymmetric stretching of H-O-H formed due to hydrogen bonding at a wavenumber of 2357 cm⁻¹ coupled with bending of a very little water molecule at 1645 cm⁻¹ if compared to that of ANNL₀ and ANNL₁. The lesser the water present in the micropores, the higher the strength.

4. Conclusions

In this research, the alkali-activated mortar was synthesized by utilizing limestone powder waste (LSPW) from the tiles manufacturing industry and natural pozzolan (NP) from a volcanic source. The effects of LSPW and NP on the workability, setting time, reaction products, strengths development, bond characteristics and the microstructural properties of the developed alkali-activated binary blending of LSPW and NP (AALN) mortar were investigated and the following are the summary of the conclusions:

1. The dearth in CaO in NP decreases the consistency of the mixtures while the more the quantity of LSPW of higher calcium source, the more the flowability of the mixture. However, setting time reduces with the higher content of LSPW due to early integration and formation of calcium silicate hydrate.
2. There was an insignificant strength development when the LSPW and NP were used independently (6–9 MPa) due to the formation of unstable aluminosilicate framework and portlandite in the former and the latter systems due to the absence of SiO₂ and CaO, respectively.
3. The optimum percentage of NP in the binary blending is 40 % while LSPW constituted 60 % in the mixture that resulted in the 28-day maximum compressive strength of 27 MPa.
4. Formation of anorthite (CaAl₂Si₂O₈) and gehlenite (Ca₀.Al₂O₃SiO₂) in the synergy of the alkali-activated NP and LSPW contributed positively to the strength development.
5. The pore-filling effect caused by the presence of calcite in the product resulted from the binary combination of NP and LSPW.
6. The rough texture of the micrograph of alkali-activated NP was characterized with high porosity turned to promote denser and smooth microstructure in the presence of LSPW.

5. Acknowledgements

The authors gratefully acknowledge the support from the Research Management Centre (RMC) Universiti Teknologi Malaysia (UTM), Grant no: 16H94. The center for Engineering Research (CER), Research Institute, King Fahd University of Petroleum and Minerals, Dhahran, Saudi Arabia and the University of Hafr Al-Batin, Hafr Al-Batin, Saudi Arabia.

References

1. Scrivener, K.L., John, V.M., Gartner, E.M. Eco-efficient cements: Potential, economically viable solutions for a low-CO₂, cementbased materials industry [Online]. 2015. URL: [https://www.devalt.org/Pdf/L2_SixThemePdfs/2016-UNEPReport-Complete4\(1\).pdf](https://www.devalt.org/Pdf/L2_SixThemePdfs/2016-UNEPReport-Complete4(1).pdf)
2. CEMBUREAU Activity Report 2015. 2015. URL: https://cembureau.eu/media/1503/2015activityreport_cembureau.pdf
3. Damtoft, J.S., Lukasik, J., Herfort, D., Sorrentino, D., Gartner, E.M. Sustainable development and climate change initiatives. 2008. 38. Pp. 115–127. DOI: 10.1016/j.cemconres.2007.09.008
4. Andrew, R.M. Global CO₂ emissions from cement production. 2017. (August). Pp. 1–52.
5. Provis, J.L., van Deventer, J.S.J. Alkali activated materials. 2014. DOI: 10.1007/978-94-007-7672-2
6. Luukkonen, T., Abdollahnejad, Z., Yliniemi, J., Kinnunen, P., Illikainen, M. One-part alkali-activated materials. Cement and Concrete Research. 2018. 103 (October). Pp. 21–34. DOI: 10.1016/j.cemconres.2017.10.001
7. Najimi, M., Ghafoori, N., Sharbaf, M. Alkali-activated natural pozzolan/slag mortars: A parametric study. Construction and Building Materials. 2018. 164. Pp. 625–643. DOI: 10.1016/j.conbuildmat.2017.12.222
8. Najimi, M., Sobhani, J., Ahmadi, B., Shekarchi, M. An experimental study on durability properties of concrete containing zeolite as a highly reactive natural pozzolan. Construction and Building Materials. 2012. 35. Pp. 1023–1033. DOI: 10.1016/j.conbuildmat.2012.04.038
9. Ibrahim, M., Megat Johari, M.A., Maslehuddin, M., Rahman, M.K., Salami, B.A., Mohamed, H.D. Influence of composition and concentration of alkaline activator on the properties of natural-pozzolan based green concrete. Construction and Building Materials. 2019. 201. Pp. 186–195. DOI: 10.1016/j.conbuildmat.2018.12.117
10. Karim, M.R., Zain, M.F.M., Jamil, M., Lai, F.C. Fabrication of a non-cement binder using slag, palm oil fuel ash and rice husk ash with sodium hydroxide. Construction and Building Materials. 2013. 49. Pp. 894–902. DOI: 10.1016/j.conbuildmat.2013.08.077
11. Salami, B.A., Megat Johari, M.A., Ahmad, Z.A., Maslehuddin, M. Impact of added water and superplasticizer on early compressive strength of selected mixtures of palm oil fuel ash-based engineered geopolymer composites. Construction and Building Materials. 2016. 109. Pp. 198–206. DOI: 10.1016/j.conbuildmat.2016.01.033

12. Kubba, Z., Fahim Huseien, G., Sam, A.R.M., Shah, K.W., Asaad, M.A., Ismail, M., Tahir, M.M., Mirza, J. Impact of curing temperatures and alkaline activators on compressive strength and porosity of ternary blended geopolymer mortars. *Case Studies in Construction Materials*. 2018. 9. Pp. e00205. DOI: 10.1016/j.cscm.2018.e00205
13. Salami, B.A., Megat Johari, M.A., Ahmad, Z.A., Maslehuddin, M., Adewumi, A.A. Impact of Al(OH)₃ addition to POFA on the compressive strength of POFA alkali-activated mortar. *Construction and Building Materials*. 2018. 190. Pp. 65–82. DOI: 10.1016/j.conbuildmat.2018.09.076
14. Yusuf, M.O. Performance of slag blended alkaline activated palm oil fuel ash mortar in sulfate environments. *Construction and Building Materials*. 2015. 98. Pp. 417–424. DOI: 10.1016/j.conbuildmat.2015.07.012
15. Najamuddin, S.K., Megat Johari, M.A., Maslehuddin, M., Yusuf, M.O. Synthesis of low temperature cured alkaline activated silicomanganese fume mortar. *Construction and Building Materials*. 2019. 200. Pp. 387–397. DOI: 10.1016/j.conbuildmat.2018.12.056
16. Deb, P.S., Nath, P., Sarker, P.K. The effects of ground granulated blast-furnace slag blending with fly ash and activator content on the workability and strength properties of geopolymer concrete cured at ambient temperature. *Materials and Design*. 2014. 62. Pp. 32–39. DOI: 10.1016/j.matdes.2014.05.001
17. Criado, M., Aperador, W., Sobrados, I. Microstructural and Mechanical Properties of Alkali Activated Colombian Raw Materials. *Materials*. 2016. 9 (3). Pp. 158. DOI: 10.3390/ma9030158
18. Lee, N.K., Lee, H.K. Setting and mechanical properties of alkali-activated fly ash/slag concrete manufactured at room temperature. *Construction and Building Materials*. 2013. 47. Pp. 1201–1209. DOI: 10.1016/j.conbuildmat.2013.05.107
19. Sinthaworn, S., Nimityongskul, P. Effects of temperature and alkaline solution on electrical conductivity measurements of pozzolanic activity. *Cement and Concrete Composites*. 2011. 33 (5). Pp. 622–627. DOI: 10.1016/j.cemconcomp.2011.02.012
20. Topçu, I.B., Toprak, M.U., Uygunoğlu, T. Durability and microstructure characteristics of alkali activated coal bottom ash geopolymer cement. *Journal of Cleaner Production*. 2014. 81. Pp. 211–217. DOI: 10.1016/j.jclepro.2014.06.037
21. Adesanya, E., Ohenoja, K., Luukkonen, T., Kinnunen, P., Illikainen, M. One-part geopolymer cement from slag and pretreated paper sludge. *Journal of Cleaner Production*. 2018. 185. Pp. 168–175. DOI: 10.1016/j.jclepro.2018.03.007
22. Erdoğan, S.T. Inexpensive intumescent alkali-activated natural pozzolan pastes. *Journal of the European Ceramic Society*. 2015. 35 (9). Pp. 2663–2670. DOI: 10.1016/j.jeurceramsoc.2015.03.017
23. Moufti, M.R., Sabtan, A.A., El-Mahdy, O.R., Shehata, W.M. Assessment of the industrial utilization of scoria materials in central Harrat Rahat, Saudi Arabia. *Engineering Geology*. 2000. 57 (3–4). Pp. 155–162. DOI: 10.1016/S0013-7952(00)00024-7
24. Goleman, Daniel; Boyatzis, Richard; Mckee, A. Perlite Statistics and Information. *Journal of Chemical Information and Modeling*. 2019. 53 (9). Pp. 1689–1699. DOI: 10.1017/CBO9781107415324.004
25. Silva, G., Castañeda, D., Kim, S., Castañeda, A., Bertolotti, B., Ortega-San-Martin, L., Aguilar, R. Analysis of the production conditions of geopolymer matrices from natural pozzolan and recycled construction and demolition wastes. Submitted to *Construction and Building Materials*. 2019. 215. Pp. 633–643. DOI: 10.1016/j.conbuildmat.2019.04.247
26. Mageed, A.A., AbdelHafez, S. Utilization of Limestone Dust in Brick Making. *Journal of Engineering Sciences*. 2012. 40 (3). Pp. 913–922.
27. Turgut, P. Limestone dust and glass powder wastes as new brick material. *Materials and Structures/Materiaux et Constructions*. 2008. 41 (5). Pp. 805–813. DOI: 10.1617/s11527-007-9284-3
28. Antoni, M., Rossen, J., Martirena, F., Scrivener, K. Cement substitution by a combination of metakaolin and limestone. *Cement and Concrete Research*. 2012. 42 (12). Pp. 1579–1589. DOI: 10.1016/j.cemconres.2012.09.006
29. Ghafoori, N., Najimi, M., Radke, B. Natural Pozzolan-based geopolymers for sustainable construction. *Environmental Earth Sciences*. 2016. 75 (14). Pp. 1–16. DOI: 10.1007/s12665-016-5898-5
30. Ibrahim, M., Azmi, M., Johari, M., Kalimur, M., Maslehuddin, M. Effect of alkaline activators and binder content on the properties of natural pozzolan-based alkali activated concrete. *Construction and Building Materials*. 2017. 147. Pp. 648–660. DOI: 10.1016/j.conbuildmat.2017.04.163
31. Cwirzen, A., Provis, J.L., Penttala, V., Habermehl-Cwirzen, K. The effect of limestone on sodium hydroxide-activated metakaolin-based geopolymers. *Construction and Building Materials*. 2014. 66. Pp. 53–62. DOI: 10.1016/j.conbuildmat.2014.05.022
32. Yuan, B., Yu, Q.L., Brouwers, H.J.H. Assessing the chemical involvement of limestone powder in sodium carbonate activated slag. *Materials and Structures/Materiaux et Constructions*. 2017. 50 (2). DOI: 10.1617/s11527-017-1003-0
33. ASTM Standard C191 Standard Test Methods for Time of Setting of Hydraulic Cement by Vicat Needle; ASTM C191-08. American Society for Testing and Materials. (C). 2008. Pp. 1–8. DOI: 10.1520/C0191-08.2
34. ASTM Standard Test Method for Flow of Hydraulic Cement Mortar. *Astm C1437-15*. 2015. Pp. 1–2. DOI: 10.1520/C1437-15.2
35. American Society of Testing Materials Standard Specification for Portland Cement. ASTM International. June 1999. Pp. 1–6. DOI: 10.1520/C0010
36. Quercia, G., Hüskén, G., Brouwers, H.J.H. Water demand of amorphous nano silica and its impact on the workability of cement paste. *Cement and Concrete Research*. 2012. 42 (2). Pp. 344–357. DOI: 10.1016/j.cemconres.2011.10.008
37. Duxson, P., Provis, J.L. Designing precursors for geopolymer cements. *Journal of the American Ceramic Society*. 2008. 91 (12). Pp. 3864–3869. DOI: 10.1111/j.1551-2916.2008.02787.x
38. Yusuf, M.O., Megat Johari, M.A., Ahmad, Z.A., Maslehuddin, M. Strength and microstructure of alkali-activated binary blended binder containing palm oil fuel ash and ground blast-furnace slag. *Construction and Building Materials*. 2014. 52. Pp. 504–510. DOI: 10.1016/j.conbuildmat.2013.11.012

Contacts:

Adeshina Adewumi, +601114240744; adewumi@graduate.utm.my
 Mohammad Ismail, +6075531503; mohammad@utm.my
 Mohd Azreen Mohd Ariffin, +60163352841; mohdazreen@utm.my
 Moruf Yusuf, +966552545213; moruf@uhb.edu.sa
 Mohammad Maslehuddin, +966500026404; muddin@kfupm.edu.sa
 Hatim Mohamed, +96656950361; dmhatim@kfupm.edu.sa



DOI: 10.18720/MCE.92.4

Bending and torsion behaviour of CFRP strengthened RC beams

R. Al-Rousan*, **I. Abo-Msamh**

Jordan University of Science and Technology, Irbid, Jordan,

**E-mail: rzalrousan@just.edu.jo*

Keywords: engineering, materials science, technology, civil engineering, structural concrete

Abstract. In the construction industry, there is growing attention of using effective external strengthening techniques such as bonding of Carbon Fiber Reinforced Polymers (CFRP) composites onto the external deficient faces of the structural members due to their ease of installation, low invasiveness, high corrosion resistance, and high strength to weight ratio. As a result, the center of consideration of the majority of previously published studies was either only on the impact of fibers on the structural behavior of reinforced concrete elements or using CFRP composite as external strengthening for flexural or shear. The intent was to arrive at the vital CFRP strengthening technique that provides an effective increase in the flexural and shear strength while maintaining ductile failure mode. Therefore, this paper investigated the behavior of simply supported RC beams strengthened using CFRP and subjected to combined bending and torsion using Nonlinear Finite Element Analysis (NLFEA). Twenty-six models have been constructed and divided into six groups to scrutinize the effect of clear span to depth ratio; CFRP length; CFRP strip spacing; and CFRP depth. The results showed that the increase in the clear span to depth ratio as well as length of CFRP leads to a notable increase in the ductility and decreases the ultimate load. The models with zero spacing CFRP strips (Fully) showed a higher considerable effect than the models with strips wrapping. Furthermore, this enhancement was the highest for group six which contains the models with the highest CFRP depth.

1. Introduction

Effect of combined bending and torsion occurs if the beam is loaded with out of plane eccentricity. Where the load is located away from the shear center axis which results in twisting the structural member with an undesirable brittle mode of failure. Although torsion is considered as a secondary effect compared to the flexural effect. Also, the torsion is negligible in most cases during the designing process. It is not the case for reinforced concrete (RC) structural members which are exposed to torsional loading in addition to the shear and flexure. The edge beams located on each floor of multi-story buildings, ring beams, spiral stairs, spandrel beams and flanged beams with T cross-section are exposed to torsion, shear, and flexure [1, 2].

Some experimental studies had been performed with different load setups to study the effect of pure shear. Pure bending combined bending and torsion or combined shear and torsion [3–5]. The effect of span length of cantilever RC beams under pure torsion had been studied using a non-linear finite element analysis. The results showed that when the span/depth ratio is equal to 4 or more, the beams have the same torsional strength but less than the beams that have smaller ratios [6]. The Modified Compression Field Theory (MCFT) was evaluated for reinforced and prestressed concrete beams subjected to combined bending and torsion. It was concluded that the MCFT could accurately determine the full behavior of such beams compared to the experimental results [7].

Existing structures may need torsional strengthening or rehabilitation due to several reasons. Some of these reasons are the increase in service load, inadequate design, change on the structure utilization, an improvement in the code regulations and seismic problems in some cases. Using Fiber Reinforced Polymers (FRP) as a strengthening material is the most recent and promising technology. It is a flexible material that can be made in any desired shape and can be introduced through a structural member either externally or internally. It is preferable in civil engineering applications because it is high corrosion resistance, high strength,

Al-Rousan, R., Abo-Msamh, I. Bending and torsion behaviour of CFRP strengthened RC beams. Magazine of Civil Engineering. 2019. 92(8). Pp. 48–62. DOI: 10.18720/MCE.92.4

Аль-Рушан Р., Або-Мсамх И. Поведение при изгибе и кручении железобетонных балок, усиленных композитным углеволокном // Инженерно-строительный журнал. 2019. № 8(92). С. 48–62. DOI: 10.18720/MCE.92.4



high stiffness, excellent fatigue performance, low weight, easy installation and good resistance to chemical attacks [8–11].

The efficiency of using CFRP for the torsional strengthening of RC beams had been studied either for rectangular or T-cross sections when subjected to pure torsion in most studies. Studying the combined effect of bending and torsion can be hardly found in the literature. Using the CFRP material can significantly increase the torsional strength and ductility. However, this enhancement can be affected by several factors such as concrete class, reinforcement ratio, number of layers, strip spacing, and wrapping scheme. Although the fully wrapping scheme is the best wrapping scheme, the difficulties of its application tend to use the U strip wrapping instead of fully wrapping. It is also recommended to increase the number of layers and decreasing the distance spaced between CFRP strips [12–18].

A new model was developed to predict the full behavior till failure of the strengthened RC beams subjected to torsion. Good agreements with the experimental results were achieved by that model comparing the torsional strength, FRP strain, and failure modes for different wrapping configurations [19]. To reduce the complexity of load setup, effort, time and cost during the experimental testing, ANSYS software had been used by many researchers. It was recommended about this software to be used since their results achieved good agreement with experimental results [20–24]. Therefore, essential issues to produce effective, economical, and successful CFRP strengthening were discussed. Also, the impact of CFRP external strengthening on the behavior of reinforced concrete beams subjected to bending and torsion received miniature consideration. The scientific problem considered in the study is indeed one of the problems in the modern theory of reinforced concrete. Despite a significant number of studies on the problem of bending with torsion, to date. There are no sufficiently reliable solutions to this problem that most fully reflect the physical nature of the problem. As a result, the torsional behavior of simply supported RC beams subjected to combined bending and torsion is studied using the nonlinear finite element analysis (NLFEA). For this purpose, validation against the previous experimental study reported by Gesund et al. [25] is firstly simulated. After that, a parametric study is extended for strengthened RC beams using different configurations of CFRP in terms of clear span to depth ratio, CFRP length, CFRP depth, and CFRP strips c-c spacing.

2. Methods

The NLFEA is a numerical method used to simplify the analysis of a variety of engineering problems. Also, to obtain their approximate solutions at a lesser cost, time, and effort compared to experimental testing. ANSYS is a general-purpose software used in this study. Twenty-six full-scale models strengthened using CFRP are developed to carry out different investigated parameters.

The experimental work performed by Gesund et al. [25] was used to validate the finite element model in this study. A total of twelve simply supported RC beams tested until failure under combined bending and torsion (Figure 1). The cross-section of the beam is 200×200 mm with a 1600 mm clear span length. All beams were reinforced using three bars of tension reinforcement and two bars of compression reinforcement with a 13 mm nominal diameter. Besides, a 10 mm nominal diameter for closed stirrups was applied at 50 mm spacing c-c (Figure 1). The beams were loaded by two-point loads at the end of two-moment arms providing out of plane eccentricity. Hence the beams were subjected to the combined effect of bending and torsion (Figure 1).

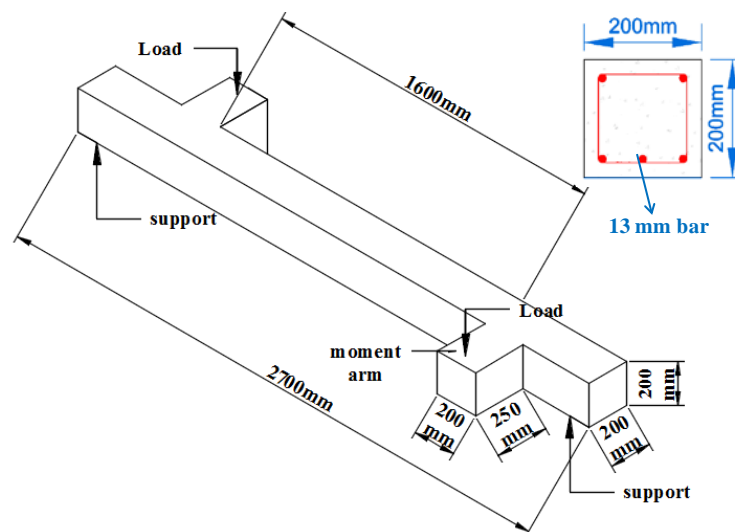


Figure 1. View of the model under load [25].

2.1. Experimental Work Review

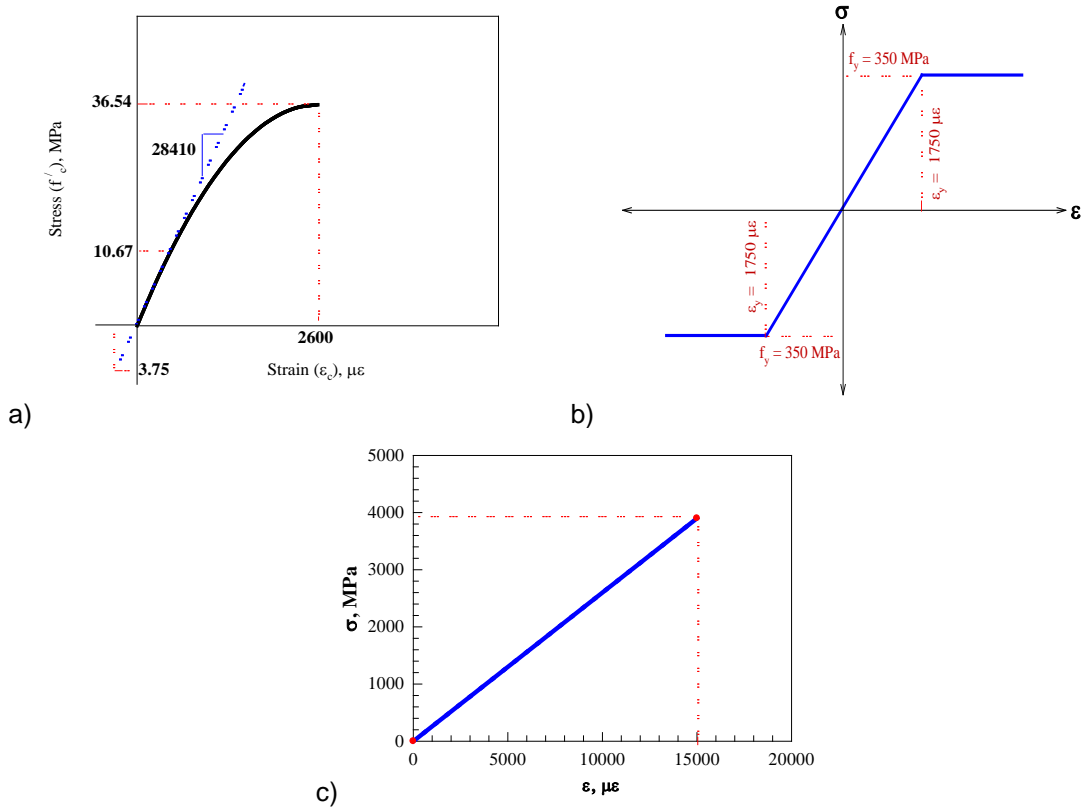


Figure 2. Stress-Strain Curve for (a) Concrete, (b) Steel, and (c) CFRP composite.

2.2. Description of Non-linear Finite Element Analysis (NLFEA)

SOLID 65 is used to model the concrete which is suitable for tension cracking, crushing in compression and plastic deformations. It is a three-dimensional element defined by eight nodes. Each node has three degrees of freedom with a presence of translations in the three nodal directions; x, y, and z for each node. Steel reinforcement is modeled using link 180, which is a uniaxial tension-compression element. It includes two nodes, and each node has three degrees of freedom. This element can predict large deflection, large strain, rotation, creep, and plasticity. SOLID 45 is used to model the loading and supporting steel plates. This element is suitable to model the dimensional solid structures defined by eight nodes. There is a presence of translations in the three nodal directions; x, y, and z for each node. This element can predict large deflection, large strain, stress stiffening, creep, and plasticity. For CFRP, the SHELL 181 element type, having four nodes is used in modeling. It is chosen because it is appropriate to analyze thin layered applications. Three translations and three rotations are considered to include the six degrees of freedom at each node.

Concrete is a brittle material having high compressive strength compared to tensile strength. The cylindrical compressive strength of concrete is 36.54 MPa. The elastic modulus of elasticity (E_c) and modulus of rupture (f_r) of concrete are 28410 MPa and 3.75 MPa, respectively, as shown in Figure 2(a). Concrete poisson's ratio is assumed 0.17 for all models. Shear transfer coefficient for open and closed cracks, β_t and β_c respectively, are important inputs needed for concrete, which indicate the condition of crack surface. In this study, a value of 0.2 and 0.9 is set for the β_t and β_c , respectively. Steel reinforcement is modeled as a bilinear isotropic material with 200 GPa for the elastic modulus of elasticity and 0.3 of poisson's ratio. Its behavior is assumed to be elastic-perfectly plastic, and the same assumption is set for tension and compression reinforcement with yielding stress of 350 MPa, as shown in Figure 2(b). Steel plates are added to the finite element model to avoid stress concentrations at the support and loading locations. These plates are steel type and defined as linear elastic isotropic material with 200 GPa for the elastic modulus of elasticity and 0.3 of poisson's ratio. Sika Wrap Hex 300C 0/90 is the CFRP type used in this study. It is a bi-directional material property with 0.166 mm thickness and having fibers in longitudinal and transverse directions. The linear elastic tensile stress-strain curve for CFRP composites is shown in Figure 2(c) and the detailed mechanical properties and poisson's ratio in all directions, are shown in Table 1.

Table 1. CFRP composites properties.

Modulus of elasticity (GPa)	Poisson's ratio	Shear modulus of elasticity (GPa)	Ultimate tensile strength (MPa)	Ultimate strain
E_x	V_{xy}	G_{xy}		
260	0.22	106.6		
E_y	V_{yz}	G_{yz}	3900	0.015
260	0.22	106.6		
E_z	V_{zx}	G_{zx}		
4.5	0.30	1.73		

The concrete beam and steel plates were modeled as solid elements while steel reinforcement was modeled as link elements. In the case of strengthened RC beams, the CFRP sheets were modeled as shell element with a mesh size of 25 mm. To ensure the perfect bond between concrete and reinforcement, the link element of steel is connected between each adjacent Solid 65 elements, hence the same nodes are shared between the two materials. The same approach is used for the CFRP sheets to provide the perfect bonding as well as for the Steel plates. The geometry of the control and strengthened model, along with the reinforcement specimens are shown in Figure 3(a), Figure 3(b) and Figure 3(c), respectively. The meshing of the CFRP sheet for both fully U wraps and strips wrapping is also shown in Figure 3(d) and Figure 3(e), respectively.

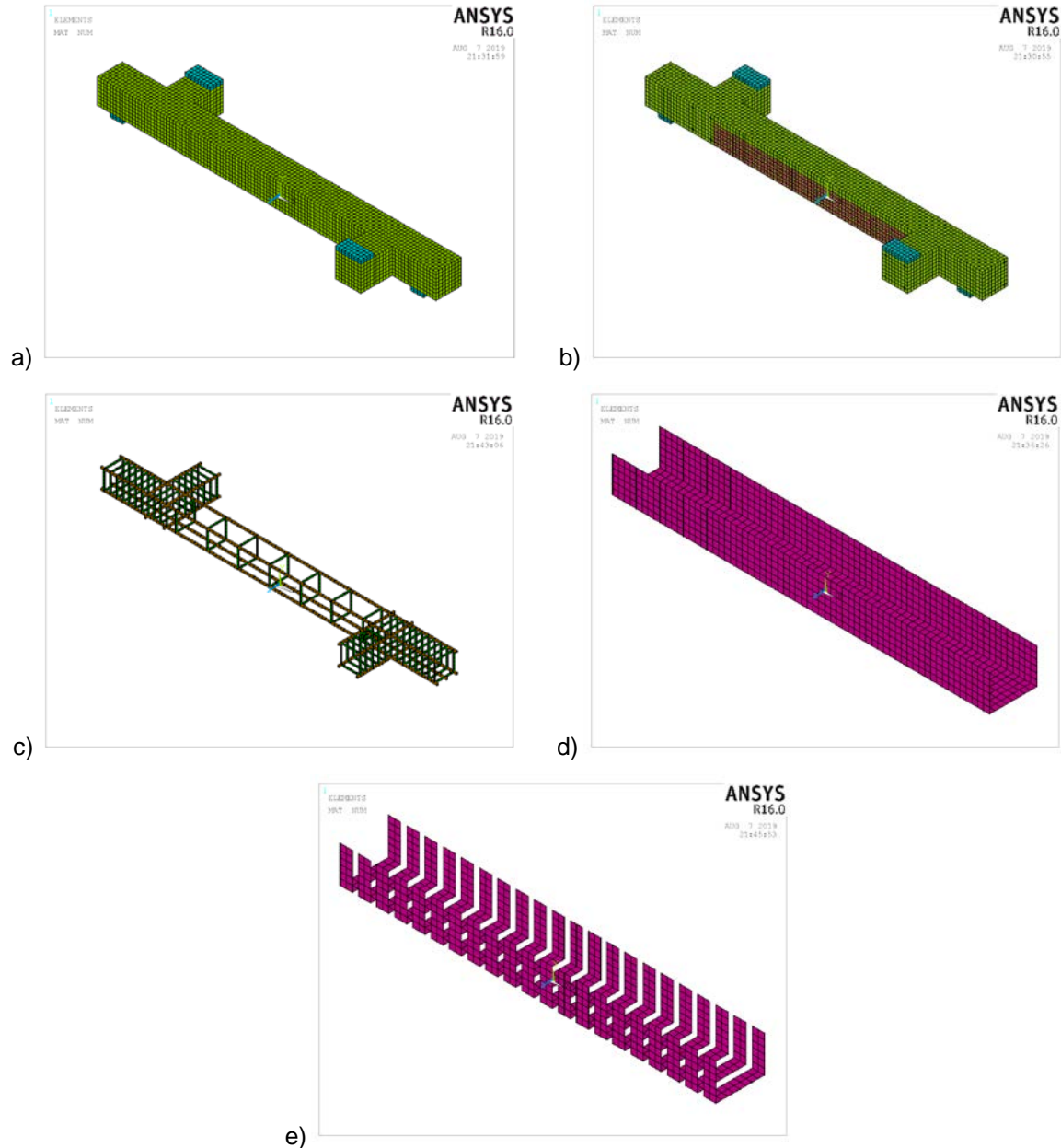


Figure 3. Geometry and meshing.

The loads are applied on the two steel plates at the end of the moment arms as line loads distributed over nine nodes. The purpose of these moment arms is to provide the twisting of the main beam. To constrain the model, displacement boundary conditions are required. At the left end of the beam the U_x , U_y , and U_z displacements are set to zero to ensure hinge support. While roller support is added at the right end of the beam by setting zero value to the U_y displacement. Figure 4 shows the loads and boundary conditions of the model. The total applied load is divided into multiple load steps or load increments. Newton–Raphson equilibrium iterations give convergence at the end of each load increment within tolerance limit equal to (0.001) and a load increment of 0.22 kN. When large numbers of cracks appear throughout the concrete, the loads are applied gradually with smaller load increments.

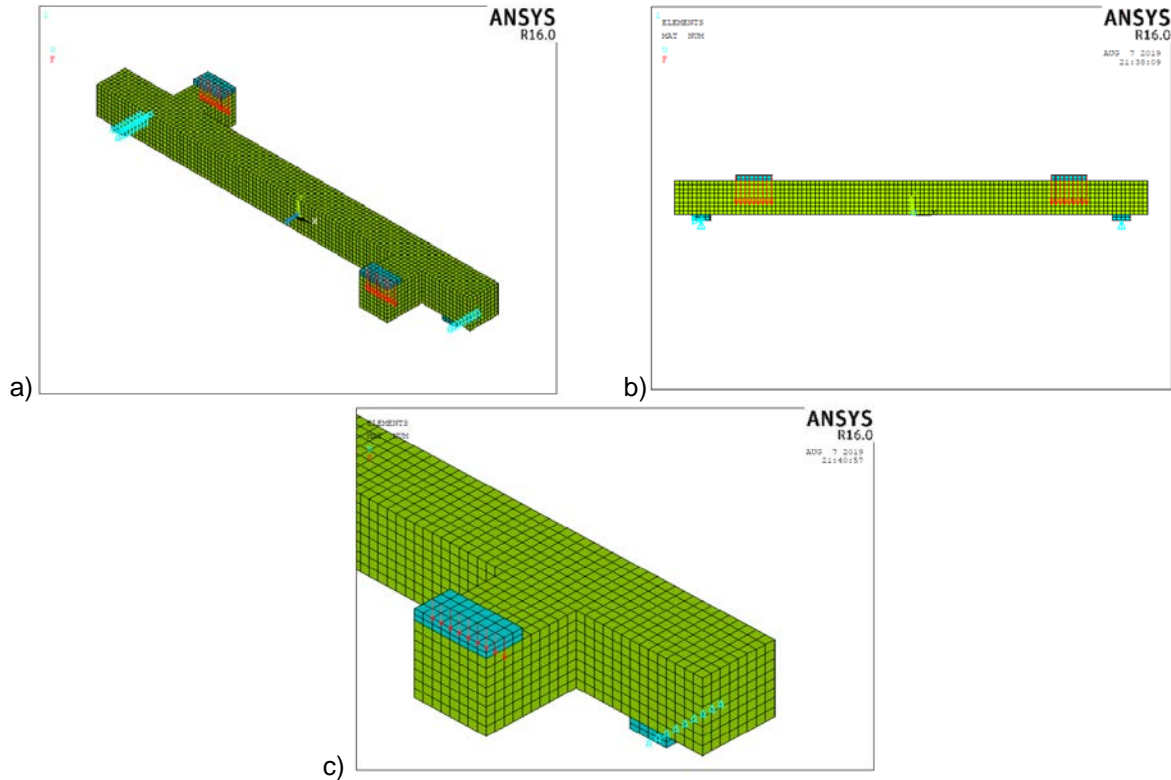


Figure 4. Loads and boundary conditions: (a) 3-D view, (b) Front view, and (c) Zoomed view.

2.3. Investigated Parameters

Twenty-six full-scale models strengthened using CFRP are developed to carry out different investigated parameters. A parametric study conducted in this research consists of six groups. The first group contains three models to study the effect of a clear span to depth ratio. 8, 6, and 4 are the clear span to depth ratios used. These models are strengthened using fully CFRP U wrap along the clear span length, and BC3 with ratios 8, 6, and 4 respectively. The other groups are modeled with the ratio equal to 8. Group 2 includes three models with different lengths of 1600 mm, 1100 mm and 800 mm. The rest four groups study the effect of two parameters; CFRP depth, and CFRP strip spacing. Four different CFRP depths of 50 mm, 100 mm, 150 mm, and 200 mm are studied for groups 3, 4, 5, and 6, respectively. Each depth group includes five models with different c-c spacing between 50 mm U strips, which are 225 mm, 175 mm, 125 mm, 75 mm and zero spacing. Figure 5 and Figure 6 show the schematic representation of CFRP strengthening configurations for the two cases of fully U-wrap and 50 mm U strip wrapping, respectively. A full description of the finite element modeling groups is shown in Table 2.

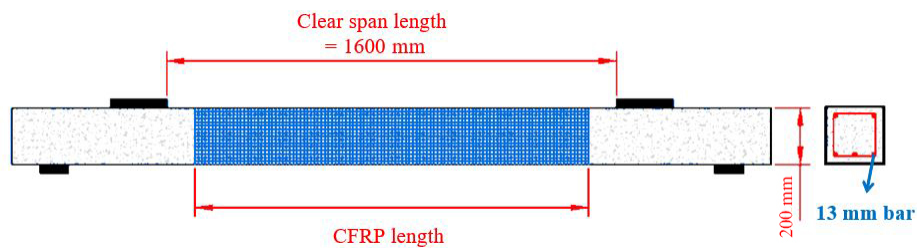


Figure 5. Schematic representation of fully CFRP U-WRAP.

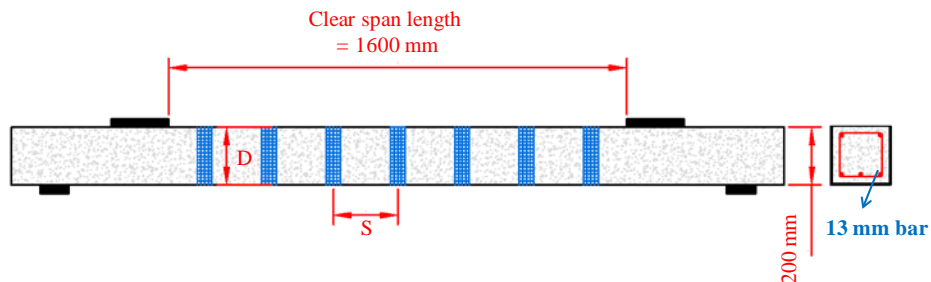


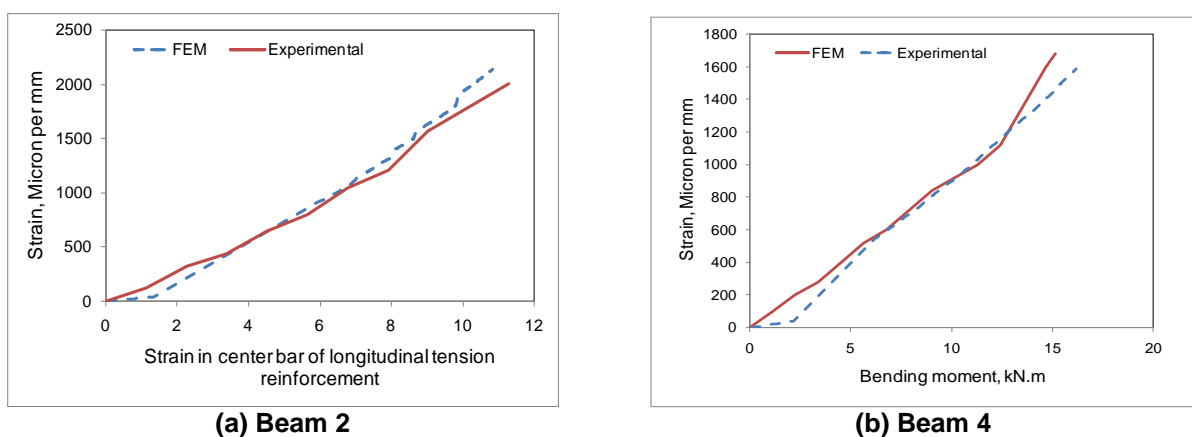
Figure 6. Schematic representation of 50 mm U strip wrapping where S is the c-c spacing between CFRP strips, and D is the CFRP depth.

Table 2. Investigated parameters.

Group number	Parameter	Beam number	Test section to depth ratio			CFRP strengthening configuration	CFRP length (mm)	CFRP Depth (mm)
			Clear span length (mm)	Depth (mm)	Ratio			
1	Clear span length to depth ratio	B1	1600	200	8	Fully FRP U wrap	1600	200
		B2	1200	200	6	Fully FRP U wrap	1200	
		B3	800	200	4	Fully FRP U wrap	800	
2	CFRP length	B4	1600	200	8	Fully FRP U wrap	1600	200
		B5	1600	200	8	Fully FRP U wrap	1100	
		B6	1600	200	8	Fully FRP U wrap	800	
3	CFRP depth	B7	1600	200	8	50 mm U strip wrapping at 225 mm c/c	1600	50
		B8	1600	200	8	50 mm U strip wrapping at 175 mm c/c		
		B9	1600	200	8	50 mm U strip wrapping at 125 mm c/c		
		B10	1600	200	8	50 mm U strip wrapping at 75 mm c/c		
		B11	1600	200	8	Fully FRP U wrap		
4	CFRP depth	B12	1600	200	8	50 mm U strip wrapping at 225 mm c/c	1600	100
		B13	1600	200	8	50 mm U strip wrapping at 175 mm c/c		
		B14	1600	200	8	50 mm U strip wrapping at 125 mm c/c		
		B15	1600	200	8	50 mm U strip wrapping at 75 mm c/c		
		B16	1600	200	8	Fully FRP U wrap		
5		B17	1600	200	8	50 mm U strip wrapping at 225 mm c/c	1600	150
		B18	1600	200	8	50 mm U strip wrapping at 175 mm c/c		
		B19	1600	200	8	50 mm U strip wrapping at 125 mm c/c		
		B20	1600	200	8	50 mm U strip wrapping at 75 mm c/c		
		B21	1600	200	8	Fully FRP U wrap		
6		B22	1600	200	8	50 mm U strip wrapping at 225 mm c/c	1600	200
		B23	1600	200	8	50 mm U strip wrapping at 175 mm c/c		
		B24	1600	200	8	50 mm U strip wrapping at 125 mm c/c		
		B25	1600	200	8	50 mm U strip wrapping at 75 mm c/c		
		B26	1600	200	8	Fully FRP U wrap		

2.4. Validation Process

The model validation is conducted in this study for the experimental study performed by Gesund et al. [25]. Bending and twisting moments at failure as well as the strain in the center bar of longitudinal reinforcement are compared with the NLFEA results. Figure 7 and Table 3 show good agreements between the finite element method and experimental results.

**Figure 7. Validation of the NLFEA results.****Table 3. Validation summary.**

Beam number	Torsion to Bending moment ratio	Bending moment at failure (kN.m)		The torsional moment at failure (kN.m)		Absolute Error %
		Experiment	FEM	Experiment	FEM	
2	1	11.52	10.9	11.52	10.9	5.3
4	0.5	15.14	16.2	7.6	8.1	-6.9

3. Results and Discussion

3.1. Load-Deflection and Torsion-Twist Behavior

Both the torsion-twist and load-deflection curves consist of three regions; the first region represents the stiffness for the un-cracked beam. The second region for the cracked beam. While, the third region relates to the damaged cross-section with large cracks, yielding of steel and CFRP failure. Table 4 illustrates the obtained results for all simulated models. The slope of each region of the load-deflection curves gives the flexural stiffness of the corresponding beam. All strengthened beams represent higher stiffness compared to the control beam in the three regions. Table 4 also shows the calculated stiffness in each region for all simulated models.

Table 4. Results for all simulated models.

Group number	Model number	Ultimate load (kN)	Ultimate deflection(mm)	Ultimate torsion (kN.m)	Ultimate angle of twist (rad)	Stiffness (kN/mm)		
						Region 1	Region 2	Region 3
Control beams	BC1	22.28	3.05	06.68	0.0120	21.50	1.46	5.02
	BC2	24.26	2.36	7.27	0.0117	31.60	1.81	8.68
	BC3	26.77	1.73	8.03	0.0110	34.70	3.63	13.3
1	B1	44.10	4.88	13.22	0.0320	23.50	2.82	8.54
	B2	45.30	3.58	13.80	0.0237	34.60	3.18	11.8
	B3	49.20	2.69	14.75	0.0220	54.00	5.54	16.7
2	B4orB1	44.10	4.88	13.22	0.0320	23.50	2.82	8.54
	B5	36.20	4.14	10.87	0.0260	23.30	2.54	8.00
	B6	32.80	4.00	9.86	0.0230	23.10	2.40	7.82
3	B7	24.82	3.39	07.44	0.0142	21.60	1.48	5.58
	B8	25.63	3.44	07.68	0.0143	21.70	1.54	5.73
	B9	26.24	3.52	07.87	0.0152	22.30	1.69	5.78
	B10	27.36	3.60	08.21	0.0155	22.50	1.79	6.00
	B11	36.21	3.94	10.86	0.0248	23.10	2.38	7.91
4	B12	25.86	3.57	07.75	0.0152	21.70	1.52	5.74
	B13	26.45	3.61	07.93	0.0155	22.20	1.57	5.78
	B14	27.38	3.68	08.21	0.0160	22.60	1.73	5.83
	B15	29.03	3.84	08.71	0.0174	22.70	1.91	6.04
	B16	38.84	4.25	11.65	0.0252	23.20	2.49	8.00
5	B17	28.25	3.97	08.47	0.0183	22.20	1.57	5.87
	B18	29.51	4.08	08.85	0.0192	22.40	1.60	5.91
	B19	30.10	4.13	09.02	0.0193	22.70	1.78	6.00
	B20	31.52	4.21	09.45	0.0196	22.90	1.96	6.07
	B21	42.60	4.61	12.81	0.0266	23.30	2.76	8.46
6	B22	31.57	4.43	09.34	0.0225	22.40	1.59	5.91
	B23	32.43	4.45	09.65	0.0231	22.60	1.62	6.12
	B24	34.60	4.56	10.01	0.0237	22.90	1.76	6.15
	B25	36.20	4.81	10.86	0.0242	23.10	1.97	6.18
	B26orB1	44.1	4.88	13.22	0.0320	23.50	2.82	8.54

3.2. Ductility and Strength ratios

The ductility indicates how much the strengthened RC beams can sustain deformations without failure. The ductility ratio is defined as the ratio of the ultimate deflection of the strengthened beam to the ultimate deflection of the control beam. Similarly, strength ratio also predicts the increase of load that the model can sustain. Table 5 shows the ductility and strength ratios for all simulated models.

3.3. CFRP strain

Figure 8 shows the typical distribution of CFRP strain through its depth for the first group. It is noticed that all simulated beams had CFRP strain below the maximum value of 0.015 as mentioned in Table 2.

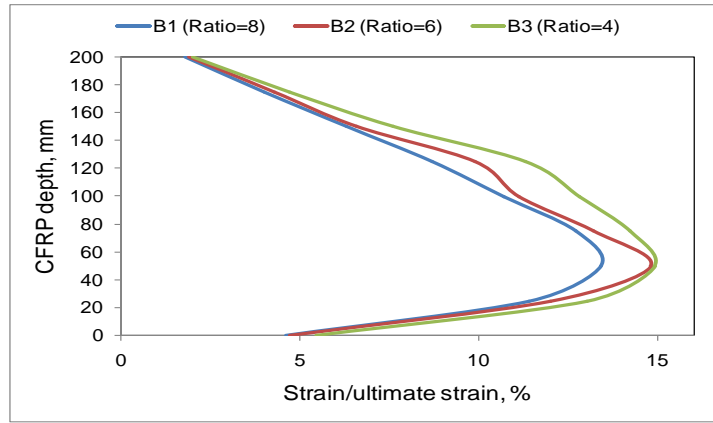


Figure 8. Typical CFRP strain for Group 1 versus ultimate strain.

Table 5. Enhancement percentage to control beam for all investigated parameters.

Group number	Model number	Torsional strength ratio	Flexural ductility ratio	Torsional ductility ratio	Percent enhancement in Stiffness			The percentage of CFRP strain to the ultimate strain
					Region 1	Region 2	Region 3	
Control beams	BC1	---	---	---	---	---	---	---
1	B1	83	55	100	109	193	170	13.4
	B2	98	60	167	115	175	135	14.8
	B3	62	36	117	155	152	125	15.0
2	B4 or B1	47	31	92	109	193	170	15.0
	B5	11	11	18	108	174	159	8.0
	B6	15	13	19	107	164	155	6.2
3	B7	18	15	27	100	101	111	1.5
	B8	23	18	29	101	105	114	2.0
	B9	71	29	107	104	115	115	2.0
	B10	16	17	27	105	122	119	2.7
	B11	19	18	29	107	163	158	8.0
4	B12	23	21	33	101	104	114	3.4
	B13	30	26	45	103	107	115	3.5
	B14	74	39	110	105	118	116	3.7
	B15	27	30	53	106	130	120	5.0
	B16	32	34	60	108	170	159	10.4
5	B17	35	35	61	103	108	117	4.9
	B18	41	38	63	104	110	118	5.1
	B19	91	51	122	106	122	119	6.0
	B20	42	45	88	107	134	121	6.0
	B21	46	46	93	108	189	169	13.7
6	B22	55	50	98	104	109	118	5.0
	B23	62	58	102	105	111	122	6.2
	B24	98	60	167	107	123	123	7.0
	B25	98	75	160	107	135	123	7.0
	B26 or B1	87	56	103	109	193	170	15.0

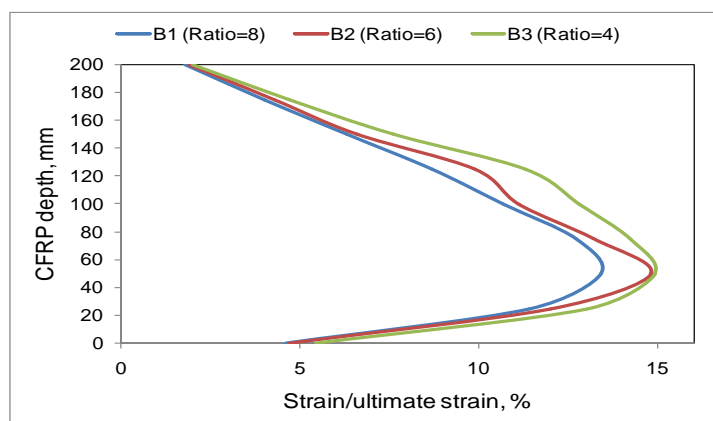


Figure 8. Typical CFRP strain for Group 1 versus ultimate strain.

3.4. Failure Mode

Figure 9 shows the crack pattern for the typically simulated beams. The first crack at an integration point is shown with a red circle outline, the second crack with a green outline, and the third crack with a blue outline. The first crack initiated from the support and then propagated toward the top of the beam in a diagonal shape. Due to the lack of CFRP wrapping along the control beam, this propagation spreads at a faster rate with individual cracks along the beam compared to the strengthened beams.

The FRP helps in distribution the stresses on the whole body of the beam. Also, the cracks were smaller and closer to each other, giving higher strength and capacity for those beams. All strengthened beams show almost similar diagonal cracks initiation. This due to the reality of similar loading and boundary conditions and the reinforcement details. However, the fully FRP U-wrap inhibits the propagation of cracks more than FRP strips. The beam strengthened with Fully FRP U wrap could sustain higher loads and deflections. The failure occurred due to the substantial wide diagonal cracks and concrete crushing followed by FRP failure.

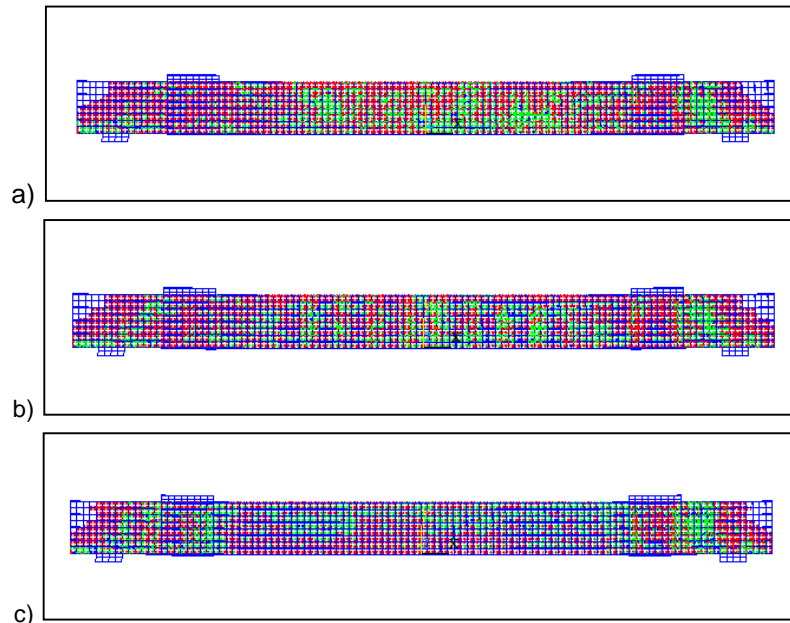


Figure 9. Crack pattern at failure: (a) control beam, (b) strengthened beams using FRP strips, and (c) strengthened beam using fully FRP U-wrap.

3.5. Effect of the clear span to depth ratio

To study the influence of the clear span to depth ratio factor, group 1 consists of three beams. B1, B2, and B3 are modeled with 8, 6 and 4 ratios, respectively. All of them are strengthened using fully CFRP U wrap. The torsional strength of the strengthened beams in this group is improved by 198 %, 187 % and 183 % for B1, B2, and B3, respectively. The flexural ductility is improved by 175 %, 156 % and 155 % over the control beam for B1, B2, and B3, respectively. While the torsional ductility is enhanced by 260 %, 203 % and 200 % for B1, B2, and B3, respectively, as shown in Table 5. Figure 10(a) and Figure 10(b) show the load-deflection and torsion-twist curves for group 1. It is noticed that the increase in the ratio leads to more increase in the flexural and torsional ductility. While the ultimate load that the beam can sustain decreases. Figure 10(c) shows the comparison between the three ratios to the ultimate load, ultimate deflection, and the ultimate angle of twist.

Furthermore, the results show the enhancement in the FRP strain and the stiffness at the three regions of the load-deflection curve. The percentage of CFRP strain value to the ultimate strain is 13.4 %, 14.8 %, and 15 % for B1, B2, and B3, respectively (Table 5). The stiffness at the initial part of the load-deflection curve is enhanced by 109 %, 115 %, and 155 % for B1, B2, and B3, respectively. In the second part the stiffness increases by 193 %, 175 % and 152 % for B1, B2, and B3, respectively. In the third part the stiffness increases by 170 %, 135 % and 125 % for B1, B2, and B3, respectively, as shown in Table 5.

3.6. Effect of CFRP length

To investigate the effect of CFRP length, a parametric study in group 2 is conducted for three different lengths; 1600 mm, 1100 mm and 800 mm. The torsional strength of the beams is enhanced by 198 %, 162 %, and 147 % for B4, B5, and B6, respectively. The flexural ductility is enhanced by 160 %, 136 % and 131 % for B4, B5, and B6, respectively, while the torsional ductility is enhanced by 267 %, 217 % and 192 % for B4, B5, and B6, respectively (Table 5). The ultimate load, ultimate torsion, and the ductility of the RC beam increase as the length of the CFRP increases. Figure 11 also verifies this conclusion.

The load-deflection and torsion-twist curves are shown in Figure 11(a) and Figure 11(b), respectively. The percentage of CFRP strain value to the ultimate strain is 15 %, 8 %, and 6.2 % for B4, B5, and B6, respectively. The stiffness at the initial part is enhanced by 109 %, 108 %, and 107 % for B4, B5, and B6, respectively. In the second part the stiffness increases by 193 %, 174 % and 164 % for B4, B5, and B6, respectively. In the third part the stiffness increases by 170 %, 159 % and 155 % for B4, B5, and B6, respectively (Table 5). These results indicate that increasing the length of CFRP lead to more enhancements in the FRP strain. Also, the stiffness at the three regions of the load-deflection curve.

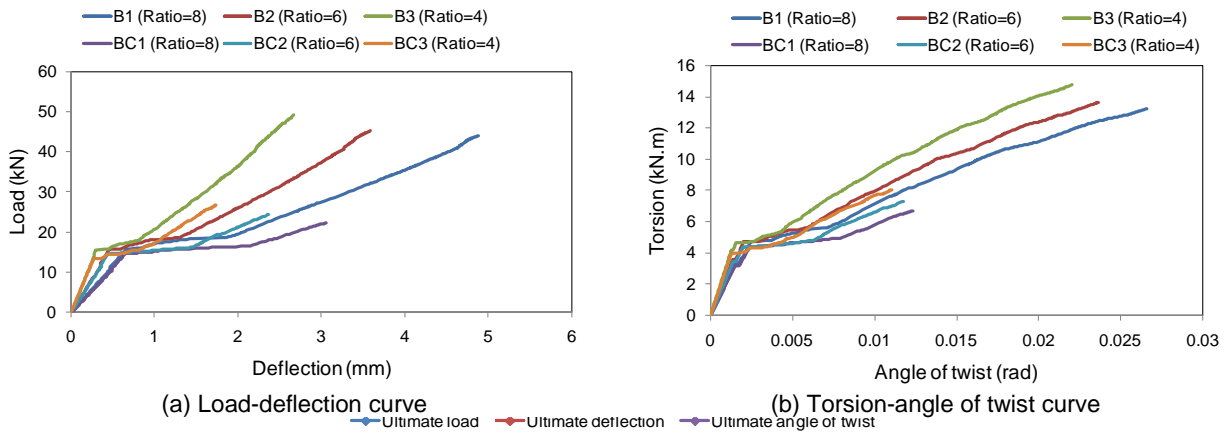


Figure 10. Group 1 results

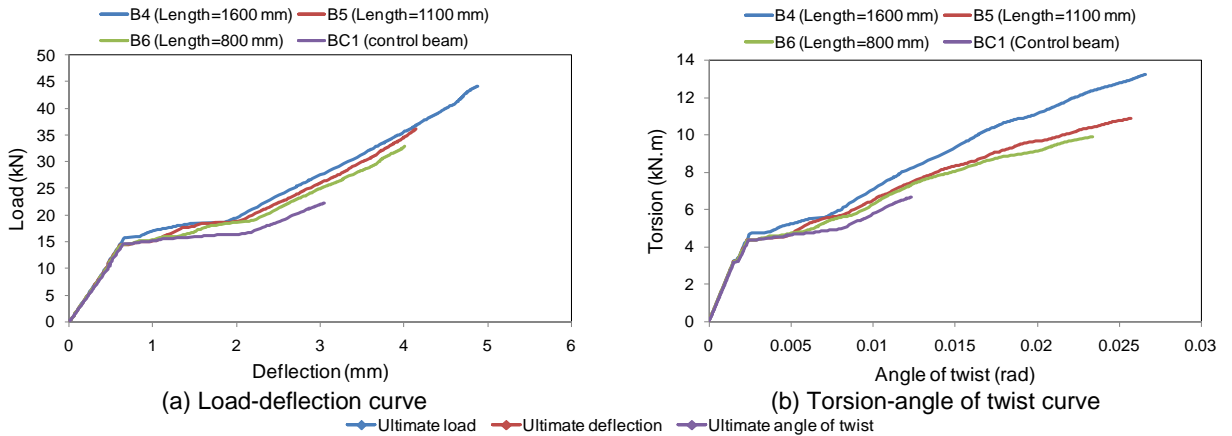


Figure 11. Group 2 results.

3.7. Effect of the CFRP Depth and CFRP Strip Spacing

To study the effect of the CFRP depth parameter, this study conducts four different depth of the beam; 50 mm, 100 mm, 150 mm, and 200 mm for groups 3, 4, 5, and 6, respectively. Each depth group includes five beams with different CFRP configuration of U strip wrapping with the spacing of 75 mm, 125 mm, 175 mm and 225 mm. The fifth beam is considered with fully U-wrap. Group 3 exhibits strength enhancement by 111 %, 115 %, 118 %, 123 % and 171 % for B7, B8, B9, B10, and B11, respectively (Figure 12 and Table 5). The flexural ductility is enhanced by 111 %, 113 %, 115 %, 118 % and 129 % for B7, B8, B9, B10, and B11, respectively. While the torsional ductility is enhanced by 118 %, 119 %, 127 %, 129 % and 207 % for B7, B8, B9, B10, and B11, respectively (Figure 12 and Table 5). The percentage of CFRP strain value to the ultimate strain is 1.5 %, 2 %, 2 %, 2.7 and 8 % for B7, B8, B9, B10, and B11, respectively (Figure 12 and Table 5). The stiffness at the initial region of the load-deflection curve is enhanced by 100.4 %, 101 %, 103.7 %, 104.7 %, and 107.4 % for B7, B8, B9, B10, and B11, respectively (Table 5). In the second region the stiffness increases by 101 %, 105 %, 115 %, 122 % and 163 % for B7, B8, B9, B10, and B11, respectively (Table 5). In the third region the stiffness increases by 111 %, 114 %, 115 %, 119 % and 158 % for B7, B8, B9, B10, and B11, respectively (Figure 12 and Table 5).

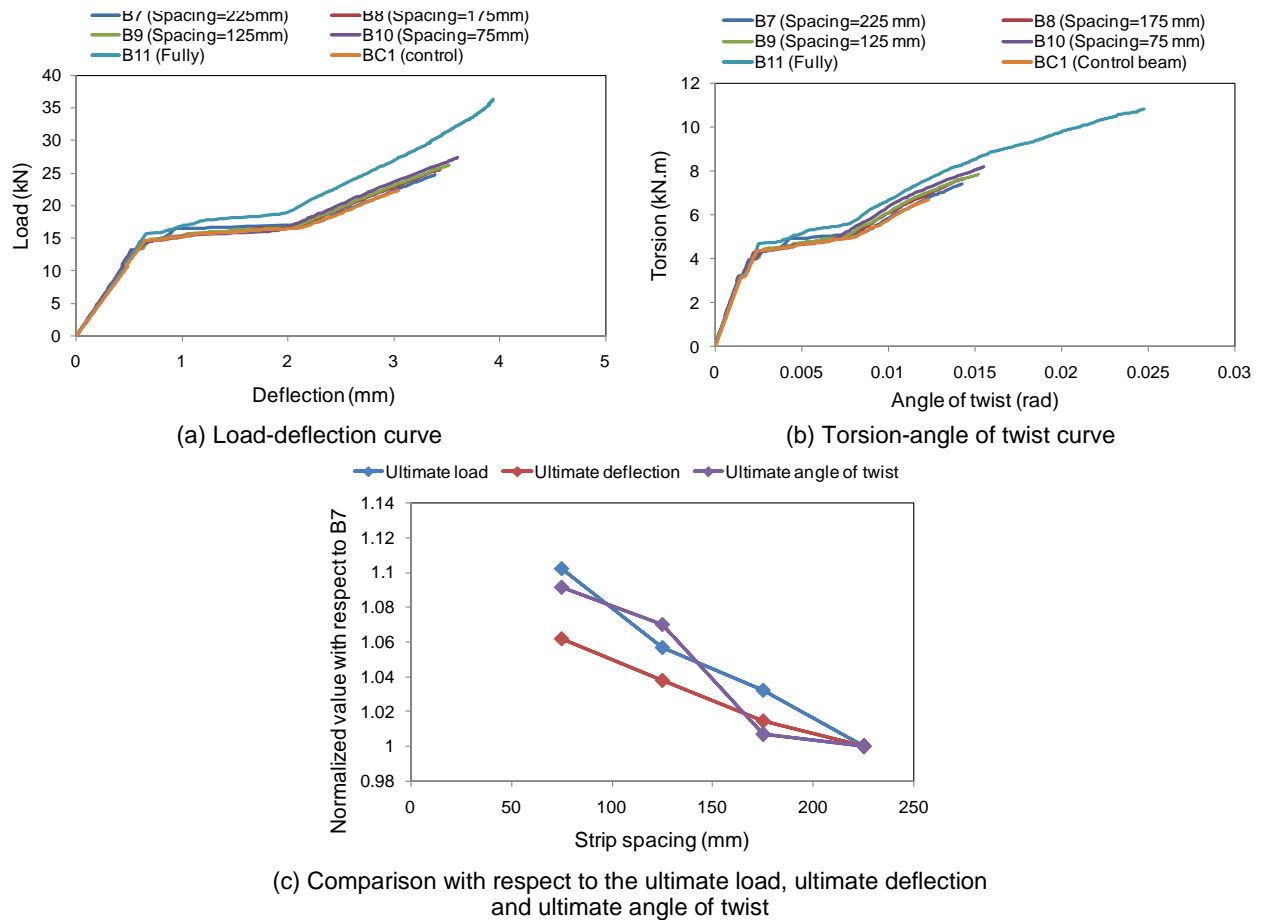


Figure 12. Group 3 results

Group 4 shows strength enhancement by 116 %, 119 %, 123 %, 130 % and 174 % for B12, B13, B14, B15, and B16, respectively (Table 5). The flexural ductility is enhanced by 117 %, 118 %, 121 %, 126 % and 139 % for B12, B13, B14, B15, and B16, respectively. While the torsional ductility is enhanced by 127 %, 129 %, 133 %, 145 % and 210 % for B12, B13, B14, B15, and B16, respectively (Figure 13 and Table 5). The percentage of CFRP strain value with respect to the ultimate strain is 3.4 %, 3.5 %, 3.7 %, 5 % and 10.4 % for B12, B13, B14, B15 and B16, respectively (Figure 13 and Table 5). The stiffness at the initial region of load-deflection curve is enhanced by 101 %, 103 %, 105 %, 106 %, and 108 % for B12, B13, B14, B15, and B16 respectively (Table 5). In the second region the stiffness increases by 104 %, 107 %, 118 %, 130 % and 170 % for B12, B13, B14, B15, and B16, respectively. In the third region the stiffness increases by 114 %, 115 %, 116 %, 120 % and 159 % for B12, B13, B14, B15, and B16, respectively (Figure 13 and Table 5).

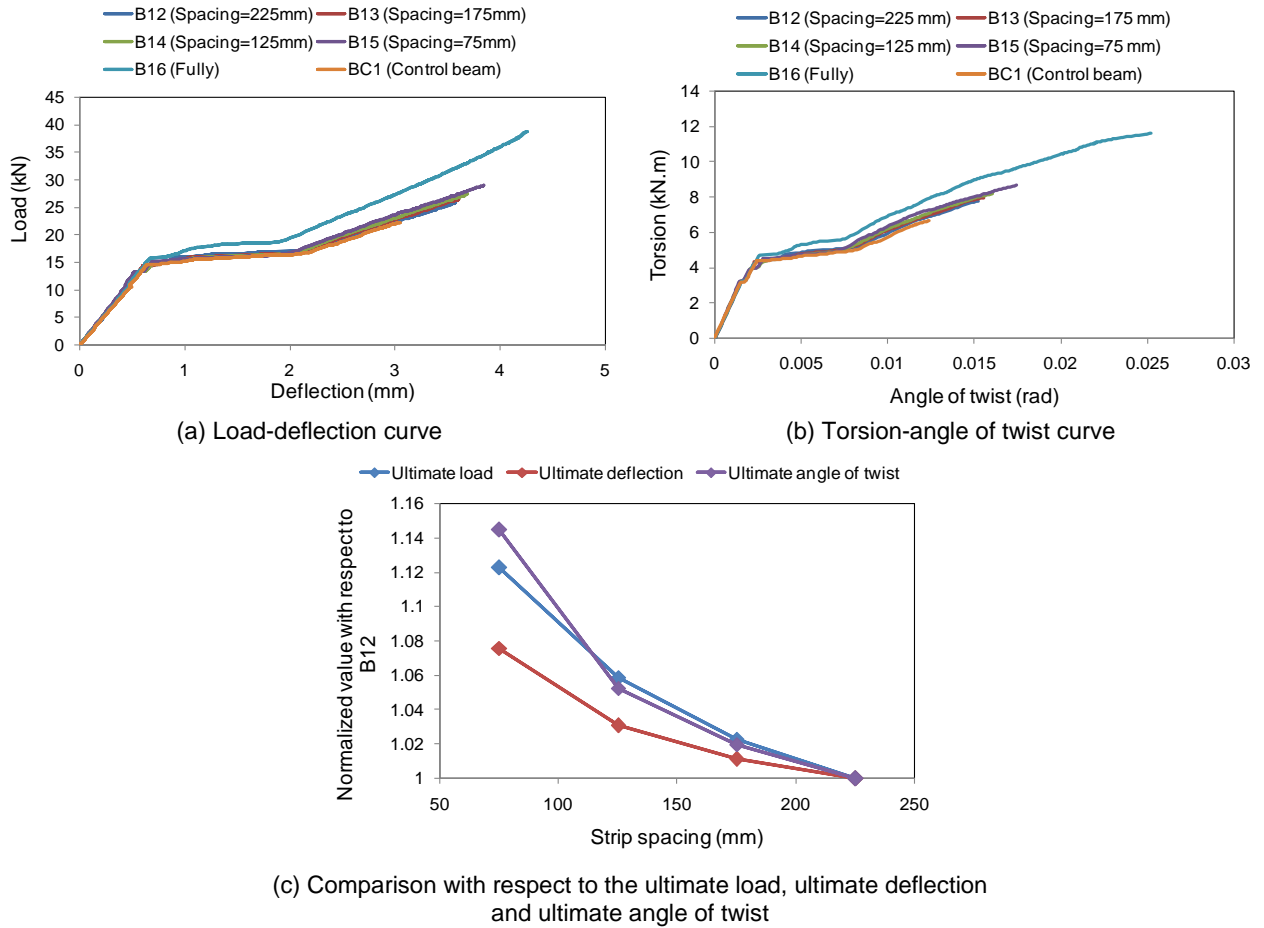
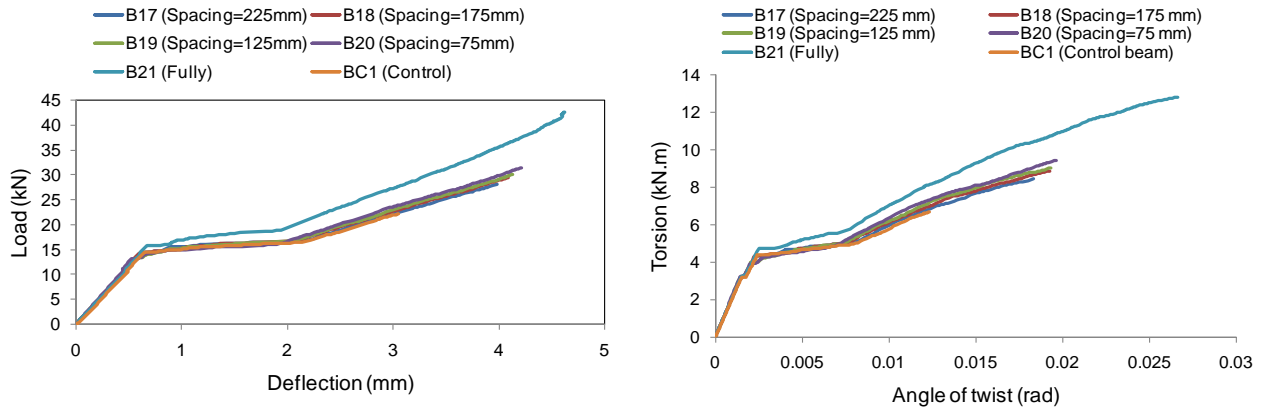


Figure 13. Group 4 results.

Group 5 exhibits torsional strength enhancement by 127 %, 132 %, 135 %, 141 % and 191 % for B17, B18, B19, B20, and B21, respectively (Table 5). The flexural ductility is enhanced by 127 %, 132 %, 135 %, 141 % and 191 % for B17, B18, B19, B20, and B21, respectively. While the torsional ductility is enhanced by 188 %, 193 %, 198 %, 202 % and 267 % for B17, B18, B19, B20, and B21, respectively (Figure 14 and Table 5). The percentage of CFRP strain value to the ultimate strain is 4.9 %, 5.1 %, 6 %, 6 % and 13.7 % for B17, B18, B19, B20, and B21, respectively (Figure 14 and Table 5). The stiffness at the initial region of the load-deflection curve is enhanced by 103 %, 104 %, 106 %, 107 %, and 108.4 % for B17, B18, B19, B20, and B21, respectively. In the second region the stiffness increases by 108 %, 110 %, 122 %, 134 % and 189 % for B17, B18, B19, B20 and B21, respectively. In the third region, the stiffness increases by 117 %, 118 %, 119 %, 121 % and 169 % for B17, B18, B19, B20, and B21, respectively (Figure 14).

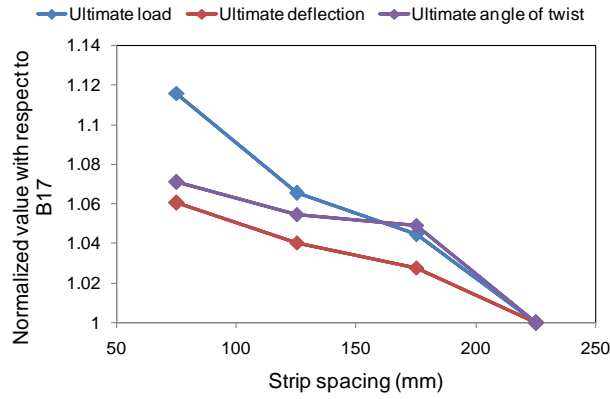
Group 6 exhibits torsional strength enhancement by 142 %, 146 %, 155 %, 162 % and 218 % for B22, B23, B24, B25 and B26, respectively (Figure 15 and Table 5). The flexural ductility is enhanced by 145 %, 146 %, 150 %, 158 % and 160 % for B22, B23, B24, B25 and B26, respectively (Figure 15). The percentage of CFRP strain value to the ultimate strain is 5 %, 6.2 %, 7 %, 7 % and 15 % for B22, B23, B24, B25, and B26, respectively (Figure 15 and Table 5). The stiffness at the initial region of the load-deflection curve is enhanced by 104 %, 105 %, 107 %, 107.4 %, and 109 % for B22, B23, B24, B25, and B26, respectively (Figure 15 and Table 5). At the second region the stiffness increases by 109 %, 111 %, 123 %, 135 % and 193 % for B22, B23, B24, B25 and B26, respectively (Figure 15 and Table 5). At the third region the stiffness increases by 118 %, 122 %, 122.5 %, 123 % and 170 % for B22, B23, B24, B25 and B26, respectively (Figure 15 and Table 5). Figure 10 to Figure 15 shows the load-deflection curves, torsion-twist curves, and the comparison between the models of each group that are 3, 4, 5, and 6. It is clear that decreasing strip spacing. The beam can sustain higher load, deflection, torsion and hence higher angle of twist.

For the same CFRP strip spacing with different depth, the enhancement increases as the CFRP depth increases, as shown in Figure 16 and Table 5. The model wrapped using fully FRP U-wrap records the highest values with the enhancement range of (171–198 %) for ultimate torsional strength and (207–267 %) for ultimate torsional ductility. Furthermore, the results show better enhancement in the FRP strain and the stiffness at the three regions of the load-deflection curve as increasing the depth of CFRP and decreasing the strip spacing.



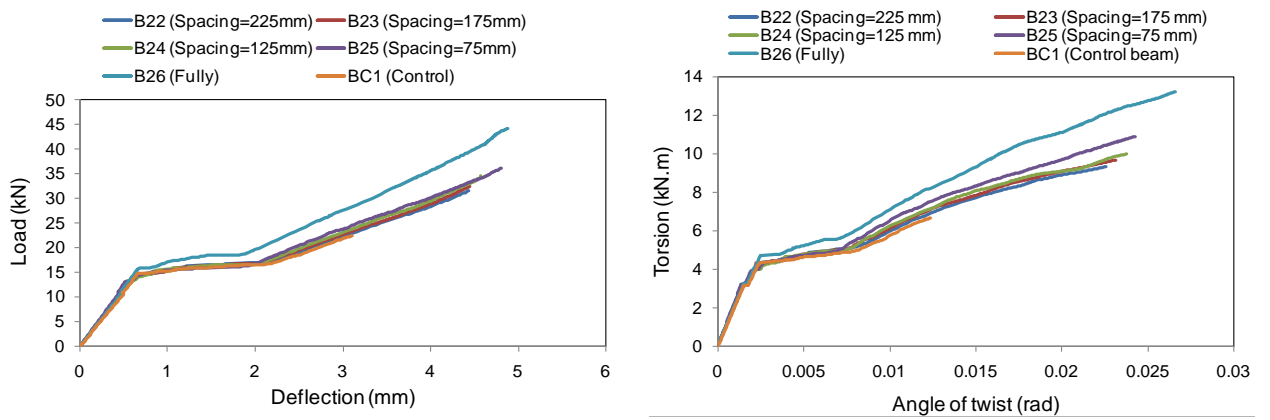
(a) Load-deflection curve

(b) Torsion-angle of twist curve



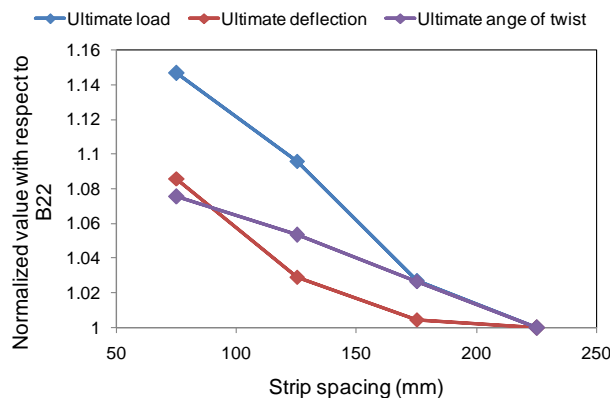
(c) Comparison with respect to the ultimate load, ultimate deflection and ultimate angle of twist

Figure 14. Group 5 results.



(a) Load-deflection curve

(b) Torsion-angle of twist curve



(c) Comparison with respect to the ultimate load, ultimate deflection and ultimate angle of twist

Figure 15. Group 6 results.

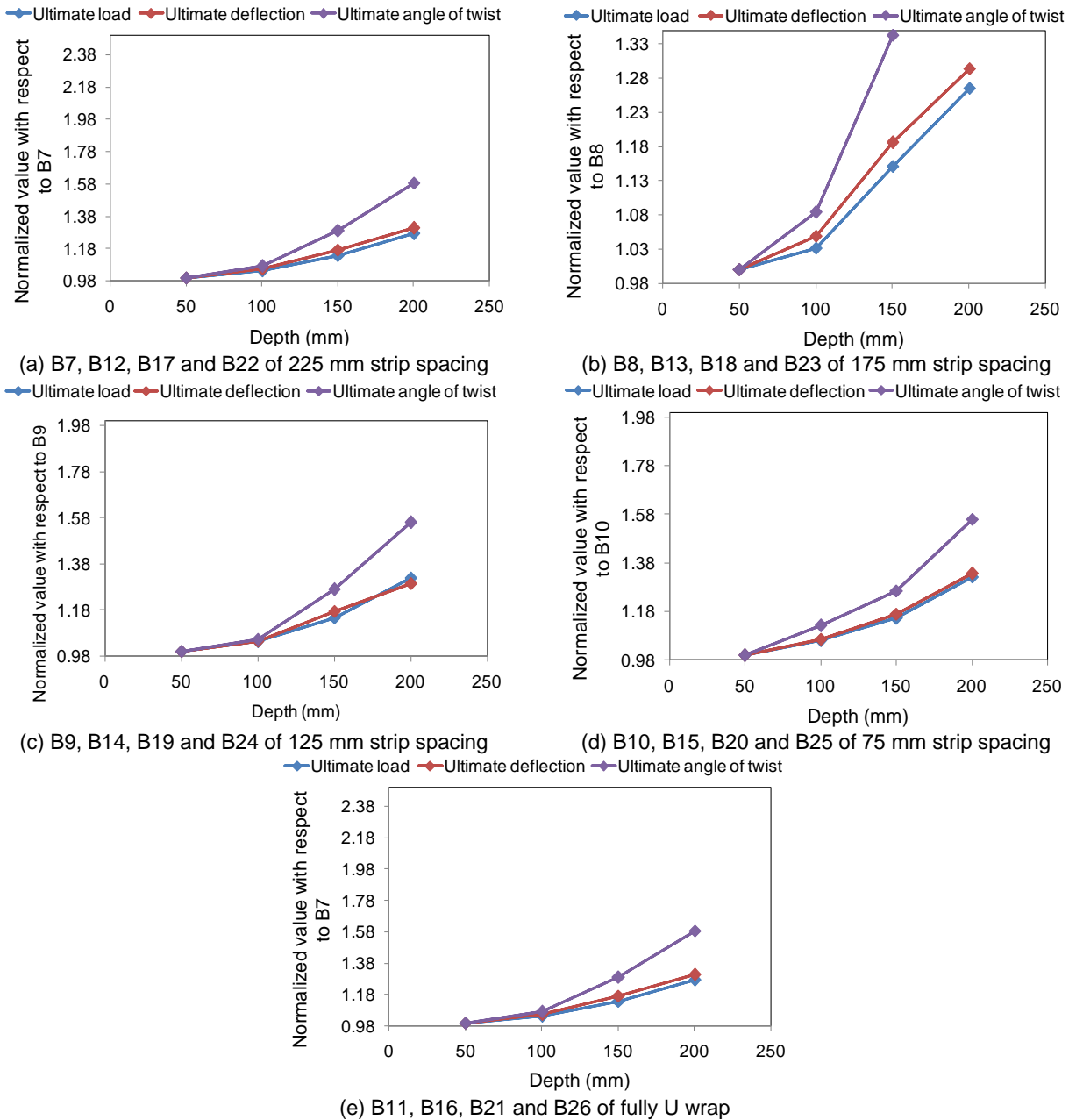


Figure 16. Comparison between strip spacing to the ultimate load, ultimate deflection and ultimate angle of twist,

3.8. Comparison of NLFEA with other results

Comparison of NLFEA with Vishnu et al. [1], the bending moment and torque for all specimens at first crack are closed to NLFEA. Due to FRP torsional resistance of beam is increased in all types of wrapping configuration. Maximum bending moment and torsional moment are resisted by Full Transverse FRP wrapping. Also, all specimens wrapped with GFRP show better torsional resistance compared to the control specimen. Results show an increase in structural behavior of the strengthened beam is almost the same performance as the NLFEA. Besides, Vishnu et al. [1] reached the same conclusion as NLFEA that the fully U wrap strengthening technique of RC beam with FRP is more efficient in resisting torsional moment compared to the vertical strip.

4. Conclusions

1. The three-dimensional finite element model provided by this study was suitable to predict the behavior of strengthened RC beams subjected to combined bending and torsion. The mode of failure, ultimate strength, ductility, stiffness, and FRP strain can be accurately predicted.

2. As increasing the length of CFRP, the beam can sustain higher load, deflection, moment and hence higher orientation.

3. The efficiency of using CFRP strips increases as decreasing the center to center spacing between them. For the same spacing, this efficiency increases as increasing the depth of CFRP.

4. Using fully FRP U wrap is more effective than CFRP strips with higher torsional strength and ductility.
5. All strengthened beams represent higher stiffness compared to the control beam in the three regions of the load-deflection curves.
6. The control beam shows a faster rate of diagonal crack propagation than the strengthened beams. This is due to the lack of CFRP wrapping along the beam. The failure occurred after substantial wide diagonal cracks and concrete crushing followed by CFRP rupture.

References

1. Kongjian, Shen, Shui Wan, Y.L. Mo, Zhengwen, Jiang. Theoretical analysis on full torsional behavior of RC beams strengthened with FRP materials. *Composite Structures*. 2018. 183(1). Pp. 347–357. DOI: 10.1016/j.compstruct.2017.03.084.
2. Jariwala, V.H., Patel, P, Purohit, S.P. Strengthening of RC beams subjected to combined torsion and bending with GFRP composites. *Procedia Engineering*. 2013. 51(1). Pp. 282–289. DOI: 10.1016/j.proeng.2013.01.038
3. Amulu, C.P., Zeagu, C.A. Experimental and analytical comparison of torsion, bending moment and shear forces in reinforced concrete beams using BS 8110, euro code 2 and ACI 318 provisions. *Nigerian Journal of Technology*. 2017. 36(3). Pp. 705–711. DOI:10.4314/njt.v36i3.7.
4. Meyyada, Y. Alabdulhady, Lesley, H. Sneed, Christian, Carloni. Torsional behavior of RC beams strengthened with PBO-FRCM composite—An experimental study. *Engineering Structures*. 2017. 136(1). Pp. 393–405. DOI: 10.1016/j.engstruct.2017.01.044
5. Gonzalez-Libreros, J.H., Sneed, L.H., D'Antino, T., Pellegrino, C. Behavior of RC beams strengthened in shear with FRP and FRCM composites. *Engineering Structures*. 2017. 150(1). Pp. 830–842. DOI: 10.1016/j.engstruct.2017.07.084
6. Shraddha, B. Tibhe, Vijaykumar, R. Rathi. Comparative Experimental Study on Torsional Behavior of RC Beam Using CFRP and GFRP Fabric Wrapping. *Procedia Technology*. 2016. 24(1). Pp. 2212–0173. DOI: 10.1016/j.protcy.2016.05.020
7. Rahal, K.N., Collins, M.P. Combined torsion and bending in reinforced and prestressed concrete beams. *ACI Structural Journal*. 2003. 100(2). Pp. 157–165. DOI: 10.14359/12479
8. Hii, AKY, Al-mahaidi, R., Asce, M. Torsional capacity of CFRP strengthened reinforced concrete beams. *Journal of Composites for Construction*. 2007. 11(1). Pp. 71–80. DOI:10.1061/(ASCE)1090-0268(2007)11:1(71).
9. Ghaidak Al-Bayati, Riadh Al-Mahaidi, M. Javad Hashemi, Robin Kalfat. Torsional strengthening of RC beams using NSM CFRP rope and innovative adhesives. *Composite Structures*. 2018. 187(1). Pp. 190–202. DOI: 10.1016/j.compstruct.2017.12.016
10. Ameli, M., Ronagh, H.R. Analytical method for evaluating ultimate torque of FRP strengthened reinforced concrete beams. *Journal of Composites for Construction*. 2007. 11(4). Pp. 384–390. DOI: 10.1061/(ASCE)1090-0268(2007)11:4(384).
11. Aravind, N., Samanta, A.K., Roy, D.S., Thanikal, J.V. Retrofitting of reinforced concrete beams using fiber reinforced polymer (FRP) composites—a review. *Journal of Urban and Environmental Engineering*. 2013. 7(1). Pp. 164–175. DOI: 10.4090/juee.2013.v7n1.164175.
12. Meyyada Y. Alabdulhady, Lesley H. Sneed, Omar I. Abdelkarim, Mohamed A. ElGawady. Finite element study on the behavior of RC beams strengthened with PBO-FRCM composite under torsion. *Composite Structures*. 2017. 179(1). Pp. 326–339. DOI: 10.1016/j.compstruct.2017.07.079
13. Al-Bayati, G., Kalfat, R., Al-Mahaidi, R., Hashemi, J. Experimental study on crack propagation of CFRP-strengthened RC beams subjected to torsion. *Australian Journal of Structural Engineering*. 2018. 19(4). Pp. 279–297. DOI: 10.1080/13287982.1523293.
14. Al-Bayati, G., Al-Mahaidi, R., Kalfat, R. Experimental investigation into the use of NSM FRP to increase the torsional resistance of RC beams using epoxy resins and cement-based adhesives. *Construction and Building Materials*. 2016. 124(1). Pp. 1153–1164. DOI: 10.1016/j.conbuildmat.2016.08.095.
15. Al-Bayati, G., Al-Mahaidi, R., Kalfat, R.. Torsional strengthening of reinforced concrete beams using different configurations of NSM FRP with epoxy resins and cement-based adhesives. *Composite Structures*. 2017. 168(1). Pp. 569–581. DOI: 10.1016/j.compstruct.2016.12.045
16. Deifalla, A., Ghobarah, A. Strengthening RC T-beams subjected to combined torsion and shear using FRP fabrics: Experimental study. *Journal of composites for construction*. 2010. 14(3). Pp. 301–311. DOI: 10.1061/(ASCE)CC.1943-5614.0000091.
17. Vishnu, H. Jariwala, Paresh, V. Patel, Sharadkumar, P. Purohit. Strengthening of RC Beams Subjected to Combined Torsion and Bending with GFRP Composites. *Procedia Engineering*. 2013. 51(1). Pp. 282–289. DOI: 10.1016/j.proeng.2013.01.038
18. Ghobarah, A., Ghorbel, M.N., Chidiac, S.E. Upgrading torsional resistance of reinforced concrete beams using fiber-reinforced polymer. *Journal of Composites for Construction*. 2002. 6(4). Pp. 257–263. DOI: 10.1061/(ASCE)1090-0268(2002)6:4(257).
19. Deifalla, A., Ghobarah, A. Full torsional behavior of RC beams wrapped with FRP: analytical model. *Journal of Composites for Construction*. 2010. 14(3). Pp. 289–300. DOI: 10.1061/(ASCE)CC.1943-5614.0000085
20. Mahmood, M.N. Nonlinear analysis of reinforced concrete beams under pure torsion. *Journal of Applied Sciences*. 2007. 7(22). Pp. 3524–3529. DOI: 10.3923/jas.2007.3524.3529
21. Prabaghar, A., Kumaran, G. Theoretical study on the behavior of rectangular concrete beams reinforced internally with GFRP reinforcements under pure torsion. *International Journal of Civil and Structural Engineering*. 2011. 2(2). Pp. 570–594. DOI: 10.6088/ijcser.00202010134.
22. Elwan, S.K. Torsion strengthening of RC beams using CFRP (parametric study). *Journal of Civil Engineering*. 2017. 21(4). Pp. 1273–1281. DOI: 10.1007/s12205-016-0156-7.
23. Zojaji, A.R. and Kabir, M.Z. Analytical approach for predicting full torsional behavior of reinforced concrete beams strengthened with FRP materials. *Scientia Iranica*. 2012. 19(2). Pp. 51–63. DOI: 10.1016/j.scient.2011.12.004.
24. Ameli, M., Ronagh, H.R., Dux, P.F. Behavior of FRP strengthened reinforced concrete beams under torsion. *Journal of Composites for Construction*. 2007. 11(2). Pp. 192–200. DOI: 10.1061/(ASCE)1090-0268(2007)11:2(192)
25. Gesund, H., Schuette, F.J., Buchanan, G.R., Gray, G.A. Ultimate strength in combined bending and torsion of concrete beams containing both longitudinal and transverse reinforcement. *Journal of the American Concrete Institute*. 1964. 61(12). Pp. 1509–1522. DOI: 10.1680/macp.1968.20.64.155.

Contacts:

Rajai Al-Rousan, +962799887574; rzalrousan@just.edu.jo
 Isra'a Abo-Msamh, +96227201000; iabomsamh@gmail.com

Al-Rousan, R., Abo-Msamh, I., 2019



DOI: 10.18720/MCE.92.5

Increasing the heat transfer efficiency of sectional radiators in building heating systems

A.P. Levsev^{a*}, E.S. Lapin^a, Q. Zhang^b

^a National Research Ogarev Mordovia State University, Saransk, Russia

^b Jiangsu University of Science and Technology, Jiangsu University of Science and Technology, Zhenjiang City, Jiangsu Province, P.R. China

* E-mail: levtzevap@mail.ru

Keywords: heat supply method, heating radiators, heat-transfer efficiency, heat-carrying agent pulsation, membrane pump, heating unit

Abstract. In heating systems of residential and public buildings, the sectional radiators are widely used as heating devices, where its heat transfer efficiency critically decreases, when the heat-carrying agent's temperature lowered. At the same time, in order to increase the heat transfer efficiency of heat-exchange equipment, the positive experience of using the pulse flows is known. The heat supply method proposed in the process of the work performing, which consists in periodic supply of hot and cold heat-carrying agent through the sectional radiators. Thermal tests of 12 sectional radiators Rifar BASE 500 type at the temperatures from 42 °C to 67 °C and pulsation frequencies of the heat-carrying agent from 0.52 Hz to 0.62 Hz, showed an increase in their efficiency at the nominal flow rate of 1.8–2.2. With an increase in the flow rate and temperature of the heat-carrying agent, the SR efficiency decreases in a pulsating mode. The study of the SR efficiency from the parameters of the heating system and their switching circuit was carried out on a mathematical model in the form of energy chain that takes into account the mass and storage capacity of the heat-carrying agent. For a parallel connection up to 10 SR, the optimal circular frequency of the heat-carrying agent pulsations was 3 rad/s, and for a serial connection it was 4.2 rad/s, which is consistent with the results of thermal tests at the level of 7 %.

1. Introduction

Modern global trends in the development of heat supply systems are aimed for reducing irrational costs and heat-carrying agent losses, while improving the quality of maintaining the temperature regime in buildings. Such trends are observed almost in all programs related to the integrated development of the cities. With the development of the heat supply systems in Russia the priority is given to the district heat supply systems from combined sources of electric and thermal energy. Experience in developing of promising urban heat supply schemes shows that the quality, efficiency and reliability of the operation of heat supply systems is associated with the new technologies and tools, which are used to create individual heating plants (IHP) at the inputs to the buildings. The mass introduction of IHP instead of the traditional heating units will not only improve the temperature regime in buildings but also it will solve the problem of ensuring a given pressure at the inputs to the buildings, while increasing the degree of centralization of heat supply systems from combined sources. However, the IHP is successfully implemented only in areas of new development, where in heating systems the panel radiators are mainly used and they are connected independently to the heating networks. At the same time, in the areas of old building development the building heating systems (heating and ventilation) are still connected to the heating networks in a dependent way through the elevator and sectional radiators (SR) are mainly used as the heating devices. As for the last ones the effectiveness of the SR (the ratio of actually achieved thermal capacity to the design one) with a decrease in the heat-carrying agent temperature of 50 °C decreases to 30 %. It has been repeatedly proved as the result of numerous energy inspections of buildings. According to the fact, that with the new construction they have recently switched to the plate radiators of the PURMO type [1]. That is why the hydraulic mode of heating networks in cities is built taking into account the transformation of thermal energy, and each heating unit has the throttling device at the input [2]. At each heating unit appeared the energy losses, for instance, in Moscow there are more than 9500 of them only in the system of OJSC

Levsev, A.P., Lapin, E.S., Zhang, Q. Increasing the heat transfer efficiency of sectional radiators in building heating systems. Magazine of Civil Engineering. 2019. 92(8). Pp. 63–75. DOI: 10.18720/MCE.92.5

Левцев А.П., Лапин Е.С., Чжан Ц. Повышение эффективности теплопередачи секционных радиаторов в системах теплоснабжения зданий // Инженерно-строительный журнал. 2019. № 8(92). С. 63–75. DOI: 10.18720/MCE.92.5



This work is licensed under a [CC BY-NC 4.0](https://creativecommons.org/licenses/by-nc/4.0/)

"MOEK". The total value of these losses is equivalent to hundreds MW of electric energy which is necessary for the city economy. Nowadays, they are trying to solve the problem of ensuring the given thermal regime of the building with optimization of the hydraulic regime of the heating network by using a mixing pump in the heating units at the inputs of the buildings, which almost increases the speed of the heat-carrying agent through the heating devices in two times, but the achieved SR efficiency has not reached the design capacity. From the 7 academic buildings of National Research Ogarev Mordovia State University in which this method was implemented, the achieved effectiveness of the SR in 2018 was at the level of 60 % of the design capacity. It did not give the expected effect, as far as an increase in the speed of the heat-carrying agent through the heating devices changes the mixing coefficient of the hot and return heat-carrying agent, therefore it reduces the power of the heating device. In addition to that, the installation of mixing pumps increased the consumption of an electric energy in academic buildings for 6 %. This situation has appeared due to the lack of reliable and inexpensive technologies for supplying the heat-carrying agent, which should be based on the research and best practices in the field of new heat supply strategies, taking into account the characteristics of hydrodynamics and heat transfer of specific heating devices.

In the world practice the attention has been focused on the intermittent heating of buildings [3] strategy, which is aimed to reduce the heat energy consumption during working hours by predicting the rational power of heating equipment, depending on the type of buildings. By mixing the period of heating and cooling, there we can see the economy for 20 % of the heat energy, due to its limitation in non-working hours. The usage of such strategy increases the power of heating equipment by 1.1–1.3 times and requires the additional costs. Among the continuous heating strategies the technologies with pulsating (pulsed) heat-carrying agent circulation and the features for their creation deserves attention, which are described in details in publications [4,5]. In these works the positive experience of oscillating flows in heat exchange equipment extends to the heat supply systems with independent connection to the heating networks, without the heating devices. Recommendations are given for the construction of such schemes; however, the quantitative estimates of the achieved efficiency of such heat supply systems are not given. The influence of the pulse flow for the energy consumption of panel radiators was studied in the works [6–8], which are contain the quantitative estimates of the increasing efficiency about 20 % with fluctuations in the pulse flow in the frequency range from 0.027 m/s to 0.051 m/s and the frequency of 0.0523 rad/s to 0.209 rad/s is obtained by modeling methods of two panel emitters while maintaining the temperature on the surface of the radiator 50 °C. It is unclear, how the panel emitters efficiency changes, while changing the amplitude consumption of the heat-carrying agent. In the work [9], which is devoted to increasing the capacity of a heating system by replacing a constant flow of a supplied heat-carrying agent with a pulsed one, using the Simulink/Matlab software, a mathematical model of the recreation room with one radiator was implemented. The pulse flow with amplitude from 0.024 kg/s to 0.048 kg/s and a frequency from 0.0017 rad/s to 0.017 Hz allows saving 22 % of thermal energy due to more uniform temperature distribution in the recreation room. The model takes into account the flow hydrodynamics, the heat transfer does not take into account the features of the channels. More detailed studies of hydrodynamics and heat transfer were performed on heat exchange equipment to specific heat transfer surfaces at the higher frequencies. In the work [10], the heat transfer enhancement for finned tube heat exchangers was studied using a pulsating air flow. The research was conducted on an experimental installation at the frequencies from 10 Hz to 50 Hz with a change in the amplitude of the air flow from 13.33 % to 15.35 %, while an increase in the heat transfer coefficient was noted within 12.3 %. For the liquid medium the heat transfer is also enhanced at the lower frequencies. The work [11] presents the results of experimental studies for a horizontally located coil for heating cold water in a reservoir. The average temperature of the heated water was maintained at 60 °C; the flow was interrupted both at the input and output of the coil with a frequency from 0 to 20 Hz at Reynolds numbers from 6220 to 16300, the average heat transfer coefficient was increased to 26 % mainly due to the fluctuations in the coil.

The intensification of heat transfer depends on the time of interruption of the heat-carrying agent flow. When the flow interruption time is reduced to a few milliseconds, the pulsating mode becomes pulsed (impulse), which is accompanied by a hydraulic shock, which energy can be successfully used, for example, for the drive of a membrane pump [5]. The experimental study of the heat exchange with a pulsating flow in a plate heat exchanger at the frequency about 1 Hz is presented in [12]. The increase in heat transfer is fixed at 25 %. A significant increase in the heat transfer in the pulsed mode at the level of 40 % has been experimentally proved by cooling powerful semiconductor converters at the frequency about 1 Hz [13].

More in-depth studies on the heat transfer enhancement using a pulsating mode for a laminar flow of the heat-carrying agent in specific channels were carried out at the Moscow Power Engineering Institute. In the works [14–16], the influence of the thermal conductivity of a liquid along the axis of the channel, the thermal resistance of the wall for a pulsating laminar flow of the heat-carrying agent was studied. A significant increase in heat transfer from heat transfer surfaces of heat exchangers is associated with flow turbulence, which is especially important for creating new designs of microchannel heat exchangers.

It is applicable for heating devices which are operate in transient conditions with Reynolds numbers from 2000 to 6000, an increase in their efficiency is also observed with pulsating and pulsed heat-carrying agent flow, depending on the frequency and amplitude. A significant increase in the efficiency of SR heating at the level of 40 % was obtained using the membrane pumps at the frequency of 0.5 Hz to 1 Hz on the IHP experimental installation are explained by a more uniform temperature distribution on the surface. It should be noted that the calculated efficiency parameters were not achieved due to the limitations of the experimental installation of the IHP [17–19].

In this regard, the aim of this work was to increase the efficiency of heat transfer of SR in building heating systems, based on pulsating supply and mixing of the heat-carrying agent due to the inclusion of a double-flow membrane pump in the IHP scheme. For realization this goal, the following tasks were solved: the choice of a method for increasing the heat transfer efficiency of SR heating based on pulsating supply and mixing of the heat-carrying agent; development of a IHP design of a building with a double-flow membrane pump and the implementation of its experimental sample; conducting hydrodynamic and thermal tests of the experimental model of IHP; simulation of the effectiveness of the SR from the parameters of the heating system and their inclusion on a mathematical model.

2. Methods

The research of the efficiency of heat transfer of SR in the heating building systems from the parameters of the heat-carrying agent, the mixing coefficient of a hot and cold flow, the amount of SR and the scheme of their inclusion, as well as the parameters of the device that creates the pulsating mode was performed using the methods:

- a complex analysis when analyzing a problem and searching for optimal design solutions for finding a method of pulsating supply and mixing of the heat-carrying agent;
- physical modeling of hydrodynamics and heat transfer in the SR at the different frequencies and amplitudes of the flow pulsations, the mixing coefficient of the heat-carrying agents in the experimental IHP installation with pulsating flow and mixing of the heat-carrying agent and automated data collection;
- the method of mathematical modeling of the heat transfer efficiency of the SR at the different frequencies of flow pulsations, mixing coefficients of the heat-carrying agents, the number of the SR and their switching schemes based on the energy chain that allow studying the processes of the different physical nature based on their analogy (heat, mechanics, electricity, hydraulics) in the frequency area;
- Mathematical statistics for processing arrays of experimental data and establishing dependencies.

The starting point for conducting the complex analysis of technologies and features for implementing pulsating supply and mixing of the heat-carrying agent was the early experimental studies of heat transfer and hydrodynamics of SR heating, carried out at the Chair of heat and power engineering at the National Research Ogarev Mordovia State University which revealed the potential for increasing their effectiveness. Studies of the effectiveness of SR were carried out using various schemes for switching the membrane pumps. According to that, it was possible only partially to realize the potential for increasing the efficiency of the SR due to the limitations of the experimental IHP installation [17–19]. In a point of a fact, the fluctuations in the flow rate of the heat-carrying agent in the early studies were not purely harmonic and there was a constant component in the total flow rate of the heat-carrying agent. In addition, there were difficulties with mixing hot and cold heat-carrying agent flows in the SR and electric energy was partially used for the drive of the membrane pump.

In this work, the realization of the potential of heat transfer efficiency of SR heating was realized through the use of a double-flow membrane pump with a pulsed heat-carrying agent flow distributor in the design of the IHP experimental installation, which generates a hydraulic shock and additionally uses it for the drive of the membrane pump [20]. Figure 1 shows a diagram of an experimental individual heating plant with a membrane pump. The scheme allows you to create the two independent circuits.

IHP with double-flow membrane pump (Figure 1) consists of feeding and return pipeline and with the left and right section of membrane pump. Both sections of the membrane pump are controlled from a pulsed flow distributor 5, connected with an electric motor drive 6. A feed pipe 1 is connected to the input of the pulsed flow distributor 5, and its outputs are connected to the chambers 3 and 4. The left section of the membrane pump 3 and the right section of the membrane pump 4 are rigidly connected to the link rod 7. The switching mechanism of the shock valves 8 is connected to the one side of a link rod 9 and on the other side to the left 10 and right 11 shock valves. Radiant space heater of the right section is connected in parallel with the hot-water calorifier 13. The left section is connected in the same way, but it has not been used in this installation.

When you turn on the electric motor drive 6 and establish the required pulsation frequency of the pulsed flow distributor 5, the heat-carrying agent is alternately supplied from the supply pipe 1 to the internal (working) parts of sections 3 and 4, where it performs the work. In the final positions of the link rod 9 the shock valves 10 and 11 are switched with the help of the mechanism of switching the shock valves 8 and the external (pumping) sections intake the heat-carrying agent through SR 12 and the hot-water calorifier 13. At the next cycle the cooled heat-carrying agent goes repeatedly through the SR 12 and hot-water calorifier 13 and pushed into the return pipeline 2. Cooled water regulating temperature is conducted by the changing the load of the hot-water calorifier. Through this process, we can see that for the one period of double-flow membrane pump work the hot or cooled heat-carrying agent goes through the SR.

There is an experimental model of IHP with a double-flow membrane pump with a capacity of 3000 l/h was implemented at the Chair of heat and power engineering of Federal State Budgetary Institution of Higher Education Ogarev Mordovia State University. The main components of the plant is shown in Figure 2, 3.

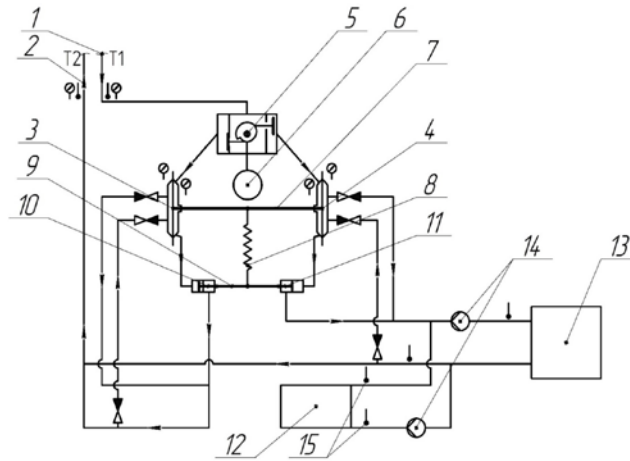


Figure 1. Scheme of experimental plant (installation) of Individual Heating Plant on the basis of double-flow membrane pump: 1 – feeding pipe line; 2 – return pipe line; 3 – the left section of membrane pump; 4 – the right section of membrane pump; 5 – pulsed flow distributor; 6 – electric motor drive; 7 – link rod; 8 – switching shock valves mechanism; 9 – link rod; 10 – the left shock valve; 11 – the right shock valve; 12 – heating device; 13 – hot-water calorifier; 14 – flow nozzle; 15 – temperature sensor.

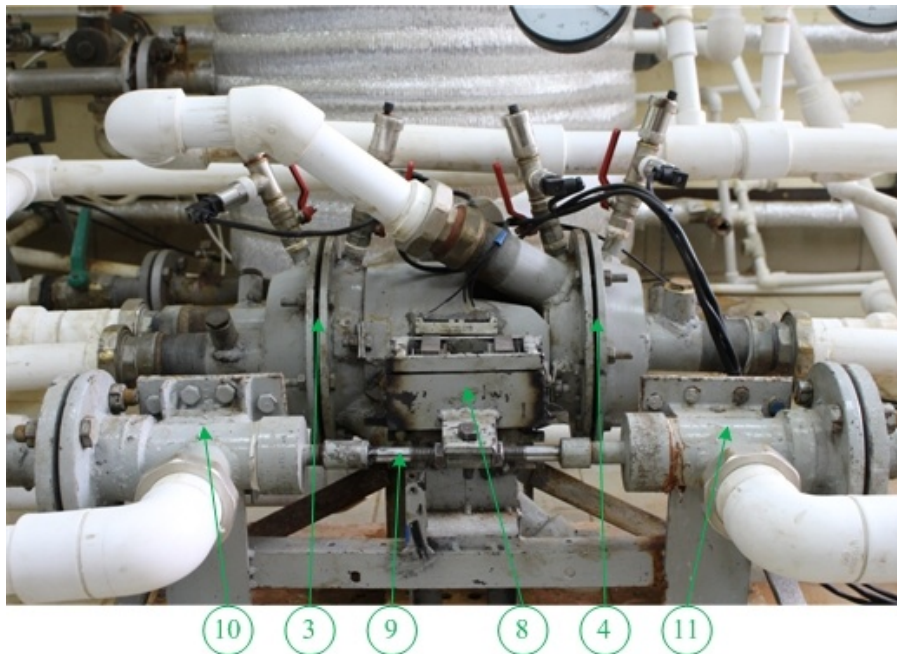


Figure 2. Physical form of experimental unit of IHP on the basis of double-flow membrane pump: 3 – Membrane pump left section; 4 – Membrane pump right section; 8 – Switching shock valves mechanism; 9 – Link rod; 10 – Left shock valve; 11 – Right shock valve.



Figure 3. Pulsed flow distributor.

3. Results and Discussion

Hydraulic tests of IHP with a double-flow membrane pump with a capacity of 3000 l/h showed that the flow rate of a double-flow membrane pump depends on the frequency of interruption of the heat-carrying agent flow. It was found that when the frequency of interruption of the heat-carrying agent flow changes from 0.5 Hz to 0.8 Hz, the flow rate (consumption) of the heat-carrying agent changes from 2000 l/h to 3000 l/h. In this case the pressure at the pump input varied within 0.536 kPa to 0.635 kPa with the same available head between the supply and return pipelines (dependencies 2–5 Figure 4). The calculated dependence of the flow rate of a double-flow membrane pump on the frequency of interruption of the heat-carrying agent flow is somewhat higher and differs from the experimental average within the limits of 4 %. The calculated dependence of the flow rate of a double-flow membrane pump on the frequency of interruption of the heat-carrying agent flow is calculated in the plugflow mode. By the least square method we obtained a regression equation for the dependence of the flow rate of a double-flow membrane pump on the frequency of interruption of the heat-carrying agent flow:

$$G = 177.46 + 3541.99 f. \quad (1)$$

Later on, the thermal tests were carried out according to the results of which the effectiveness of the SR was evaluated in various modes. During thermal tests of IHP with a double-flow membrane pump with a capacity of 3000 l/h, temperature parameters 15 and flow rate 14 of the heat-carrying agent at the input and output of 12 SR Rifar BASE 500 type were recorded. Hereinafter, by the temperature differences at the input and output of the SR, its efficiency was calculated depending on the flow rate of the heat-carrying agent at the certain frequency. The results of calculating the efficiency of SR at four averaged temperatures of the heat-carrying agent (42 °C, 50 °C, 58 °C, and 67 °C) are presented in the form of graphs (Figure 5). In this case the heat-carrying agent's flow through the SR varied from 60 l/h to 360 l/h. Nominal heat-carrying agent flow through the SR is 120 l/h. With an averaged temperature of the heat-carrying agent of 42 °C and nominal flow rate (Figure 5, a), the highest SR efficiency is 0.54 at the heat-carrying agent pulsation frequency of 0.62 Hz. With an increase in the flow rate of the heat-carrying agent through the SR, the efficiency decreases and at the flow rate of 300 l/h it becomes equal to the stationary mode. In a stationary mode the efficiency with increasing flow rate also increases from 0.25 to 0.32. At the averaged heat-carrying agent/s temperature of 50 °C (Figure 5, b), the SR efficiency is 0.52 at the nominal flow rate and frequency of 0.57 Hz. In the stationary mode the efficiency with increasing flow rate also increases from 0.28 to 0.42. At the averaged heat-carrying agent's temperature of 58 °C (Figure 5, c), the highest SR efficiency is 1.03 at the frequency of 0.62 Hz, which decreases with increasing heat-carrying agent's flow rate, and at the flow rate of 240 l/h it becomes equal to the stationary mode. In the stationary mode the efficiency with increasing flow rate also increases from 0.53 to 0.67. With the averaged temperature of the heat-carrying agent at the inlet to the SR equal to 67 °C (Figure 5, d), the greatest efficiency of the SR is 1.28 at the frequency of 0.57 Hz, which decreases with increasing flow rate and with the rate of 180 l / h is approaches to the stationary mode. In the stationary mode the efficiency with increasing flow rate also increases from 0.72 to 0.85. Thus, the SR efficiency at the nominal flow rate of the heat-carrying agent in a pulsating mode, depending on the temperature at the inlet and the pulsations frequency increases by 1.8 – 2.2 times. Moreover, with increasing temperature at the inlet to the SR, the relative value of the efficiency decreases. The frequency of pulsations of the heat-carrying agent has a significant impact on achieving maximum SR efficiency and is determined by its design capacities. With an increase in the heat-carrying agent's flow rate, the efficiency of the SR in the pulsating mode decreases intensively with the high average temperature of the heat-carrying agent.

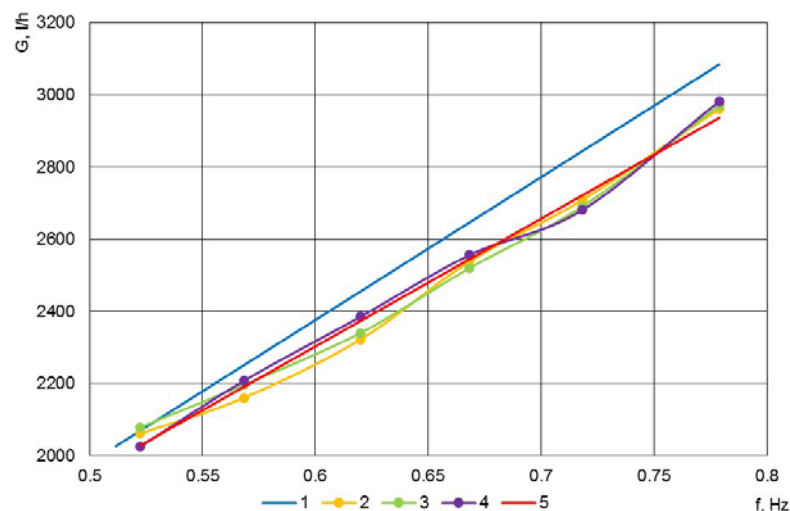


Figure 4. Hydraulic characteristics of IHP on the basis of double-flow membrane pump with different pressure at the input of pump chambers: 1 – calculated; 2 – $P_3=568$ kPa; 3 – $P_2=536$ kPa; 4 – $P_1=635$ kPa; 5 – according to the least square method.

The efficiency of the SR depends on both parameters of the heat-carrying agent and the thermophysical properties of the device itself. The last we can include the mass of the heat-carrying agent, thermal and capacitive resistance. For obtaining the equations describing the movement of heat flows, it is convenient to represent them in the form of an energy chain of SR with a section of the heating network (Figure 6) [21].

Special feature for IHP with double-flow membrane pump is the pulsating regime i.e. flow enthalpy h , J/kg and the mass rate (consumption) g , kg/s, which is periodically changes in time.

The energy chain of the SR with the participation of heat engineering devices includes three links: the first is thermal – it takes into account the decrease in enthalpy due to the mass m , kg and the heat-carrying agent; the second link-is transformative, it is converts an enthalpy h , J/kg, in temperature t , °C, and the mass flow rate g , kg/s, to the specific heat flow rate q , W/°C, through the heat capacity c ; the third link is heat, which takes into account the SR temperature drop with the help of thermal true resistances R_1, R_2, R_3 , °C²/W, corresponding from the heat-carrying agent to the area of heating surface, thermal conductivity of the wall and from the wall to the air and also with accumulating ability of water with ductility l_1 , W/s, and accumulating ability of the wall ductility l_2 , W/s.

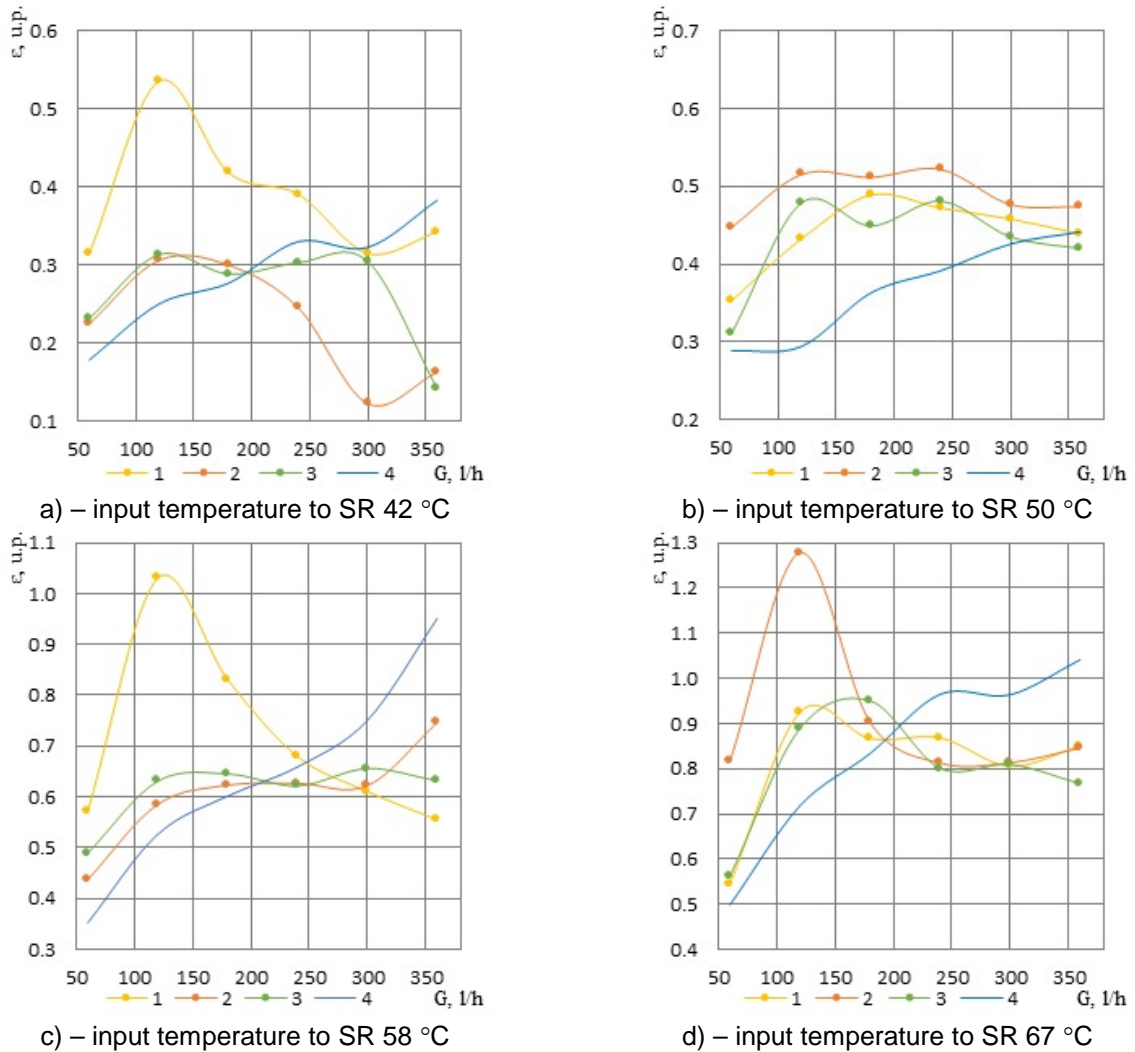


Figure 5. The efficiency of bimetallic sectional radiators which are connected to double-flow membrane pump: 1 – 0.623 Hz; 2 – 0.572 Hz; 3 – 0.523 Hz; 4 – stationary.

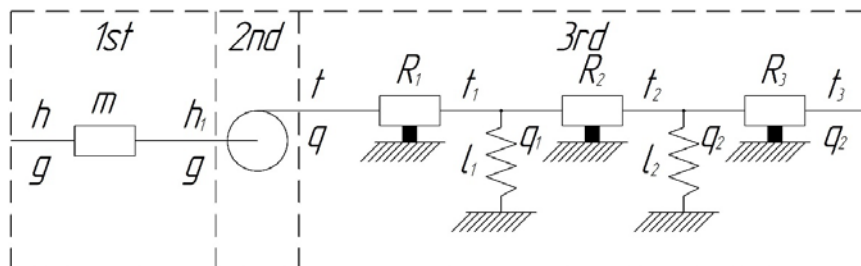


Figure 6. SR's energy chain with the section of heating network.

Chain components equation:

$$\begin{array}{ccc}
 \text{1st} & \text{2nd} & \text{3rd} \\
 \left\{ \begin{array}{l} h = m\dot{g} + h_1, \\ g = q. \end{array} \right. & \left\{ \begin{array}{l} h_1 = ct, \\ g = \frac{q}{c}. \end{array} \right. & \left\{ \begin{array}{l} t = R_1q + R_2q_1 + R_3q_2 + t_3, \\ q = l_1\dot{t}_1 + l_2\dot{t}_2 + q_2. \end{array} \right. \quad (2)
 \end{array}$$

During the modeling process it was necessary to find out how the output of SR temperature will change t_3 , °C, depending of its removal from the source (IHP with double-flow membrane pump), and also what kind of effect has the parallel and compounding connection of SR.

Let's imagine the SR output temperature $t_3 = t_{30} + \bar{t}_3$ and specific heat flow rate $q_2 = q_{20} + \bar{q}_2$ in the form of a constant component and deviation.

q , W/°C equation:

$$\begin{aligned}
 q &= l_1R_2l_2R_3\ddot{\bar{q}}_2 + l_1R_2l_2\ddot{\bar{t}}_3 + (l_1R_2 + l_1R_3 + l_2R_3)\dot{\bar{q}}_2 + (l_1 + l_2)\dot{\bar{t}}_3 + \bar{q}_2 + q_{20} = \\
 &= a_1\ddot{\bar{q}}_2 + a_2\dot{\bar{q}}_2 + \bar{q}_2 + q_{20} + b_1\ddot{\bar{t}}_3 + b_2\dot{\bar{t}}_3. \quad (3)
 \end{aligned}$$

There are expressions for coefficients:

$$a_1 = l_1R_2l_2R_3; \quad a_2 = l_1R_2 + l_1R_3 + l_2R_3; \quad b_1 = l_1R_2l_2; \quad b_2 = l_1 + l_2.$$

t , °C equation:

$$\begin{aligned}
 t &= R_1a_1\ddot{\bar{q}}_2 + R_1a_2\dot{\bar{q}}_2 + R_1\bar{q}_2 + R_1q_{20} + R_1b_1\ddot{\bar{t}}_3 + R_1b_2\dot{\bar{t}}_3 + \\
 &+ R_2l_2R_3\dot{\bar{q}}_2 + R_2l_2\dot{\bar{t}}_3 + R_2q_{20} + R_2\bar{q}_2 + R_3q_{20} + R_3\bar{q}_2 + t_{30} + \bar{t}_3 = \\
 &= a_3\ddot{\bar{q}}_2 + a_4\dot{\bar{q}}_2 + a_5\bar{q}_2 + a_6q_{20} + b_3\ddot{\bar{t}}_3 + b_4\dot{\bar{t}}_3 + \bar{t}_3 + t_{30}. \quad (4)
 \end{aligned}$$

There are expressions for coefficients:

$$a_3 = R_1a_1; \quad a_4 = R_1a_2 + R_2l_2R_3; \quad a_5 = R_1 + R_2 + R_3; \quad a_6 = R_1 + R_2; \quad b_3 = R_1b_1; \quad b_4 = R_1b_2 + R_2l_2.$$

h , J/kg equation:

$$\begin{aligned}
 h &= \frac{ma_1}{c}\ddot{\bar{q}}_2 + \left(\frac{ma_2}{c} + a_3c\right)\dot{\bar{q}}_2 + \left(\frac{m}{c} + a_4c\right)\bar{q}_2 + a_5c\bar{q}_2 + \\
 &+ a_6cq_{20} + \frac{mb_1}{c}\ddot{\bar{t}}_3 + b_3c\dot{\bar{t}}_3 + \left(\frac{mb_2}{c} + b_4c\right)\bar{t}_3 + c\bar{t}_3 + ct_{30} = \\
 &= a_7\ddot{\bar{q}}_2 + a_8\dot{\bar{q}}_2 + a_9\bar{q}_2 + a_{10}\bar{q}_2 + a_{11}q_{20} + b_5\ddot{\bar{t}}_3 + b_6\dot{\bar{t}}_3 + b_7\bar{t}_3 + c\bar{t}_3 + ct_{30}. \quad (5)
 \end{aligned}$$

There are coefficient values:

$$\begin{aligned}
 a_7 &= \frac{ma_1}{c}; \quad a_8 = \frac{ma_2}{c} + a_3c; \quad a_9 = \frac{m}{c} + a_4c; \quad a_{10} = a_5c; \quad a_{11} = a_6cq_{20}; \\
 b_5 &= \frac{mb_1}{c}; \quad b_6 = b_3c; \quad b_7 = \frac{mb_2}{c} + b_4c; \quad b_8 = c + 1.
 \end{aligned}$$

Image equation:

$$(a_7s^3 + a_8s^2 + a_9s + a_{10} + 1)Q_2(s) = -(b_5s^3 + b_6s^2 + b_7s + c + 1)T_3(s). \quad (6)$$

The complex resistance of the chain output:

$$Z(s) = \frac{T_3(s)}{Q_2(s)} = \frac{a_7s^3 + a_8s^2 + a_9s + a_{10} + 1}{-b_5s^3 - b_6s^2 - b_7s - c - 1}. \quad (7)$$

Chain frequency function:

$$Z(j\Omega) = \frac{a_7 b_5 \Omega^6 + (a_8 b_5 + a_7 b_6) j \Omega^5 + (a_9 b_5 - a_7 b_7 - a_8 b_6) \Omega^4}{(b_6 \Omega^2 - b_8)^2 + (b_5 j \Omega^3 - b_7 j \Omega)^2} + \frac{(a_7 b_8 + a_8 b_7 + a_9 b_6 + a_{11} b_5) j \Omega^3 + (a_8 b_8 + a_9 b_7 + a_{11} b_6) \Omega^2 - (a_9 b_8 + a_{11} b_7) j \Omega - a_1 b_8}{(b_6 \Omega^2 - b_8)^2 + (b_5 j \Omega^3 - b_7 j \Omega)^2}. \quad (8)$$

Real part:

$$\text{Re}(j\Omega) = \frac{a_7 b_5 \Omega^6 + (a_9 b_5 - a_7 b_7 - a_8 b_6) \Omega^4 + (a_8 b_8 + a_9 b_7 + a_{11} b_6) \Omega^2 - a_1 b_8}{(b_6 \Omega^2 - b_8)^2 - (b_7 \Omega - b_5 \Omega^3)^2}. \quad (9)$$

Imaginary part:

$$\text{Im}(j\Omega) = \frac{(a_8 b_5 + a_7 b_6) \Omega^5 + (a_7 b_8 + a_8 b_7 + a_9 b_6 + a_{11} b_5) \Omega^3 - (a_9 b_8 + a_{11} b_7) \Omega}{(b_6 \Omega^2 - b_8)^2 - (b_7 \Omega - b_5 \Omega^3)^2} j. \quad (10)$$

Amplitude-frequency characteristics:

$$A(j\Omega) = \sqrt{\text{Re}(j\Omega)^2 + \text{Im}(j\Omega)^2}. \quad (11)$$

The efficiency of sectional radiators, according to this model, was estimated by the value of the temperature drop at the output of the device t_3 , °C, with the single input exposure q_2 , W/°C. It is specified that the temperature t_3 , °C, will go up less, so the efficiency will be higher, comparing with the basic operation.

Thermal true resistances of the chain R_1 , R_2 , R_3 , °C²/W, were selected based on the temperature drop during the passing of the heat flow. Moreover, the same temperature drop according to the experimental conditions was strictly maintained. The ratio between these resistances was taken in accordance with the distribution of heat transfer coefficients. The value of ductility was chosen based on changes in the volume of the heat-carrying agent and heat capacity depending on the material of the pipe and sectional radiators. The mass of the heat-carrying agent was taken based on the diameter of the pipe and its length. Initial parameters for predicting the switching modes of sectional radiators: basic; parallel and sequential connection (Table 1).

Table 1. Parameters for operation modeling.

№	Operation	E-Chain parameters					Heat-carrying agent parameters		
		m , kg	R_1 , °C ² /W	R_2 , °C ² /W	R_3 , °C ² /W	l_1 , W/s	l_2 , W/s	t_n , °C	g , kg/s
1	basic	6	0.774	0.04	36.13	0.01	0.2	48.6	0.0333
2	parallel	8.4	0.387	0.02	18.37	0.01	0.2	48.6	0.0333
3	sequential	9	1.5	0.08	72	0.01	0.1	48.6	0.0333
4	With increased mass	8	0.774	0.04	36.13	0.01	0.2	48.6	0.0666

Modeling results are given in amplitude-frequency characteristic in three modes of operation (Figure 7).

As we can see from the amplitude-frequency characteristics graphs in the basic operation mode the greatest decrease in temperature at the output of the SR for a single surge in specific heat flow is observed at the circular frequency of 3.6 rad/s and corresponds to 3.6 °C which completely coincides with the experimentally obtained dependences of the SR efficiency at the given circular frequency (curve 2 of Figure 5). When the SR is connected in parallel, the thermal true resistance is reduced due to the better mixing of the heat-carrying agent. the circular frequency, which has the greatest decrease in temperature at the output of the SR is 3 rad/s, it corresponds to 2.23 °C. It follows that in order to provide the improved SR efficiency, it is necessary to switch to the angular frequency of 3 rad/s (0.47 Hz). With sequential SR connection the thermal true resistances are increasing for 3 times. The heat-carrying agent mass increases to 2.4 kg. As for the last SR output temperature, so it increases to 6.7 °C and the circular frequency goes higher and it shows 4.2 rad/s. In this case, the flow rate of the heat-carrying agent is not changing. According to this fact, it is necessary to increase the flow rate of SR in two times with the sequential connection. The last operation mode corresponds to the basic parameters with the increased mass. In this operation mode the circular frequency decreases to 3 rad/s and the minimum temperature at the output of the last SR is 4.33 °C

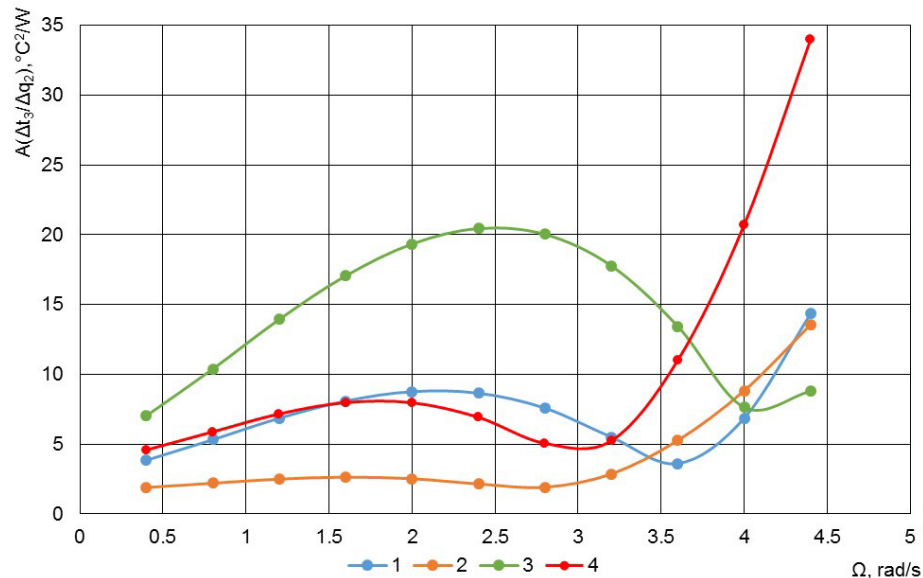


Figure 7. Amplitude-frequency characteristics of energy chain: 1 – basic powering SR; 2 – parallel connection SR; 3 – sequential connection of SR; 4 – with increasing the mass of the heat-carrying agent to the basic operation.

4. Conclusion

1. In heating systems of residential and public buildings, SR are widely used as heating devices due to their compactness. Resistance to pressure drops high corrosion resistance and good aesthetic qualities. However, in practice they showed a low efficiency (power reduction) with a decrease in the heat-carrying agent temperature which is typical for the spring-autumn period of the heating system work. This disadvantage is compensated by installing an additional number of sections in the SR or using the electric energy for heating purposes which is inefficient in the context of the implementation of the energy conservation policy. At the level of implementation of urban energy-saving programs with the introduction of IHP based on traditional technologies, they are trying to solve this problem, however. Nowadays it has been possible to realize the potential for increasing the efficiency of heat supply systems with SR only partially. Among non-traditional technologies and developments in world practice over the past ten years much attention has been focused on the heating systems with pulsating (pulsed) heat-carrying agent circulation. This allows not only increasing the heat transfer efficiency from the surfaces of heating devices up to 40 %, but to reduce the consumption of thermal energy up to 20 % due to equalization of indoor temperature. However, the experience is still insufficient for using these developments in the IHP schemes of buildings with SR. The researches of the heat transfer and hydrodynamics of heat-exchange equipment in most of the works has the one-sided character and were carried out by mathematical modeling methods for one heater at a constant temperature of the heat-carrying agent at the input. According to the fact, increasing the efficiency of heat transfer of SR in building heat supply systems based on pulsating supply and mixing of the heat-carrying agent due to the inclusion of a non-volatile double-flow membrane pump in the IHP scheme has scientific and practical value.

2. A method is proposed for increasing the efficiency of heat supply systems of buildings with SR based on pulsating supply and mixing of a heat carrying agent. The essence of the method consists in periodically passing through SR heating of hot and cooled pulsating heat-carrying agent. The pulsating flow rate and temperature of the heat-carrying agent with the frequency up to 1 Hz makes it possible to increase the efficiency of SR about two times due to a more uniform temperature distribution on the heat transfer surface. For realization, this method in the heating systems of buildings with SR, an IHP scheme was developed and tested on the basis of a non-volatile dual-flow diaphragm pump, using up to 20 meters of the available pressure of the heating network.

3. Hydraulic tests of the IHP on the basis of a non-volatile double-flow membrane pump with a capacity of 3000 l/h showed that the flow rate of a dual-flow diaphragm pump from 2000 l/h to 3000 l/h is regulated by the frequency of pulsations of the heat-carrying agent from 0.5 Hz to 0.8 Hz and has a linear relationship. The calculated dependence of the flow rate of a double-flow membrane pump on the frequency of interruption of the heat-carrying agent flow obtained using the least squares method in the form of a regression equation differs from the experimental average within 4 %. The linear dependence of the flow rate on the frequency of a double-flow membrane pump allows it to accurately keep track according to the number of cycles without the use of expensive heat meters.

4. In the process of thermal tests of 12 SR Rifar BASE 500 type connected to IHP based on a double-flow membrane pump, with the temperatures from 42 °C to 67 °C and pulsation frequencies of the heat-carrying agent from 0.52 Hz to 0.62 Hz, was found its efficiency increase at the nominal flow rate of 1.8 – 2.2.

Moreover, with temperature increase of the heat-carrying agent at the entrance to the SR, the relative value of the efficiency decreases relative to the stationary mode. The frequency of the heat-carrying agent pulsations has a significant impact on achieving maximum SR efficiency and determined by its design features. With an increase in the flow rate of the heat-carrying agent, the SR efficiency in a pulsating mode decreases intensively with the high temperature at the entrance.

5. The prediction of the heat transfer of several SR included in the building heating systems was carried out with the mathematical model in the form of energy chain that takes into account the mass of the heat-carrying agent in the pipelines of the heating network and SR, as well as thermal active and storage resistances. The simulation results are presented in the form amplitude-frequency characteristics (temperature increment at the output of the last SR in the heating system to the heat flow increment). The adequacy of the model was tested in the basic mode for one SR at the circular frequency of 3.6 rad/s, while the decrease in temperature at its output amounted 3.6 °C, which completely coincides with the experimentally obtained dependences of the effectiveness of the SR at this frequency. For a parallel connection up to 10 SR the optimum circular frequency of the pulsations of the heat-carrying agent was 3 rad/s, and for a sequential connection – 4.2 rad/s, which is consistent with the thermal test results at the level of 7 %.

6. The results of this research can be used in the design of IHP with pulsed circulation and mixing of the heat-carrying agent for heat buildings supply with dependent connection to the heating network which will ensure the required temperature conditions in the recreation rooms throughout the heating period at the low heat-carrying agent temperatures, also will reduce the heat energy consumption and simplify the heat carrying agent accounting and eliminates the cost for circulation pumps drive.

5. Acknowledgments

The work was carried out under the grant of the Russian Foundation for Basic Research 18-48-130008.

References

- Miladze, V. Energoeffektivnost stalnykh panelnykh radiatorov v nizkotemperaturnykh sistemakh otopeniya [Energy efficiency of steel panel radiators in low-temperature heating systems]. *Santekhnika, otopeniye, konditsionirovaniye*. 2015. 165(9). Pp. 44–45. (rus)
- Manyuk, V.I., Kaplinskiy, Ya.I., i dr. Spravochnik po naladke i ekspluatatsii vodyanykh teplovykh setey [Guide to the adjustment and operation of water heating networks]. M.: Stroyizdat, 1982. 215 p. (rus)
- Xu, B., Zhou, S., Hu, W. An intermittent heating strategy by predicting warm-up time for office buildings in Beijing. *Energy Build.* 2017. No. 155. Pp. 35–42. DOI: 10.1016/j.enbuild.2017.08.062
- Makeev, A.N. Implementation of pulse heat supply for dependent connection of customers. *Magazine of Civil Engineering*. 2018. 83(7). Pp. 114–125. doi: 10.18720/MCE.83.11.
- Makeyev, A.N. Theory of pulse circulation of the heater in the heat supply system with independent subscription of subscribers. *Nauchnyy zhurnal stroitelstva i arkhitektury*. 2018. 50(2). Pp. 11–20.
- Embaye, M., Al-Dadah, R.K., Mahmoud, S. Thermal performance of hydronic radiator with flow pulsation – Numerical investigation. *Applied Thermal Engineering*. 2015. Vol. 80. Pp. 109–117. DOI: 10.1016/j.applthermaleng.2014.12.056
- Embaye, M., Al-Dadah, R.K., Mahmoud, S. The effect of flow pulsation on the heating performance of panel radiators in central heating systems: CFD analysis. In *WIT Transactions on Engineering Sciences*. 2014. Vol. 83. Pp. 27–38. DOI: 10.2495/HT140031
- Calisir, T., Yazar, H., Baskaya, S. Determination of the effects of different inlet-outlet locations and temperatures on PCCP panel radiator heat transfer and fluid flow characteristics. *International Journal of Thermal Sciences*. 2017. Vol. 121. Pp. 322–335. DOI: 10.1016/j.ijthermalsci.2017.07.026
- Embaye, M., Al-Dadah, R.K., Mahmoud, S. Effect of flow pulsation on energy consumption of a radiator in a centrally heated building. *International Journal of Low-Carbon Technologies*. Vol. 11. Pp. 119–129. DOI: 10.1093/ijlct/ctu024
- Wantha, C. Effect and heat transfer correlations of finned tube heat exchanger under unsteady pulsating flows. *International Journal of Heat and Mass Transfer*. 2016. Vol. 99. Pp. 141–148. DOI: 10.1016/j.ijheatmasstransfer.2016.03.102
- Kharvani, H.R., Doshmanziari, F.I., Zohir, A.E., Jalali-Vahid, D. An experimental investigation of heat transfer in a spiral-coil tube with pulsating turbulent water flow. *Heat and Mass Transfer/Waerme- Und Stoffuebertragung*. 2016. 52(9). Pp. 1779–1789. DOI: 10.1007/s00231-015-1697-x
- Qian, H., Kudashev, S., Plotnikov, V. Experimental Study on Heat Transfer of Pulsating Flow Enhanced the Plate Heat Exchanger. *Bulletin of Science and Practice*. 2019. No. 5. Pp. 81–92. DOI: 10.33619/2414-2948/45/09
- Levtsev, A.P., Makeev, A.N., Kudashev S.F. Pulsating heat transfer enhancement in the liquid cooling system of power semiconductor converter. *Indian Journal of Science and Technology*. 2016. 9(11). Pp. 1–5. DOI: 10.17485/ijst/2016/v9i11/89419
- Valuyeva, Ye.P., Purdin, M.S. Hydrodynamics and heat transfer for pulsating laminar flow in channels. *Thermal Engineering*. 2015. 62(9). Pp. 636–644.
- Valuyeva, Ye.P., Purdin, M.S. The pulsating laminar flow in a rectangular channel. *Thermophysics and Aeromechanics*. 2015. 22(6). Pp. 733–744.
- Valuyeva, Ye.P., Purdin, M.S. An investigation into heat transfer for a pulsating laminar flow in a rectangular channel with a boundary condition of the first kind. *High Temperature*. 2017. 55(4). Pp. 622–625.
- Levtsev, A.P., Lapin, Ye.S. Efficiency of sectional radiators at low temperature temperatures. *Conference Proceedings: XX Mezhdunarodnoy nauchno-prakticheskoy konferentsii "Goroda Rossii: problemy stroitelstva, inzhenernogo obespecheniya, blagoustroystva i ekologii"*. Penza: RIO PGAU, 2018. Pp. 72–76. (rus)
- Levtsev, A.P., Lapin, Ye.S., Bikunova, M.V., Salmin, V.V. Design features and evaluation of equipment for pulsed coolant. *Regional Architecture and Engineering*. 2018. No. 4. Pp. 151–158. (rus)
- Levtsev, A.P., Lapin, Ye.S. Use of an energy efficient membrane pump in a scheme of an individual thermal point of a building. *Privolzhskiy nauchnyy zhurnal*. 2018. No. 4. Pp. 53–59.

20. Levsev, A.P., Lapin, Ye.S., Mogdarev, M.P. Individualnyy teplovoy punkt s membrannym nasosom [Individual heat point with diaphragm pump] Patent Russia no. 183885, 2018.
21. Levsev, A.P. Impulsnyye sistemy teplo- i vodosnabzheniya: monografiya. A. P. Levsev, A. N. Makeyev; pod obshch. red. d-ra tekhn. nauk prof. A. P. Levseva. Saransk: Izd-vo Mordov. un-ta, 2015. 172 p.

Contacts:

Alexey Levsev, +7(906)1633200; levzevap@mail.ru

Evgeniy Lapin, +7(902)6693219; evgeniy-lapin@yandex.ru

Qianwen Zhang, +7(834)2254101; 543785883@qq.com

© Levsev, A.P., Lapin, E.S., Zhang, Q., 2019



DOI: 10.18720/MCE.92.5

Повышение эффективности теплопередачи секционных радиаторов в системах теплоснабжения зданий

А.П. Левцев^{а*}, Е.С. Лапин^а, Ц. Чжан^б

^а Национальный исследовательский Мордовский государственный университет им. Н.П. Огарёва, г. Саранск, Россия

^б Университет науки и техники Цзянсу, Университет науки и техники Цзянсу, г. Чжэньцзян, провинция Цзянсу, КНР

* E-mail: levtzevap@mail.ru

Ключевые слова: способ теплоснабжения, радиаторы отопления, эффективность теплопередачи, пульсация теплоносителя, мембранный насос, тепловой пункт

Аннотация. В системах теплоснабжения жилых и общественных зданий в качестве отопительных приборов широко используются секционные радиаторы (СР), эффективность теплопередачи которых при понижении температуры теплоносителя снижается до 30 %. На практике низкая эффективность СР компенсируется за счет установки дополнительного числа секций и использования электрической энергии на нужды отопления, что в условиях реализации политики энергосбережения нерационально. В процессе выполнения работы предложен способ теплоснабжения, заключающийся в периодической подаче горячего и холодного теплоносителя через СР, который реализован в схеме лабораторной установки ИТП на базе энергоэффективного двухпоточного мембранного насоса производительностью 3000 л/ч, которая имеет возможность изменять диапазон частот от 0,3 до 1 Гц. В результате гидравлических испытаний двухпоточного мембранного насоса установлена линейная зависимость расхода от частоты пульсаций теплоносителя на частотах до 1 Гц. Тепловые испытания 12 СР типа Rifar BASE 500 в пульсирующем режиме на частотах от 0,5 Гц до 0,8 Гц, при средней температуре теплоносителя 48 °С и среднем расходе 120 л/ч показали, что эффективность теплопередачи СР зависит от частоты пульсаций теплоносителя. Наибольшая эффективность СР зафиксирована на круговой частоте 3,6 рад/с и составила 53 %. Исследование эффективности СР от параметров теплосети и схемы их включения выполнялось на математической модели в виде энергетической цепи, которая учитывает массу теплоносителя в трубопроводах тепловой сети и СР, термические сопротивления теплосети и СР, а также аккумулирующую способность воды в трубопроводах тепловой сети и СР. Для параллельного соединения до 10 СР оптимальная круговая частота пульсаций теплоносителя составила 3 рад/с, а для последовательного – 4,2 рад/с, при которых достигается наибольшая эффективность теплопередачи.

Литература

1. Миладзе В. Энергоэффективность стальных панельных радиаторов в низкотемпературных системах отопления // Сантехника, отопление, кондиционирование. 2015. № 9 (165). С. 44–45.
2. Манюк В.И., Каплинский Я.И. и др. Справочник по наладке и эксплуатации водяных тепловых сетей. М.: Стройиздат, 1982. 215 с.
3. Xu B., Zhou S., Hu W. An intermittent heating strategy by predicting warm-up time for office buildings in Beijing // Energy Build. 2017. No 155. Pp. 35–42. DOI: 10.1016/j.enbuild.2017.08.062
4. Макеев А.Н. Обеспечение импульсного теплоснабжения для зависимого присоединения абонентов // Инженерно-строительный журнал. 2018. № 7(83). С. 114–125. DOI: 10.18720/MCE.83.11
5. Макеев А.Н. Теория организации импульсной циркуляции теплоносителя в системе теплоснабжения с независимым присоединением абонентов // Научный журнал строительства и архитектуры. 2018. № 2(50). С. 11–20.
6. Embaye M., Al-Dadah R. K., Mahmoud S. Thermal performance of hydronic radiator with flow pulsation – Numerical investigation // Applied Thermal Engineering. 2015. Vol. 80. Pp. 109–117. DOI: 10.1016/j.applthermaleng.2014.12.056
7. Embaye M., Al-Dadah R.K., Mahmoud S. The effect of flow pulsation on the heating performance of panel radiators in central heating systems: CFD analysis // In WIT Transactions on Engineering Sciences. 2014. Vol. 83. Pp. 27–38. DOI: 10.2495/HT140031
8. Calisir T., Yazar H., Baskaya S. Determination of the effects of different inlet-outlet locations and temperatures on PCCP panel radiator heat transfer and fluid flow characteristics // International Journal of Thermal Sciences. 2017. Vol. 121. Pp. 322–335. DOI: 10.1016/j.ijthermalsci.2017.07.026

9. Embaye M., Al-Dadah R. K., Mahmoud S. Effect of flow pulsation on energy consumption of a radiator in a centrally heated building // International Journal of Low-Carbon Technologies. Vol. 11. Pp. 119–129. DOI: 10.1093/ijlct/ctu024
10. Wantha C. Effect and heat transfer correlations of finned tube heat exchanger under unsteady pulsating flows // International Journal of Heat and Mass Transfer. 2016. Vol. 99. Pp. 141–148. DOI: 10.1016/j.ijheatmasstransfer.2016.03.102
11. Kharvani H.R., Doshmanziari F.I., Zohir A.E., Jalali-Vahid D. An experimental investigation of heat transfer in a spiral-coil tube with pulsating turbulent water flow // Heat and Mass Transfer/Waerme- Und Stoffuebertragung. 2016. 52(9). Pp. 1779–1789. DOI: 10.1007/s00231-015-1697-x
12. Qian H., Kudashev S., Plotnikov V. Experimental Study on Heat Transfer of Pulsating Flow Enhanced the Plate Heat Exchanger // Bulletin of Science and Practice. 2019. No. 5. Pp. 81–92. DOI: 10.33619/2414-2948/45/09
13. Levtzev A.P., Makeev A.N., Kudashev S.F Pulsating heat transfer enhancement in the liquid cooling system of power semiconductor converter // Indian Journal of Science and Technology. 2016. 9(11). Pp. 1–5. DOI: 10.17485/ijst/2016/v9i11/89419
14. Valuyeva Ye.P., Purdin M.S. Hydrodynamics and heat transfer for pulsating laminar flow in channels // Thermal Engineering. 2015. 62(9). Pp. 636–644.
15. Valuyeva Ye.P., Purdin M.S. The pulsating laminar flow in a rectangular channel // Thermophysics and Aeromechanics. 2015. 22(6). Pp. 733–744.
16. Valuyeva Ye.P., Purdin M.S. An investigation into heat transfer for a pulsating laminar flow in a rectangular channel with a boundary condition of the first kind // High Temperature. 2017. № 4(55). Pp. 622–625.
17. Левцев А.П., Лапин Е.С. Эффективность секционных радиаторов при низких температурах теплоносителя // Города России: проблемы строительства, инженерного обеспечения, благоустройства и экологии: сб. ст. XX Междунар. науч.-практ. конф. Пенза: РИО ПГАУ, 2018. С. 72–76.
18. Левцев А.П., Лапин Е.С., Бикунова М.В., Салмин В.В. Конструктивны особенности и оценка работы оборудования для импульсной подачи теплоносителя // Региональная архитектура и строительство. 2018. № 4. С. 151–158.
19. Левцев А.П., Лапин Е.С. Использование энергоэффективного мембранного насоса в схеме индивидуального теплового пункта здания // Приволжский научный журнал. 2018. № 4. С. 53–59.
20. Пат. 183885 РФ, МПК F24D 3/0, F24D 3/02, Индивидуальный тепловой пункт с мембранным насосом / Левцев А.П., Лапин Е.С., Могдарев М.П.; заявитель и патентообладатель ФГБОУ ВО «Национальный исследовательский Мордовский государственный университет им. Н.П. Огарева». № 2018120830; заявл. 06.06.2018; опубл. 08.10.2018.
21. Левцев А.П. Импульсные системы тепло- и водоснабжения: монография / А. П. Левцев, А. Н. Макеев; под общ. ред. д-ра техн. наук проф. А.П. Левцева. Саранск: Изд-во Мордов. ун-та, 2015. 172 с.

Контактные данные:

Алексей Павлович Левцев, +7(906)1633200; эл. почта: levtzevap@mail.ru

Евгений Сергеевич Лапин, +7(902)6693219; эл. почта: evgeniy-lapin@yandex.ru

Цяньвень Чжан, +7(834)2254101; эл. почта: 543785883@qq.com



DOI: 10.18720/MCE.92.6

CFD simulation of the convective flows in the vertical caverns

M.R. Petrichenko, V.V. Sergeev, D. Nemova*, E.V. Kotov, D.S. Andreeva
Peter the Great St. Petersburg Polytechnic University, St. Petersburg, Russia
* E-mail: nemova_dv@spbstu.ru

Keywords: average velocity, building and construction, CFD, civil and structural engineering, enclosing structure, energy efficiency, heat-gravitational motion, CFD simulation, computational fluid dynamics simulations, residential building

Abstract. The purpose of this paper is determination the critical geometric dimensions of a three-dimensional vertical heated cavern. In this rate the convection's contribution to heat transfer will be limited due to thermal conductivity at a fixture temperature drop. The model validated and verified by comparison with the experimental results. A stable non-stationary flow regime is observed for Rayleigh number $Ra = 15,000$, because the temperature fields in different cross-sections of the flow coincide. For the flow with Rayleigh number $Ra = 15,000$, the nonstationary formulation without the turbulence model did not give the required convergence on residuals. So it was calculated by using the three-dimensional RANS approach closed with the k-w SST turbulence model. In this case the flow is unstable in the third direction, therefore it is impossible to consider the cavern as a heat insulator at numbers $Ra = 10,000$ and above.

1. Introduction

The thermal insulation of the building used in hinged ventilated facade is one of the main factors promoting decrease the thermal losses. However, the insulation eventually collapses under the influence of various phenomena, loses its integrity, structure and thermal insulation properties. In addition, thermal insulation materials for facade walls are quite expensive. In addition, the energy efficiency of the building can be improved using non-conventional energy sources [1].

One of the possibilities to exclude the use of thermal insulation materials in ventilated facade systems is the use of closed caverns in the air gap, which the geometric dimensions allows to minimize the contribution of air convection to heat transfer. Natural convection in between two vertical plates has been studied by many researchers under different types of boundary conditions on the channel walls in the presence or absence of channel's input and output effects. The main attention in the literature is paid to the case of lifting flow at symmetric heating of vertical plates.

J.L. Wright, H. Jin, K.G.T. Hollands, D. Naylor experimentally studied the natural convection of gas (air) at $Pr = 0.7$ in a vertical cavity with various heat aluminum walls. The flow was visualized using smoke and a laser light source [2].

In [3–6], considerable attention is paid to the stability of stationary convective flows. The authors have made many studies of flows between flat parallel walls. To simulate the flow and heat transfer of a liquid in a vertical channel, unsteady two-dimensional Navier-Stokes equations in the vorticity-current function variables were solved. There is a graph of the dependence of the minimum critical Grashof's number on the Prandtl number when the flow instability is observed. In [7], the authors studied the linear stability of the natural convection of a liquid between vertical plates of different temperatures using the collocation method. It was found that for $Pr < 12.45$ the critical Grashof's number is almost independent of the Prandtl number (for

Petrichenko, M.R., Sergeev, V.V., Nemova, D., Kotov, E.V., Andreeva, D.S. CFD simulation of the convective flows in the vertical caverns. Magazine of Civil Engineering. 2019. 92(8). Pp. 76–83. DOI: 10.18720/MCE.92.6

Петриченко М.Р., Сергеев В.В., Немова Д.В., Котов Е.В., Андреева Д.С. CFD-моделирование конвективных течений в вертикальных кавернах // Инженерно-строительный журнал. 2019. № 8(92). С. 76–83. DOI: 10.18720/MCE.92.6



$Pr = 0.71$ and $Pr = 7$ the field stability differs little, while for $Pr > 12.45$ the instability threshold depends noticeably on the Prandtl number).

The analysis of heat transfer performance of nanofluids for laminar flow was fully made with forced convection with two zones: one adiabatic and one with uniform wall heat flux. In particular, the heat transfer coefficient of water-based nanofluids is increased by 3.4–27.8% under fixed Reynolds number compared with that of pure water. Also, the enhancement of heat transfer coefficient is larger than that of the effective thermal conductivity at the same volume concentration [8–10].

A lot of research about convective heat transfer were conducted numerically [11–25].

However, to date, the prospects for the use of three-dimensional caverns in the air gap of ventilated facade systems have not been determined.

The purpose of this paper is determination the critical geometric dimensions of a three-dimensional vertical heated cavern. In this rate, the flow in the three-dimensional cavern will be close to the stationary and convection's contribution to heat transfer will be limited due to thermal conductivity at a fixture temperature drop. The results of the work can be applied by the development of ventilated facade systems. To achieve this goal, it is necessary to solve the following tasks:

1. To develop a mathematical model of a three-dimensional RANS approach closed with the k- ω SST turbulence model in conjunction with the energy equation

2. To perform numerical simulation in the ANSYS software package to determine the characteristics of the heat flow, and also for the validation and verification of the model by comparison with the experimental results

2. Materials and Methods

2.1. Mathematical model of flow in vertical heated cavern

To consider the air flow a rectangular area elongated in the vertical direction is selected (Figure 1). The ratio of height to width is varying in the range $A > 20$. On the side walls the constant temperature condition is set, the upper and lower walls are adiabatic.

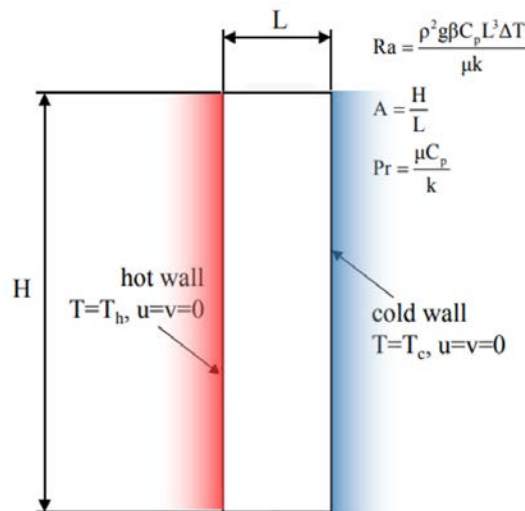


Figure 1. Computational domain for two-dimensional formulation.

Convection and heat transfer in the presented calculation described by Navier-Stokes equations in their non-stationary formulation taking into account the Boussinesq' approximation. In this case it reduces the problem to the calculation of incompressible fluid and gas flow in the presence of mass force proportional to the local temperature drop. We obtain the equations:

$$\nabla \cdot V = 0 \quad (1)$$

$$(V \nabla) V = \nu \nabla^2 \cdot V + g \beta T \gamma \quad (2)$$

$$V \nabla T = a \nabla^2 T \quad (3)$$

V is velocity of the liquid;

T is temperature;

- p is modified pressure;
- ρ is average density;
- g is acceleration of gravity;
- ν is coefficient of kinematic viscosity,
- a is coefficient of thermal conductivity;
- β is coefficient of volumetric expansion;
- γ is unit vector directed vertically upwards.

Introducing dimensionless variables: distance is h , time is h^2/ν , velocity is $g\beta\Delta Th^2/\nu$, temperature is ΔT (temperature difference), pressure is $pg\beta\Delta Th$, we obtain a system:

$$\nabla \cdot V = 0 \tag{4}$$

$$Gr[(V \nabla) V_0 + (V_0 \nabla) V] = \nabla^2 V + T \gamma \tag{5}$$

$$Gr [V \nabla T_0 + V_0 \nabla T] = 1/Pr \nabla^2 T \tag{6}$$

The velocity and temperature profiles of the main current in dimensionless variables V_0 and T_0 have the form:

$$V_0 = 1/6(x^2 - x), T_0 = -x \tag{7}$$

The problem contains two dimensionless parameters that determine the similarity of convective flows—the Grashof's and Prandtl number:

$$Pr = \nu/a, Gr = (g\beta\Delta TL^3)/\nu^2 \tag{8}$$

2.2. Numerical simulation of flow in vertical heated cavern

For the calculations, an area having a size of $L \times 20L \times 20L$ was chosen. The problem was solved in a dimensionless setting. Initially the calculations were performed in three-dimensional formulation for Rayleigh numbers $Ra = 7,300$ and $Ra = 15,000$. Calculations for Rayleigh numbers $Ra = 7,300$ are performed in a nonstationary laminar setting. Temperature fields in different sections of the computational domain are shown in Figure 2.

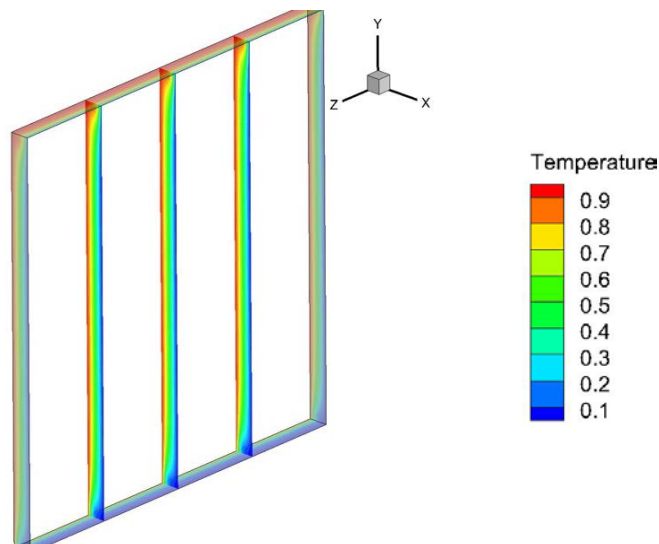


Figure 2. Temperature fields in different sections of the computational domain for Rayleigh numbers $Ra = 7,300$.

The three-dimensional calculation is performed to show that at Rayleigh number $Ra = 7,300$ the flow inside the cavern is stable in the third direction. This is evident from the temperature profiles in different sections. Similar results were obtained for the Rayleigh number $Ra = 10,000$. The current became unsteady, but was not changed in any section of XY. From this, we can conclude that for the calculation of flows with lower Rayleigh number we can limit ourselves to a two-dimensional formulation.

3. Results and Discussions

3.1. Results

The results of calculations are presented in the central vertical section of the calculated area for all the Rayleigh numbers considered, since the size of the calculated area in the third direction does not affect the obtained results (Figures 3–4).

Since at Rayleigh numbers below $Ra = 10,000$ the flow is stable in the third direction, it is possible to proceed to the two-dimensional formulation.

Figure 3 shows the longitudinal velocity fields depending on the Rayleigh number.

With an increase of the Rayleigh number, the flow becomes nonstationary but it remains two-dimensional.

The flow is two-dimensional and laminar for all considered flow regimes. Calculations for Rayleigh numbers $Ra = 6,800$ and $Ra = 7,300$ showed convergence only in non-stationary formulation.

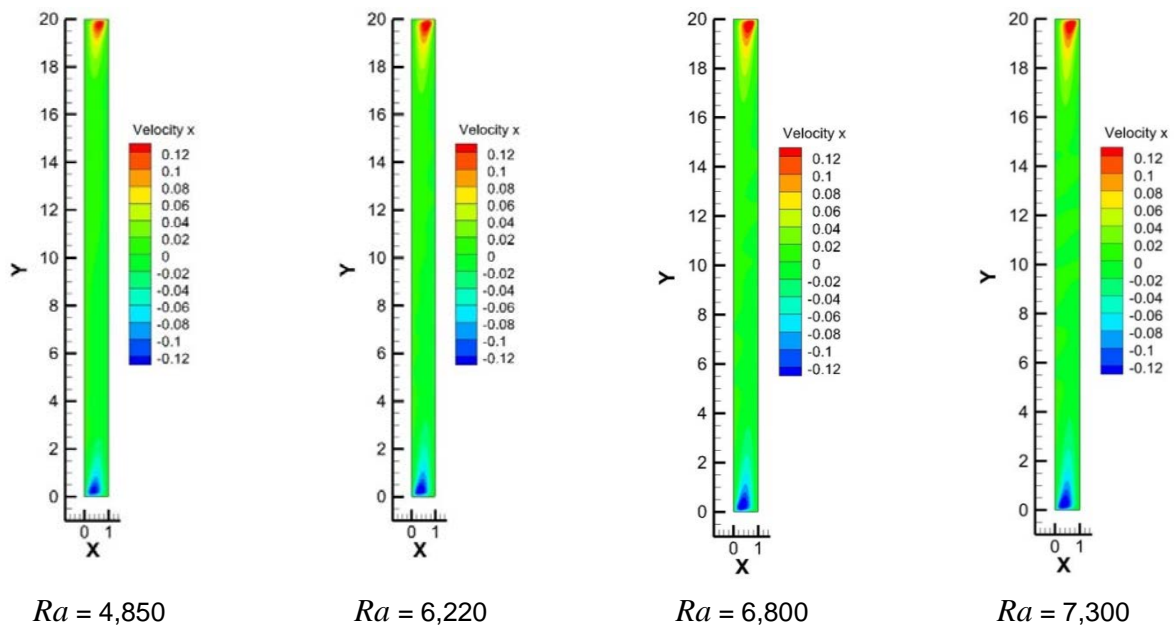


Figure 3. Fields of longitudinal velocity in the vertical cross-section of the calculated area for different Rayleigh numbers.

The temperature fields Rayleigh numbers less than $Ra = 10,000$ are qualitatively similar. The temperature field for $Ra = 4,850$ are shown in Figure 4.

It assumes that the heat transfer resistance of the cavity can be calculated as:

$$R = \delta/\lambda \quad (9)$$

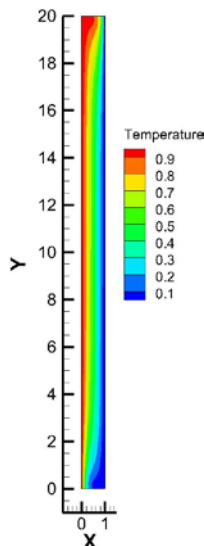


Figure 4. The temperature field for $Ra = 4,850$.

Since the critical Rayleigh number is known, at which there is no transition to a three-dimensional flow, it is possible to estimate the temperature difference on the walls that permissible for the operation of the cavern as a heat insulator:

$$\Delta T \leq 10000 (va/g\beta L^3) \quad (10)$$

As the number Ra increases, the linearity gradually disappears. The linearity limit is marked at $Ra = 10,000$.

If condition (5) is performed, the temperature distribution across the cavern is linear and the thermal resistance of the cavern is determined only by its thickness and the coefficient of molecular thermal conductivity of the air. Linear temperature profiles are shown at Figure 5.

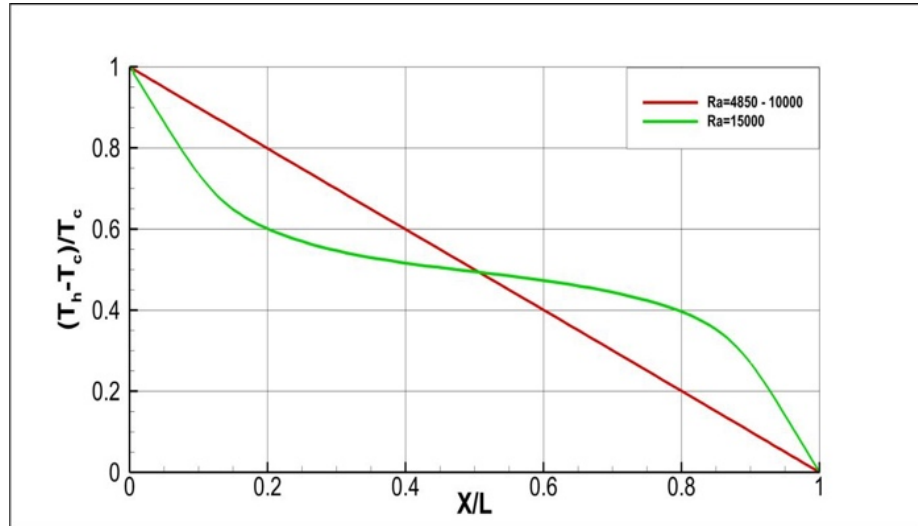


Figure 5. The linear temperature profiles.

If condition (5) is achieved, the cavern with air consider as a heat-conducting solid medium. It is possible to achieve the equivalence of its thermal properties to the insulation properties by varying the geometric dimensions of the cavern. Thus, these results can be applied in the design of facade systems by using a vertical cavern with air instead of insulation.

3.2. Discussion

Natural convection between two vertical plates was studied in the course of research by researchers under various types of boundary conditions on the channel walls. [2-6]. In this case, the main attention in the literature is given to the case of upward flow with symmetric heating of the plates.

J.L. Wright, H. Jin, K.G.T. Hollands, D. Naylor experimentally studied the natural convection of gas (air) at $Pr = 0.7$ in a vertical cavity with various heat aluminum walls. The flow was visualized using smoke and a laser light source [2].

The authors of the article varied the Rayleigh numbers in the range from $Ra = 4,800$ to $Ra = 54,800$, which made it possible to observe various flow regimes using smoke, shown in Figure 6:

- $Ra = 4,850-6,220$ is stable stationary mode. The course was slow and stable, no secondary structures were observed.
- $Ra = 6,800$ is the appearance of secondary currents. The authors, relying on the formulas for their experiment, calculated that the critical number would be $Rac = 6,376$. But the secondary current was observed at $Ra = 6,819$. The secondary currents rotated together with the primary, they were stable with the exception that the secondary elements moved slowly.
- $Ra = 7,300-8,600$ is steady non-stationary mode. The flow pattern in this range of Rayleigh numbers is similar to the flow structure at $Ra = 6,800$. With an increase in Ra from 7,300 to 8,600, the flow pattern changed and developed as follows: a) the primary flow moves closer to the walls and the speed of the primary flow increases; b) everything continues to rotate together with the primary stream. Secondary currents move downward, increasing in size with increasing Ra ; c) small fluctuations were observed over time; d) the shape of the secondary currents became more rounded, while at $Ra = 6,800$ they looked like elongated ovals.

- $Ra = 9,600–10,500$ is secondary currents formed in non-stationary mode. With an increase in the Rayleigh number to approximately $Ra = 104$, the flow in the core became unstable, namely, the flow structure is often disturbed by the movements of the secondary currents. The resulting structures moved and rotated faster, so the direction of flow was no longer always from the bottom up or vice versa (it was sometimes observed that two vortices usually moved in opposite directions, to opposite walls). It was also observed in the experiment that the structures suddenly began to disappear from the plane of the laser light, making it possible to conclude that with increasing Ra the flow becomes three-dimensional.
- $Ra = 11,600–12,600$ is three-dimensional flow. The direction of motion of the vortices was generally chaotic. It was obvious that the flow in this range is three-dimensional, but the magnitude of the vortices in the third direction in such a narrow cavity was small compared with the movement in the vertical direction.
- $Ra = 13,600–54,800$ is transition to a fully turbulent flow. It was found that the magnitude of the vibrations of three-dimensional vortices increased with increasing Ra . The flow became more and more chaotic, turbulent, secondary structures moved faster and more vigorously than usual

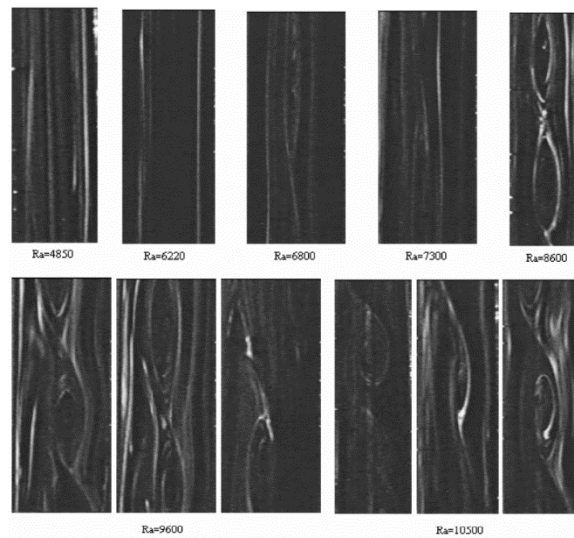


Figure 6. Flow pattern at different Ra numbers.

In [34], considerable attention was paid to the stability of stationary convective flows. The authors have done many studies of flows between flat parallel walls. To simulate the flow and heat transfer of a liquid in a vertical channel, unsteady two-dimensional Navier – Stokes equations were solved in vorticity variables — the stream function.

4. Conclusion

It can be concluded from the obtained results:

1. A stable non-stationary flow regime is observed for such Rayleigh number, because the temperature fields in different cross-sections of the flow coincide.

For the flow with Rayleigh number $Ra = 15,000$, the nonstationary formulation without the turbulence model did not give the required convergence on residuals. So it was calculated by using the RANS approach closed by the k-w SST turbulence model. In this case the flow is unstable in the third direction, therefore it is impossible to consider the cavern as a heat insulator at numbers $Ra = 10,000$ and above.

2. A long narrow channel, viscous free-convective flow-over approximated by two-dimensional over.

3. The stability of the flow in vertical cavern with symmetric conditions is proved.

4. The occurrence of the circulation flow is due to the asymmetry of the limiting temperature conditions at the ends of the cavern.

5. Thus, in conditions of low-Reynolds viscous flow, the cavern plays the role of a thermal insulator with thermal resistance h/λ , where λ is the coefficient of thermal conductivity of air.

6. If condition $\Delta T \leq 10000 (va/g\beta L^3)$ is performed, the temperature distribution in the cavern is linear and the thermal resistance of the cavern is determined only by its thickness and the coefficient of molecular thermal conductivity of the air.

7. If condition $\Delta T \leq 10000 (va/g\beta L^3)$ is achieved, it is possible to consider the cavern with air as a heat-conducting solid medium. By varying the geometric dimensions of the cavern, it is possible to achieve the equivalence of its thermal properties to the insulation properties. Thus, these results can be applied in the design of facade systems by using the vertical cavern with air instead of insulation.

References

- López-Ordóñez, C.F., Roset, J., Rojas-Cortorreal, G. Analysis of the direct solar radiation in the streets of barcelona, based on the relation between its morphology and vegetation [Análisis de la radiación solar directa en las calles de barcelona, en base a la relación entre su morfología y vegetación]. *Architecture, City and Environment*. 2017. 12(34). Pp. 45–68. DOI: 10.5821/ace.12.34.4708
- Wright, J.L., Jin, H., Hollands, K.G.T., Naylor, D. Flow visualization of natural convection in a tall, air-filled vertical cavity. *International Journal of Heat and Mass Transfer*. 2006. 49(5-6). Pp. 889–904. DOI: 10.1016/j.ijheatmasstransfer.2005.06.045
- HoPper, D., Jaganathan, D., Orr, J.L., Shi, J., Simeski, F., Yin, M., Liu, J.T.C. Heat transfer in nanofluid boundary layer near adiabatic wall. *Journal of Nanofluids*. 2018. 7(6). Pp. 1297–1302. DOI: 10.1166/jon.2018.1551
- Lewandowski, W.M., Rymys, M., Denda, H. Natural convection in symmetrically heated vertical channels *International Journal of Thermal Sciences*. 2018. 134. Pp. 530–540. DOI: 10.1016/j.ijthermalsci.2018.08.036
- Amala, S., Mahanthesh, B. Hybrid nanofluid flow over a vertical rotating plate in the presence of hall current, nonlinear convection and heat absorption *Journal of Nanofluids*. 2018. 7(6). Pp. 1138–1148. DOI: 10.1166/jon.2018.1550
- Leporini, M., Corvaro, F., Marchetti, B., Polonara, F., Benucci, M. Experimental and numerical investigation of natural convection in tilted square cavity filled with air. *Experimental Thermal and Fluid Science*. 2018. 99. Pp. 572–583. DOI: 10.1016/j.exptthermflusci.2018.08.023
- Minea, A.A., Murshed, S.M.S. A review on development of ionic liquid based nanofluids and their heat transfer behavior. *Renewable and Sustainable*. 2018. *Energy Reviews*. 91. Pp. 584–599. DOI: 10.1016/j.rser.2018.04.021
- Chereches, E.I., Sharma, K.V., Minea, A.A. A numerical approach in describing ionanofluids behavior in laminar and turbulent flow *Continuum Mechanics and Thermodynamics*. 2018. 30(3). Pp. 657–666. DOI: 10.1007/s00161-018-0634-x
- Minea, A.-A., El-Maghlany, W.M. Natural convection heat transfer utilizing ionic nanofluids with temperature-dependent thermophysical properties *Chemical Engineering Science*. 2017. 174. Pp. 13–24. DOI: 10.1016/j.ces.2017.08.028
- Gorshkov, A.S., Vatin, N.I., Rymkevich, P.P., Kydrevich, O.O. Payback period of investments in energy saving *Magazine of Civil Engineering*. 2018. 78(2). Pp. 65–75. DOI: 10.18720/MCE.78.5
- Ananin, M., Perfilyeva, N., Vedishcheva, I., Vatin, N. Investigation of different materials usage expediency for a low-rise public building from the energy efficiency standpoint *IOP Conference Series: Materials Science and Engineering*. 2018. 365(2). DOI: 10.1088/1757-899X/365/2/022014
- Chechevichkin, A.V., Vatin, N.I., Samonin, V.V., Grekov, M.A. Purification of hot water by zeolite modified with manganese dioxide. *Magazine of Civil Engineering*. 2017. 76 (8). Pp. 201–213. DOI: 10.18720/MCE.76.18
- Khrapunov, E.F., Chumakov, Y.S. Unsteady processes in a natural convective plume. *Journal of Physics: Conference Series*. 2018. 1038(1). DOI: 10.1088/1742-6596/1038/1/012132
- Yaroslavtseva, N.A., Ivanov, N.G. Numerical simulation of natural convection in wedge-shaped domain with isothermal free surface. *Journal of Physics: Conference Series*. 2017. 929(1) DOI: 10.1088/1742-6596/929/1/012097
- Khrapunov, E.F., Potechin, I.V., Chumakov, Y.S. Structure of a free convective flow over a horizontal heated surface under conditions of conjugate heat transfe. *Journal of Physics: Conference Series*. 2017. 891(1) DOI: 10.1088/1742-6596/891/1/012081
- Kharkov, N.S. Nonstationary heat and mass transfer in the multilayer building construction with ventilation channels. *Journal of Physics: Conference Series*. 2017. 891(1). DOI: 10.1088/1742-6596/891/1/012116
- Vitokhin, E.Y., Ivanova, E.A. Dispersion relations for the hyperbolic thermal conductivity, thermoelasticity and thermoviscoelasticity. *Continuum Mechanics and Thermodynamics*. 2017. 29(6). Pp. 1219–1240. DOI: 10.1007/s00161-017-0574-x
- Statsenko, E.A., Musorina, T.A., Ostrovaia, A.F., Olshevskiy, V.Ya., Antuskov, A.L. Moisture transport in the ventilated channel with heating by coil. *Magazine of Civil Engineering*. 2017. 70(2). Pp. 11–17. DOI: 10.18720/MCE.70.2
- Loktionova, E.A., Malyshevsky, D.Y., Schemelinin, D.I., Zaborova, D.D. Vertical distribution of compact air jets in the hall of an ice arena. *Advances and Trends in Engineering Sciences and Technologies II - Proceedings of the 2nd International Conference on Engineering Sciences and Technologies, ESaT 2016*. 2017. Pp. 531–536.
- Musorina, T., Olshevskiy, V., Ostrovaia, A., Statsenko, E. Experimental Assessment of Moisture Transfer in the Vertical Ventilated Channel *MATEC Web of Conferences*, 2016. 73. No. 02002. DOI: 10.1051/mateconf/20167302002
- Sorokins, J., Borodinecs, A., Zemitis, J. Application of ground-to-air heat exchanger for preheating of supply air. *IOP Conference Series: Earth and Environmental Science*. 2017. 90(1). DOI: 10.1088/1755-1315/90/1/012002
- Ovchinnikov, P., Borodinecs, A., Strelets, K. Utilization potential of low temperature hydronic space heating systems: A comparative review. *Building and Environment*. 2017. 112. Pp. 88–98. DOI: 10.1016/j.buildenv.2016.11.029
- Baranova, D., Sovetnikov, D., Semashkina, D., Borodinecs, A. Correlation of energy efficiency and thermal comfort depending on the ventilation strategy. *Procedia Engineering*. 2017. 205. Pp. 503–510. DOI: 10.1016/j.proeng.2017.10.403
- Sánchez, M.N., Giancola, E., Blanco, E., Soutullo, S., Suárez, M.J. Experimental validation of a numerical model of a ventilated façade with horizontal and vertical open joints. *Energies*. 2019. 13(1). DOI: 10.3390/en13010146
- Soutullo, S., Sánchez, M.N., Enríquez, R., Olmedo, R., Jimenez, M.J. Bioclimatic vs conventional building: Experimental quantification of the thermal improvements. *Energy Procedia*. 2017. 122. Pp. 823–828. DOI: 10.1016/j.egypro.2017.07.413
- Kosutova, K., van Hooff, T., Vanderwel, C., Blocken, B., Hensen, J. Cross-ventilation in a generic isolated building equipped with louvers: Wind-tunnel experiments and CFD simulations. *Building and Environment*. 2019. 154. Pp. 263–280. DOI: 10.1016/j.buildenv.2019.03.019
- Saadatian, O., Sopian, K., Lim, C.H., Asim, N., Sulaiman, M.Y. Trombe walls: A review of opportunities and challenges in research and development. *Renewable and Sustainable Energy Reviews*. 2012. 16(8). Pp. 6340–6351. DOI: 10.1016/j.rser.2012.06.032
- Evins, R. A review of computational optimisation methods applied to sustainable building design. *Renewable and Sustainable Energy Reviews*. 2013. 22. Pp. 230–245. DOI: 10.1016/j.rser.2013.02.004

29. Ramponi, R., Blocken, B. CFD simulation of cross-ventilation flow for different isolated building configurations: Validation with wind tunnel measurements and analysis of physical and numerical diffusion effects. *Journal of Wind Engineering and Industrial Aerodynamics*. 2012. 104-106. Pp. 408–418. DOI: 10.1016/j.jweia.2012.02.005
30. Jomehzadeh, F., Nejat, P., Calautit, J.K., Yusof, M.B.M., Zaki, S.A., Hughes, B.R., Yazid, M.N.A.W.M. A review on windcatcher for passive cooling and natural ventilation in buildings, Part 1: Indoor air quality and thermal comfort assessment. *Renewable and Sustainable Energy Reviews*. 2017. 70. Pp. 736–756. DOI: 10.1016/j.rser.2016.11.254
31. Wang, Y., Shukla, A., Liu, S. A state of art review on methodologies for heat transfer and energy flow characteristics of the active building envelopes. *Renewable and Sustainable Energy Reviews*. 2017. 78. Pp. 1102–1116. DOI: 10.1016/j.rser.2017.05.015
32. Santiago, J.-L., Rivas, E., Sanchez, B., Buccolieri, R., Martin, F. The impact of planting trees on NOx concentrations: The case of the Plaza de la Cruz neighborhood in Pamplona (Spain). *Atmosphere*. 2017. 8(7). DOI: 10.3390/atmos8070131
33. Fantucci, S., Serra, V. Investigating the performance of reflective insulation and low emissivity paints for the energy retrofit of roof attics. *Energy and Buildings*. 2019. 182. Pp. 300–310. DOI: 10.1016/j.enbuild.2018.10.003
34. Rebinder, P.A. *Izbrannyye trudy. Poverkhnostnyye yavleniya v dispersnykh sistemakh. Fiziko-khimicheskaya mekhanika* [Selected works. Surface phenomena in disperse systems. Physico-chemical mechanics]. Moscow: Nauka, 1991. 384 p.
35. Polubarinova Cochina, P.Y. *Izbrannyye trudy. Gidrodinamika i teoriya fil'tratsii* [Selected works. Fluid flow and filtration theory]. Moscow: Nauka, 1991. 353 p.

Contacts:

Mikhail Petrichenko, +7(921)3300429; fonpetrich@mail.ru

Vitaly Sergeev, +7(921)9805437; sergeev_vitaly@mail.ru

Darya Nemova, +7(921)8900267; nemova_dv@spbstu.ru

Evgeny Kotov, +7(921)3461312; ekotov.cfd@gmail.com

Darya Andreeva, +7(931)2564594; tarasovads@gmail.com

© Petrichenko M.R., Sergeev V.V., Nemova D., Kotov E.V., Andreeva D.S., 2019



DOI: 10.18720/MCE.92.7

Timber frame buildings with efficient junction designs for earthquake-prone areas

T.A. Belash*, **Zh.V. Ivanova**

Petersburg State Transport University, St. Petersburg, Russia

** E-mail: belashta@mail.ru*

Keywords: low-rise buildings, timber structures, earthquake resistance, timber frame buildings, design and experimental studies

Abstract. The object of the study is a timber building of frame type, consisting of timber vertical posts, lower and upper binding, a system of connections (horizontal and vertical), elements of overlap and coating (roof). The impact of an earthquake of different intensity and frequency on the seismic resistance of a timber building is considered. Seismic stability was assessed on the basis of experimental and theoretical studies. Experimental methods were performed on laboratory facilities and large-scale models. Taking into account the experimental data obtained, the calculation and theoretical evaluation of the frame building on simple and complex models under the influence of different intensity and frequency composition was performed. It is established that the frequency composition of seismic impact significantly affects the seismic resistance of frame buildings. It is recommended when designing these buildings to assign their dynamic parameters (period of natural oscillations) depending on the forecast of the prevailing period of seismic oscillations of the construction area, which will more effectively solve the layout of the nodal joints of the frame. It is recommended to introduce additional materials and devices having pliability and high dissipative properties into nodal connections.

1. Introduction

Currently, the use of timber structures in earthquake-resistant buildings is getting more widespread in buildings for various purposes. This is primarily due to the specific properties of the material from which the building structures are made. As is known, the benefits of wood structures include: low weight, low coefficient of thermal expansion, resistance to chemical media, good transportability, cheaper than steel and reinforced concrete, and less labor-consuming than steel and reinforced concrete. However, their disadvantages include flammability, deformability and decay. These properties are usually taken into account in for the design and construction of timber buildings.

Today the range of timber building materials contains dozens of items. The most popular among them are frame products, which are embodied in various civil building designs. Popularity of this type of timber structures is mainly associated with more rational consumption of timber and ability to ensure high energy performance during building operation. In addition, no hoisting machinery is required for construction of such buildings. This is the reason why timber frame buildings have become widely spread in various climatic regions, including those with complicated geological and seismic conditions both in Russia and abroad. The fundamental constructive solution of this building is shown in Figure 1.

The short-term development program adopted in Russia is intended to increase the construction of lightweight frame structures by a factor of 4 times or more. In the USA, more than 80 % of newly built timber houses are of frame type. This type of timber buildings is widely accepted in such seismically active countries as China and Japan. Publications of many Russian and foreign professionals [1–4] describe the main reasons why these buildings are so popular in seismic areas. First of all, they include the following: potential development of plastic deformations in the considered structural solutions; significant yielding that allows to

Belash, T.A., Ivanova, Zh.V. Timber frame buildings with efficient junction designs for earthquake-prone areas. Magazine of Civil Engineering. 2019. 92(8). Pp. 84–95. DOI: 10.18720/MCE.92.7

Белаш Т.А., Иванова Ж.В. Деревянные здания каркасного типа с эффективными конструкциями узловых соединений для сейсмически активных районов // Инженерно-строительный журнал. 2019. № 8(92). С. 84–95. DOI: 10.18720/MCE.92.7



This work is licensed under a [CC BY-NC 4.0](https://creativecommons.org/licenses/by-nc/4.0/)

accommodate earthquake loads; structures of this type also have a good capability to damp arising vibrations, etc. Seismic resistant behavior of these buildings during earthquakes is confirmed by the survey of timber frame buildings after Kemino-Chui earthquake in 1938 [5], Fukuisk earthquake in 1948 [6], the Chkhaltinsky earthquake in 1963 [5] and others. It should be noted that the buildings examined after Chkhaltinsky earthquake were erected on flexible posts from 1.5 m to 1.8 m high [5].

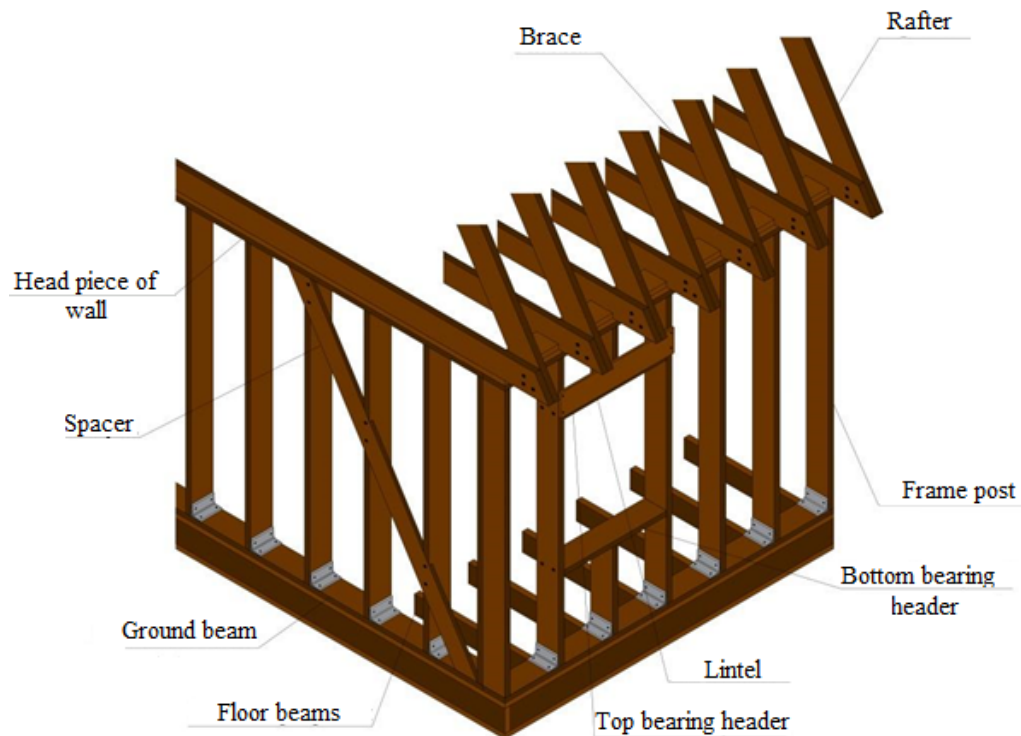


Figure 1. Timber framework arrangement.

In current earthquake-resistant timber frame construction industry, certain design approaches for these buildings are in place, including the following measures. The main frame studs and braces shall be secured to the ground beam using anchor bolts and metal plates (clamps) made of strip steel securely embedded in the foundation (Figure 2, a-c). Fastening to interfloor plates is made using drift bolts similar to fastening of interfloor beams to intermediate posts (Figure 2, d). Building stiffness is achieved using oblique siding of the frame wall structure. Nails, clamps and pads [3] shall be used to joint frame components in the nodes.

However, despite the set of the above listed structural measures, timber frame buildings can be severely damaged during earthquakes. This is primarily due to the fact that the seismic impact spectrum contains different frequency components, which, on the one hand, are not dangerous for this type of buildings that was confirmed by the investigation of strong earthquakes (examples of which are listed above), and on the other hand, seismic impacts may contain low-frequency components which cause serious oscillation buildup in the frame building.

Figure 3 shows examples of such destructive impacts caused mainly by the failure of frame nodes as result of large displacements of the foundation. As described in [7–10], in two-storey buildings, the weakened ground floors were damaged or completely destroyed, while the upper floors remained undamaged. A frequent type of damage in these buildings is the lack of a strong bracing between the timber portion and foundation. Significant damage and failure occur in stub-in and mortise joints.

The review of theoretical and experimental studies of timber frame buildings conducted in the recent years by many authors, including the authors of this publication, in Russia and abroad [11–64] shows their significance and scale. Meanwhile, to assess the real picture of the stress-strain condition of timber frame buildings based on the elastic and dissipative properties of nodes, as well as on the accumulated experience of behavior of these buildings during various types of earthquakes, additional studies and updates are required using new software packages and advanced experimental facilities.

On the basis of the above, the object of the study is a timber framework building of civil purpose, in which the main attention is paid to the structural work of node joints under seismic impacts taking into account the peculiarities of their manifestation, namely various effects of frequency character and its intensity. Various rigid and dissipative parameters of the timber frame are considered, taking into account which the complete assessment of seismic resistance of the building as a whole was carried out.

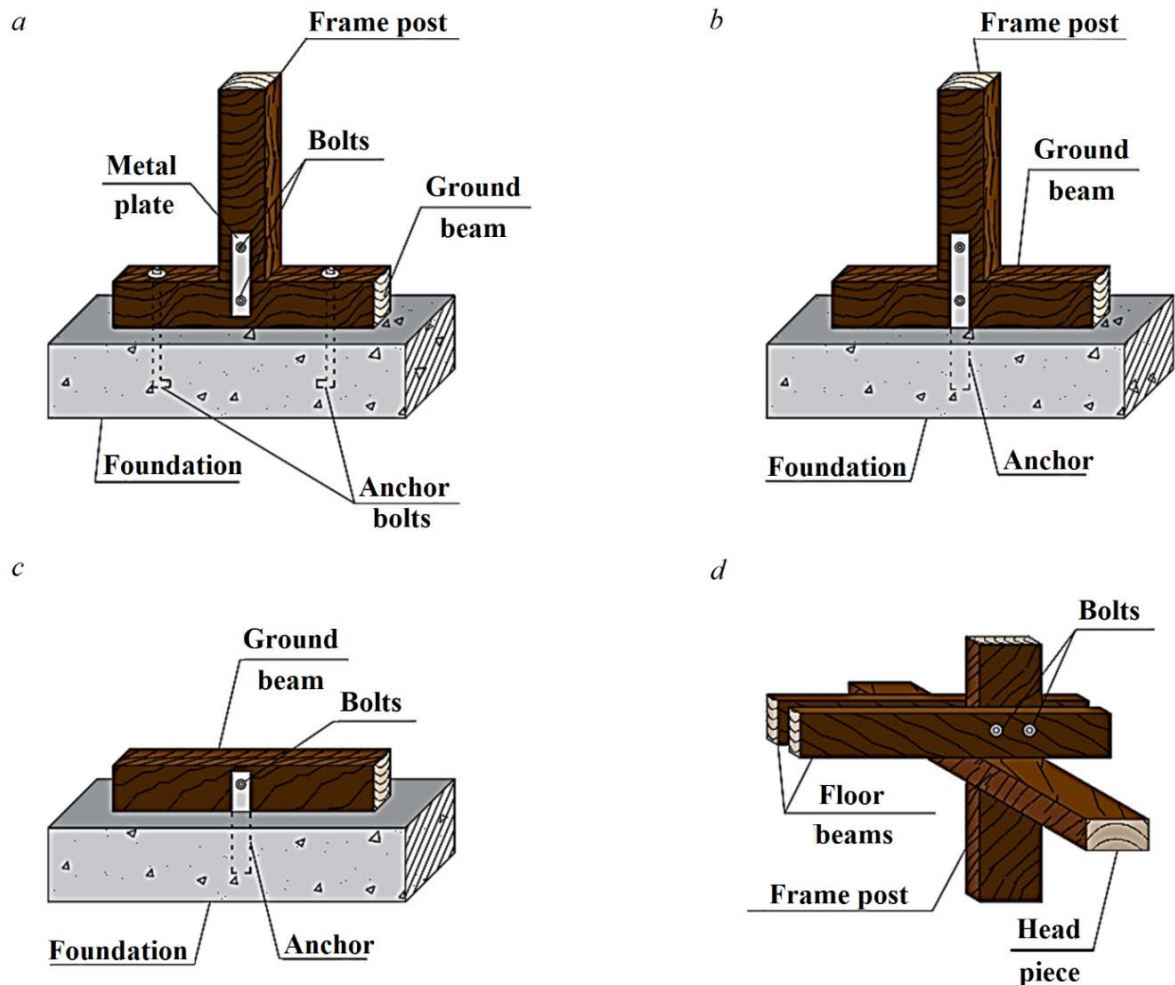


Figure 2. Connection options: between frame building studs and ground beam at the intersections of walls (a, b) and in intervals (c); floor beam-to-post joint (d).

It should be noted that earlier studies in Russia and abroad did not fully take into account the above-mentioned factors, both at seismic impacts and at various design solutions of timber frame buildings. In the normative practice, there are practically no recommendations on the design of timber frame buildings.

In this connection, the results of the studies presented in this article make it possible to estimate more objectively the seismic resistance of such buildings in seismic areas and thus to expand the possibility of their use.

2. Method

For real assessment of stress-strain condition of timber frame buildings, a set of experimental studies was carried out, which included two test stages.

At the first stage, mechanical and dissipative properties of the main members and nodes of a timber frame building were assessed. The test was carried out on various versions of frame post-to-beam nodes and on wall segments. The studies were carried out using dedicated laboratory facilities and included static and dynamic loading stages. Dynamic loading was applied using short-term and long-term cyclic load at forced oscillations with a frequency of 3Hz, 5Hz and 8Hz. Examples of the design versions of the "post – beam" test nodes with various dowel connection options are shown in Figure 4. A general view of the test facilities is shown in Figure 5. The wall was assumed with a post-to-post width of 1.2 m and a height of 3 m per floor (Figure 6). The wall test included the assessment of damping properties of the structure by logarithmic decrement and natural vibration frequency, and quasistatic bend test of the wall also performed. Bearing capacity of the structure was evaluated based on the test results.



Figure 3. Examples of timber frame building failures: a – March 1970 Geiz (Turkey) [8–9]; b – earthquake in San Francisco (USA) in 1989; c – earthquake in Norwich, California (USA), in 1994 [10]; d – earthquake in Kumamoto (Japan) in April, 2016 [7].

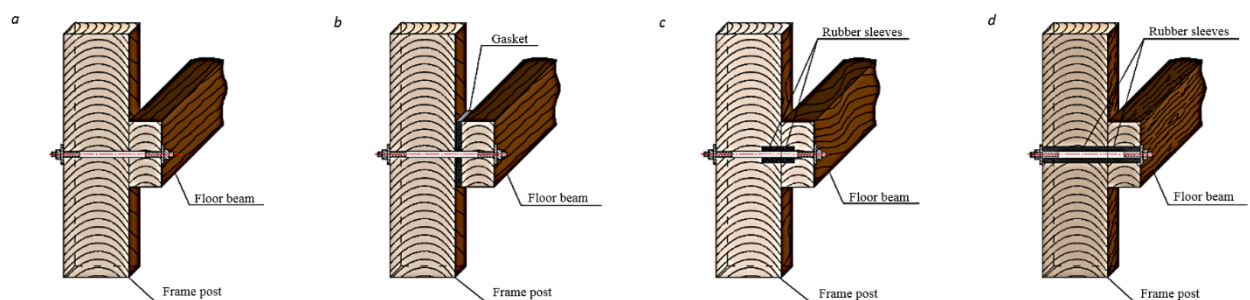


Figure 4. Versions of the test models of "post – beam" nodes: a – dowel connection version; b – gasket made various materials (steel, rubber) is installed between the post and a beam; c – using a rubber sleeve with a length equal to 1/3 length of the node components; d – using a rubber sleeve with a length equal to the entire length of the node components.

At the second stage, the obtained characteristics and parameters were checked, updated and used to develop final recommendations for evaluation of timber frame building performance. The study was carried out on a large-scale model of a frame building, a general view of which is shown in Figure 7. The tests were carried out on a specially designed bench capable of accommodating items with horizontal dimensions of 7.0 m x 2.5 m and a height up to 6.0 m. Cable sensors were used to record the movements of the model. Data collection, recording and control were carried out using a dedicated system with a capacity of 64 channels installed at the test bench.

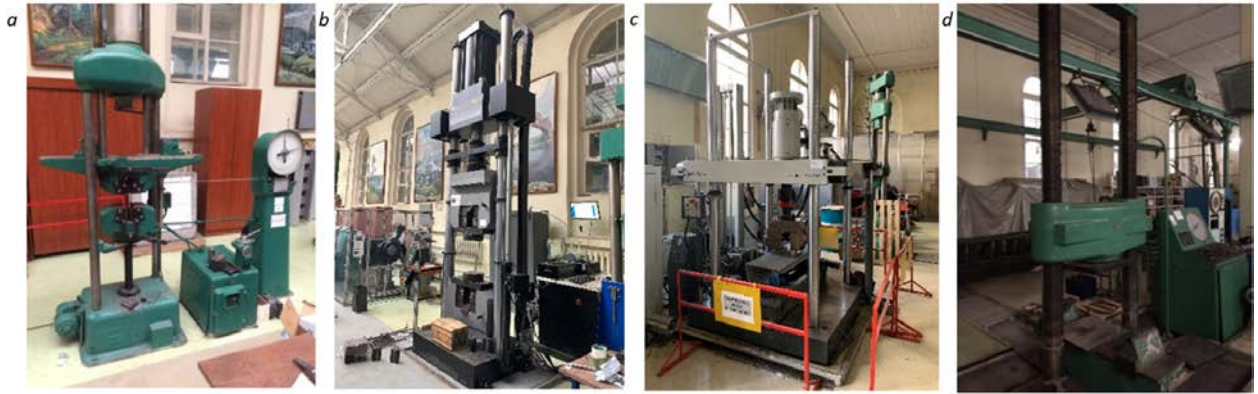


Figure 5. General view of the installations: a – TsDM-30 general-purpose machine (Germany); b – HB-250 testing machine (pulsator) (Germany); c – general-purpose static test machine with SATEC 1200KN-J3D hydraulic drive (USA); d – PPM-250 universal press (Russia).

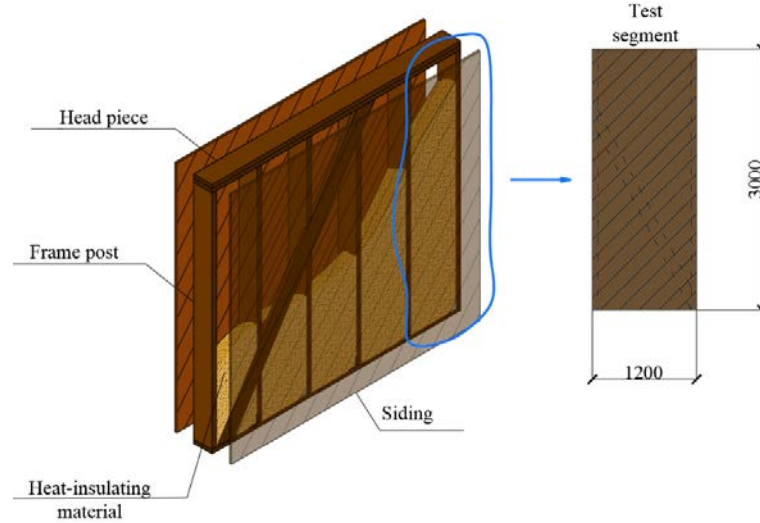


Figure 6. General view of the wall and test segment.



Figure 7. General view of the model mounted on the test bench.

The experimental studies were used to conduct a theoretical analysis of the behavior of this type of timber buildings. The studies were carried out according to the specified method using the spectral calculation and dynamic methods for actual earthquake accelerograms. Examples of calculation models used for the analysis are shown in Figure 8.

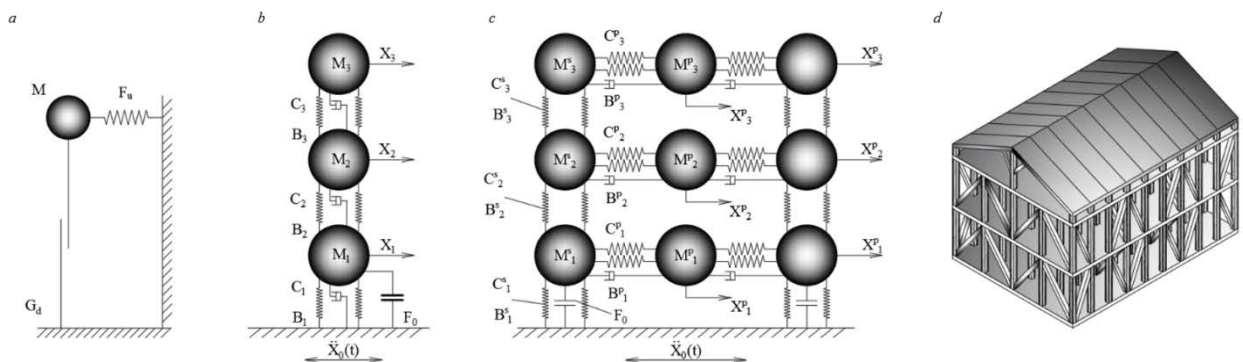


Figure 8. Design models of the building: a – single-mass nonlinear oscillator; b – basic linear model; c – building model with yielding bracing; d – three-dimensional finite element model.

As the initial object, a two-storey frame building was adopted with natural period of oscillations within 0.1 sec. During the study, the stiffness parameters of the building were varied. To consider foundation yielding, spring elements were included in the calculation model, stiffness factors of which corresponded to various soil conditions. In previous studies, the authors showed the need for yielding in frame nodes [4, 58, 60]. In this regard, when performing further studies, additional yielding parameters and damping factors were included in the elastic restraints between the floors and frame. To perform dynamic calculations, accelerograms of strong earthquakes with a fairly wide frequency range were selected. Dynamic calculations were performed by numerical integration according to the 4th order Runge-Kutta method. Three-dimensional performance test of the building was carried out by the finite element method using COSMOS V.2.9 software package.

3. Results and Discussions

The results of the studies are partially reflected in the publications by the authors [57–60]. It should be noted that the actual behavior of a timber frame building during earthquakes essentially depends on the design of all nodes which, on the one hand, must have a certain yielding and stiffness and, on the other hand, have sufficiently high potential dissipative properties that limit dangerous displacements during low-frequency impacts. Some results of experimental studies are shown in the form of diagrams in Figure 9.

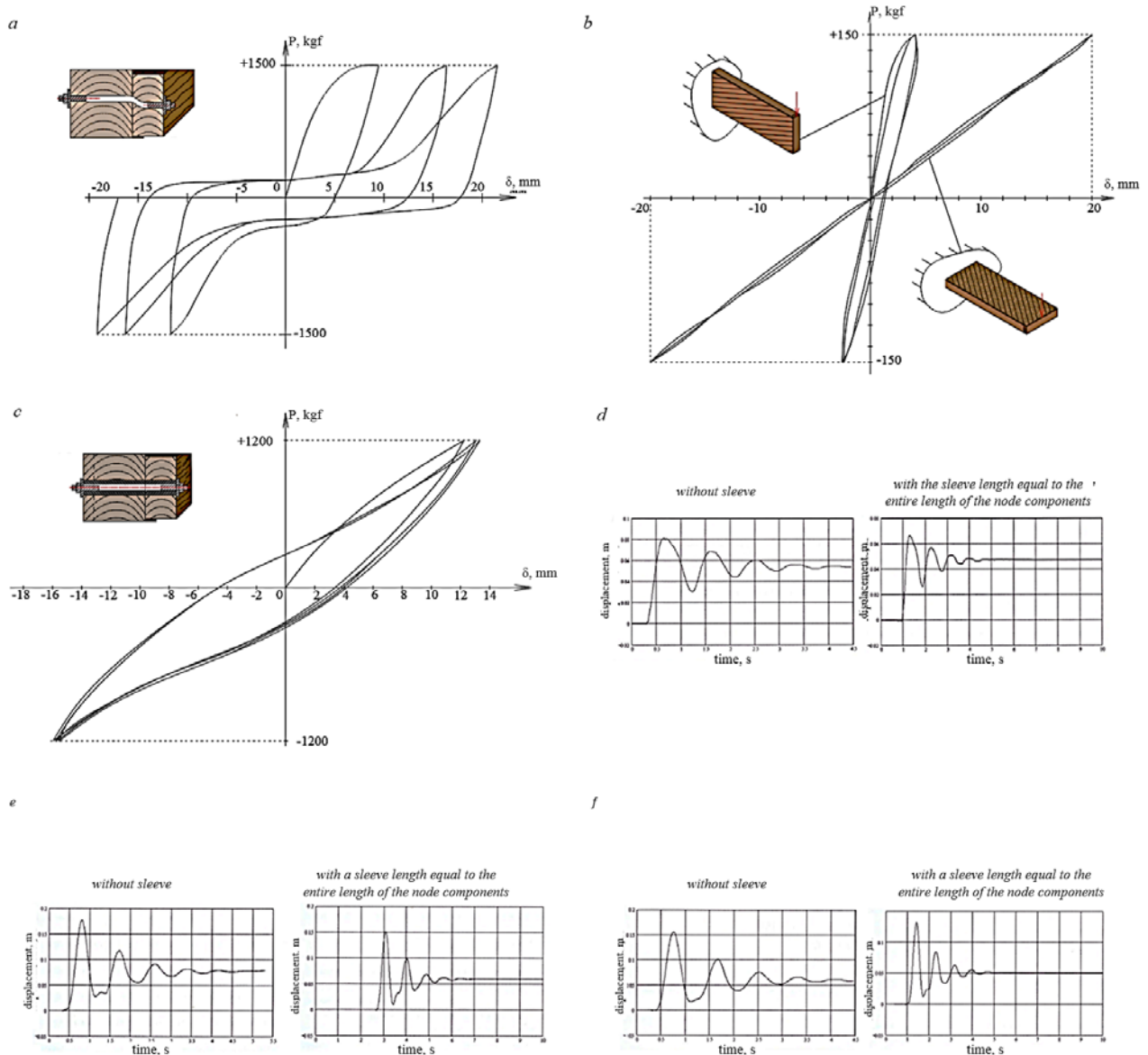


Figure 9. The results of experimental studies: a – «post – beam» node strain diagram; b – wall bending strain diagram; c – «post – beam» node strain diagram with a sleeve length equal to the entire length of the element; d – vibration mode (at the framing beam level) of the timber frame building foundation when exposed to magnitude 8; e – vibration mode of the upper part of the building when exposed to magnitude 8; f – vibration mode of the upper part of the building when exposed to magnitude 9.

During the experimental study, various designs of the main nodes such as «post – beam» nodes were used. The experimental studies have shown that rubber sleeves of various lengths inserted in the nodes

changed the stress-strain condition of the node as compared to a traditional dowel joint. So, compression of timber in the initial hole without a rubber sleeve ranged from 2 mm to 3 mm, while no compression occurred when a rubber sleeve was inserted.

The results of the theoretical analysis of the seismic resistance of timber frame buildings confirm the results of the previous studies of the impact of yielding and dissipative properties of components materials on the stress-strain condition of timber structures under earthquake loads with various frequency content. For this, it is necessary to ensure a reasonable relationship between the period of natural vibration of the building and the prevailing period of earthquake when assigning certain parameters of vibration damping to the building structures. So, to reduce the earthquake load by a factor of 2 or more, it is necessary to ensure a natural vibration period of the building in the range from 0.8 s to 1 s, which is achieved by certain yielding of the attachment nodes of floors and frame posts. The introduction of additional elements, for example, the use of rubber sleeves, etc., allows you to achieve the desired result. At the same time, the deformability of the nodes shall be at least 6 cm to 10 cm.

The results obtained allow us to conclude that the proposed structural solutions of nodal connections are highly efficient compared with existing proposals presented in [62–64].

4. Conclusion

1. The stress-strain condition of timber frame buildings during earthquakes significantly depends on the nature of the seismic impact and its frequency content which has a significant influence on its seismic resistance.

2. For design of timber frame buildings in areas of seismic activity, it is recommended to assign the fundamental period the building depending on the predicted prevailing period of seismic vibrations in the construction area.

3. In the case of strongly pronounced high-frequency vibrations, the frame nodes shall include yielding components such as rubber gaskets. For low-frequency impacts, dangerous movements arising from these vibrations shall be preferably limited by the insertion of additional components with enhanced dissipative properties. For this special materials or damping devices may be used.

4. When data on the frequency content of seismic impacts to reduce seismic loads by a factor of 2 or more are not available, the yielding parameters of support anchors shall be assigned based on the natural vibration period of the building, which shall be in range from 0.5 s to 0.8 s, while the deformability of the nodes shall be at least 6 cm.

5. The performed studies confirmed the results previously obtained by the authors regarding the influence of design of timber frame building nodes and dissipative properties of building materials on the stress-strain condition of timber structures under seismic loads. In this regard, it is recommended that the most careful approach be used when designing frame nodes and selecting the best materials and products for them.

References

1. Kirkham, W.J., Gupta, R., Miller, T.H. State of the art: Seismic behavior of wood-frame residential structures. *Journal of Structural Engineering* (United States). 2014. 4(140). Pp. 1–19. DOI: 10.1061/(ASCE)ST.1943-541X.0000861.
2. Falk, R.H., Soltis, L.A. Seismic behavior of low-rise wood-framed buildings. [Online]. URL: <https://www.fpl.fs.fed.us/documnts/pdf/1988/falk88b.pdf> (date of application: 02.09.2019).
3. Martemyanov, A.I. *Proektirovanie i stroitel'stvo zdaniy i sooruzhenij v sejsmicheskikh rajonah* [Design and construction of buildings and structures in seismic areas]. M.: Stroyizdat, 1985. 255 p. (rus)
4. Belash, T.A., Ivanova, Zh.V. *Issledovanie sejsmostojkosti derevyannyh zdaniy* [Study of earthquake resistance of timber buildings]. *Sejsmostojkoe stroitel'stvo. Bezopasnost' sooruzhenij*. 2003. No. 2. Pp. 28–31. (rus)
5. Polyakov, S.V. *Posledstviya sil'nyh zemletryasenij* [Consequences of strong earthquakes]. M.: Stroyizdat, 1978. 311 p. (rus)
6. Byhovskij, V.A. *Inzhenernoj analiz posledstvij zemletryasenij v Yfponii i SSHA* [Engineering analysis of earthquake consequences in Japan and the USA]. M. Gosstroyizdat, 1961. 194 p. (rus)
7. Consider earthquake resistance when buying real estate in Japan [Online]. URL: <https://japanpropertycentral.com/2016/05/consider-earthquake-resistance-when-buying-real-estate-in-japan/> EN (reference date: 02.09.2019).
8. Şahin Güçhan, N. Observations on earthquake resistance of traditional timber-framed houses in Turkey. *Building and Environment*. 2007. 2(42). Pp. 840–851. DOI: 10.1016/j.buildenv.2005.09.027.
9. AHŞAP YAPILARIN DEPREM DAYANIKLILIĞI [EARTHQUAKE RESISTANCE OF WOODEN STRUCTURES] [Online]. URL: https://www.researchgate.net/publication/328478181_AHSAP_YAPILARIN_DEPREM_DAYANIKLILIGI_TR (reference date: 02.09.2019). (tur)
10. Seismic Upgrades for Old Houses [Online]. URL: <https://www.oldhouseonline.com/repairs-and-how-to/seismic-upgrades-for-old-houses> (reference date: 02.09.2019).
11. Goda, K., Yoshikawa, H. Incremental dynamic analysis of wood-frame houses in Canada: Effects of dominant earthquake scenarios on seismic fragility. *Soil Dynamics and Earthquake Engineering*. 2013. No. 48. Pp. 1–14.
12. Han, Y., Davidson, R.A., Black, G., Pei, S. A regional perspective on defining seismic performance objectives for woodframe buildings. *Structural Safety*. 2013. No. 43. Pp. 50–59. DOI: 10.1016/j.strusafe.2013.03.002.

13. Goda, K., Atkinson, G.M., Hong, H.P. Seismic loss estimation of wood-frame houses in south-western British Columbia. *Structural Safety*. 2011. 2(33). Pp. 123–135. DOI: 10.1016/j.strusafe.2010.11.001.
14. Ahn, K.J., Baek, C. Local characteristics of light-framed wood buildings in preparation for wind load. *Applied Mechanics and Materials*. 2013. No. 284–287. Pp. 1264–1268. DOI: 10.4028/www.scientific.net/AMM.284-287.1264.
15. Hong, S.G., Hong, N.K., Lee, S.Y. Hysteretic behavior of Korean traditional wooden frames. *Advanced Materials Research*. 2010. No. 133–134. Pp. 703–708. DOI: 10.4028/www.scientific.net/AMR.133-134.703.
16. Black, G., Davidson, R.A., Pei, S., Lindt, J. van de. Empirical loss analysis to support definition of seismic performance objectives for woodframe buildings. *Structural Safety*. 2010. 3(32). Pp. 209–219. DOI: 10.1016/j.strusafe.2010.02.003.
17. Yin, Y.J., Li, Y. Seismic collapse risk of light-frame wood construction considering aleatoric and epistemic uncertainties. *Structural Safety*. 2010. 32(4). Pp. 250–261. DOI: 10.1016/j.strusafe.2010.03.012
18. Porcu, M.C., Bosu, C., Gavrić, I. Non-linear dynamic analysis to assess the seismic performance of cross-laminated timber structures. *Journal of Building Engineering*. 2018. No. 19. Pp. 480–493. DOI: 10.1016/j.jobe.2018.06.008.
19. Kaliyanda, A.R., Rammer, D.R., Rowlands, R.E. Three-Dimensional Nonlinear Finite-Element Analysis of Wood–Steel Bolted Joints Subjected to Large Deformations. *Journal of Structural Engineering*. 2019. 145(10). 04019108.
20. Foliente, G.C. Hysteresis Modeling of Wood Joints and Structural Systems // *Journal of Structural Engineering*. 1995. 121(6). Pp. 1013–1022. DOI: 10.1061/(asce)0733-9445(1995)121:6(1013).
21. Casagrande, D., Grossi, P., Tomasi, R. Shake table tests on a full-scale timber-frame building with gypsum fibre boards. *European Journal of Wood and Wood Products*. 2016. 3(74). Pp. 425–442. DOI: 10.1007/s00107-016-1013-6.
22. Pu, W., Liu, C., Zhang, H., Kasai, K. Seismic control design for slip hysteretic timber structures based on tuning the equivalent stiffness. *Engineering Structures*. 2016. No. 128. Pp. 199–214. DOI: 10.1016/j.engstruct.2016.09.041.
23. Pu, W., Wu, M. Ductility demands and residual displacements of pinching hysteretic timber structures subjected to seismic sequences. *Soil Dynamics and Earthquake Engineering*. 2018. No. 114. Pp. 392–403. DOI: 10.1016/j.soildyn.2018.07.037.
24. Rinaldin, G., Fragiaco, M. Non-linear simulation of shaking-table tests on 3- and 7-storey X-Lam timber buildings. *Engineering Structures*. 2016. No. 113. Pp. 133–148. DOI: 10.1016/j.engstruct.2016.01.055.
25. Shen, Y.L., Schneider, J., Tesfamariam, S., Stierner, S.F., Mu, Z.G. Hysteresis behavior of bracket connection in cross-laminated-timber shear walls. *Construction and Building Materials*. 2013. No. 48. Pp. 980–991. DOI: 10.1016/j.conbuildmat.2013.07.050.
26. Casagrande, D., Rossi, S., Sartori, T., Tomasi, R. Proposal of an analytical procedure and a simplified numerical model for elastic response of single-storey timber shear-walls. *Construction and Building Materials*. 2016. No. 102. Pp. 1101–1112. DOI: 10.1016/j.conbuildmat.2014.12.114.
27. Dackermann, U., Elsener, R., Li, J., Crews, K. A comparative study of using static and ultrasonic material testing methods to determine the anisotropic material properties of wood. *Construction and Building Materials*. 2016. No. 102. Pp. 963–976. DOI: 10.1016/j.conbuildmat.2015.07.195.
28. Ugalde, D., Almazán, J.L., Santa María, H., Guindos, P. Seismic protection technologies for timber structures: a review. *European Journal of Wood and Wood Products*. 2019. 2(77). Pp. 173–194. DOI: 10.1007/s00107-019-01389-9.
29. Bahmani, P., Van De Lindt, J.W., Gershfeld, M., Mochizuki, G.L., Pryor, S.E., Rammer, D. Experimental Seismic Behavior of a Full-Scale Four-Story Soft-Story Wood-Frame Building with Retrofits. I: Building Design, Retrofit Methodology, and Numerical Validation. *Journal of Structural Engineering (United States)*. 2016. 4(142). Pp. 1–14. DOI: 10.1061/(ASCE)ST.1943-541X.0001207.
30. Poletti, E., Vasconcelos, G. Seismic behaviour and retrofitting of timber frame walls // *Advanced Materials Research*. 2013. No. 778. Pp. 706–713. DOI: 10.4028/www.scientific.net/AMR.778.706.
31. Grazide, C., Cointe, A., Coureau, J.L., Morel, S., Dumail, J.F. Wood heterogeneities and failure load of timber structural elements: a statistical approach. *Wood Science and Technology*. 2015. 2(49). Pp. 421–440. DOI: 10.1007/s00226-015-0706-z.
32. Aktaş, Y.D., Akyüz, U., Türer, A., Erdil, B., Güçhan, N.Ş. Seismic resistance evaluation of traditional ottoman TimberFrame Himiş houses: Frame loadings and material tests. *Earthquake Spectra*. 2014. 4(30). Pp. 1711–1732. DOI: 10.1193/011412EQS011M.
33. Brignola, A., Pampanin, S., Podestà, S. Experimental Evaluation of the In-Plane Stiffness of Timber Diaphragms // *Earthquake Spectra*. 2012. 4(28). Pp. 1687–1709. DOI: 10.1193/1.4000088.
34. Kharrazi, M.H.K., Ventura, C.E. Vibration frequencies of woodframe residential construction. *Earthquake Spectra*. 2006. 4(22). Pp. 1015–1034. DOI: 10.1193/1.2360699.
35. Mahdi, H., Hadi, H., Olounabadi, S.A.A., Ahmad, H. Earthquake Risks and Effects of Earthquake Load on Behavior of Wood Frame Structure by Using International Residential Code (IRC). *International Journal of Engineering and Advanced Technology*. 2015. 4(5). Pp. 8–23.
36. Naeim, F. *The Seismic Design Handbook*. Kluwer Academic Publishers. New York, 2001. 816 p.
37. Snow, M., Asiz, A., Chen, Z., Chui, Y.H. North American practices for connections in wood construction. *Progress in Structural Engineering and Materials*. 2006. 2(8). Pp. 39–48. DOI: 10.1002/pse.212.
38. McLain, T. E., Thangjitham, S. Bolted Wood Joint Yield Model. *Journal of Structural Engineering*. 1983. 109(8). Pp. 1820–1835. DOI: 10.1061/(asce)0733-9445(1983)109:8(1820).
39. Mergos, P., Beyer, K. Displacement-based seismic design of symmetric single-storey wood-frame buildings with the aid of N2 method. *Frontiers in Built Environment*. 2015. No. 1. Pp. 1–10. DOI: 10.3389/fbuil.2015.00010.
40. Filiatrault, A., Isoda, H., Folz, B. Hysteretic damping of wood framed buildings. *Engineering Structures*. 2003. 4(25). Pp. 461–471. DOI: 10.1016/S0141-0296(02)00187-6.
41. Pintarič, K., Premrov, M. Mathematical modelling of timber-framed walls using fictive diagonal elements. *Applied Mathematical Modelling*. 2013. 16–17(37). Pp. 8051–8059. DOI: 10.1016/j.apm.2013.02.050.
42. Vogrinec, K., Premrov, M., Kozem Šilih, E. Simplified modelling of timber-framed walls under lateral loads. *Engineering Structures*. 2016. No. 111. Pp. 275–284. DOI: 10.1016/j.engstruct.2015.12.029.
43. Rossi, S., Casagrande, D., Tomasi, R., Piazza, M. Seismic elastic analysis of light timber-frame multi-storey buildings: Proposal of an iterative approach. *Construction and Building Materials*. 2016. No. 102. Pp. 1154–1167. DOI: 10.1016/j.conbuildmat.2015.09.037.
44. Folz, B., Filiatrault, A. Cyclic Analysis of Wood Shear Walls. *Journal of Structural Engineering*. 2001. 127(4). Pp. 433–441. DOI: 10.1061/(ASCE)0733-9445(2001)127:4(433)
45. Pang, W., Rosowsky, D.V. Direct displacement procedure for performance-based seismic design of mid-rise wood-framed structures. *Earthquake Spectra*. 2009. 3(25). Pp. 583–605. DOI: 10.1193/1.3158932.

46. Källsner, B., Girhammar, U.A. Horizontal Stabilisation of Sheathed Timber Frame Structures Using Plastic Design Methods - Introducing a Handbook Part 4: Design in Ultimate Limit State. *Procedia Engineering*. 2016. No. 161. Pp. 645–654. DOI: 10.1016/j.proeng.2016.08.722.
47. Dhonju, R., D'Amico, B., Kermani, A., Porteous, J., Zhang, B. Parametric Evaluation of Racking Performance of Platform Timber Framed Walls. *Structures*. 2017. No. 12. Pp. 75–87. DOI: 10.1016/j.istruc.2017.08.003.
48. Alaei, S.A.M., Sullivan, T., Rogers, C.A., Nascimbene, R. Semi-empirical method to predict the displacement capacity and resistance of cold-formed steel frame wood-panel shear walls. *World Conference on Timber Engineering (WCTE)*. Auckland, 2012. No. 5. Pp. 450–455.
49. Girhammar, U.A., Källsner, B. Tests and Analyses of Slotted-In Steel-Plate Connections in Composite Timber Shear Wall Panels. *Advances in Civil Engineering*. 2017. No. 2017. Pp. 1–20. DOI: 10.1155/2017/7259014.
50. Vessby, J., Källsner, B., Olsson, A., Girhammar, U.A. Evaluation of softening behaviour of timber light-frame walls subjected to in-plane forces using simple FE models. *Engineering Structures*. 2014. No. 81. Pp. 464–479. DOI: 10.1016/j.engstruct.2014.09.032.
51. Ni, C., Kim, S.-Y., Chen, H., Lu, X. An Assessment Study of Seismic Resistance of Two-story Wood-frame Housing by Shaking Table Tests. *LHI Journal of Land, Housing, and Urban Affairs*. 2012. 1(3). Pp. 79–82. DOI: 10.5804/lhj.2012.3.1.79.
52. Dinehart, D.W., Shenton, H.W., Elliot, T.E. The dynamic response of wood frame shear walls with viscoelastic dampers. *Earthquake Spectra*. 1999. 15(1). Pp. 67–86.
53. Symans, M.D., Cofer, W.F., Du, Y., Fridley, K.J. Seismic Behavior of Wood-framed Structures with Viscous Fluid Dampers. *Earthquake Spectra*. 2004. 20(2). Pp. 451–482.
54. Dinehart, D.W., Hoffman, R.M., Sekin, A.A. Viscoelastic Polymer Hold Down Device for Wood Shear Walls. *Proceedings of the 8th World Conference on Timber Engineering*. Lahti, Finland, 2004. Pp. 247–251.
55. Dinehart, D.W., Blasetti, A.S. Comparison of Energy Dissipation, Stiffness, and Damage of Structural Oriented Strand Board (OSB), Conventional Gypsum, and Viscoelastic Gypsum Shearwalls Subjected to Cyclic Loads. *Buildings*. 2012. 3(2). Pp. 173–202. DOI: 10.3390/buildings2030173.
56. Uehan, F., Nakamura, Y. Ground motion characteristics around Kobe city detected by micro tremor measurement – The great hanshin earthquake disaster. *Eleventh World Conference on Earthquake Engineering*. Acapulco, Mexico, 1996. P. 714.
57. Belash, T.A., Ivanova, Zh.V., Demishin, S.V. Eksperimental'nye issledovaniya sejsmostojkosti derevyannyh zdaniy [Experimental studies of earthquake resistance of timber buildings]. *Sejsmostojkoe stroitel'stvo. Bezopasnost' sooruzhenij*. 2010. No. 6. Pp. 29–31. (rus)
58. Benin, A.V., Ivanova, Zh.V. Eksperimental'nye issledovaniya mekhanicheskikh svoystv uzlov derevyannogo zdaniya pri sejsmicheskikh vozdeystviyah [Experimental studies of the mechanical properties of nodes of timber building under seismic impacts]. *Sejsmostojkoe stroitel'stvo. Bezopasnost' sooruzhenij*. 2000. No. 2. Pp. 19–21. (rus)
59. Ivanova, Zh.V. Nelinejnij dinamicheskij analiz sejsmostojkosti derevyannyh konstrukcij [Nonlinear dynamic analysis of earthquake resistance of timber structures]. *Sejsmostojkoe stroitel'stvo. Bezopasnost' sooruzhenij*. 2005. No. 1. Pp. 7–8. (rus)
60. Belash, T.A., Ivanova, Zh.V. Obzor teoreticheskikh i eksperimental'nyh issledovaniy sejsmostojkosti derevyannyh konstrukcij [Review of the theoretical and experimental studies of earthquake resistance of timber structures]. *Sejsmostojkoe stroitel'stvo. Bezopasnost' sooruzhenij*. 2006. No. 4. Pp. 50–54. (rus)
61. Mostafaei, H., Al-Chatti, Q., Popovski, M., Tesfamariam, S., Bénichou, N. Seismic performance of wood mid-rise structures. *NRC Publications Archive*. Canada, 2013. 42 p.
62. Poletti, E., Vasconcelos, G., Branco, J.M., Koukouviki, A.M. Performance evaluation of traditional timber joints under cyclic loading and their influence on the seismic response of timber frame structures. *Construction and Building Materials*. 2016. No. 127. Pp. 321–334. DOI: 10.1016/j.conbuildmat.2016.09.122.
63. Leimke, J., Kasal, B., Polocoser, T., Guindos, P. Improved Moment-Resisting Timber Frames For Earthquake-Prone Areas Part I : Structural Connections. *CLEM + CIMAD 2017: II Latin American Congress on Timber Structures; II Ibero-American Congress on Construction Timber*. Junín, Buenos Aires, Argentina. 2017. No. 1. Pp. 1–11.
64. Leimke, J., Kasal, B., Polocoser, T., Guindos, P. Improved Moment-Resisting Timber Frames For Earthquake-Prone Areas Part II : Shaking Table Tests. *CLEM + CIMAD 2017: II Latin American Congress on Timber Structures; II Ibero-American Congress on Construction Timber*. Junín, Buenos Aires, Argentina. 2017. No. 1. Pp. 1–10.

Contacts:

Tatiana Belash, +7(921)9910115; belashta@mail.ru
Zhanna Ivanova, +7(921)9818419; syrmava@mail.ru



DOI: 10.18720/MCE.92.7

Деревянные здания каркасного типа с эффективными конструкциями узловых соединений для сейсмически активных районов

Т.А. Белаш*, Ж.В. Иванова

Петербургский государственный университет путей сообщения Императора Александра I,
Санкт-Петербург, Россия

* E-mail: belashta@mail.ru

Ключевые слова: малоэтажное строительство, деревянные конструкции, сейсмостойкость, деревянные здания каркасного типа, расчетно-экспериментальные исследования

Аннотация. Объектом исследования является деревянное здание каркасного типа, состоящее из деревянных вертикальных стоек, нижней и верхней обвязки, системы связей (горизонтальных и вертикальных), элементов перекрытия и покрытия (крыша). Рассматривается воздействие землетрясения различной интенсивности и частотного характера на сейсмостойкость деревянного здания. Оценка сейсмостойкости произведена на основании экспериментальных и расчетно-теоретических исследований. Экспериментальные методы выполнялись на лабораторных установках и крупномасштабных моделях. С учетом полученных экспериментальных данных выполнена расчетно-теоретическая оценка каркасного здания на простых и сложных моделях при воздействии различной интенсивности и частотного состава. Установлено, что частотный состав сейсмического воздействия существенным образом влияет на сейсмостойкость каркасных зданий. Рекомендуется при проектировании этих зданий назначать их динамические параметры (период собственных колебаний) в зависимости от прогноза преобладающего периода сейсмических колебаний района строительства, что позволит более эффективно решать компоновку узловых соединений каркаса. Рекомендуется в узловые соединения вводить дополнительные материалы и устройства, обладающие податливостью и высокими диссипативными свойствами.

Литература

1. Kirkham W.J., Gupta R., Miller T.H. State of the art: Seismic behavior of wood-frame residential structures // Journal of Structural Engineering (United States). 2014. No. 4(140). Pp. 1–19. DOI: 10.1061/(ASCE)ST.1943-541X.0000861.
2. Falk R.H., Soltis L.A. Seismic behavior of low-rise wood-framed buildings. [Электронный ресурс]. URL: <https://www.fpl.fs.fed.us/documnts/pdf1988/falk88b.pdf> (дата обращения: 02.09.2019).
3. Мартеньянов А.И. Проектирование и строительство зданий и сооружений в сейсмических районах. М.: Стройиздат, 1985. 255 с.
4. Белаш Т.А., Иванова Ж.В. Исследование сейсмостойкости деревянных зданий // Сейсмостойкое строительство. Безопасность сооружений. 2003. № 2. С. 28–31.
5. Поляков С.В. Последствия сильных землетрясений. М.: Стройиздат, 1978. 311 с.
6. Быховский В.А. Инженерной анализ последствий землетрясений в Японии и США. М.: Госстройиздат, 1961. 194 с.
7. Consider earthquake resistance when buying real estate in Japan [Электронный ресурс]. URL: <https://japanpropertycentral.com/2016/05/consider-earthquake-resistance-when-buying-real-estate-in-japan/> EN (дата обращения: 02.09.2019).
8. Şahin Güçhan N. Observations on earthquake resistance of traditional timber-framed houses in Turkey // Building and Environment. 2007. No. 2(42). Pp. 840–851. DOI: 10.1016/j.buildenv.2005.09.027.
9. AHŞAP YAPILARIN DEPREM DAYANIKLILIĞI [EARTHQUAKE RESISTANCE OF WOODEN STRUCTURES] [Электронный ресурс]. URL: https://www.researchgate.net/publication/328478181_AHŞAP_YAPILARIN_DEPREM_DAYANIKLILIGI_TR (дата обращения: 02.09.2019). (tur)
10. Seismic Upgrades for Old Houses [Электронный ресурс]. URL: <https://www.oldhouseonline.com/repairs-and-how-to/seismic-upgrades-for-old-houses> (дата обращения: 02.09.2019).
11. Goda K., Yoshikawa H. Incremental dynamic analysis of wood-frame houses in Canada: Effects of dominant earthquake scenarios on seismic fragility // Soil Dynamics and Earthquake Engineering. 2013. No. 48. Pp. 1–14.
12. Han Y., Davidson R.A., Black G., Pei S. A regional perspective on defining seismic performance objectives for woodframe buildings // Structural Safety. 2013. No. 43. Pp. 50–59. DOI: 10.1016/j.strusafe.2013.03.002.
13. Goda K., Atkinson G.M., Hong H.P. Seismic loss estimation of wood-frame houses in south-western British Columbia // Structural Safety. 2011. No. 2(33). Pp. 123–135. DOI: 10.1016/j.strusafe.2010.11.001.

14. Ahn K.J., Baek C. Local characteristics of light-framed wood buildings in preparation for wind load // *Applied Mechanics and Materials*. 2013. No. 284–287. Pp. 1264–1268. DOI: 10.4028/www.scientific.net/AMM.284-287.1264.
15. Hong S.G., Hong N.K., Lee S.Y. Hysteretic behavior of Korean traditional wooden frames // *Advanced Materials Research*. 2010. No. 133–134. Pp. 703–708. DOI: 10.4028/www.scientific.net/AMR.133-134.703.
16. Black G., Davidson R.A., Pei S., Lindt J. van de. Empirical loss analysis to support definition of seismic performance objectives for woodframe buildings // *Structural Safety*. 2010. No. 3(32). Pp. 209–219. DOI: 10.1016/j.strusafe.2010.02.003.
17. Yin Y.J., Li Y. Seismic collapse risk of light-frame wood construction considering aleatoric and epistemic uncertainties // *Structural Safety*. 2010. No. 32(4). Pp. 250–261. DOI: 10.1016/j.strusafe.2010.03.012
18. Porcu M.C., Bosu C., Gavrić I. Non-linear dynamic analysis to assess the seismic performance of cross-laminated timber structures // *Journal of Building Engineering*. 2018. No. 19. Pp. 480–493. DOI: 10.1016/j.jobe.2018.06.008.
19. Kaliyanda A.R., Rammer D.R., Rowlands R.E. Three-Dimensional Nonlinear Finite-Element Analysis of Wood–Steel Bolted Joints Subjected to Large Deformations // *Journal of Structural Engineering*. 2019. No. 145(10). 04019108.
20. Foliente G. C. Hysteresis Modeling of Wood Joints and Structural Systems // *Journal of Structural Engineering*. 1995. No. 121(6). Pp. 1013–1022. DOI: 10.1061/(asce)0733-9445(1995)121:6(1013).
21. Casagrande D., Grossi P., Tomasi R. Shake table tests on a full-scale timber-frame building with gypsum fibre boards // *European Journal of Wood and Wood Products*. 2016. No. 3(74). Pp. 425–442. DOI: 10.1007/s00107-016-1013-6.
22. Pu W., Liu C., Zhang H., Kasai K. Seismic control design for slip hysteretic timber structures based on tuning the equivalent stiffness // *Engineering Structures*. 2016. No. 128. Pp. 199–214. DOI: 10.1016/j.engstruct.2016.09.041.
23. Pu W., Wu M. Ductility demands and residual displacements of pinching hysteretic timber structures subjected to seismic sequences // *Soil Dynamics and Earthquake Engineering*. 2018. No. 114. Pp. 392–403. DOI: 10.1016/j.soildyn.2018.07.037.
24. Rinaldin G., Fragiaco M. Non-linear simulation of shaking-table tests on 3- and 7-storey X-Lam timber buildings // *Engineering Structures*. 2016. No. 113. Pp. 133–148. DOI: 10.1016/j.engstruct.2016.01.055.
25. Shen Y.L., Schneider J., Tesfamariam S., Stiemi S.F., Mu Z.G. Hysteresis behavior of bracket connection in cross-laminated-timber shear walls // *Construction and Building Materials*. 2013. No. 48. Pp. 980–991. DOI: 10.1016/j.conbuildmat.2013.07.050.
26. Casagrande D., Rossi S., Sartori T., Tomasi R. Proposal of an analytical procedure and a simplified numerical model for elastic response of single-storey timber shear-walls // *Construction and Building Materials*. 2016. No. 102. Pp. 1101–1112. DOI: 10.1016/j.conbuildmat.2014.12.114.
27. Dackermann U., Elsener R., Li J., Crews K. A comparative study of using static and ultrasonic material testing methods to determine the anisotropic material properties of wood // *Construction and Building Materials*. 2016. No. 102. Pp. 963–976. DOI: 10.1016/j.conbuildmat.2015.07.195.
28. Ugalde D., Almazán J.L., Santa María H., Guindos P. Seismic protection technologies for timber structures: a review // *European Journal of Wood and Wood Products*. 2019. No. 2(77). Pp. 173–194. DOI: 10.1007/s00107-019-01389-9.
29. Bahmani P., Van De Lindt J.W., Gershfeld M., Mochizuki G.L., Pryor S.E., Rammer D. Experimental Seismic Behavior of a Full-Scale Four-Story Soft-Story Wood-Frame Building with Retrofits. I: Building Design, Retrofit Methodology, and Numerical Validation // *Journal of Structural Engineering (United States)*. 2016. No. 4(142). Pp. 1–14. DOI: 10.1061/(ASCE)ST.1943-541X.0001207.
30. Poletti E., Vasconcelos G. Seismic behaviour and retrofitting of timber frame walls // *Advanced Materials Research*. 2013. No. 778. Pp. 706–713. DOI: 10.4028/www.scientific.net/AMR.778.706.
31. Grazide C., Cointe A., Coureau J.L., Morel S., Dumail J.F. Wood heterogeneities and failure load of timber structural elements: a statistical approach // *Wood Science and Technology*. 2015. No. 2(49). Pp. 421–440. DOI: 10.1007/s00226-015-0706-z.
32. Aktaş Y.D., Akyüz U., Türer A., Erdil B., Güçhan N.Ş. Seismic resistance evaluation of traditional ottoman TimberFrame Himiş houses: Frame loadings and material tests // *Earthquake Spectra*. 2014. No. 4(30). Pp. 1711–1732. DOI: 10.1193/011412EQS011M.
33. Brignola A., Pampanin S., Podestà S. Experimental Evaluation of the In-Plane Stiffness of Timber Diaphragms // *Earthquake Spectra*. 2012. No. 4(28). Pp. 1687–1709. DOI: 10.1193/1.4000088.
34. Kharrazi M.H.K., Ventura C.E. Vibration frequencies of woodframe residential construction // *Earthquake Spectra*. 2006. No. 4(22). Pp. 1015–1034. DOI: 10.1193/1.2360699.
35. Mahdi H., Hadi H., Olounabadi S.A.A., Ahmad H. Earthquake Risks and Effects of Earthquake Load on Behavior of Wood Frame Structure by Using International Residential Code (IRC) // *International Journal of Engineering and Advanced Technology*. 2015. No. 4(5). Pp. 8–23.
36. Naeim F. *The Seismic Design Handbook*. New York: Kluwer Academic Publishers, 2001. 816 p.
37. Snow M., Asiz A., Chen Z., Chui Y.H. North American practices for connections in wood construction // *Progress in Structural Engineering and Materials*. 2006. No. 2(8). Pp. 39–48. DOI: 10.1002/pse.212.
38. McLain T. E., Thangjitham S. Bolted Wood Joint Yield Model // *Journal of Structural Engineering*. 1983. No. 109(8). Pp. 1820–1835. DOI: 10.1061/(asce)0733-9445(1983)109:8(1820).
39. Mergos P., Beyer K. Displacement-based seismic design of symmetric single-storey wood-frame buildings with the aid of N2 method // *Frontiers in Built Environment*. 2015. No. 1. Pp. 1–10. DOI: 10.3389/fbuil.2015.00010.
40. Filiatrault A., Isoda H., Folz B. Hysteretic damping of wood framed buildings // *Engineering Structures*. 2003. No. 4(25). Pp. 461–471. DOI: 10.1016/S0141-0296(02)00187-6.
41. Pintarič K., Premrov M. Mathematical modelling of timber-framed walls using fictive diagonal elements // *Applied Mathematical Modelling*. 2013. No. 16/17(37). Pp. 8051–8059. DOI: 10.1016/j.apm.2013.02.050.
42. Vogrinec K., Premrov M., Kozem Šilih E. Simplified modelling of timber-framed walls under lateral loads // *Engineering Structures*. 2016. No. 111. Pp. 275–284. DOI: 10.1016/j.engstruct.2015.12.029.
43. Rossi S., Casagrande D., Tomasi R., Piazza M. Seismic elastic analysis of light timber-frame multi-storey buildings: Proposal of an iterative approach // *Construction and Building Materials*. 2016. No. 102. Pp. 1154–1167. DOI: 10.1016/j.conbuildmat.2015.09.037.
44. Folz B., Filiatrault A. Cyclic Analysis of Wood Shear Walls // *Journal of Structural Engineering*. 2001. No. 127(4). Pp. 433–441. DOI: 10.1061/(ASCE)0733-9445(2001)127:4(433)
45. Pang W., Rosowsky D.V. Direct displacement procedure for performance-based seismic design of mid-rise wood-framed structures // *Earthquake Spectra*. 2009. No. 3(25). Pp. 583–605. DOI: 10.1193/1.3158932.
46. Källsner B., Girhammar U.A. Horizontal Stabilisation of Sheathed Timber Frame Structures Using Plastic Design Methods - Introducing a Handbook Part 4: Design in Ultimate Limit State // *Procedia Engineering*. 2016. No. 161. Pp. 645–654. DOI: 10.1016/j.proeng.2016.08.722.

47. Dhonju R., D'Amico B., Kermani A., Porteous J., Zhang B. Parametric Evaluation of Racking Performance of Platform Timber Framed Walls // Structures. 2017. No. 12. Pp. 75–87. DOI: 10.1016/j.istruc.2017.08.003.
48. Alaei S.A.M., Sullivan T., Rogers C.A., Nascimbene R. Semi-empirical method to predict the displacement capacity and resistance of cold-formed steel frame wood-panel shear walls // World Conference on Timber Engineering (WCTE). Auckland, 2012. No. 5. Pp. 450–455.
49. Girhammar U.A., Källsner B. Tests and Analyses of Slotted-In Steel-Plate Connections in Composite Timber Shear Wall Panels. Advances in Civil Engineering. 2017. No. 2017. Pp. 1–20. DOI: 10.1155/2017/7259014.
50. Vessby J., Källsner B., Olsson A., Girhammar U.A. Evaluation of softening behaviour of timber light-frame walls subjected to in-plane forces using simple FE models // Engineering Structures. 2014. No. 81. Pp. 464–479. DOI: 10.1016/j.engstruct.2014.09.032.
51. Ni C., Kim S.-Y., Chen H., Lu X. An Assessment Study of Seismic Resistance of Two-story Wood-frame Housing by Shaking Table Tests // LHI Journal of Land, Housing, and Urban Affairs. 2012. No. 1(3). Pp. 79–82. DOI: 10.5804/lhij.2012.3.1.79.
52. Dinehart D.W., Shenton H.W., Elliot T.E. The dynamic response of wood frame shear walls with viscoelastic dampers // Earthquake Spectra. 1999. No. 15(1). Pp. 67–86.
53. Symans M.D., Cofer W.F., Du Y., Fridley K.J. Seismic Behavior of Wood-framed Structures with Viscous Fluid Dampers // Earthquake Spectra. 2004. No. 20(2). Pp. 451–482.
54. Dinehart D.W., Hoffman R.M., Sekin A.A. Viscoelastic Polymer Hold Down Device for Wood Shear Walls // Proceedings of the 8th World Conference on Timber Engineering. Lahti, Finland, 2004. Pp. 247–251.
55. Dinehart D.W., Blasetti A.S. Comparison of Energy Dissipation, Stiffness, and Damage of Structural Oriented Strand Board (OSB), Conventional Gypsum, and Viscoelastic Gypsum Shearwalls Subjected to Cyclic Loads // Buildings. 2012. No. 3(2). Pp. 173–202. DOI: 10.3390/buildings2030173.
56. Uehan F., Nakamura Y. Ground motion characteristics around Kobe city detected by micro tremor measurement – The great hanshin earthquake disaster // Eleventh World Conference on Earthquake Engineering. Acapulco, Mexico, 1996. p. 714.
57. Белаш Т.А., Иванова Ж.В., Демишин С.В. Экспериментальные исследования сейсмостойкости деревянных зданий // Сейсмостойкое строительство. Безопасность сооружений. 2010. № 6. С. 29–31.
58. Бенин А.В., Иванова Ж.В. Экспериментальные исследования механических свойств узлов деревянного здания при сейсмических воздействиях // Сейсмостойкое строительство. Безопасность сооружений. 2000. № 2. С. 19–21.
59. Иванова Ж.В. Нелинейный динамический анализ сейсмостойкости деревянных конструкций // Сейсмостойкое строительство. Безопасность сооружений. 2005. № 1. С. 7–8.
60. Белаш Т.А., Иванова Ж.В. Обзор теоретических и экспериментальных исследований сейсмостойкости деревянных конструкций // Сейсмостойкое строительство. Безопасность сооружений. 2006. №4. С. 50–54.
61. Mostafaei H., Al-Chatti Q., Popovski M., Tesfamariam S., Bénichou N. Seismic performance of wood mid-rise structures. NRC Publications Archive. Canada, 2013. 42 p.
62. Poletti E., Vasconcelos G., Branco J.M., Koukouviki A.M. Performance evaluation of traditional timber joints under cyclic loading and their influence on the seismic response of timber frame structures // Construction and Building Materials. 2016. No. 127. Pp. 321–334. DOI: 10.1016/j.conbuildmat.2016.09.122.
63. Leimke J., Kasal B., Polocoser T., Guindos P. Improved Moment-Resisting Timber Frames For Earthquake-Prone Areas Part I : Structural Connections // CLEM + CIMAD 2017: II Latin American Congress on Timber Structures; II Ibero-American Congress on Construction Timber. Junín, Buenos Aires, Argentina. 2017. No. 1. Pp. 1–11.
64. Leimke J., Kasal B., Polocoser T., Guindos P. Improved Moment-Resisting Timber Frames For Earthquake-Prone Areas Part II : Shaking Table Tests // CLEM + CIMAD 2017: II Latin American Congress on Timber Structures; II Ibero-American Congress on Construction Timber. Junín, Buenos Aires, Argentina. 2017. No. 1. Pp. 1–10.

Контактные данные:

Татьяна Александровна Белаш, +7(921)9910115; эл. почта: belashta@mail.ru

Жанна Васильевна Иванова, +7(921)9818419; эл. почта: syrma@mail.ru



DOI: 10.18720/MCE.92.8

Clinkerless slag-silica binder: hydration process and hardening kinetics

G.S Slavcheva^a, D.O. Baidzhanov^b, M.A. Khan^b, M.A. Shvedova^c, Y.K. Imanov^b

^a Voronezh State Technical University, Voronezh, Russia

^b Karaganda State Technical University, Karaganda, Republic of Kazakhstan

^c Voronezh State University of Architecture and Civil Engineering, Voronezh, Russia

* E-mail: gslavcheva@yandex.ru

Keywords: clinkerless binder, industrial waste, hydration, flocculation, hardening, phase composition, compressive strength

Abstract. The article discusses the results of experimental studies comply with modern approaches to the production of high-performance clinkerless binder in order to ensure the possibility of obtaining high-strength composites based on them, hardening under normal temperature and humidity conditions, with-out heat treatment. The binder, belonging to the class slag-alkaline binders, was obtained by grinding all components together in the presence of superplasticizers and a high content of silica fume. The laser granulometry method, XRD – method were used to estimate the particle size, phase composition of the original components and the clinkerless binder. The flocculation and hardening kinetics was evaluated by the penetrometric method and mechanical tests. The data of the phase composition change of the binder, plastic strength, features of mechanical behavior at different stages of hardening are obtained. As a result, the distinctive features of the main periods of heterogeneous processes of structure formation of the resulting binder are revealed. It was found that the high content of microsilica and particles with a diameter of $d \sim 1 \div 6 \mu\text{m}$ in the composition of clinkerless binder, activated during grinding, allowed to increase their hydraulic activity. As a result, the speed of clinkerless binder setting and hardening under normal temperature and humidity conditions corresponds to the speed of these processes for Portland cement. Setting rate and strength characteristics of clinkerless slag-silica binder meet the requirements for physical and mechanical properties of cement class 32.5 according to EN 197-1: 2000.

1. Introduction

One of the key problems of modern materials science is the development of new types of effective cementitious materials, providing the creation of new generation concrete with high physical and mechanical characteristics and operational stability. At the same time, the high material and energy intensity of the production of clinker cement determines the need for the development and implementation of low- and clinkerless alternative types of binders.

Currently, in the class of clinkerless binders, the most studied in terms of properties, compositions, structure are slag-alkali binders. For more than 60 years of research in the classical works of Bozhenov P.I., Budnikov P.P., Volzhensky A.V., Glukhovskiy V.D., Brandstetr J., Davidovits J., Malolepshi J., Sato K., Shi S., Skwara F., Wang S.D., and others the theoretical foundations of alkaline activation of slag were formed, the principles of controlling the processes of structure formation and hardening of slag-alkali binders were developed. As a result, the compositions of a wide range of these binders were developed, industrial technologies for the production of building products and structures based on them were created, the corresponding regulatory framework was formed. However, obtaining effective concretes based on slag-alkali

Slavcheva, G.S., Baidzhanov, D.O., Khan, M.A., Shvedova, M.A., Imanov, Y.K. Clinkerless slag-silica binder: hydration process and hardening kinetics. Magazine of Civil Engineering. 2019. 92(8). Pp. 96–105. DOI: 10.18720/MCE.92.8

Славчева Г.С., Байджанов Д.О., Хан М.А., Шведова М.А., Иманов Е.К. Бесклинкерное шлако-кремнеземистое вяжущее: параметры структурообразования и кинетика твердения // Инженерно-строительный журнал. 2019. № 8(92). С. 96–105. DOI: 10.18720/MCE.92.8



binders developed in the period of the 60–70s of the last century turned out to be possible only with their heat and moisture treatment used in a factory.

In modern realities, when the volumes of monolithic construction increase, the use of classic slag-alkali binders is rather limited. Therefore, modern research in the field of alternative clinkerless binders and, in particular, slag-alkali binders are associated with the possibility of obtaining high-strength composites based on them, hardening in normal temperature and humidity conditions, without heat treatment.

Two factors are the basis for obtaining a new generation of slag alkaline binders. Firstly, this is the use of binders of micro- and nanodispersed fillers with hydraulic activity. Secondly, it is the mechanochemical activation of binders during grinding.

The well-known developments of slag-alkali binders of the modern period [1–21] showed wide possibilities in comparison with clinker cement for controlling the composition, structure and properties of artificial stone building composites based on them. This is ensured by the introduction of mineral fillers and modifiers in the composition of these binders. The general and particular patterns of the influence of the material and particle size distribution, dispersion and surface potential of certain types of slag, mineral additives and alkaline additives on the structure formation and properties of paste and stone based on slag-alkali binders [1–14] were studied. Various works studied the effect on structure formation, hardening and the complex of properties of binding fly ash additives [15], waste sand [16], ground silica sand and micro-silica [17–18], zeolite-containing carbonate-silicon [19] and aluminum silicate [20] mineral additives. As a result, it was proved that it is the use of hydraulically active micro- and nanodispersed mineral modifiers that allows one to obtain binders that achieve strength up to 50 MPa without heat treatment.

However, the most effective ways of adding these modifiers (with joint or separate grinding), their optimal dosages, and also the rational dispersion of slag-alkali binders have not been clearly defined.

The results of experimental studies discussed in this article are correlated with modern approaches to obtaining highly effective clinkerless binders belonging to the class of slag alkaline. At the preliminary stage of research, the authors optimized, according to the criterion of strength, the composition of a new variety of cinder-alkaline binders based on granulated blast-furnace slag, silica fume, quicklime, two-water gypsum and powdery C-3 superplasticizer. Distinctive features of clinkerless slag-silica binder (CSSB) are:

- 1) obtaining by co-grinding all components in the presence of superplasticizer,
- 2) a high dosage of silica fume (20 %),
- 3) a high specific surface area of 900 m²/kg.

The scientific approach to substantiating the composition and method of obtaining this binder is based on the implementation of the “top-down” nanotechnological principle [21]. It is believed that it is the joint grinding of all components that will provide a change in the energy state of the structure and, accordingly, the physical and/or physicochemical activity of surface and internal volumes of solid particles as they are being ground. In this case, the introduction of a superplasticizer as a surface-active substance during grinding will contribute to amorphization of the surface of binder particles, their saturation with structural defects of the nanoscale range. The achieved high specific surface area of the binder will determine the predominance of nano- and micro-sized particles in its composition. As a result, it is supposed to increase the rate of structure formation and hardening of the binder precisely due to nanotechnological activation of its components at the manufacturing stage, using the hydraulic potential of nano- and micro-sized particles at the hardening stage.

The aim of the work was to assess the applicability of clinkerless slag-silica binder (CSSB) as a hydraulic binder of normal hardening based on comprehensive studies of phase composition, structuration process and hardening. The objectives of the study included:

- assessment of the particle size distribution of the initial components and the CSSB obtained to evaluate the content of nano- and micro-sized particles in their composition;
- studying changes in phase composition of CSSB during hydration and structuration processes;
- assessment of flocculation and hardening kinetics of CSSB

2. Materials and Methods¹

The following raw materials were used to obtain clinkerless slag-silica binder:

- granulated blast-furnace slag from LLP “Arcelor Mittal” plant (Temirtau, Kazakhstan) with a lime factor of 0.75;

¹ The studies were conducted in the laboratory of the Collective Use Center Named After Professor Yu. M. Borisov (Voronezh State Technical University, Russia)

- microsilica of MKU-95 grade with a mass fraction of $\text{SiO}_2 = 96.85\%$;
- building lime of activity of 86.2% ;
- gypsum (gypsum dihydrate);
- powder superplasticizer S-3 based on naphthalenesulfonates.

The binder was obtained by dry joint grinding of raw materials. The ratio of the components is the know-how of the authors and is not published since the composition of the binder is at the patenting stage (patent application No 2018/0444.1 “Clinkerless binder from industrial wastes”, Kazakhstan).

Operational control of the binder dispersion by its specific surface area was carried out by the method of air permeation on the PSH-8A device. The granulometric compositions of the microsilica and binder were studied using the laser particle size analyzer ANALYSETTE 22 Nano Tec.

The structuration process, flocculation and hardening kinetics were studied in the “CSSB + water” system, $W/CSSB = 0.3$, which was assigned based on the standard normal consistency of fresh binder paste.

After mixing the CSSB with water, the flocculation process of fresh binder paste was controlled in two ways. The setting times were determined on a Vicat apparatus according to Russian State Standard GOST 30744-2001 “Cements. Methods of testing with using polyfraction standard sand”.

The setting kinetics was evaluated by the plastic strength index P_{pl} , determined using a universal penetrometer Geopocket S068. To determine the plastic strength, fresh binder paste was placed in a ring with a diameter of 150 mm and a height of 55 mm. The determination of plastic strength was performed by immersing a standard penetrometer plunger (6.4 mm) to a predetermined mark (to a depth of 5 mm). The readings were taken on an internal scale in kgf/cm^2 , the value of plastic strength P_{pl} was determined based on the fact that $1 \text{ kgf/cm}^2 = 98.0665 \text{ kPa}$. Tests were carried out from the moment the mixture was prepared until the moment it began to set (determined using a Vicat apparatus) every 15 minutes. For each test period, 12 measurements were made.

The CSSB hardening kinetics was evaluated by testing samples – cubes $5 \times 5 \times 5 \text{ cm}$ in size after 1, 3, 7, 14, 28 days of hardening under normal temperature and humidity conditions ($t = 20^\circ\text{C}$, $\text{RH} = 95 \pm 5\%$). The strength testing was carried out on a universal 4-column floor hydraulic test system INSTRON Sates 1500 HDS. As a result of the tests, the full diagrams “strain σ – displacement Δ ” were obtained. According to the tests, the compressive strength and elastic modulus were determined. To ensure the statistical reliability of the results of physical and mechanical tests, the number of samples in the series was 6 pieces. The intra-series coefficient of variability of the test results was 7–10 %.

The phase composition of the clinkerless binder was controlled by the XRD-method (ARL X'TRA diffractometer, $\text{CuK}\alpha$ radiation ($\lambda = 1.541788 \text{ \AA}$) after 1, 3, 7, 14, 28 days of hardening under normal temperature and humidity conditions. X-ray decoding and phase identification were carried out using PDWin 4.0.

3. Results

According to the laser granulometry data (Figure 1, Table 1), it was found that the composition of the clinkerless slag silica binder is characterized by polydispersity, with almost half of ultramicrodispersed particles (40 % with a diameter of $d \sim 1 \div 6 \mu\text{m}$ and 8 % with a diameter of $d < 1 \mu\text{m}$). The granulometry of microsilica as the most dispersed initial binder component is characterized by a peaked distribution, that is, its composition is close to monodisperse, and is represented mainly by particles $d = 15.6 \mu\text{m}$. A comparison of the granulometry of the CSSB with the granulometric composition of microsilica shows a significant increase in the ultramicrodispersed component as a result of grinding.

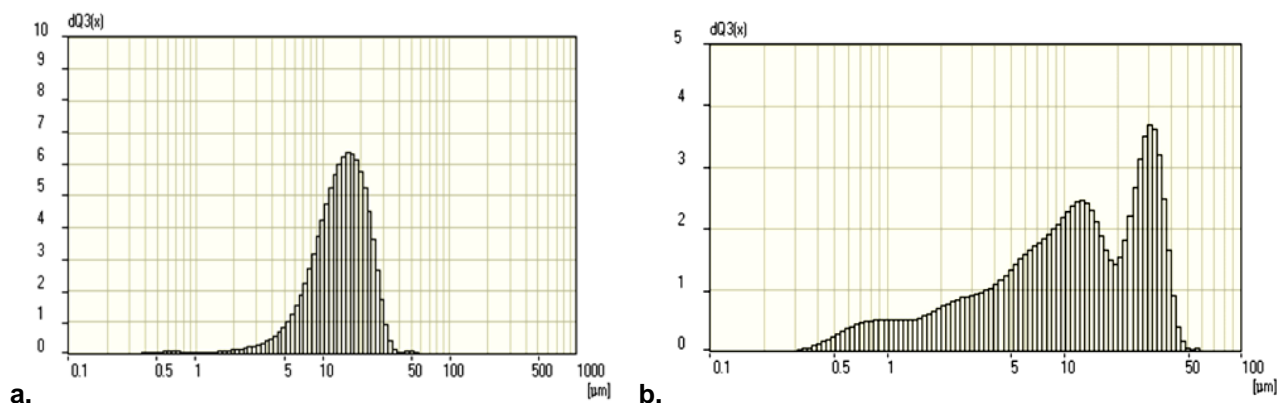


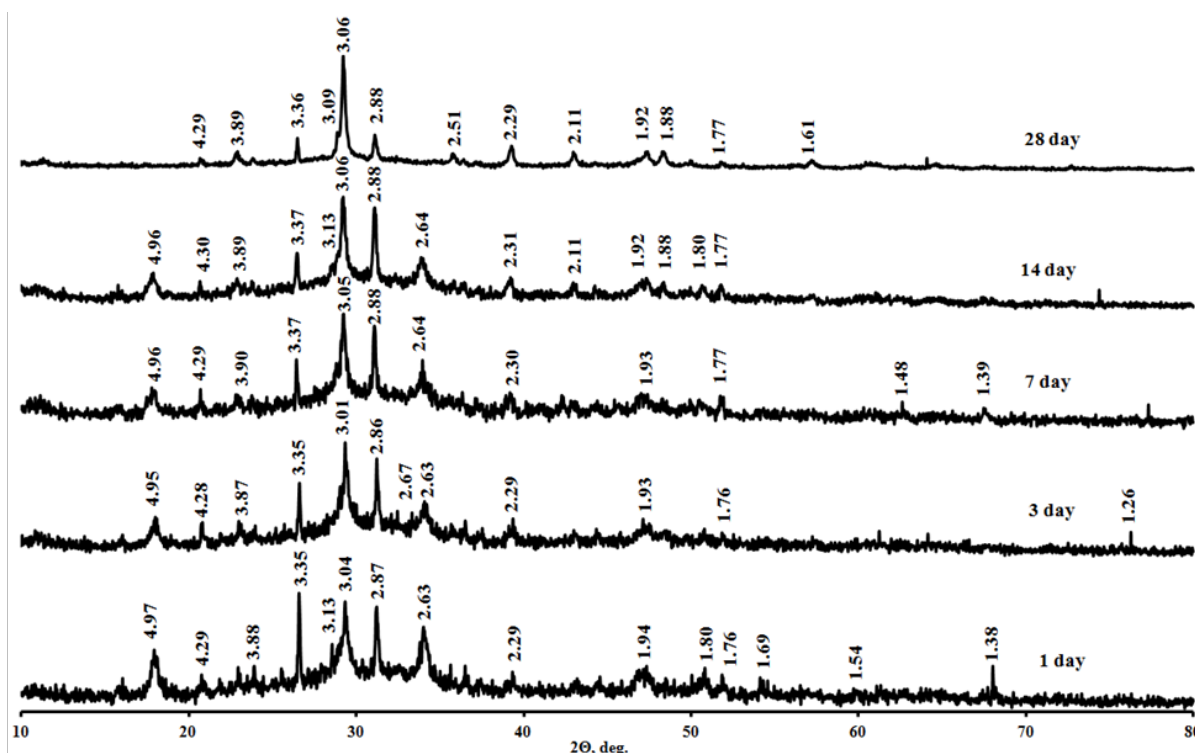
Figure 1. Particles range of clinkerless slag-alkaline binder (a) and silica fume (b).

Table 1. Granulometry of clinkerless slag-silica binder and microsilica.

No	Name	Data (Analyzette22)	
		ω particles, %	d , μm
1	Microsilica	93	15.6
		7	≤ 15.6
2	Clinkerless slag-silica binder	31	30
		22	12
		12	6
		27	3
		8	≤ 1

According to the data of X-ray diffractometry analysis (Figure 2), the slag, which is part of the clinkerless slag-silica binder, is traditionally X-ray amorphous, since there are no clearly defined intensity peaks for the X-ray diffraction pattern, but only blurry, low-intensity peaks, which blur into a halo, which is due to the high content of the glassy phase. However, in the X-ray diffraction pattern, several peaks can be distinguished, which correspond to one of the main crystalline phases of slag – the mellite phase $8\text{CaO}\cdot 3\text{Al}_2\text{O}_3\cdot \text{MgO}\cdot 5\text{SiO}_2$.

An analysis of the data of X-ray diffractometric studies of a clinkerless binder (Figure 3) showed that throughout the entire hardening time, a small initial phase of mellite is present in the studied system $8\text{CaO}\cdot 3\text{Al}_2\text{O}_3\cdot \text{MgO}\cdot 5\text{SiO}_2$. Its presence is natural, since according to the classical concepts formed in the works of the school of A.V. Volzhensky [22], the hydraulic activity of the slag phases decreases as follows: tricalcium silicate – calcium aluminoferrites – β - $2\text{CaO}\cdot \text{SiO}_2$ – main slag glass – acidic slag glass – mellite – β - $2\text{CaO}\cdot \text{SiO}_2$ – merwinite – monticellite – low basic aluminosilicates and calcium silicates. The amount of mellite phase is insignificant and it completely disappears by the twenty-eighth day of hardening.

**Figure 3. XRD pattern of hardened system «clinkerless slag-silica binder + water» ($W/CSSB = 0.3$).**

Designations:

$6\text{CaO}\cdot 4\text{SiO}_2\cdot 3\text{H}_2\text{O}$ ($d = 4.31, 3.11, 2.26, 1.95, 1.76$);

$2\text{CaO}\cdot \text{SiO}_2\cdot \text{H}_2\text{O}$ ($d = 3.34, 2.92, 2.25, 1.86, 1.75$);

$(\text{CaO})_x\cdot \text{SiO}_2\cdot z\text{H}_2\text{O}$ ($d = 4.92, 3.05, 2.93, 2.80, 1.83$);

$x\text{CaO}\cdot \text{SiO}_2\cdot z\text{H}_2\text{O}$ ($d = 3.07, 2.97, 2.80, 2.28, 1.83$);

$\text{CaO}\cdot \text{Al}_2\text{O}_3\cdot 2\text{SiO}_2\cdot 4\text{H}_2\text{O}$ ($d = 4.91, 4.27, 3.34, 3.19, 2.70$);

$3\text{CaO}\cdot \text{Al}_2\text{O}_3\cdot 3\text{CaSO}_4\cdot 31\text{H}_2\text{O}$ ($d = 4.98, 3.88, 1.90, 1.87, 1.76$).

The hydrate neoplasms of the studied system are predominantly represented by high and low basic calcium hydrosilicates ($6\text{CaO}\cdot 4\text{SiO}_2\cdot 3\text{H}_2\text{O}$, $2\text{CaO}\cdot \text{SiO}_2\cdot \text{H}_2\text{O}$, $(\text{CaO})_x\cdot \text{SiO}_2\cdot z\text{H}_2\text{O}$, $x\text{CaO}\cdot \text{SiO}_2\cdot z\text{H}_2\text{O}$), calcium

hydroaluminosilicate ($\text{CaO}\cdot\text{Al}_2\text{O}_3\cdot 2\text{SiO}_2\cdot 2\text{H}_2\text{O}$) and ettringite ($3\text{CaO}\cdot\text{Al}_2\text{O}_3\cdot 3\text{CaSO}_4\cdot 31\text{H}_2\text{O}$). The content of these phases in the process of hydration and hardening of a clinkerless binder is constantly changing. So, on the first day of hardening, the phases of highly basic calcium hydrosilicates and the phase of calcium hydroaluminosilicate are predominantly seen in the system. The amount of these phases decreases over time. Low-basic tobermorite-like calcium hydrosilicates ($(\text{CaO})_x\cdot\text{SiO}_2\cdot z\text{H}_2\text{O}$, $x\text{CaO}\cdot\text{SiO}_2\cdot z\text{H}_2\text{O}$) appear in the studied system by the seventh day of hardening, while their content is constantly increasing. The ettringite phase is recorded only to the twenty-eighth day from the beginning of hardening. It is important to note that, in this system, the crystalline phase of portlandite is not observed at any moment of hardening ($\text{Ca}(\text{OH})_2$).

According to the standard definition of setting time, the beginning of the setting of CSSB is fixed after 95 minutes, the end – after 150 minutes. Meanwhile, on the curve of the setting kinetics (Figure 4), one can clearly distinguish three periods:

- 1) 0–40 minutes is lack of a set of plastic strength;
- 2) 40–80 min is a slow increase in plastic strength;
- 3) 80–150 min is intensive growth of plastic strength until it reaches 387 kPa, corresponding to the end of the setting.

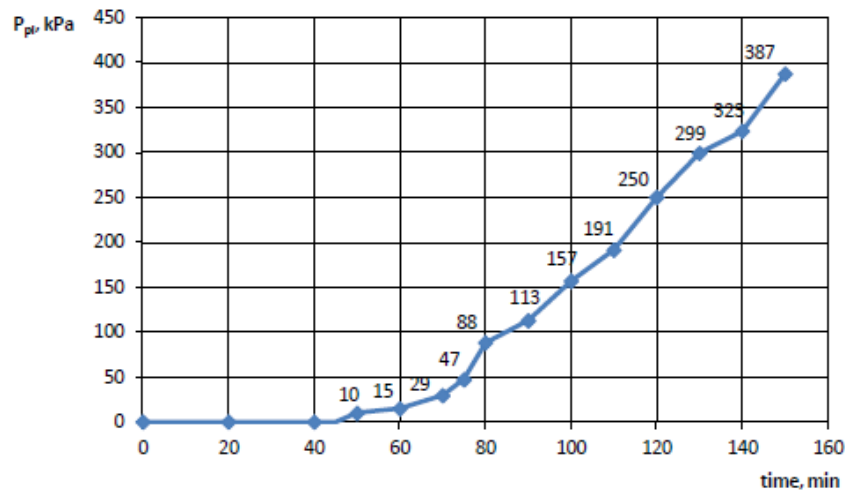


Figure 4. Flocculation kinetics of fresh CSSB-paste.

It was found that the appearance of the deformation diagrams (Figure 5) of the hardened binder paste differs significantly at different hardening times. So, at the age of 1 day, the elasticity zone is absent on the diagram, that is, the destruction occurs according to the pseudoplastic type. On the diagrams of deformation of samples, hardened for 3, 7, 28 days, the elastic zone is clearly fixed, the length of the de

scending branch of the diagram decreases. Thus, as hardening increases, rigidity increases and the plasticity of the system decreases. However, on the deformation diagrams of samples aged 14 days, the reappearance of the zone of plastic deformations was recorded, which corresponded to a temporary decrease in the modulus of elasticity. The kinetic curve of hardening (Figure 6) shows an intensive increase in strength up to 3 days of hardening, in the period of 3–14 days, strength increases by 30 %, and in the period of 14–28 days – almost by 2 times. It is important to emphasize that during the periods of 1–3 days and 14–28 days, a significant increase in the modulus of elasticity of the hardened binder paste occurs, it increases by 4 and 5 times, respectively (Table 2).

4. Discussion

The hydration and hardening of CSSB differ from the traditionally distinguished stages of the hydration of cement systems.

Classically [23, 24], the process of hydration of Portland cement is divided into periods

– initial and pre-induction ($\tau = 0\text{--}30$ min), when the rapid nucleation of particles of the primary hydrate CSH occurs;

– induction ($\tau = 30$ min 2 hours) – the growth of CSH primary and secondary hydrate films on cement grains that block the flow of water to the clinker nodule and slow down the hydration and setting process;

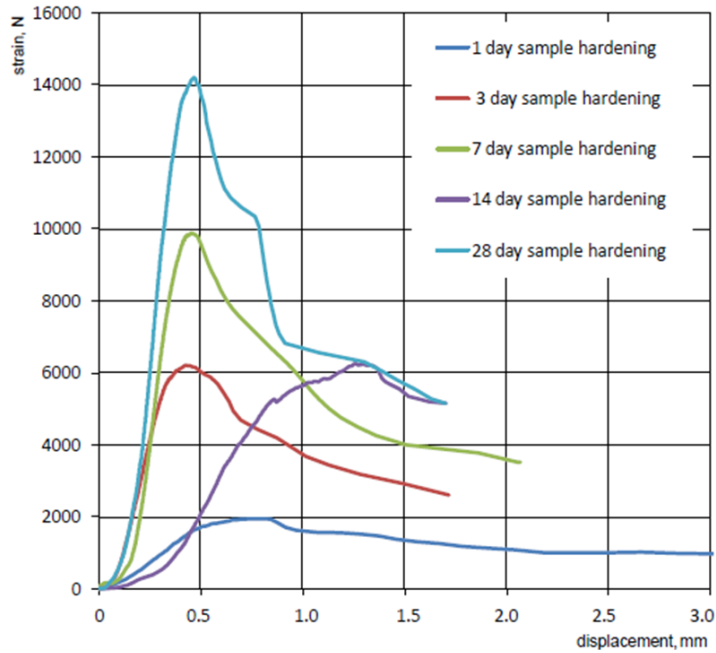


Figure 5. Tested hardened CSSB pastes «strain σ – displacement Δ » experimental results.

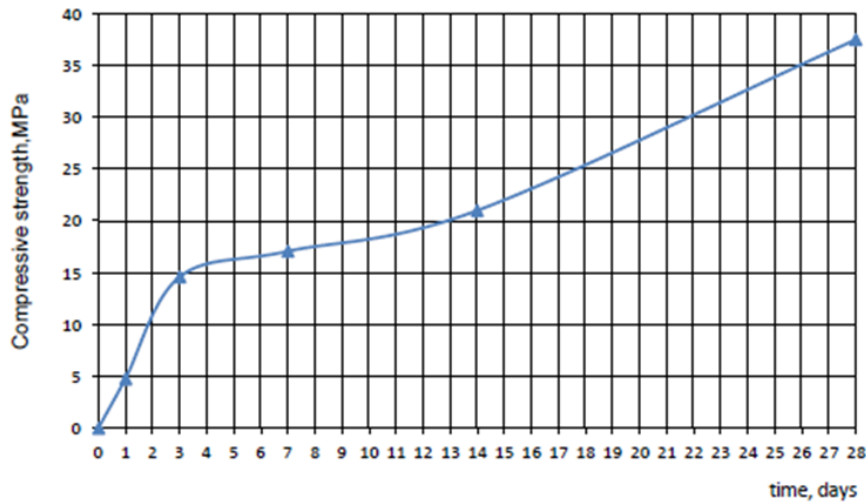


Figure 6. Hardening kinetics of CSSB.

Table 2. Hardening kinetics data.

Time, days	1	3	7	14	28
Compressive strength, MPa	4.7	14.6	17.1	21.0	37.5
Young's modulus, MPa	340	1390	1536	676	3398

– acceleration ($\tau = 2\text{--}12$ hours) – agglomeration of primary and secondary hydrates of CSH, the formation of crystalline intergrowths, the process of mass crystallization of $\text{Ca}(\text{OH})_2$, as a result of which the system sets and quickly hardens;

– deceleration (12 hours – 7 days) – hydration of C_2S , topochemical transformations of agglomerates of the secondary hydrate into the tertiary, about 30 % of cement enters the reaction by the age of about 7 days, as a result, this is the period of the most intensive increase in strength;

– slow interaction ($\tau \geq 7$ days) – recrystallization during spontaneous and self-organizing structure formation with the formation of a single three-dimensional structure of cementitious substance, which is accompanied by a slow monotonous increase in strength.

According to the obtained flocculation curve (Figure 4), the CSSB is characterized by practically the absence of an increase of plastic strength in the period up to 80 min from the moment of flocculation. It can be assumed that the reason for this is the slow dissolution of slag grains and the delay in the onset of hydration phases. Only after 80 minutes does the intensive growth of plastic strength begin, as a result, the setting onset time (150 minutes) corresponds to the standard range of setting onset time for Portland cement (120–160 minutes).

If for Portland cement, the acceleration period is associated with the formation of a spatial framework in the system as a result of mass crystallization of $\text{Ca}(\text{OH})_2$, for CSSB the crystalline phase of portlandite is not observed even on the first day of hardening. During this period, highly basic primary calcium hydrosilicates $2\text{CaO}\cdot\text{SiO}_2\cdot\text{H}_2\text{O}$ prevail in hydration products, which are classified as a dendrite-like and amorphous morphological type, which leads to low strength of crystallization contacts [25]. Therefore, it is logical that by the first day of hardening the system has an anomalous deformation diagram for solids (Figure 5), low strength and modulus of elasticity.

In a period of 1 to 3 days of hardening of CSAB, the most intensive increase in the strength of the system and its elasticity occurs. The deformation diagrams clearly show the elasticity zone, which may be due to the formation of a crystalline framework from the phases of the secondary hydrates $6\text{CaO}\cdot 4\text{SiO}_2\cdot 3\text{H}_2\text{O}$ of fibrous-needle morphology, crystals of ettringite and AFt-phases, which ensure the greatest number and strength of contacts in a volume unit. The presence of secondary hydrates, a rapid increase in strength allows us to correlate this period with the period of deceleration of the hydration process.

However, further characteristics of the CSSB hardening process are significantly different from cement systems. In the period of 3–14 days, the strengthening of the system slows down dramatically, and the sample deformation diagram on the 14th day of hardening again acquires an anomalous character, characterized by a long plateau of pseudoplastic deformations. This is naturally accompanied by a decrease in the modulus of elasticity by more than two times with respect to its value at the age of 7 days. This may be due to the repeated mass formation of primary hydrates $2\text{CaO}\cdot\text{SiO}_2\cdot\text{H}_2\text{O}$. As a result, crystallization pressure can occur in the already formed crystalline framework, and the combination of $2\text{CaO}\cdot\text{SiO}_2\cdot\text{H}_2\text{O}$ crystals, as noted above, has a low strength of crystallization contacts.

In 14–28 days, there is an intensive increase in the strength and elasticity of the system, which can be correlated with the processes of self-organized structure formation [25]. In the hardening system, the content of low-basic tobermorite-like calcium hydrosilicates $(\text{CaO})_x\cdot\text{SiO}_2\cdot z\text{H}_2\text{O}$, $x\text{CaO}\cdot\text{SiO}_2\cdot z\text{H}_2\text{O}$ increases, which have a fibrous-needle morphology and provide an increase in the energy of destruction due to a large number of randomly placed in the volume contacts and interfaces.

It is important to emphasize that during all hardening periods, the portlandite $\text{Ca}(\text{OH})_2$ phase is absent in the composition of CSSB hydration products. This indicates that the solution very quickly reaches saturation with HSiO_3^- , SiO_3^{2-} , $\text{H}_2\text{SiO}_4^{2-}$, Al^{3+} , AlO_2^- ions, which bind Ca^{2+} , CaOH^+ cations to hydrate compounds, preventing the crystallization of Portlandite $\text{Ca}(\text{OH})_2$. Also, one of the least active slag phases, the mellite phase $8\text{CaO}\cdot 3\text{Al}_2\text{O}_3\cdot\text{MgO}\cdot 5\text{SiO}_2$, almost immediately disappears in the hydrated binder. On this basis, it can be argued that the resulting binder is characterized by high hydraulic activity. Most likely, this is ensured by the good solubility of ultramicrodispersed particles with a diameter of $d \sim 1\div 6 \mu\text{m}$ with an amorphized surface, which is the result of mechanochemical activation during grinding in the presence of C-3 superplasticizer as a complex of surface-active substances.

5. Conclusions

1. The results of a comprehensive assessment of the characteristics of the clinkerless slag-silica binder and the parameters of its structure formation and hardening made it possible to confirm the effectiveness of nanotechnological activation of its components at the manufacturing stage, using the hydraulic potential of nano- and micro-sized particles at the hardening stage. It is the presence of an increased amount of microsilica and almost 50 % of ultramicrodispersed particles with a diameter of $d \sim 1 \div 6 \mu\text{m}$ in the composition of CSSB that made it possible to increase the hydraulic activity of the binder and ensure its setting and hardening speed under normal temperature and humidity conditions ($t = 20 \text{ }^\circ\text{C}$, $\text{RH} = 95 \pm 5 \%$), comparable to the rate of these processes for Portland cement.

2. As a result of studying the changes of CSSB phase composition during hydration and structuration processes, it was established that CSSB has high hydraulic activity. In the hardening system, the content of low-basic tobermorite-like calcium hydrosilicates $(\text{CaO})_x\cdot\text{SiO}_2\cdot z\text{H}_2\text{O}$, $x\text{CaO}\cdot\text{SiO}_2\cdot z\text{H}_2\text{O}$ increases, which have a fibrous-needle morphology and provide an increase in the energy of destruction due to a large number of randomly placed in the volume contacts and interfaces.

3. CSSB is characterized by the onset of setting after 150 minutes, strength 17.1 MPa at the age of 7 days, 37.5 MPa at 28 days. The setting and strength indicators of the clinkerless slag-silica binder meet the requirements for physico-mechanical properties of cement grade 32.5 EN 197-1:2000 "Cement – Part 1: Composition, specifications and conformity criteria for common cements". This allows us to recommend the resulting binder for the manufacturing building products and structures both in factory and in building conditions.

6. Acknowledgement

This research work has been financed by the Russian Foundation for Basic Research (RFBR), Project 19-38-50028.

References

1. Rakhimova, N.R., Rakhimov, R.Z. The influence of the type and content zeolite containing additions on the properties and composition slag-alkaline bindings with liquid glass solution. Non-Traditional Cement & Concrete III. Proceedings of the International Symposium. Brno, June 10–12, 2008. Pp. 640–646.
2. Rakhimov, R.Z., Rakhimova, N.R. Properties, composition and structure of the slag-alkaline stone with microsilica adding. Non-Traditional Cement & Concrete III. Proceedings of the International Symposium. Brno. June 10–12. 2008. Pp. 647–652.
3. Rakhimova, N.R., Rakhimov, R.Z. Alkali-activated cements and mortars based on blast furnace slag and redclay brick waste. Materials and Design. 2015. No. 8. Pp. 324–331. DOI: 10.1016/j.matdes.2015.06.182
4. Akhmetzhanov, T., Danenova, G., Rusanov, A. Optimization of Low-Clinker Binder Production Technological Parameters. Key Engineering Materials. 2016. Vol. 683. Pp. 243–249. DOI: 10.4028/www.scientific.net/KEM.683.243
5. Ludwig, H.-M. Future cements and their properties. Cement International. 2012, Vol. 10. No. 4. Pp. 80–89.
6. Franco de Carvalho, J.M., Melo, T.V.D., Fontes, W.C., Batista, J.O.D.S., Brigolini, G.J., Peixoto, R.A.F. More eco-efficient concrete: An approach on optimization in the production and use of waste-based supplementary cementing materials. Construction and Building Materials. 2019. Vol. 206. Pp. 397–409. DOI: 10.1016/j.conbuildmat.2019.02.054.
7. Mikheenkov, M.A., Sheshukov, O.Y., Nekrasov, I.V., Egiazar'yan, D.K., Lobanov, D.A. Production of mineral binder from steel-smelting slag. Steel in Translation. 2016. Vol. 46. No. 3. Pp. 232–235. DOI: 10.3103/S0967091216030098.
8. Erofeev, V.T., Rodin, A.I., Yakunin, V.V., Bogatov, A.D., Bochkin, V.S., Chegodajkin, A.M. Alkali-activated slag binders from rock-wool production wastes. Magazine of Civil Engineering. 2018. 82(6). Pp. 219–227. DOI: 10.18720/MCE.82.20. (rus)
9. Sun, Z., Lin, X., Liu, P., Wang, D., Vollpracht, A., Oeser, M. Study of alkali activated slag as alternative pavement binder. Construction and Building Materials. 2018. Vol. 186. Pp. 626–634. DOI 10.1016/j.conbuildmat.2018.07.154.
10. Fediuk, R.S., Mochalov, A.V., Pezin, D.N., Liseitsev, Y.L. Composite Binders for Concretes with Improved Impact Endurance. Inorganic Materials: Applied Research. 2019. No. 10(5). Pp. 1177–1184.
11. Tan, H., Deng, X., He, X., et al. Compressive strength and hydration process of wet-grinded granulated blast-furnace slag activated by sodium sulfate and sodium carbonate. Cement and Concrete Composites. 2019. Vol. 97. Pp. 387–398. DOI: 10.1016/j.cemconcomp.2019.01.012.
12. Gartner, E., Sui, T. Alternative cement clinkers. Cement and Concrete Research. 2018. Vol. 114. Pp. 27–39. DOI: 10.1016/j.cemconres.2017.02.002.
13. Janowska-Renkas, E., Kowalska, J. Use of fly ash from fluidized bed boilers in clinker-slag-ash based binders. MATEC Web of Conferences. 2018. Vol. 174. No. 02002. DOI: 10.1051/mateconf/201817402002.
14. Sokov, V.N. Complex Clinker-Less Binder Made from Refractory Wastes and Products Based on it. Refractories & Industrial Ceramics. 2016. Vol. 57. No. 2. Pp. 185–188. DOI 10.1007/s11148-016-9951-4.
15. Funk, B., Trettin, R., Zoz, H. From slag to high performance concrete – Manufacturing FuturBeton. Materials Today: Proceedings. 2017. Vol. 4. Pp. 81–86. DOI: 10.1016/j.matpr.2017.09.171.
16. Mikheenkov, M.A., Sheshukov, O.Y., Nekrasov, I.V., Egiazar'yan, D.K., Lobanov, D.A. Production of mineral binder from steel-smelting slag. Steel in Translation. 2016. Vol. 46. No. 3. Pp. 232–235. DOI: 10.3103/s0967091216030098
17. Khudhair, M.H.R., Elyoubi, M.S., Elharfi, A. Development of a new hydraulic binder (composite cement) based on a mixture of natural Pozzolan active 'PN' and Pure Limestone 'P,Lime': Study of the physical-chemical and mechanical properties. Journal of Materials and Environmental Science. 2017. Vol. 8. No. 3. Pp. 902–910.
18. Erofeev, V.T., Rodin, A.I., Yakunin, V.V., Bogatov, A.D., Bochkin, V.S., Chegodajkin, A.M. Alkali-activated slag binders from rock-wool production wastes. Magazine of Civil Engineering. 2018. Vol. 82. No. 6. Pp. 219–227. DOI: 10.18720/MCE.82.20. (rus)
19. Chernyshev, E.M., Artamonova, O.V., Slavcheva, G.S. Concepts and technology base nanomodification of structures of building composites. Part 3: effective nanomodification of systems and structures of cement hardening cement stone (criteria and conditions). Stroitel' nye Materialy [Construction Materials]. 2015. No. 9. Pp. 54–63.
20. Volzhensky, A.V., Burov, Yu.S., Vinogradov, B.N., Gladkikh, K.V. Betony i izdeliia na osnove shlakov i zol [Concrete and products based on slag and ashes]. Stroyizdat. Moscow, 1969. 392 p. (rus)
21. Pashchenko, A.A. Teoriya tsementa [Theory of cement]. Budivelnik. Kiev, 1991. 168 p. (rus)
22. Granovsky, I.G. Strukturnoobrazovanie v miner-al'nykh viazhushchikh sistemakh [Structuring in mineral binders systems]. Naukova Dumka. Kiev, 1984. 300 p. (rus)
23. Artamonova, O.V., Slavcheva, G.S. Structure of cement systems as objects of nanomodification. Scientific Herald of the Voronezh State University of Architecture and Civil Engineering. Construction and Architecture. 2016. No. 1(29). Pp. 13–26.

Contacts:

Galina Slavcheva, +7(960)1329475; gslavcheva@yandex.ru
 Djumageldy Baidzhanov, +7(7212)569506; BDO3@yandex.ru
 Maxim Khan, +7(777)6101686; han_maks@mail.ru
 Maria Shvedova, +7(951)8610601; marishwedowa@mail.ru
 Yedil Imanov, +7(747)3443017; e.imanov91@mail.ru

© Slavcheva, G.S., Baidzhanov, D.O., Khan, M.A., Shvedova, M.A., Imanov, Y.K., 2019



DOI: 10.18720/MCE.92.8

Бесклинкерное шлако-кремнеземистое вяжущее: параметры структурообразования и кинетика твердения

Г.С. Славчева^{а*}, Д.О. Байджанов^б, М.А. Хан^б, М.А. Шведова^с, Е.К. Иманов^б

^а Воронежский государственный технический университет, г. Воронеж, Россия

^б Карагандинский государственный технический университет, г. Караганда, Республика Казахстан

^с Воронежский государственный архитектурно-строительный университет, г. Воронеж, Россия

* E-mail: gslavcheva@yandex.ru

Ключевые слова: бесклинкерное вяжущее, техногенное сырье, структурообразование, схватывание, твердение, фазовый состав, прочность

Аннотация. В статье рассматриваются результаты экспериментальных исследований, выполненные с целью обеспечения возможности получения высокопрочных композитов на основе бесклинкерного вяжущего, твердеющего в условиях нормальной температуры и влажности, без тепловой обработки. Разработанное авторами вяжущее, относящееся к классу шлако-щелочных, было получено путем совместного помола всех компонентов в присутствии суперпластификатора, его состав отличается от известных аналогов высоким содержанием микрокремнезема. Метод лазерной гранулометрии, XRD – метод были использованы для оценки размера частиц, фазового состава исходных компонентов и бесклинкерного вяжущего. Кинетика схватывания оценивалась пенетро-метрическим методом. Кинетика твердения оценивалась по результатам механических испытаний образцов через 1, 3, 7, 14, 28 суток твердения. В результате выявлены отличительные особенности основных периодов гетерогенных процессов структурообразования полученного вяжущего, отличительные особенности кинетики схватывания, механического поведения на разных этапах твердения в нормальных температурно-влажностных условиях. Установлено, что присутствие в составе повышенного количества микрокремнезема, и почти 50 % активированных при помоле частиц диаметром $d \sim 1 \div 6 \mu\text{m}$ позволило повысить гидравлическую активность вяжущего и обеспечить скорость его схватывания и твердения в нормальных температурно-влажностных условиях, сопоставимую со скоростью данных процессов для портландцемента. Показатель схватывания и прочностные показатели бесклинкерного вяжущего соответствуют требованиям к физико-механическим показателям цемента марки 32.5 согласно EN 197-1:2000.

Литература

1. Rakhimova N.R., Rakhimov R.Z. The influence of the type and content zeolite containing additions on the properties and composition slag-alkaline bindings with liquid glass solution // Non-Traditional Cement & Concrete III. Proceedings of the International Symposium. Brno. June 10–12. 2008. Pp. 640–646.
2. Rakhimov R.Z., Rakhimova N.R. Properties, composition and structure of the slag-alkaline stone with microsilica adding // Non-Traditional Cement & Concrete III. Proceedings of the International Symposium. Brno. June 10–12. 2008. Pp. 647–652.
3. Rakhimova N.R., Rakhimov R.Z. Alkali-activated cements and mortars based on blast furnace slag and redclay brick waste // Materials and Design. 2015. No. 8. 23. Pp. 324–331. DOI: 10.1016/j.matdes.2015.06.182
4. Akhmetzhanov T., Danenova G., Rusanov A. Optimization of Low-Clinker Binder Production Technological Parameters // Key Engineering Materials. 2016. Vol. 683. Pp. 243–249. DOI: 10.4028/www.scientific.net/KEM.683.243
5. Ludwig H.-M. Future cements and their properties // Cement International. 2012. Vol. 10. No. 4. Pp. 80–89.
6. Franco de Carvalho J.M., Melo, T.V.D., Fontes, W.C., Batista, J.O.D.S., Brigolini, G.J., Peixoto, R.A.F. More eco-efficient concrete: An approach on optimization in the production and use of waste-based supplementary cementing materials // Construction and Building Materials. 2019. 206. Pp. 397–409. DOI 10.1016/j.conbuildmat.2019.02.054.
7. Mikheenkov M.A., Sheshukov O.Y., Nekrasov I.V., Egiazar'yan D.K., Lobanov D.A. Production of mineral binder from steel-smelting slag // Steel in Translation. 2016. Vol. 46. No. 3. Pp. 232–235. DOI: 10.3103/S0967091216030098.
8. Ерофеев В.Т., Родин А.И., Якунин В.В., Богатов А.Д., Бочкин В.С., Чегодайкин А.М. Шлако-щелочные вяжущие из отходов производства минеральной ваты // Инженерно-строительный журнал. 2018. № 6(82). С. 219–227. DOI: 10.18720/MCE.82.20
9. Sun Z., Lin X., Liu P., Wang D., Vollpracht A., Oeser M. Study of alkali activated slag as alternative pavement binder // Construction and Building Materials. 2018. Vol. 186. Pp. 626–634. DOI 10.1016/j.conbuildmat.2018.07.154.
10. Fediuk R.S., Mochalov A.V., Pezin D.N., Liseitsev Y.L. Composite Binders for Concretes with Improved Impact Endurance // Inorganic Materials: Applied Research. 2019. No. 10(5). Pp. 1177–1184.

11. Tan H., Deng X., He X., et al. Compressive strength and hydration process of wet-grinded granulated blast-furnace slag activated by sodium sulfate and sodium carbonate // *Cement and Concrete Composites*. 2019. No. 97. Pp. 387–398. DOI: 10.1016/j.cemconcomp.2019.01.012.
12. Gartner E., Sui T. Alternative cement clinkers // *Cement and Concrete Research*. 2018. Vol. 144. Pp. 27–39. DOI: 10.1016/j.cemconres.2017.02.002.
13. Janowska-Renkas E., Kowalska J. Use of fly ash from fluidized bed boilers in clinker-slag-ash based binders // *MATEC Web of Conferences*. 2018. Vol. 174. Article number 02002. DOI: 10.1051/mateconf/201817402002.
14. Sokov V.N. Complex Clinker-Less Binder Made from Refractory Wastes and Products Based on it // *Refractories & Industrial Ceramics*. 2016. Vol. 57. No. 2, 1 July 2016. Pp. 185–188. DOI 10.1007/s11148-016-9951-4.
15. Funk B., Trettin R., Zoz H. From slag to high performance concrete – Manufacturing FuturBeton // *Materials Today: Proceedings*. Vol. 4, 2017. Pp. 81–86. DOI: 10.1016/j.matpr.2017.09.171.
16. Mikheenkov M.A., Sheshukov O.Yu., Nekrasov I.V., Egiazar'yan D.K., Lobanov D.A. Production of mineral binder from steel-smelting slag // *Steel in Translation*. 2016. Vol. 46. No. 3. Pp. 232–235. DOI: 10.3103/s0967091216030098
17. Khudhair M.H.R., Elyoubi M.S., Elharfi A. Development of a new hydraulic binder (composite cement) based on a mixture of natural Pozzolan active 'PN' and Pure Limestone 'P,Lime': Study of the physical-chemical and mechanical properties // *Journal of Materials and Environmental Science*. 2017. Vol. 8. No. 3. 2017. Pp. 902–910.
18. Ерофеев В.Т., Родин А.И., Якунин В.В., Богатов А.Д., Бочкин В.С., Чеодайкин А.М. Шлакощелочные вяжущие из отходов производства минеральной ваты // *Инженерно-строительный журнал*. 2018. № 6(82). С. 219–227. DOI: 10.18720/МСЕ.82.20
19. Чернышов Е.М., Артамонова О.В., Славчева Г.С. Концепции и основания технологий нано-модифицирования структур строительных композитов. Часть 3. Эффективное наномодифицирование систем твердения цемента и структуры цементного камня (критерии и условия) // *Строительные материалы*. 2015. № 9. С. 54–63.
20. Волженский А.В., Буров Ю.С., Виноградов Б.Н., Гладких К.В. Бетоны и изделия на основе шлаков и зол. М.: Стройиздат. 1969. 392 с.
21. Пашенко А.А. Теория цемента. Киев: Будівельник, 1991. 168 с.
22. Грановский И.Г. Структурообразование в минеральных вяжущих системах. Киев: Наукова думка, 1984. 300 с.
23. Artamonova O.V., Slavcheva G.S. Structure of cement systems as objects of nanomodification // *Scientific Herald of the Voronezh State University of Architecture and Civil Engineering. Construction and Architecture*. 2016. No. 1(29). Pp. 13–26.

Контактные данные:

Галина Станиславовна Славчева, +7(960)1329475; эл. почта: gslavcheva@yandex.ru

Джумагельды Омарович Байджанов, +7(7212)569506; эл. почта: BDO3@yandex.ru

Максим Александрович Хан, +7(777)6101686; эл. почта: han_maks@mail.ru

Мария Александровна Шведова, +7(951)8610601; эл. почта: marishwedowa@mail.ru

Едил Куттыбаевич Иманов, +7(747)3443017; эл. почта: e.imanov91@mail.ru

© Славчева Г.С., Байджанов Д.О., Хан М.А., Шведова М.А., Иманов Е.К., 2019



DOI: 10.18720/MCE.92.9

CO₂ curing of hydrated lime modified pervious concretes

H. Rahmani*, **M. Montazer Gheib**

University of Zanjan, Zanjan, Iran

* E-mail: hrahmani@znu.ac.ir

Keywords: carbonation curing, CO₂ absorption, hydrated lime, pervious concrete

Abstract. This paper presents the effect of carbonation curing on the properties of hydrated lime modified pervious concretes. Also, CO₂ absorption capacity (COAC) of the mixtures was investigated to more explanation of the results. Three mix designs containing of 0, 15 and 30 % of hydrated lime were considered. Water to cement ratio, cementitious material content, inner pressure of the chamber and workability of the mixtures were kept constant. Concrete samples were cured in the CO₂ chamber and then the conducted experiments were performed and the results compared with the results of moist cured concretes. The results showed a significant increase in the mechanical properties of the concretes at the initial time of CO₂ curing. Carbonation reactions were approximately stopped after 12 hours of CO₂ curing in which the concrete properties after 12 hours of CO₂ curing were closed together. Also, COAC of the mixtures increased by increasing hydrated lime substitution.

1. Introduction

Carbon dioxide (CO₂) as one of the major greenhouse gases causes world climate changes. It has been estimated that the CO₂ emission will be increased during the next decades, nevertheless the CO₂ concentration in the atmosphere is higher than the maximum allowable concentration. Therefore, sequestration of CO₂ is essential to reduce its concentration in the atmosphere [1]. Geological sequestration of CO₂ in oceans and other fluid storages such as aquifers and oil wells are in progress [2]. However, some minerals can react chemically with CO₂ and produce carbonates. Calcium and Calcium-silicate minerals can properly convert CO₂ to calcium carbonates, but they are rarely found in the nature. However, popular synthetic materials such as Portland cement as a calcium-silicate material and hydrated lime as a calcium material can be efficiently used to mineralize CO₂ to calcium carbonate. This process of direct sequestration of CO₂ is called carbonation curing or CO₂ curing of cement-based materials, where appropriate curing provides a proper mineralization of CO₂ [1, 3–5]. Since the pervious concretes are more porous, it is estimated that the mineralization of CO₂ is simply completed. Therefore, CO₂ curing of the hydrated lime modified pervious concretes is the main object of this study.

1 kg cement can absorb 0.5 kg CO₂ to form 1.5 kg silica gel and calcium carbonates [1]. Reactivity of calcium silicates and mineral admixtures with CO₂ were systematically studied by the researchers [6–9]. Carbonation curing or CO₂ curing improves compressive strength, surface hardness and durability of non-reinforced cement-based products [10–12]. However, the carbonation process reduces the pH of concrete and initiate the corrosion of reinforcing bars in concrete [13–16]. Therefore, non-reinforced concretes have a great potential to friendly absorb CO₂. This would be appreciated by the manufacturers of cement-based materials when CO₂ curing is accelerated by increasing of curing temperature, pressure, CO₂ concentration, porosity of concrete and water to cement ratio and also by adjusting the proper relative humidity (RH) of the chamber [17–19]. In addition, cement replacement materials and novel concretes have been investigated to absorb CO₂ in the last decades [9, 12, 17, 19–22]. For instance, Monkman and Shao have used slag-cement concrete to bind CO₂ [12] and Kou et al. and Zhan et al. have investigated CO₂ curing of concretes prepared with recycled aggregates [19–21]. Also, CO₂ curing of self-compacting and lightweight concretes have been systematically investigated by Shamsad et al. and Shi and Wu, respectively [17, 22]. Nevertheless several researchers have investigated carbonation curing of concretes including novel ones, but there is a limit research on CO₂ curing of pervious concretes [23, 24]. For instance, Hasegawa has investigated static and dynamic carbonation curing of pervious concrete using ordinary Portland cement and Portland limestone cement and concluded that the early carbonation curing (2 hours for static and 30 minutes for dynamic carbonation curing) significantly improves the

Rahmani, H., Montazer Gheib, M. CO₂ curing of hydrated lime modified pervious concretes. Magazine of Civil Engineering. 2019. 92(8). Pp. 106–114. DOI: 10.18720/MCE.92.9

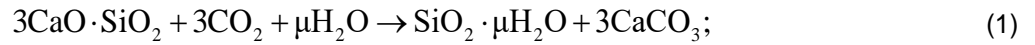
Рахмани Х., Монтазер Гейб М. Насыщение CO₂ гидратированного известью модифицированного проницаемого бетона // Инженерно-строительный журнал. 2019. № 8(92). С. 106–114. DOI: 10.18720/MCE.92.9



This work is licensed under a CC BY-NC 4.0

physical and mechanical properties of the concretes [23]. Sidhu indicated that the pervious concretes with 12 hours of CO₂ curing showed the highest compressive strength and the lowest porosity when they were compared with other curing regimes [24].

The major chemical reactions of CO₂ curing of cement-based materials such as concrete are given by Equations (1) and (2) [1, 5, 9, 17]. Also, CO₂ reacts with Ca(OH)₂ and forms CaCO₃, where the rate of reactions depends on the rate of CO₂ diffusion [5].



Nevertheless a lot of researches have been conducted on the properties and the durability of pervious concretes including modified ones [25–30], but carbonation curing of pervious concretes has not been completely investigated. Therefore CO₂ curing of pervious concretes is investigated in this study. Also, since hydrated lime can react with CO₂ and accelerate the CO₂ curing process of the concretes, substitution of hydrated lime is considered in the mixtures up to 30 % of cement to absorb more CO₂. It is predicted that the properties of pervious concretes will diminish in case of more substitution of hydrated lime because of low content of cement in the mixtures. Consequently, main objects of this study are the increasing of CO₂ absorption capacity and the improvement of mechanical and physical properties of pervious concretes simultaneously by means of carbonation curing.

2. Methods

2.1. Materials

Locally sourced ordinary Portland cement type I-425 and hydrated lime respectively produced by Kordestan and Espandar Company were used as cementitious materials. Chemical composition and L.O.I of the binders are shown in Table 1. Hydrated lime or calcium hydroxide is decomposed into calcium oxide and water when it is heated up to 500° and therefore its L.O.I is significant.

Table 1. Chemical composition and physical properties of the cement and hydrated lime (%).

	CaO	SiO ₂	Fe ₂ O ₃	Al ₂ O ₃	MgO	SO ₃	Ca(OH) ₂	L.O.I
Cement	64.2	22.2	3.6	4.9	1.41	1.76	–	0.7
Hydrated lime	72.26	–	–	–	3.02	–	91.14	23.74

Locally sourced crushed coarse silica aggregate was used to make the pervious concretes without using fine aggregates. Physical properties of the aggregate were measured according to ASTM C127 and ASTM C566 and the results are shown in Table 2. Also grading curve of the aggregate, which was measured according to ASTM C136, and lower and upper limit of ASTM C33, size number of 67 (4.75–19.0 mm) for pervious concretes, are shown in Figure 1. It is clear that the grading curve of the aggregate that is close to the lower limit of the ASTM standard is appropriate to produce pervious concretes.

Renewable silica gel with capacity of 40 % of water absorption was used to absorb the evaporated water in the CO₂ chamber during the carbonation curing of the pervious concretes.

Table 2. Physical properties of the aggregates.

Physical property	Maximum nominal size (mm)	Water absorption (%)	Moisture content (%)	Specific gravity (t/m ³)
Coarse aggregate	19	1.8	0.9	2.57

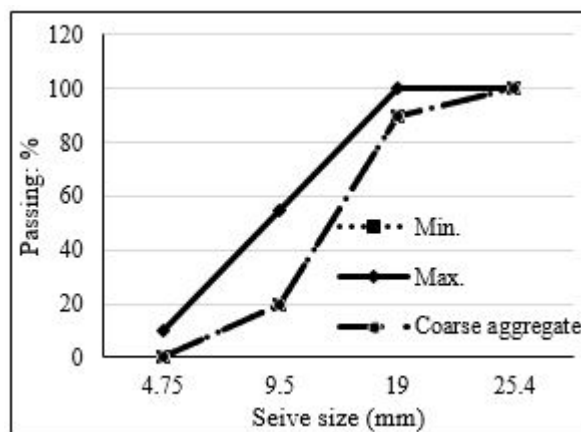


Figure 1. Grading curve of the coarse aggregate and lower and upper limits of ASTM C33.

2.2. Mix designs

Three mixtures containing 0, 15 and 30 % substitution of the hydrated lime were considered, where the mixture without substitution of hydrated lime was considered as the control one. The control mixture was designed using ACI 211.3R-02 [31] by assuming the compressive strength of 15 MPa and void content of 20 %, where water to cement ratio and the cement content were obtained equal to 0.35 and 350 kg/m³, respectively to obtain a desired pervious concrete. Slump of all mixtures were obtained lower than 20 mm and therefore there was no need to use superplasticizer. Water to binder ratio was kept constant in the mixtures. Details of the mixtures are summarized in Table 3.

Table 3. Details of mix designs.

	Cement (kg/m ³)	Hydrated lime (kg/m ³)	Hydrated lime (%)	Coarse aggregate (kg/m ³)
C1	350	0	0	1539
C2	297.5	52.5	15	1539
C3	245	105	30	1539

All mixtures were mixed for at least 3 minutes and the fresh concretes were then placed in the moulds ready to be compacted. Dimensions of the moulds which depend on the experiment type are mentioned in the next section. All mixtures were poured in three layers and each layer was gently compacted with 16 mm diameter of a bar in a same manner. Specimens were demoulded after 24 hours of moist curing and were then placed in a water bath (moist curing) or in the CO₂ chamber (CO₂ curing, see Figure 2). Considered specimens for CO₂ curing had been dried for 2 hours at a laboratory room before applying carbonation process to reduce their moisture content as the same as control room.

2.3. Experiments

Compressive and tensile strength, void content, permeability and CO₂ absorption capacity of the pervious concretes were investigated in this study, where the experiments were conducted at the age of 3, 7 and 28 days of moist curing and 1, 2, 4, 6, 12 and 24 hours of CO₂ curing. Two specimens were considered for each experiment and their average was reported. Compressive strength and void content testing were performed on 100×100×100 mm cubic specimens according to the BS 1881-116 test method. Void content of the specimens can be calculated using Equation (3), where W_1 is the oven dry weight of the specimen, W_2 is the weight of the immersed specimen in water, Vol is the volume of the specimen and ρ_w is the water density [32].

$$V_c(\%) = 1 - \left[\frac{W_1 - W_2}{\rho_w \times Vol} \right] \times 100. \quad (3)$$

Tensile strength testing was carried out on 100×200 mm cylindrical specimens according to ASTM C496. Water permeability of the 100×100 mm cylindrical specimens was measured according to Darcy's law. Permeability coefficient (k (cm/s)) of the specimens is calculated using Equation (4), where α and A (cm²) are the cross section area of the tube and the specimen, respectively, L (cm) is the specimen length, h_1 and h_2 (cm) are the water head in the tube before and after the measurements, respectively and t (s) is the time of head loss from h_1 to h_2 [33].

$$k = \frac{\alpha \cdot L}{A \cdot t} \times \ln \left(\frac{h_1}{h_2} \right). \quad (4)$$

CO₂ absorption capacity (COAC) test was conducted to explanation of the physical and mechanical properties of the CO₂ cured pervious concretes containing hydrated lime powders. No additional specimens were considered to COAC determination. First, the CO₂ cured cubic specimens were tested for the considered purpose and then were completely dried for 24 hours at the temperature of 105 °C. Then, some binder powder about 40 g were prepared by separation of the coarse aggregates from the specimens. Finally, COAC of the powders was determined by measuring the mass loss of the powder between 500 °C and 850 °C [14] and using Equation (5), where M_{850} and M_{500} are the powder mass at the correlated temperatures. Binder powders were placed into the oven and retained for 1 hour at the relevant temperature to achieve the constant mass.

$$COAC(\%) = \frac{M_{500} - M_{850}}{M_{500}} \times 100. \quad (5)$$

2.4. Carbonation curing of the specimens

The setup similar to the research of Kou et al [21] was used to apply CO₂ curing on the hydrated lime modified pervious concretes and schematic process of CO₂ curing is shown in Figure 2. To process the CO₂ curing, first the specimens were placed in the chamber and a vacuum was then applied to the chamber before

the CO₂ injection. Then, CO₂ gas having a purity of 97 % was used to simulate a point source. The pressure inside the chamber was kept constant equal to 1 MPa using a regulator to ensure a continuous supply of CO₂ gas. Temperature and humidity of the chamber were continuously controlled during the curing time using a group sensor. CO₂ curing time of the mixtures was considered equal to 1, 2, 4, 6, 12 and 24 hours. Then the CO₂ cured specimens were tested corresponding to the test program. Temperature of the chamber varied between 16–25 °C and the humidity of the chamber was controlled using silica gel. It should be noted that further silica gels were needed to absorb the evaporated water because of high porosity of the specimens.

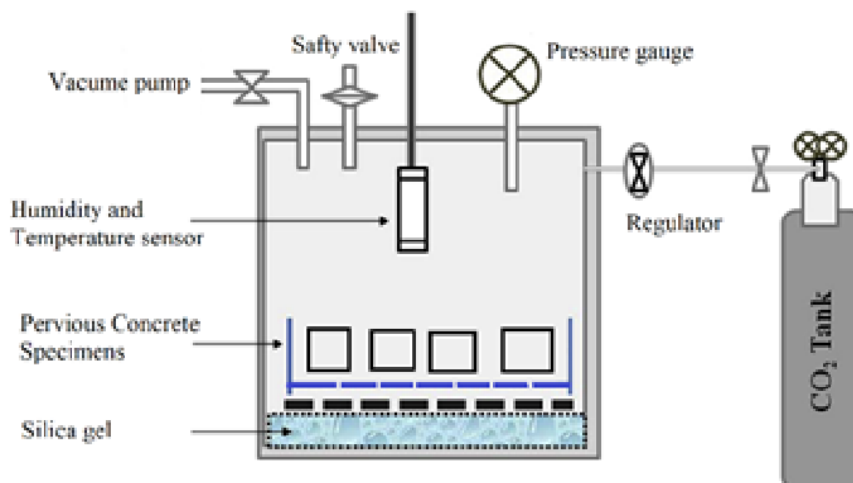


Figure 2. Schematic process of CO₂ curing similar to [21].

3. Results and discussion

3.1. Compressive strength

The results of the compressive strength tests are shown in Table 4 and Figures 3, 4. Table 4 shows the measured results and Figure 3 shows the compressive strength development over curing time in both cases of curing. Figure 4 shows the variations of relative compressive strength of CO₂ cured samples to the relevant 28 days compressive strength of moist cured samples.

Figure 3-a shows the control mixture was obtained the desired compressive strength after 28 days of moist curing. Also, mixtures covered about 50 % and 75 % of 28 days compressive strength after 3 and 7 days of moist curing, respectively. Figures 3-b and 4 show that the compressive strength increases with the increasing CO₂ curing time, where the increasing rate decreases with time in which the control mixture was obtained 45 % of 28 days moist cured compressive strength after 2 hours of CO₂ curing. This result is consistent with those found with the CO₂ curing of slag cement concrete [12]. These improvements are about 66 and 82 %, respectively after 6 and 12 hours of CO₂ curing. Also, the strength of C1 increased by 43 % and 74 % when CO₂ curing time was increased from 1 to 2 and 4 hours, respectively. These values have been reported about 16 % and 25 %, respectively for lightweight concretes [17]. Baojian et al. have reported 28 % and 42 % increasing in the strength when CO₂ curing time was increased from 6 to 12 and 24 hour [34], respectively for recycled aggregate concretes while these values are obtained about 24 % and 28 %, respectively in this study. Porous media of pervious concretes facilitates the penetration of CO₂ gas and therefore improvements are significant at the early ages of CO₂ curing in comparison with other concretes and consequently these improvements are declined for the later ages. Improvement of the compressive strength after 12 hours of CO₂ curing is negligible. Similar results were obtained for the concretes containing hydrated lime powder. Since the specimens are porous, CO₂ gas can simply be directed inside the specimens and the chemical reactions are completed. Therefore, first hours of initial CO₂ curing is more effective and can be simply used in the curing process of concretes.

Table 4. The results of the compressive strengths (MPa).

Mixture code	Moist curing (days)			CO ₂ Curing (hours)					
	3	7	28	1	2	4	6	12	24
C1	7.01	10.40	14.94	4.70	6.73	8.20	9.82	12.19	12.53
C2	8.04	11.52	15.58	5.03	7.25	9.18	10.05	12.68	12.94
C3	6.03	7.95	10.07	2.58	4.80	6.45	6.86	8.55	8.80

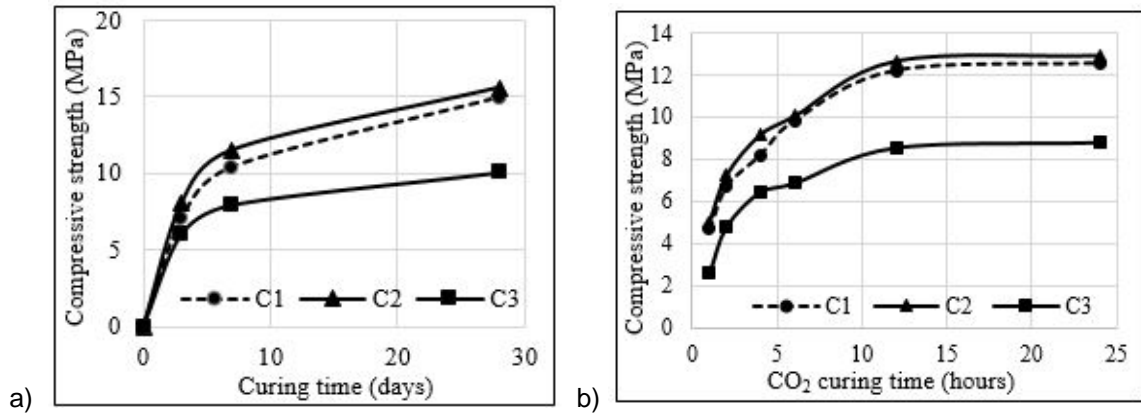


Figure 3. Compressive strength of the mixtures, a) moist cured and b) CO₂ cured.

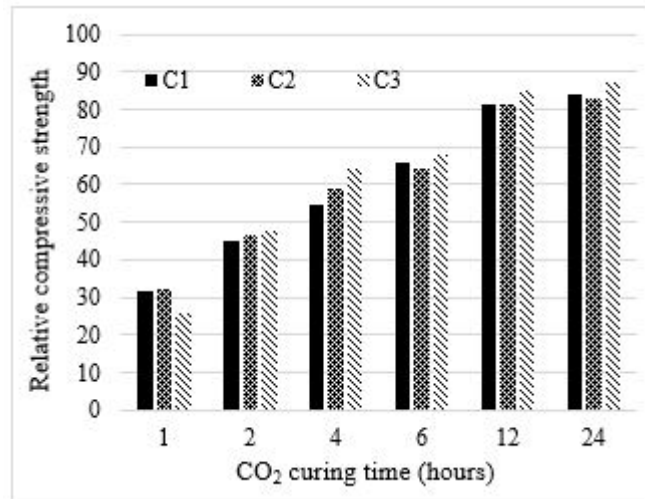


Figure 4. Relative compressive strength of CO₂ cured concretes to the relevant 28 days moist cured concretes.

Mixtures containing 15 % of hydrated lime showed higher compressive strength in both curing cases, but the mixture with substitution of 30 % hydrated lime showed lower compressive strength. This is due to in fact that the cementitious behavior of the hydrated lime is less than the cement and the 15 % substitution of the cement by hydrated lime make a dense structure of the binder. It is nevertheless predicted that the concretes containing 30 % hydrated lime absorb more CO₂ gas (see the COAC results), but their compressive strength are still lower than the control concretes.

3.2 Tensile strength

The results of tensile strengths tests are shown in Table 5. Results are similar to the compressive strength test results and the tensile strengths increase with increasing the curing time in both case of curing regimes. Table 6 present the tensile/compressive ratios and it is clear that the ratio decreased by increasing the curing time. The ratio was reached to 0.12–0.14 at the end of curing time. When the curing is continued, the compressive strength is increased more than tensile strength since the micro-cracks control the tensile strength [35] and therefore the tensile/compressive ratio is decreased.

Table 5. The results of the tensile strengths (MPa).

Mixture code	Moist curing (days)			CO ₂ Curing (hours)					
	3	7	28	1	2	4	6	12	24
C1	1.04	1.51	2.01	0.55	0.98	1.11	1.17	1.24	1.56
C2	1.05	1.43	2.00	0.72	0.90	0.99	1.22	1.30	1.55
C3	0.98	1.10	1.26	0.58	0.70	0.95	1.02	1.15	1.23

Table 6. Tensile/compressive ratio of the pervious concretes.

Mixture code	Moist curing (days)			CO ₂ Curing (hours)					
	3	7	28	1	2	4	6	12	24
C1	0.15	0.15	0.13	0.12	0.15	0.14	0.12	0.10	0.12
C2	0.13	0.12	0.13	0.14	0.12	0.11	0.12	0.10	0.12
C3	0.16	0.14	0.12	0.22	0.15	0.15	0.15	0.13	0.14

3.3. Void content

Void content of the specimens at the relevant curing times are shown in Table 7. It is clear that the void content of the concretes decreases with the increase of curing time in both cases of curing regimes and the reduction in Void content after 12 hours of CO₂ curing can be neglected similar to the compressive strength test results. Also, void contents of pervious concretes are controlled by aggregate composition rather than the porosity of the binder and therefore the variations of the void contents are ranged between 16.46–18.92 % according to Table 6.

Table 7. Void content of the pervious concretes (%).

Mixture code	Moist curing (days)			CO ₂ Curing (hours)					
	3	7	28	1	2	4	6	12	24
C1	18.64	17.80	17.09	17.65	17.50	17.40	16.81	16.63	16.57
C2	18.13	17.35	16.55	17.25	17.25	17.10	16.82	16.63	16.46
C3	18.92	18.31	17.43	18.80	18.34	17.68	17.47	17.12	17.10

Void contents of the mixtures are obtained in the predicted range of the mix designs, but the void content of the concretes containing hydrated lime after 12 hours of CO₂ curing is lower than that of the relevant mixtures after 28 days of moist curing. It is clarify that the mixtures containing hydrated lime have high ability to absorb further CO₂ gas. Figure 5 shows the relation between the compressive strength and void content in case of CO₂ curing, where the compressive strength is directly depended to the void content and it is increased by decreasing the void content.

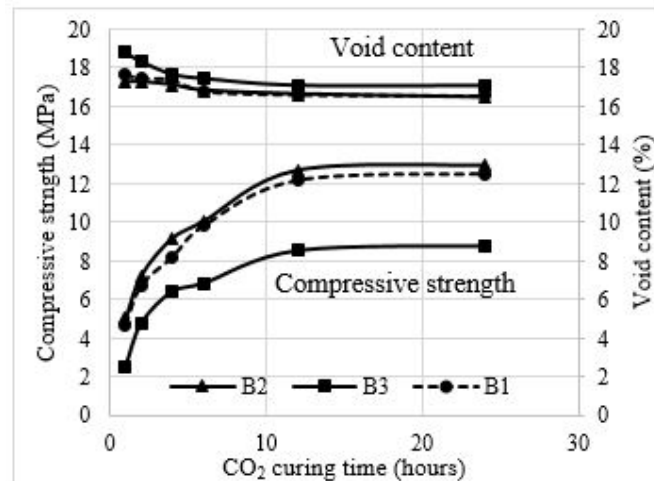


Figure 5. Validation of compressive strength and void content.

3.4. Water Permeability

Permeability coefficient of the specimens were calculated using Equation (5) and the results are summarized in Table 8. Water permeability of the concrete specimens depends on the connectivity of the pores and it is estimated that the permeability and void content are correlated and the results (see Figure 6) confirm such correlation and the permeability increases by increasing the void content. Also, permeability of the concretes decreases by increasing the curing time in both cases of curing.

Table 8. Permeability coefficients of the hydrated lime modified pervious concretes (cm/s).

Mixture code	Moist curing (days)			CO ₂ Curing (hours)					
	3	7	28	1	2	4	6	12	24
C1	6.63	5.37	5.30	7.00	6.84	6.48	5.60	5.06	5.08
C2	6.21	4.85	4.45	6.31	5.99	5.61	5.26	5.01	4.75
C3	7.21	6.82	6.48	8.37	7.30	6.77	6.72	6.50	6.50

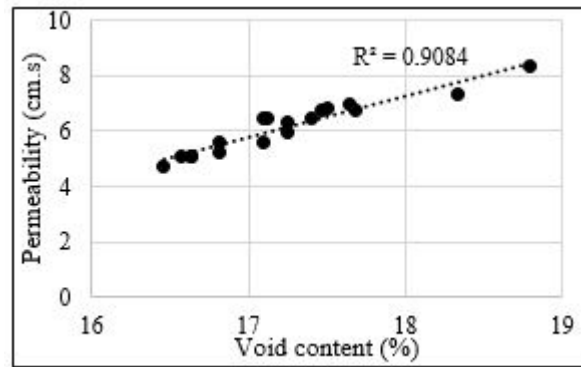


Figure 6. Correlation between permeability coefficient and void content.

3.5. CO₂ absorption capacity (COAC)

COAC of the concrete samples are shown in Figure 7, where the COAC of all mixtures was increased by increasing the curing time, but COAC at the first 2 hours of CO₂ curing covered about 70 % of COAC after 24 hours of CO₂ curing. Also, COAC was increased with the increasing of hydrated lime content. Moreover, concretes containing hydrated lime powders showed more potential to absorb CO₂ and the COAC of the hydrated lime modified concretes relatively is more than that of the control one, where the C2 and C3 were obtained 142 % and 192 % of COAC in comparison to the control one during the first hour of CO₂ curing. Figure 8, which shows the relative COAC of hydrated lime modified concretes to the relevant control one, clarify that the hydrated lime modified concretes have more potential than the control one despite of their low cement content. High volume of pores and high permeability coefficient of the concretes results in high permeation of CO₂ gas and high absorption of CO₂ during the initial time of curing. Also, high content of Ca(OH)₂ in the mixtures containing hydrated lime substitution increases the chemical reactions and lead to high carbonation content in the hydrated lime modified concretes. Moreover, increasing in the COAC after 12 hours of curing can be neglected.

Furthermore, COAC of the control mixture increased by 123 % and 167 % when CO₂ curing time was increased from 1 to 2 and 4 hours, respectively. These values have been reported about 5 % and 13 %, respectively for lightweight concretes [17]. Baojian et al. have reported 11 % and 33 % increasing in the COAC when CO₂ curing time was increased from 6 to 12 and 24 hour [34], respectively for recycled aggregate concretes while these values are about 5.9 % and 6.2 %, respectively in this study. Porous structure of pervious concretes simplifies the penetration of CO₂ gas into the concretes and therefore COACs are significant at the early ages of CO₂ curing in comparison with other concretes and consequently COACs are significantly reduced for the later ages.

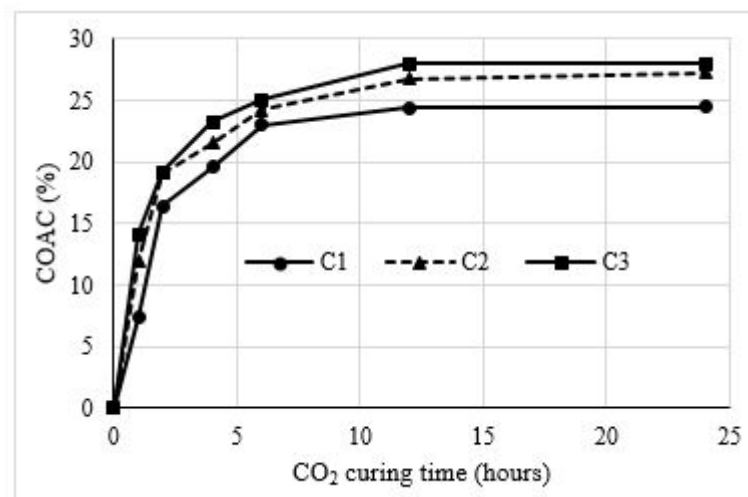


Figure 7. COAC of the pervious concrete over CO₂ curing time.

It is recommended to consider time of CO₂ curing of pervious concretes lower than 6 hours by respect of COAC result, while it is recommended about 12 hours of CO₂ curing by respect of obtaining mechanical properties.

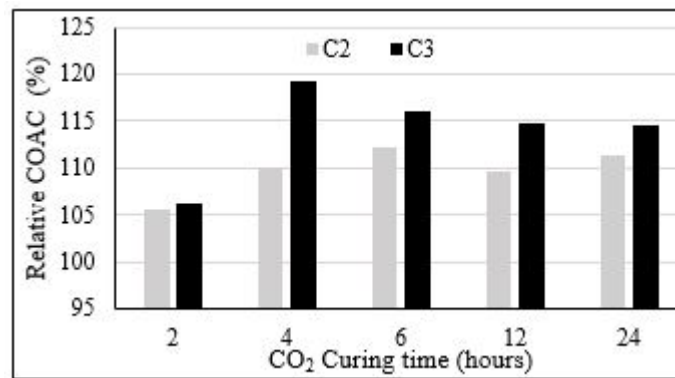


Figure 8. Relative COAC of the mixtures to the COAC of the control mixture.

4. Conclusion

An experimental program was conducted to investigate the effect of CO₂ curing on the physical and mechanical properties of pervious concretes with substitution of hydrated lime powders up to 30 % of cement. Moist curing and CO₂ curing were applied by up to 28 days and 24 hours, respectively. Also, CO₂ absorption capacity of the mixtures was investigated. The results of the conducted experiments are summarized as follows.

- 1- The major carbonation reactions of the pervious concretes were occurred in the first two hours of curing and then reactions were slowly continued up to 12 hours and then were approximately stopped.
- 2- Compressive strength of the CO₂ cured pervious concretes were obtained by up to 87 % of relevant compressive strength after 28 days of moist curing.
- 3- Hydrated lime substitution increases the CO₂ absorption capacity, where the 15–30 % replacement of hydrated lime increased the COAC up to 15 %.
- 4- Void content of the CO₂ cured hydrated lime modified concretes was less than the relevant void content of 28 days moist cured mixtures which confirms high CO₂ absorption capacity of the hydrated lime modified concretes.

5. Acknowledgments

The authors gratefully acknowledge University of Zanjan for support of this study as an MSc thesis.

References

1. Shao, Y., Mirza, M.S., Wu, X. CO₂ sequestration using calcium-silicate concrete [Online]. Canadian Journal of Civil Engineering. 2006. 33. Pp. 776–784. URL: <https://dx.doi.org/10.1139/05-105>.
2. Mourits, F. Capture and Sequestration of Greenhouse Gases in Canada (December 1997). 2012.
3. Penner, L., O'Connor, W.K., Dahlin, D.C., Gerdemann, S., Rush, G.E. Mineral carbonation: Energy costs of pretreatment options and insights gained from flow loop reaction studies. 3rd Annual Conference on Carbon Capture & Sequestration. 5(February)2004. Pp. 1–18.
4. Huijgen, W.J.J., Witkamp, G.J., Comans, R.N.J. Mineral CO₂ sequestration by steel slag carbonation. Environmental Science and Technology. 2005. 39(24). Pp. 9676–9682. DOI: 10.1021/es050795f.
5. Tu, Z., Shi, C., Farzadnia, N. Effect of limestone powder content on the early-age properties of CO₂-cured concrete. Journal of Materials in Civil Engineering. 2018. 30(8). Pp. 1–12. DOI: 10.1061/(ASCE)MT.1943-5533.0002232.
6. Young, J.F., Berger, R.L., Breese, J. Accelerated Curing of Compacted Calcium Silicate Mortars on Exposure to CO₂. Journal of the American Ceramic Society. 1974. 57(9). Pp. 394–397. DOI: 10.1111/j.1151-2916.1974.tb11420.x.
7. Berger, R.L., Young, J.F., Leung, K. Acceleration of Hydration of Calcium Silicates by Carbon Dioxide Treatment. Nature Physical Science. 1972. 240(97). Pp. 16–18. DOI: 10.1038/physci240016a0.
8. Goodbrake, C.J., Young, J.F., Berger, R.L. Reaction of Beta-Dicalcium Silicate and Tricalcium Silicate with Carbon Dioxide and Water Vapor. Journal of the American Ceramic Society. 1979. 62(3–4). Pp. 168–171. DOI: 10.1111/j.1151-2916.1979.tb19046.x.
9. Qin, L., Gao, X., Chen, T. Influence of mineral admixtures on carbonation curing of cement paste. Construction and Building Materials. 2019. 212. Pp. 653–662. DOI: 10.1016/j.conbuildmat.2019.04.033.
10. Ho, D.W.S., Lewis, R.K. Carbonation of concrete and its prediction. Cement and Concrete Research. 1987. 17(3). Pp. 489–504. DOI: 10.1016/0008-8846(87)90012-3.
11. Hermawan, S., Hata, T. Development technology of rapid production of high-strength cement-bonded particleboard by using gaseous or supercritical carbon dioxide curing. Proceedings of Inorganic-Bonded Wood and Fiber Composite Materials. 1998. Pp. 70–87.
12. Monkman, S., Shao, Y. Assessing the carbonation behavior of cementitious materials. Journal of Materials in Civil Engineering. 2006. 18(6). Pp. 768–776. DOI: 10.1061/(ASCE)0899-1561(2006)18:6(768).
13. Živica, V. Corrosion of reinforcement induced by environment containing chloride and carbon dioxide. Bulletin of Materials Science. 2003. 26(6). Pp. 605–608. DOI: 10.1007/BF02704323.
14. Montemor, M.F., Cunha, M.P., Ferreira, M.G., Simões, A.M. Corrosion behaviour of rebars in fly ash mortar exposed to carbon dioxide and chlorides. Cement and Concrete Composites. 2002. 24(1). Pp. 45–53. DOI: 10.1016/S0958-9465(01)00025-7.

15. Zhang, D., Shao, Y. Enhancing Chloride Corrosion Resistance of Precast Reinforced Concrete by Carbonation Curing. *ACI Materials Journal*. 2019. 116(3). DOI: 10.14359/51714461.
16. Zhan, B.J., Xuan, D.X., Zeng, W., Poon, C.S. Carbonation treatment of recycled concrete aggregate: Effect on transport properties and steel corrosion of recycled aggregate concrete. *Cement and Concrete Composites*. 2019. 104(May). Pp. 103360. DOI: 10.1016/j.cemconcomp.2019.103360.
17. Shi, C., Wu, Y. Studies on some factors affecting CO₂ curing of lightweight concrete products. *Resources, Conservation and Recycling*. 2008. 52(8–9). Pp. 1087–1092. DOI: 10.1016/j.resconrec.2008.05.002.
18. Shao, Y.; and Shi, C. Carbonation curing for making concrete products—an old concept and a renewed interest. 6th International Symposium on Cement and Concrete. 2006. Pp. 823–830.
19. Zhan, B.J., Xuan, D.X., Poon, C.S., Shi, C.J. Effect of curing parameters on CO₂ curing of concrete blocks containing recycled aggregates. *Cement and Concrete Composites*. 2016. 71. Pp. 122–130. DOI: 10.1016/j.cemconcomp.2016.05.002.
20. Zhan, B.J., Poon, C.S., Shi, C.J. Materials characteristics affecting CO₂ curing of concrete blocks containing recycled aggregates. *Cement and Concrete Composites*. 2016. 67. Pp. 50–59. DOI: 10.1016/j.cemconcomp.2015.12.003.
21. Kou, S.C., Zhan, B.J., Poon, C.S. Use of a CO₂ curing step to improve the properties of concrete prepared with recycled aggregates. *Cement and Concrete Composites*. 2014. 45. Pp. 22–28. DOI: 10.1016/j.cemconcomp.2013.09.008.
22. Ahmad, S., Assaggaf, R.A., Adekunle, S.K., Al-Amoudi, O.S.B., Maslehuddin, M., Ali, S.I. Influence of accelerated carbonation curing on the properties of self-compacting concrete mixtures containing different mineral fillers. *European Journal of Environmental and Civil Engineering*. 2019. 0(0). Pp. 1–18. DOI: 10.1080/19648189.2019.1649197.
23. Hasegawa, L.I.I. Carbonation curing and performance of pervious concrete using Portland limestone cement. McGill, 2011.
24. Sidhu, G.S. Effect of Accelerated Carbonation Curing On Properties of Pervious Concrete: An Effective Way of CO₂ Sequestration and Water Conservation. Thapar Institute, 2019.
25. Lian, C., Zhuge, Y., Beecham, S. The relationship between porosity and strength for porous concrete. *Construction and Building Materials*. 2011. 25(11). Pp. 4294–4298. DOI: 10.1016/j.conbuildmat.2011.05.005.
26. Aamer Rafique Bhutta, M., Hasanah, N., Farhayu, N., Hussin, M.W., Tahir, M.B.M., Mirza, J. Properties of porous concrete from waste crushed concrete (recycled aggregate). *Construction and Building Materials*. 2013. 47. Pp. 1243–1248. DOI: 10.1016/j.conbuildmat.2013.06.022.
27. De Solomihac, H., Videla, C., Fernández, B., Castro, J. Porous concrete mixtures for pervious urban pavements. *Materiales de Construcción*. 2007. 57(287). Pp. 23–36.
28. Shen, W., Shan, L., Zhang, T., Ma, H., Cai, Z., Shi, H. Investigation on polymer-rubber aggregate modified porous concrete. *Construction and Building Materials*. 2013. 38. Pp. 667–674. DOI: 10.1016/j.conbuildmat.2012.09.006.
29. Bhutta, M.A.R., Tsuruta, K., Mirza, J. Evaluation of high-performance porous concrete properties. *Construction and Building Materials*. 2012. 31. Pp. 67–73. DOI: 10.1016/j.conbuildmat.2011.12.024.
30. Park, S.B., Seo, D.S., Lee, J. Studies on the sound absorption characteristics of porous concrete based on the content of recycled aggregate and target void ratio. *Cement and Concrete Research*. 2005. 35(9). Pp. 1846–1854. DOI: 10.1016/j.cemconres.2004.12.009.
31. ACI 211.3R. Guide for Selecting Proportions for No-Slump Concrete. 211.3R2002.
32. Park, S.B., Tia, M. An experimental study on the water-purification properties of porous concrete. *Cement and Concrete Research*. 2004. 34(2). Pp. 177–184. DOI: 10.1016/S0008-8846(03)00223-0.
33. Neithalath, N., Weiss, J., Olek, J. Characterizing Enhanced Porosity Concrete using electrical impedance to predict acoustic and hydraulic performance. *Cement and Concrete Research*. 2006. 36(11). Pp. 2074–2085. DOI: 10.1016/j.cemconres.2006.09.001.
34. Baojian, Z., Chisun, P., Caijun, S. CO₂ curing for improving the properties of concrete blocks containing recycled aggregates. *Cement and Concrete Composites*. 2013. 42. Pp. 1–8. DOI: 10.1016/j.cemconcomp.2013.04.013.
35. Mehta, P.K., Monteiro, P.J.M. *Concrete: Microstructure, Properties, and Materials*. 3rd ed. McGraw-Hill. New York, 2005.

Contacts:

Hamid Rahmani, +982433054057; hrahmani@znu.ac.ir

Mohammad Montazer Gheib, +989369635763; mohammadmontazer.ci@gmail.com



DOI: 10.18720/MCE.92.10

Road organo-mineral mixtures based on oil sludge

O.N. Ilina*, **I.B. Ilin**,

Kazan State University of Architecture and Engineering, Kazan, Russia,

** E-mail: ilinaon@inbox.ru*

Keywords: oil sludge, organo-mineral mixture, road, technology of road construction, recycle

Abstract. Nowadays the development and implementation of modern construction technologies using oil wastes is gaining importance in road construction. Most of these wastes are stored in lagoons, which occupy vast territories, pollute the atmosphere, groundwater, soil and harm the environment. The purpose of the study is the development of organo-mineral mixtures composition based on oil sludge and technology for road construction with their application. The experimental research methods include the determination of strength, water resistance, water saturation, and swelling indicators of materials of various compositions. We also established optimal limits for factors variation that ensure the required reliability of the results. As a result of experimental studies we established that the optimal content of solid oil sludge in the composition of the developed materials is 30%, crushed stone –70% and the content of Portland cement is 6%. Physical and mechanical properties of the organo-mineral mixture based on oil sludge comply with regulatory requirements. During experimental and industrial implementation of the research results on 4 experimental road sections we developed road pavement base construction technology of organo-mineral mixture based on oil sludge. It is performed by commercially available road-building machines with leading mechanisms recycler using the method called “mixing on the road”. We developed the operation schedule of oil sludge preliminary preparation at the special plant. Prepared oil sludge is a secondary raw product for road construction materials that is uniform in colour, grain composition, mass fraction of water and oil. Suggested modern technology for road pavement base construction allows making the oil sludge processing cycle absolutely complete and eliminates the formation of industrial by-products. This is an integral part of natural resources rational use and saving in material resources consumption. Technology application also contributes to the environment ecological state improvement in the areas of oil production and refining.

1. Introduction

In road construction, the integrated utilization of industrial wastes is currently gaining importance, taking into account the growth of environmental problems and a decrease in the level of target natural components in the feedstock. The task of raw materials integrated use for the road construction industry is natural materials rational use and the involvement of industrial waste in the process. Industrial waste can be of many types [1–5]. They differ in grain size composition, chemical composition and degree of safety. Therefore, the main trend in measures to protect the population and the environment from industrial waste harmful effects is the development and implementation of modern technologies for road construction using industrial waste and recycled products efficient use in the regions' economy [6-10]. Oil sludge represents waste from the oil industry which is formed during the operation of oil fields due to discharges during oil treatment, tank cleaning, drilling activity, and discharges during testing and workover.

The annual oil production in Russia continues to grow steadily from 488 million tons in 2008 to 555.7 million tons in 2018, while oil refining depth is about 80%. The bulk of oil in Russia is now produced in three:

- Khanty-Mansiysk Autonomous District, the Krasnoyarsk Region (West-Siberian Basin) – up to 70% of All-Russia oil production;

Ilina, O.N., Ilin, I.B. Road organo-mineral mixtures based on oil sludge. Magazine of Civil Engineering. 2019. 92(8). Pp. 115–126. DOI: 10.18720/MCE.92.10

Ильина О.Н., Ильин И.Б. Дорожные органоминеральные смеси на основе нефтяного шлама // Инженерно-строительный журнал. 2019. № 8(92). С. 115–126. DOI: 10.18720/MCE.92.10



This work is licensed under a [CC BY-NC 4.0](https://creativecommons.org/licenses/by-nc/4.0/)

- Tatarstan, Bashkortostan, the Orenburg Region (Volga-Ural Basin) – up to 20% of All-Russia oil production;
- Khanty-Mansiysk Autonomous District, the Komi Republic (Timan-Pechora Basin) – up to 10% of All-Russia oil production.

The annual volume of oil sludge formation in the Russian Federation varies depending on the source from 10 to 25 million tons while the volume of use and disposal of this waste is not more than 10%. In the Republic of Tatarstan where the oil industry is highly developed, oil production in 2018 reached 35 million tons, the volume of oil sludge is also increasing annually about 200 thousand tons and taking into consideration the accumulated volumes, there are reserves of oil sludge for the possibility of building 500 km of roads. Most of this waste is stored in lagoons, which occupy vast territories, polluting the atmosphere, groundwater, soil, and causing enormous damage to the environment. Nowadays the most common methods for the disposal of oil sludge can be classified into mechanical, physical and chemical, thermal, biochemical and combined methods [11-16]. The common disadvantage of the disposal methods and technologies for oil sludge processing is their poor efficiency and high material, energy and financial costs for their implementation; the disposal cycle is also incomplete and produces secondary waste. The introduction of a particular processing technology depends on the composition of the raw materials used, the nature of the oil sludge, the ratio of organic and inorganic components in them, environmental requirements, as well as the technical capabilities of the plant. All these factors make it difficult to process oil sludge fully and intensively with extreme environmental safety and non-waste technology.

Oil sludge has a wide range of composition and physical and mechanical characteristics. Resins, paraffins and other high molecular weight compounds that are parts of oil sludge have surface-active and binding properties. It is this feature of oil sludge that can be effectively used in road construction, which is confirmed by previous studies [17–22]. The Republic of Tatarstan has significant reserves of weak mineral materials which can be effectively used in road construction after special treatment with binders. Based on economic and environmental prerequisites some part of the material while processing may be presented by oil sludge. The purpose of the study is the development of organo-mineral mixtures compositions based on oil sludge and the technology of pavement base construction applying them. To achieve it, the following tasks are defined: research and optimization of the composition of organo-mineral mixtures based on oil sludge; development of technology for pavement base construction with oil sludge preliminary preparation; experimental and production implementation of the research results.

2. Methods

Experimental studies of organo-mineral mixtures based on oil sludge were carried out in accordance with the International standard of Commonwealth of Independent States GOST 30491 "Organic-mineral mixtures and soils, reinforced with organic and complex binders, for road and airfield construction" [23]. At the stage of exploration, we investigated and optimized the compositions of the developed materials based on oil sludge, and established the optimal limits for factors variation, we also developed and mastered methodology to ensure the required reliability of the results. When the content of oil sludge is more than 50 %, even with a sharp increase in the required amount of expensive imported binder, Portland cement, characteristic value of the material is not always achieved, and when the content of oil sludge is less than 30 %, the volume of disposal of this waste is reduced, which is not feasible both economically and technically. Thus at the research main phase the composition of the developed material includes crushed limestone 50–70 % and solid oil sludge in the amount of 30–50 %, as a binder we used Portland cement up to 12 %, water up to 8 %.

Manufacturing, storage and testing of samples of organo-mineral mixtures based on oil sludge was carried out in accordance with the International standard of Commonwealth of Independent States GOST 12801 [24]. Samples were created in the following sequence: first, we mixed crushed stone and oil sludge until a homogeneous mixture was obtained. Next, we added cement and water which were then mixed. Then we placed the obtained mixture into cylinder molds with the diameter and height of 71.4 mm. Dimensions of cylinder molds are selected taking into account the maximum size of the aggregate. Metal cylinder molds were precluded with mineral oil. Compaction of samples from the mixture was carried out on hydraulic press MS-500 under a pressure of 40.0 ± 0.5 MPa for 3.0 ± 1.0 min. During compaction, a two-sided load application was ensured, which we achieved by transferring pressure to the compacted mixture through two liners moving freely towards each other in the mold. The samples from mixtures were stored at the temperature of $20 \text{ }^\circ\text{C} \pm 5 \text{ }^\circ\text{C}$ in a tub with a hydraulically sealed desiccator. Tests for water-saturated samples from mixtures were carried out for 48 hours. During the first 6 hours samples were immersed into water at 1/3 of the height, the remaining 42 hours – at full height. Density is found according to the International standard of Commonwealth of Independent States GOST 12801 [24].

The determination of the compressive strength includes determining the load required for sample failure under given conditions. The samples compressive strength is determined using the press at the press plate rate of motion (3.0 ± 0.3) mm/min. The sample is placed in the center of the press bottom plate, then we lower the top plate and stop it 1.5–2 mm above the surface level of the sample. We can achieve the same result by

a corresponding rise of the press bottom plate. After that, we turn on the electric motor of the press and start loading the sample. The maximum dynamometer indicated value is taken as the ultimate breaking load.

Compressive strength R_{STR} , MPa, is calculated according to the formula [24]:

$$R_{STR} = \frac{P}{F} 10^{-2}, \quad (1)$$

P is ultimate breaking load, N;

F is original cross-sectional area of the sample, cm²;

10^{-2} is conversion factor in MPa.

The arithmetic mean of the tests of three samples is taken as the result of the determination. Determination of water saturation represents the determination of the amount of water absorbed by the sample at a given saturation mode. Samples from mixtures, weighed in air and in water, are placed into a vessel with water at the temperature of (20 ± 2) °C. The water level above the samples should be at least 3 cm. Full water saturation of samples with a height and diameter of 70 mm is carried out for 3 days, while in all cases, on the first day, the samples are immersed into water at 1/3 of the height, and on the subsequent days – completely. To prevent drying of the samples immersed in water at 1/3 of the height, saturation is carried out in a hydraulically sealed tub. After that, the samples are removed from the vessel, weighed in water, and then wiped with a soft cloth or filter paper and weighed in air.

Water saturation of the sample W , %, is calculated according to the formula [24]:

$$W = \frac{m_5 - m}{m_2 - m_1} 100, \quad (2)$$

m is mass of the sample weighed in the air, g;

m_1 is mass of the sample weighed in water, g;

m_2 is mass of the sample, kept in water during 30 min and weighed in air, g;

m_5 is mass of water saturated sample weighed in air, g.

Arithmetic mean of three values rounded to the first decimal place is considered as the result of water saturation determination.

Swelling is defined as sample volumetric gain after its saturation with water. To determine the swelling we use the data obtained in determining the average density and water saturation.

Swelling of the sample H , % by volume, is calculated according to the formula [24]:

$$S = \frac{(m_5 - m_6) - (m_2 - m_1)}{m_2 - m_1} 100, \quad (3)$$

m_6 is mass of water saturated sample weighed in water, g.

The arithmetic mean of three defined values rounded to the first decimal place is taken as the result of swelling determination.

The value of water resistance coefficient includes the assessment of the decrease in compressive strength of the samples after exposure to water under vacuum. Samples from mixtures, weighed in air and in water, are placed in a vessel with water at the temperature of (20 ± 2) °C. The water level above the samples should be at least 3 cm. The vessel with the samples is placed in a vacuum plant, where the pressure of not more than 2000 Pa (15 mm Hg) is created and maintained for 1 h. Then the pressure is brought to atmospheric pressure and the samples are kept in the same vessel with water at the temperature of (20 ± 2) °C for 30 minutes. After that, the samples are removed from the vessel, weighed in water, wiped with a soft cloth and weighed in air.

Water resistance is calculated with the accuracy up to the second decimal place by the formula [24]:

$$K_B = \frac{R_{STR}^W}{R_{STR}^{20}}, \quad (4)$$

R_{STR}^W is compression resistance of water saturated samples at the temperature (20 ± 2) °C, MPa;

R_{STR}^{20} is compression resistance of samples before water saturation at the temperature (20 ± 2) °C, MPa.

The studies were conducted using the local crushed stone M400, obtained in the quarry of the Republic of Tatarstan. Table 1 shows the physical and mechanical properties of the crushed stone; Table 2 represents the grain composition of the crushed stone.

Table 1. Physical and mechanical properties of the crushed stone mixture.

Fraction size, mm	Packed density, kg/m ³	Water absorption, %	Wear value grade	Strength grade	Frost resistance grade index	Optimum moisture content%
0–20	1700	7.9	13	400	10	6

Table 2. Grain composition of the crushed stone mixture.

Grains maximum size, mm	Total sieve residue percentage with the size of the mesh, mm						
	10	5	2.5	1.25	0.63	0.315	0.14
20	5	25	35	50	60	75	85

Oil sludge for laboratory research was selected from the lagoons and has the composition presented in Table 3. The content of the most active components of the oil sludge i.e. asphaltenes and resins is 5.5–11 %.

Table 3. Composition of the oil sludge.

Content, % mass					
Asphaltenes	Resins	Paraffines	Unsaturated hydrocarbons	Water	Mechanical admixtures
1.5–4.0	4.0–7.0	10.0–50.0	6.0–10.0	2.0–10.0	40.0–60.0

For mixture processing we used Portland cement CEM II 42.5N DO which is highly recommended for road construction [25]. Process water meets the requirements of the standard [26].

3. Results and Discussions

The results of experimental studies of organo-mineral mixtures based on oil sludge showed the compliance of their indices with the standard values. The main results of organo-mineral mixtures indices are given in Table 4, Figures 1–4. Analysis of the data obtained shows that the optimal content of solid oil sludge in the composition of the developed materials is 30 %, crushed stone is 70 % and the content of Portland cement is 6%. Adding of a binder (Portland cement) into the organo-mineral mixture provides 1.25–1.28 times increase in the material compressive strength and ensures compliance with regulatory requirements (Figure 1). Organo-mineral mixture water saturation and swelling indices decrease with 1.4 times increase in the amount of oil sludge (Figure 3).

Table 4. Physical and mechanical parameters of organo-mineral mixtures.

Position	Mixtures composition, %				ρ , g/cm ³	Results of testing the mixture sample sat 28 days				
	Oil sludge	Portland cement	Crushed stone M400			R_{STR} , MPa	R_{water} , MPa	Water resistance coef.	W, %	H, %
1	50	6	50		1.90	1.89	1.46	0.77	4.63	0.87
2	50	8	50		1.91	2.10	1.88	0.89	5.04	0.82
3	50	10	50		1.92	2.10	1.90	0.90	4.80	0.71
4	50	12	50		1.93	2.34	1.87	0.80	3.82	0.52
5	30	6	70		1.96	2.29	1.77	0.77	5.39	0.69
6	30	8	70		1.96	2.30	1.99	0.86	5.45	0.70
7	30	10	70		1.96	2.35	1.98	0.84	5.35	0.59
8	30	12	70		1.96	2.71	2.22	0.82	5.26	0.54
9	Requirements of the International standard of Commonwealth of Independent States GOST 30491						≥ 1.4	≥ 0.6	≤ 10	≤ 2

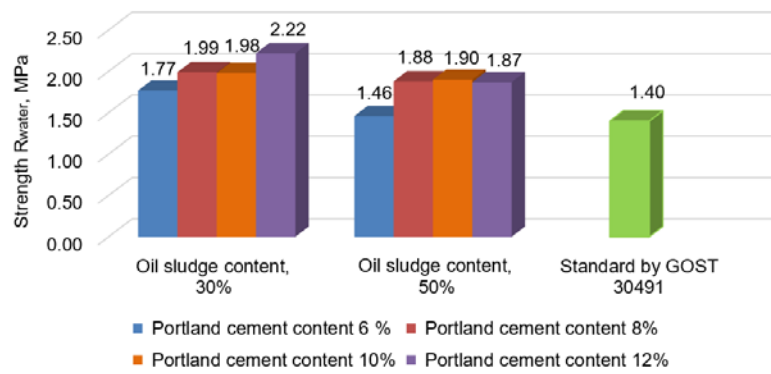


Figure 1. Compressive strength of water-saturated samples depending on the content of Portland cement and oil sludge.

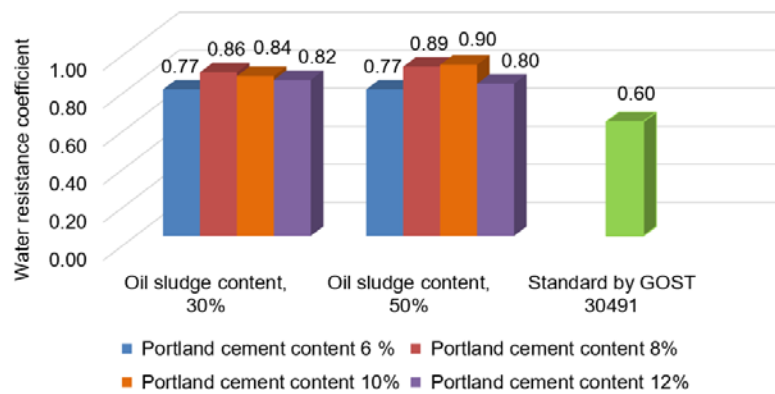


Figure 2. Samples' water resistance coefficient depending on the content of Portland cement and oil sludge.

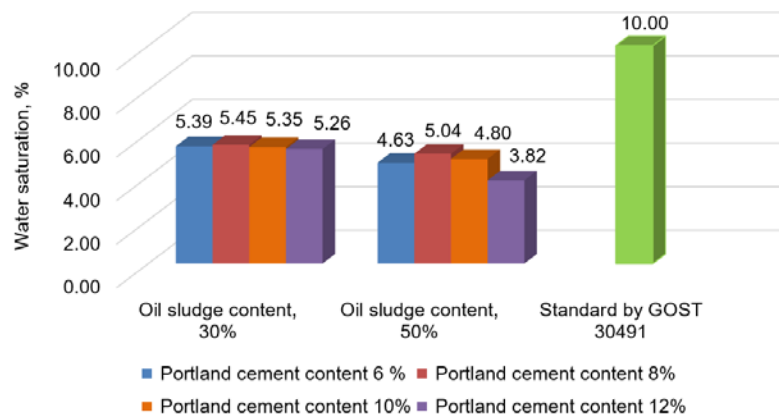


Figure 3. Samples water saturation depending on Portland cement and oil sludge content.

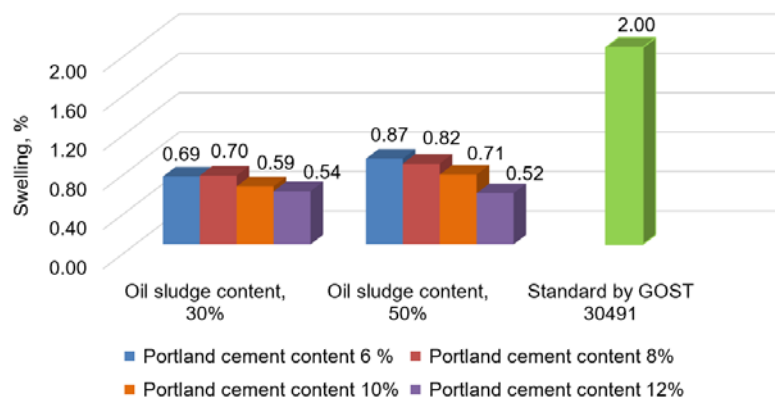


Figure 4. Samples swelling depending on Portland cement and oil sludge content.

Processing of the research results was performed using elements of the analysis of variance and regression analysis (Figure 5). The correctness of strength, water saturation and swelling indicators dependence description is confirmed, after evaluating the value of the coefficients using the method of successive regression analysis, the following mathematical models are obtained which link the characteristics of the organo-mineral mixture with the content of oil sludge (X_1), crushed stone (X_2) and cement (X_3):

$$R_{STR} = -3.09414 + 0.03449X_1 + 0.05229X_2 + 0.35471X_3 - 0.02262X_3^2$$

$$W = -1.25771 + 0.17802X_1 + 0.01477X_2 + 0.13038X_3$$

$$S = -2.15029 + 0.0462X_1 + 0.02656X_2 + 0.04168X_3 - 0.01582X_3^2$$

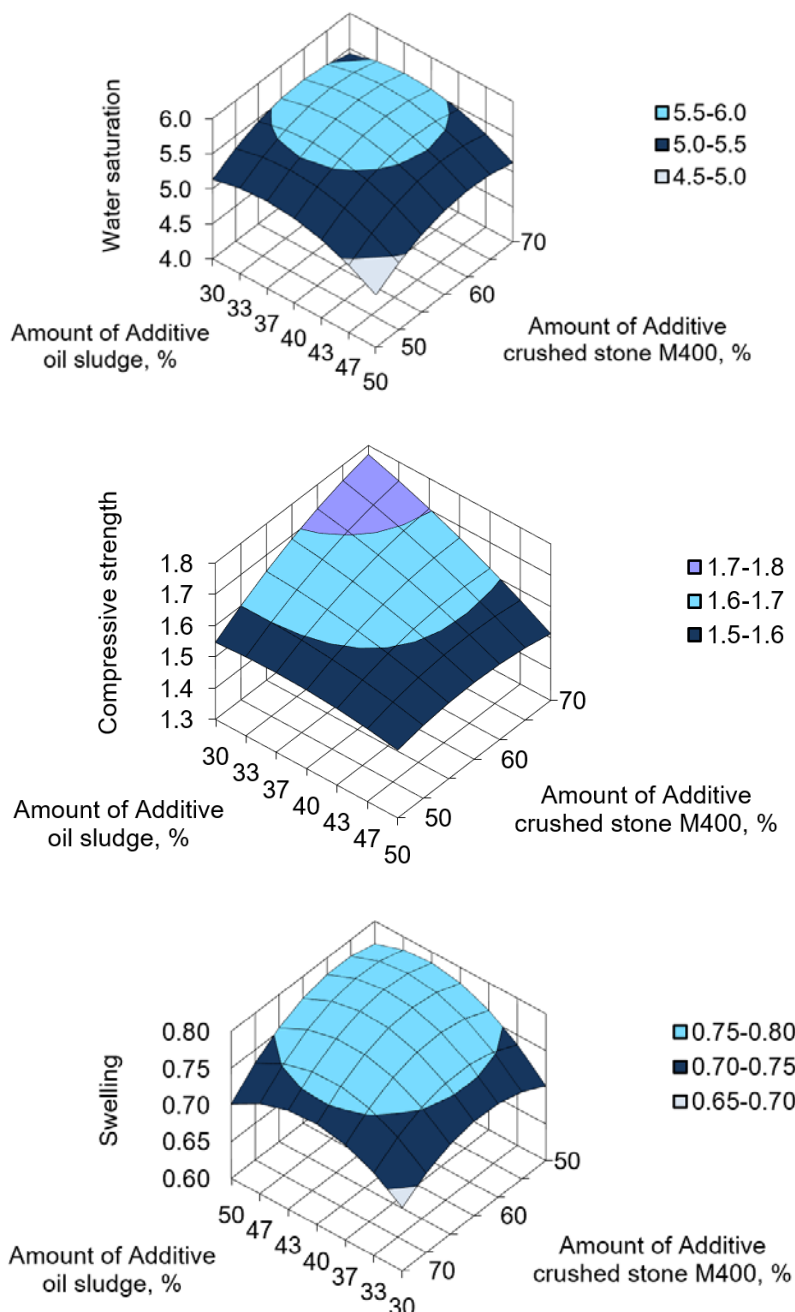


Figure 5. The influence of solid oil sludge, crushed stone and Portland cement content on the indicators of compressive strength, water saturation and swelling of the developed material.

Based on research and development of the technological parameters of organo-mineral mixtures creation and application for their intended purpose, a scheme for preliminary technological preparation of oil sludge was developed and introduced to ensure its uniformity in composition and properties. To obtain a sufficiently uniform organo-mineral mixture, the characteristics of which largely depend on the amount of oil sludge and its composition, it is necessary to achieve the uniform spreading of its components. Oil sludge with higher uniformity of composition and properties was obtained after processing it in the oil sludge plant. The

operation schedule represents (Figure 6): using a loader we deliver oil sludge estimated volume from the lagoon to the preparation and storage site, then we load it into the preliminary preparation receiving hopper, then we process it in the mixer and transfer to the loader by conveyor, then oil sludge is transported by dump truck to site or stacked on the site of preparation and storage.

Prepared oil sludge is a material homogeneous in color, composition, moisture and according to physicochemical parameters must meet the requirements and norms given in Table 5.

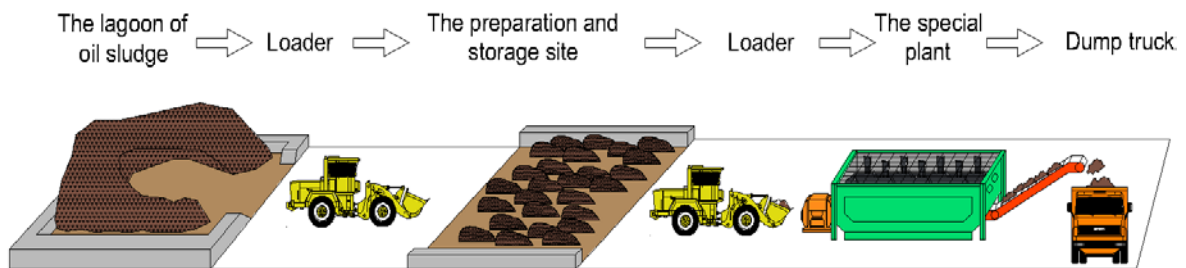


Figure 6. Operation schedule for oil sludge preparation using the plant.

Table 5. Physical and chemical parameters of the product “Prepared Solid Oil Sludge” (PSOS) – Akmal”.

№	Parameter name	Parameter value
1	Grain (granulometric) composition up to 20 mm,% by weight, not less	95
2	Density, g/cm ³	1.4–1.7
3	Mass percentage of oil (oil products),% in the limit	10–30
4	Mass percentage of mechanical impurities,% in the limit	50–70
5	Mass percentage of water,% , not exceeding	20
6	Total specific effective activity of natural radionuclides, Bq/kg, not exceeding	1500

When developing the road building technology using oil sludge, the following factors were taken into account: characteristics and suitability of local mineral materials; the need and relevance of improving the mineral material granulometric composition; composition and readiness degree of oil sludge; methods of preparing the mixture; type of pavement and requirements for the structural layer made from the material including oil sludge; ensuring the specified productivity of the construction work flow; weather and climatic conditions of the construction area; type of binding material, its composition and features, and, if necessary, the composition and properties of active additives and activators. The road construction technology using oil sludge is carried out with the complex mechanization of the entire given process of work using modern high-performance machines and equipment. Physical and mechanical properties of the processed material in the structural layer of the pavement depend on compliance with the requirements for the properties of the source materials and on the total effect of sequentially performed process operations. Taking into account the factors mentioned above and specific features of the road construction technology development using solid oil sludge, the following methods of work performance are developed:

- the work performance technology with the preparation of an organo-mineral mixture based on oil sludge in a mixing plant and subsequent mixture transportation to the laying area;

- the work performance technology with the preparation of an organo-mineral mixture based on oil sludge by the “mixing on the road” method using mixing equipment (recyclers, mounted road milling machines).

The experimental and industrial implementation of research results was carried out by arranging 4 experimental road sections, the execution of works was conducted using the method called “mixing on the road” which was fulfilled by the recycler Wirtgen WR 2400 from 2016 to 2019. When determining the operational method, the key factor was the availability of mixing equipment (Wirtgen WR2400 recycler) and the possibility of its delivery to the sites, taking into account the optimal distance of oil sludge transportation of about 100 km. Pavement and base regeneration using recyclers is a popular and demanded method in our

region, therefore, the recyclers are operated for the entire construction season on federal, regional and local roads, and the recycler drivers are experienced and highly qualified specialists, which is also considered significant for experimental construction. In 2019, the experimental road section was arranged during the repair of the Aznakayevo – VerkhniyeStyarle – Kuk-Tyaka highway km28 + 800 - km32 + 400 in the Aznakayevsky municipal region of the Republic of Tatarstan in accordance with the following designed structure (Figure 7).

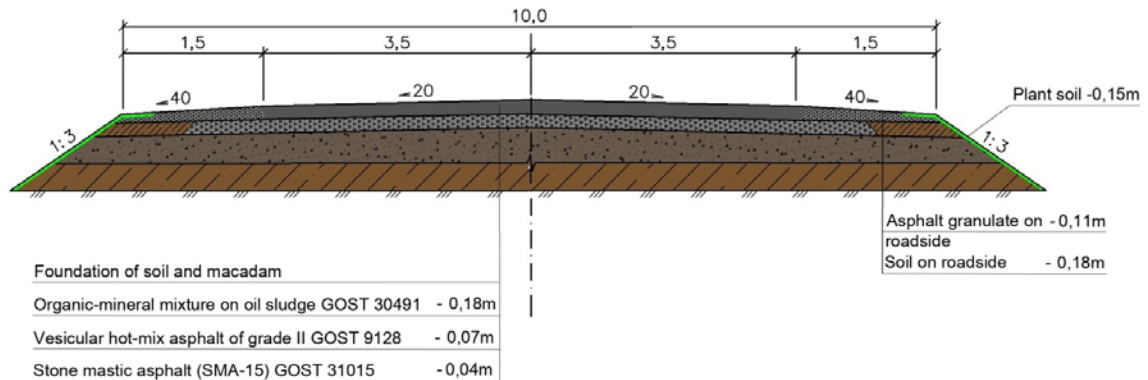


Figure 7. The design of pavement with the base of organo-mineral mixture based on oil sludge.

Firstly, the existing asphalt concrete pavement with the thickness of 5 cm was milled with a road milling machine and asphalt breakage was removed by dump trucks. Next, the base and the pavement were constructed and finishing works were carried out.

Manufacturing process of the pavement base made from organo-mineral mixtures based upon oil sludge is as follows:

The process of crushed stone and oil sludge delivery in the stacks was carried out by dump trucks.

Crushed stone spreading was fulfilled by the loader, planning was carried out by a motor grader.

Oil sludge spreading was fulfilled by the loader, planning was carried out by a motor grader.

Crushed stone and oil sludge mixing is carried out by Wirtgen WR2400 recycler (Figure 8).

Water was delivered and poured by a water-jetting machine.

The binder (Portland cement) was delivered by a cement lorry.

The binder (Portland cement) was spread by a cement spreader – semi-trailer van. (Figures 9).

Final mixing of materials was carried out by a recycler Wirtgen WR 2400.

The mixture was compacted using combination rollers with 8 passes along one track with overlapping the track 1/3 of the width of the drum with the speed of 1.5–2 km/h.

Mixture leveling and surface planning was performed by a grader. We also made control measurements of evenness, slopes and elevations.

Maintenance of the laid coat was carried out by pouring bitumen BND 90/130 with a flow rate of 0.8 l/m² taking into account pavement base tack coat which is applied before placing asphalt concrete mixture because asphalt concrete was applied first two days after pavement base construction according to the conventional process.



Figure 8. Recycler Wirtgen WR 2400.



Figure 9. Cement spreader – semi-trailer van Bomag BS12000.

The operation and monitoring of the experimental sections of the road under construction is carried out with the subsequent study of the samples of the material cutting out in accordance with regulatory requirements. We received the results of physical and mechanical parameters of the material and the total specific effective activity of radionuclides, all parameters meet to the requirements of the standard.

When comparing pavement estimated cost we considered the traditional pavement base made from imported crushed stone M800 and the base from an organo-mineral mixture based on oil sludge. We found out that it is possible to save 1,668,805 rubles, i.e. 30% of pavement base estimated cost due to the use of the developed material per 1 km (Fig. 10).

Thus, unlike other methods of oil sludge recycling such as pyrolysis, coking, microwave processing, burning, decanting, etc., [11–16] the proposed modern technology for pavement base construction allows making the oil sludge recycling cycle totally complete and to exclude the formation of industrial by-products, which contributes to the improvement of the environment ecological state in the areas of oil production and refining.

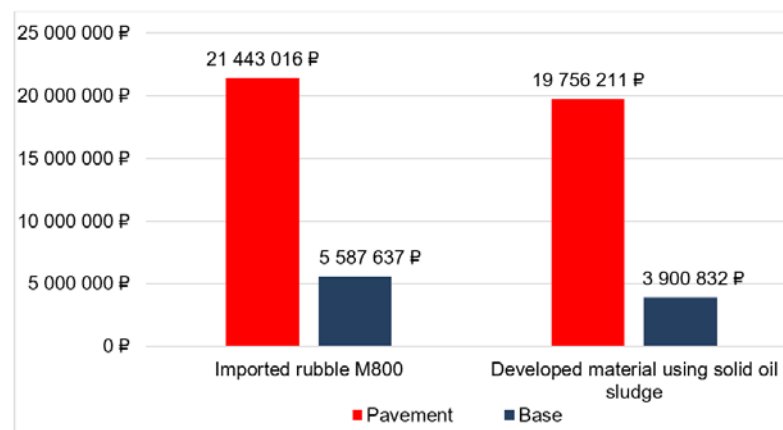


Figure 10. Pavement cost comparison using imported crushed stone M800 and organo-mineral mixture based on oil sludge.

4. Conclusion

1. Using experimental research we found the optimal composition of organo-mineral mixture based on oil sludge. Optimal content of oil sludge in composition of materials under development is 30 %, content of crashed stone M400 is 70 % and content of Portland cement is 6 % of organo-mineral mixture's mineral part. The studied parameters of strength, water resistance coefficient, water saturation and swelling of the organo-mineral mixture based on oil sludge comply with regulatory requirements.

2. During experimental and industrial implementation of the research results we developed the pavement base construction technology using organo-mineral mixture based on oil sludge for four experimental road sections. It is carried out by commercially available road-building machines with a driving mechanism - a recycler using the "mixing on the road" method. We also fulfilled operation and monitoring of experimental road construction sections.

3. We developed an operation schedule for oil sludge preliminary preparation on the special plant to ensure its uniformity in composition and properties, which allows integrated use of oil sludge as a secondary raw material for road construction in modern conditions and is an integral part of rational use of natural resources and saving material resources.

References

1. Tsokur, O.S., Litvinova, T.A., Kosulina, T.P. Primenenie nailuchshih dostupnyh tehnologij dlya utilizacii promyshlennyh othodov [The use of best available techniques for recycling industrial waste]. IV Mezhdunarodnaja nauchnaja jekologicheskaja konferencija Problemy rekultivacii othodov byta, promyshlennogo i sel'skohozjajstvennogo proizvodstva. [Proceedings IV International scientific ecological conference Problems of reclamation of domestic solid waste, industrial and agricultural production waste]. Krasnodar: KGAU, 2015. Pp. 728–732. (rus)
2. Potravny, I.M., Novoselov, A.L., Novoselova, I.Yu. Optimizing the use of resources of technogenic deposits taking into account uncertainties. *Economy of region*. 2017. 13(4). Pp. 1280–1290. DOI: 10.17059/2017-4-24.
3. Li, H., Li, J., Zhao, X., Zhang, G., Kong, Q. Management of waste lubricant oil (WLO): WLO-to-energy through gasification process. *Petroleum Science and Technology*. 2018. 36(16). Pp. 1229–1234. DOI: 10.1080/10916466.2018.1465973.
4. Piatak, N.M., Parsons, M.B., Seal, R.R. Characteristics and environmental aspects of slag: A review. *Applied Geochemistry*. 2015. No. 57. Pp. 236–266. DOI: 10.1016/j.apgeochem.2014.04.009.
5. Arulrajah, A., Mohammadinia, A., Phummiphon, I., Horpibulsuk, S., Samingthong, W. Stabilization of Recycled Demolition Aggregates by Geopolymers comprising Calcium Carbide Residue, Fly Ash and Slag precursors. *Construction and Building Materials*. 2016. 114. Pp. 864–873. DOI: 10.1016/j.conbuildmat.2016.03.150.
6. Demirbas, A. Waste management, waste resource facilities and waste conversion processes. *Energy Conversion and Management*. 2011. 52(2). Pp. 1280–1287. DOI: 10.1016/j.enconman.2010.09.025.
7. Gruyaert, E., Robeyst, N., De Belie, N. Study of the hydration of Portland cement blended with blast-furnace slag by calorimetry and thermogravimetry. *Journal of thermal analysis and calorimetry*. 2010. 102(3). Pp. 941–951. DOI: 10.1007/s10973-010-0841-6.
8. Teltaev, B.B., Ergozhin, E.E., Izmailova, G.G., Amaniyazov, B.T., Dzhusipbekov, U.Zh., Nurgalieva, G.O., Utin, T.M. Sostav dlya osnovaniya dorozhnyh odezhd [Composition for the foundation of pavement] Patent Kazakhstan no. 30806, 2015. (kz)
9. Kiyants, A.V. Concrete with recycled polyethylene terephthalate fiber. *Magazine of Civil Engineering*. 2018. 84(8). Pp. 109–118. DOI: 10.18720/MCE.84.11.
10. Smol, M., Kulczycka, J., Henclik, A., Gorazda, K., Wzorek, Z. The possible use of sewage sludge ash (SSA) in the construction industry as a way towards a circular economy2015. *Journal of Cleaner Production*. 2015. No. 95. Pp. 45–54. DOI: 10.1016/j.jclepro.2015.02.051.
11. Zhang, J., Liu, J., Siddiqui, M.K., Nazeer, W. Energy and economic aspects of synthesis gas production from oil sludge and plastic waste. *Petroleum Science and Technology*. 2019. 37(4). Pp. 430–435. DOI: 10.1080/10916466.2018.1550501.
12. Jin, Y., Zheng, X., Chi, Y., Ni, M. Experimental study and assessment of different measurement methods of water in oil sludge. *Drying technology*. 2014. 32 (3). Pp. 251–257. DOI: 10.1080/07373937.2013.811251.
13. Heidarzadeh, N., Gitipour, S., Abdoli, M.A. Characterization of oily sludge from a Tehran oil refinery. *Waste Management & Research*. 2010. 28(10). Pp. 921–927. DOI: 10.1177/0734242X09345794.
14. Kosulina, T.P., Solntseva, T.A. Sposob obezvrezhivaniya neftesoderzhashhih shlamov [Method of decontaminating oily mud]. Patent Russia no. 2395466, 2010. (rus)
15. Shen, Y., Chen, X., Wang, J., Ge, X., Chen, M. Oil sludge recycling by ash-catalyzed pyrolysis-reforming processes. *Fuel*. 2016. 182. Pp. 871–878. DOI: 10.1016/j.fuel.2016.05.102.
16. Johnson, O.A., Affam, A.C. Petroleum sludge treatment and disposal: A review. *Environmental Engineering Research*. 2019. 24(2). Pp. 191–201. DOI: 10.4491/EER.2018.134.
17. Litvinova, T.A., Kosulina, T.P. Sposob poluchenija organomineral'noj dobavki k stroitel'nym materialam [Method of obtaining organo-mineral additive to building materials]. Patent Russia no. 2548441, 2015. (rus)
18. Bokovikova, T.N., Sperber, D.R., Sperber, E.R., Volkova, C.C. Ispolzovaniye nefteshlamov v stroitelstve dorozhnykh pokrytiy i odezhd [Application of oil-slimes in road base and surface construction]. *Neftegazovoye delo [Petroleum engineering]*. 2011. 2. Pp. 311–315. (rus)
19. Hassanzadeh, M., Tayebi, L., Dezfouli, H. Investigation of factors affecting on viscosity reduction of sludge from Iranian crude oil storage tanks. *Petroleum Science*. 2018. 15(3). Pp. 634–643. DOI: 10.1007/s12182-018-0247-9.
20. Gang, L., Shuhai, G., Hanfeng, Y. Thermal treatment of heavy oily sludge: resource recovery and potential utilization of residual asphalt-like emulsion as a stabilization/solidification material. *RSC Advances*. 2015. 5(127). Pp. 105299–105306. DOI: 10.1039/C5RA14574K.
21. Al Zubaidy, I.A.H., Al-Tamimi, A.K. Production of sustainable pavement with oil sludge. *Road Materials and Pavement Design*. 2014. 15(3). Pp. 691–700. DOI: 10.1080/14680629.2014.908139.
22. Teltayev, B.B., Rossi, C.O., Ashimova, S. Composition and rheological characteristics of bitumen in short-term and long-term aging. *Magazine of Civil Engineering*. 2018. 81(5). Pp. 93–101. DOI: 10.18720/MCE.81.10.
23. International standard of Commonwealth of Independent States GOST 30491-2012. Smesi organomineralnyye i grunty. ukreplennyye organicheskiye vyazhushchimi. dlya dorozhnogo i aerodromnogo stroitelstva. Tekhnicheskiye usloviya [Organomineral mixtures and soils stabilized by organic binders for road and airfield construction. Specifications]. (rus)
24. International standard of Commonwealth of Independent States GOST 12801-98. Materialy na osnove organicheskikh vyazhushchikh dlya dorozhnogo i aerodromnogo stroitelstva. Metody ispytaniy [Materials on the basis of organic binders for road and airfield construction. Test methods]. (rus)
25. International standard of Commonwealth of Independent States GOST 10178-85. Portlandsement i shlakoportlandsement. Tekhnicheskiye usloviya [Portland cement and portland blastfurnace slag cement. Specifications]. (rus)
26. International standard of Commonwealth of Independent States GOST 23732-2011. Voda dlya betonov i stroitelnykh rastvorov. Tekhnicheskiye usloviya [Water for concrete and mortars. Specifications]. (rus)

Contacts:

Olga Ilina, +7(987)2975616; *ilinaon@inbox.ru*

Ignat Ilin, +7(919)6379750; *ilignat97@mail.ru*



DOI: 10.18720/MCE.92.10

Дорожные органоминеральные смеси на основе нефтяного шлама

О.Н. Ильина *, И.Б. Ильин,

Казанский государственный архитектурно-строительный университет, г. Казань, Россия,

** E-mail: ilinaon@inbox.ru*

Ключевые слова: нефтяной шлам, органо-минеральные смеси, автомобильные дороги, технология строительства, утилизация

Аннотация. В настоящее время актуальное значение в дорожном строительстве приобретает разработка и внедрение современных технологий строительства с применением нефтяных отходов. Большая часть таких отходов хранится в прудах-накопителях, которые занимают огромные территории, загрязняют атмосферу, грунтовые воды, почву и наносят вред окружающей среде. Цель исследований является разработка составов органоминеральных смесей на основе нефтяного шлама и технологии строительства оснований автомобильных дорог с их применением. Методика экспериментальных исследований заключалась в определении показателей прочности, водостойкости, водонасыщения, набухания материалов различного состава, также устанавливались оптимальные пределы варьирования факторов, обеспечивающие требуемую надежность результатов. В результате исследований установлено, что оптимальное содержание нефтяного шлама в составе разработанных смесей составляет 30%, щебня – 70%, содержание портландцемента составляет 6%, физико-механические показатели органоминеральной смеси на основе нефтяного шлама соответствуют нормативным требованиям. При опытно-промышленном внедрении результатов исследований на 4 экспериментальных участках автомобильных дорог разработана технология строительства оснований автомобильных дорог из органоминеральной смеси на основе нефтяного шлама серийно выпускаемыми дорожно-строительными машинами с ведущим механизмом – ресайклером методом «смещения на дороге». Разработана технологическая схема предварительной подготовки нефтяного шлама на установке. Подготовленный нефтяной шлам представляет собой однородное по цвету, зерновому составу, массовой доли воды и нефти вторичное сырье для дорожно-строительных материалов. Предложенная современная технология строительства оснований автомобильных дорог позволяет сделать цикл утилизации нефтяных шламов полностью завершенным и исключить образование побочных отходов. Это является неотъемлемой частью рационального природопользования и экономии материальных ресурсов, способствует улучшению экологического состояния окружающей природной среды в районах добычи и переработки нефти.

Литература

1. Цокур О.С., Литвинова Т.А., Косулина Т.П. Применение наилучших доступных технологий для утилизации промышленных отходов // IV Международная научная экологическая конференция Проблемы рекультивации отходов быта, промышленного и сельскохозяйственного производства. Краснодар: КГАУ, 2015. С. 728–732.
2. Потравный И.М., Новоселов А.Л., Новоселова И.Ю. Оптимизация использования ресурсов техногенных месторождений с учетом факторов неопределенности // Экономика региона. 2017. № 13(4). С. 1280–1290. DOI: 10.17059/2017-4-24.
3. Li H., Li J., Zhao X., Zhang G., Kong Q. Management of waste lubricant oil (WLO): WLO-to-energy through gasification process // Petroleum Science and Technology. 2018. № 36(16). Pp. 1229–1234. DOI: 10.1080/10916466.2018.1465973.
4. Piatak N.M., Parsons M.B., Seal R.R. Characteristics and environmental aspects of slag: A review // Applied Geochemistry. 2015. № 57. Pp. 236–266. DOI: 10.1016/j.apgeochem.2014.04.009.
5. Demirbas A. Waste management, waste resource facilities and waste conversion processes // Energy Conversion and Management. 2011. № 52(2). Pp. 1280–1287. DOI: 10.1016/j.enconman.2010.09.025.
6. Arulrajah A., Mohammadinia A., Phummiphan I., Horpibulsuk S., Samingthong W. Stabilization of Recycled Demolition Aggregates by Geopolymers comprising Calcium Carbide Residue, Fly Ash and Slag precursors // Construction and Building Materials. 2016. № 114. Pp. 864–873. DOI: 10.1016/j.conbuildmat.2016.03.150.
7. Gruyaert E., Robeyst N., De Belie N. Study of the hydration of portland cement blended with blast-furnace slag by calorimetry and thermogravimetry // Journal of thermal analysis and calorimetry. 2010. № 102(3). Pp. 941–951. DOI: 10.1007/s10973-010-0841-6.
8. Пат. 30806 РК, МПК E01C 3/00, Состав для основания дорожных одежд / Телтаев Б.Б., Ергожин Е.Е., Имаилова Г.Г., Аманиязов Б.Т., Джусипбеков У.Ж., Нургалиева Г.О., Утин Т.М.; заявитель и патентообладатель АО «КАЗДОРНИИ», АО «ИХН» - № 2014/1837.1; заявл. 12.12.14; опубл. 25.12.15, Бюл. № 12.

9. Киянец А.В. Бетон с добавлением фибры из переработанного полиэтилентерефталата // Инженерно-строительный журнал. 2018. № 8(84). С. 109–118. DOI: 10.18720/MCE.84.11.
10. Smol M., Kulczycka J., Henclik A., Gorazda K., Wzorek Z. The possible use of sewage sludge ash (SSA) in the construction industry as a way towards a circular economy // Journal of Cleaner Production. 2015. № 95. Pp. 45–54. DOI: 10.1016/j.jclepro.2015.02.051.
11. Zhang J., Liu J., Siddiqui M.K., Nazeer W. Energy and economic aspects of synthesis gas production from oil sludge and plastic waste // Petroleum Science and Technology. 2019. № 37(4). Pp. 430–435. DOI: 10.1080/10916466.2018.1550501.
12. Jin Y., Zheng X., Chi Y., Ni M. Experimental study and assessment of different measurement methods of water in oil sludge // Drying technology. 2014. № 32(3). Pp. 251–257. DOI: 10.1080/07373937.2013.811251.
13. Heidarzadeh N., Gitipour S., Abdoli M.A. Characterization of oily sludge from a Tehran oil refinery // Waste Management & Research. 2010. № 28(10). Pp. 921–927. DOI: 10.1177/0734242X09345794.
14. Пат. 2395466 РФ, МПК C02F 11/14, B09B 3/00, Способ обезвреживания нефтесодержащих шламов / Косулина Т.П., Солнцева Т.А.; заявитель и патентообладатель ГОУВПО «КубГТУ» – № 2008147569/15; заявл. 02.12.08; опубл. 27.07.10, Бюл. № 21.
15. Shen Y., Chen X., Wang J., Ge X., Chen M. Oil sludge recycling by ash-catalyzed pyrolysis-reforming processes // Fuel. 2016. № 182. Pp. 871–878. DOI: 10.1016/j.fuel.2016.05.102.
16. Johnson O.A., Affam A.C. Petroleum sludge treatment and disposal: A review // Environmental Engineering Research. 2019. № 24(2). Pp. 191–201. DOI: 10.4491/EER.2018.134.
17. Пат. 2548441 РФ, МПК C02F 11/14, C04B 18/00, Способ получения органоминеральной добавки к строительным материалам / Литвинова Т.А., Косулина Т.П.; заявитель и патентообладатель ГОУВПО «КубГТУ» – № 2013155369/05; заявл. 12.12.13; опубл. 20.04.15, Бюл. № 11.
18. Боковикова Т.Н., Шпербер Д.Р., Шпербер Е.Р., Волкова С.С. Использование нефтешламов в строительстве дорожных покрытий и одежд // Нефтегазовое дело. № 2. 2011. С. 311–315.
19. Hassanzadeh M., Tayebi L., Dezfouli H. Investigation of factors affecting on viscosity reduction of sludge from Iranian crude oil storage tanks // Petroleum Science. 2018. № 15(3). Pp. 634–643. DOI: 10.1007/s12182-018-0247-9.
20. Gang L., Shuhai G., Hanfeng Y. Thermal treatment of heavy oily sludge: resource recovery and potential utilization of residual asphalt-like emulsion as a stabilization/solidification material // RSC Advances. 2015. № 5(127). Pp. 105299–105306. DOI: 10.1039/C5RA14574K.
21. Al Zubaidy I.A.H., Al-Tamimi A.K. Production of sustainable pavement with oil sludge // Road Materials and Pavement Design. 2014. № 15(3). Pp. 691–700. DOI: 10.1080/14680629.2014.908139.
22. Телтаев Б.Б., Росси Ч.О., Ашимова С.Ж. Состав и реологические характеристики битума при кратковременном и длительном старении // Инженерно-строительный журнал. 2018. № 5(81). С. 93–101. DOI: 10.18720/MCE.81.10.
23. Межгосударственный стандарт ГОСТ 30491-2012. Смеси органоминеральные и грунты, укрепленные органическими вяжущими, для дорожного и аэродромного строительства. Технические условия.
24. Межгосударственный стандарт ГОСТ 12801-98. Материалы на основе органических вяжущих для дорожного и аэродромного строительства. Методы испытаний.
25. Межгосударственный стандарт ГОСТ 10178-85. Портландцемент и шлакопортландцемент. Технические условия.
26. Межгосударственный стандарт ГОСТ 23732-2011. Вода для бетонов и строительных растворов. Технические условия.

Контактные данные:

Ольга Николаевна Ильина, +7(987)2975616; ilinaon@inbox.ru

Игнат Борисович Ильин, +7(919)6379750; ilignat97@mail.ru

© Ильина О.Н., Ильин И.Б., 2019



DOI: 10.18720/MCE.92.11

Stress-strain state of a glass panel with adhesive point fixings

E.N. Gerasimova^a, A.V. Galyamichev^a, M.K. Mikhaylova^b, S. Dogru^c

^a Peter the Great St. Petersburg Polytechnic University, St. Petersburg, Russia

^b NIUPTS «Mezhhregional'nyy institut okonnykh i fasadnykh konstruksiy», St. Petersburg, Russia

^c Istanbul Okan University, Istanbul, Turkey

* E-mail: katyageras17@gmail.com

Keywords: adhesion, adhesive joints, glass, stress concentration, structural glass

Abstract. The article is devoted to the study on the bearing capacity of the glazing with adhesive point fixings. This article provides evaluation of such factors as applied load, edge distance, panel thickness and number of point fixtures and their influence on stress-strain state of a glazing panel. Calculation of the panels under various conditions was performed by means of Finite Element Method (FEM). Results of the calculation show dependencies between considered factors and stress-strain state of a panel and present an overview of the on the possibilities of usage of such structures in accordance with Ultimate Limit State and Serviceability Limit State.

1. Introduction

Nowadays facade glazing is the most widespread type of enclosing structure used in public buildings and facilities. Structural façade, the particular type of translucent facade structures, allows to avoid presence of visible elements of the framework outside the building. It also increases the amount of daylight coming through enclosing structure and creates uniform and smooth surface of the façade.

A.A. Magay and N.V. Dubynin in the article [1] classify translucent facades by architectural and structural criteria. Based on second feature, the authors distinguish mullion-transom, frame, spider, structural, semi-structural, ventilated and panel types of facades. They also analyze the structural solutions and practical application of these options.

The main research purpose of [2] is the classification of a structural glazing.

Drass M., Schneider J., Odenbreit C., Kolling S. in [3–7] describe the main characteristics of Transparent Silicone Structural Adhesive (TSSA) and investigate the new nano-model of this material.

Pascual C., Montali J., Overend M. in article “Adhesively-bonded GFRP-glass sandwich components for structurally efficient glazing applications” show the results of the torsion and shear tests performed on silicone samples and introduce new analytic models for determination of deflections and stresses in the structure fixed by silicone adhesives [8].

Sitte S., Brasseur M.J., Carbary L.D., Wolf A.T. in their research “Preliminary Evaluation of the Mechanical Properties and Durability of Transparent Structural Silicone Adhesive (TSSA) for Point Fixing in Glazing” perform a preliminary evaluation of TSSA and present information regarding its durability and physical properties. Authors in [14–20] consider adhesive point fixation by means of TSSA and subject samples to various tests with following analysis of the results.

Articles [10, 11] are dedicated to the consideration of wind loads which act on façade structures. Authors in [12, 13] investigate problems which arise in curtain wall during its exploitation.

The object of study presented in this research is a stress-strain state of glass façade panels which have point fixation to bearing structure (route of a spider fitting in a structural glazing)

Gerasimova, E.N., Galyamichev, A.V., Mikhaylova, M.K., Dogru, S. Stress-strain state of a glass panel with adhesive point fixings. Magazine of Civil Engineering. 2019. 92(8). Pp. 127–141. DOI: 10.18720/MCE.92.11

Герасимова Е.Н., Галыамичев А.В., Михайлова М.К., Догру С. Напряженно-деформированное состояние панели из стекла с точечным клеевым креплением // Инженерно-строительный журнал. 2019. № 8(92). С. 127–141. DOI: 10.18720/MCE.92.11



Nowadays there is neither normative documentation for design of a structural glazing nor for evaluation of an adhesive point fixation. In foreign references researchers analyze the material itself, but without further investigation of its performance within the structure.

The main purpose of this research work was a determination of the factors which directly influence design of a curtain wall with adhesive point fixation.

Authors analyzed the results of a panel calculation while changing following parameters:

- Number of point fixtures;
- Thickness of a façade panel;
- Value of fixture edge distance.

Dow Corning is at the moment a major manufacturer of silicone adhesives. The technical guideline of this company [22] provides the percentage distribution of applied load to each fixture. Present article also verifies the information provided by the manufacturer.

The calculation was carried out on example of the most common panels with the dimensions 600×1200 mm, 1100×2100 mm and 2100×4200 mm, where first value is a width and second is a height of a panel. These sizes were adopted in order to investigate the panels of different dimensions but with the same side ratio.



Figure 1. Silicone film of a thickness of 1 mm [21].



Figure 2. View of a fixture from outside [21].



Figure 3. View of a fixture from inside [21].

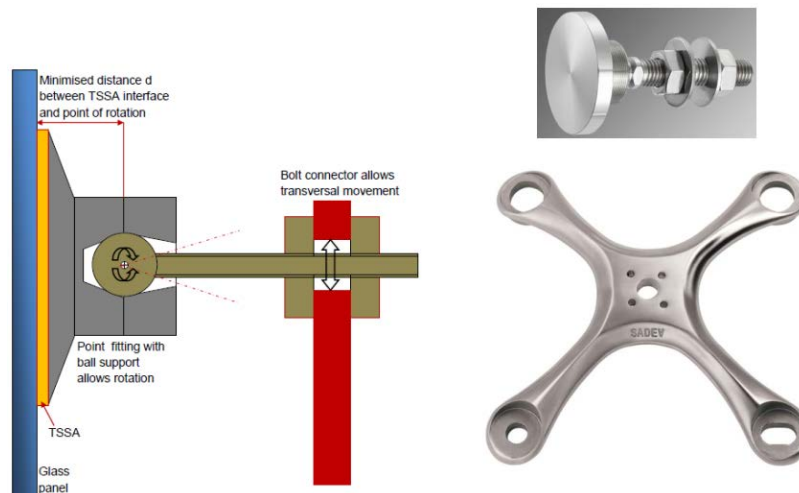


Figure 4. Fixture detail [22].

2. Methods

2.1. Physical model

Flat toughened glass with following characteristics according to Russian State Standard GOST 30698-2014 "Tempered glass" was used for the analysis:

- Density:

$$\rho = 2500 \text{ km/m}^3;$$

- Young's modulus:

$$E = 70\,000 \text{ N/mm}^2;$$

- Poisson's ratio:

$$\nu = 0.2$$

- Considered thickness of a panel:

$$t = 8, 10, 12, 14, 16, 18 \text{ mm};$$

- Considered number of point fixtures:

$$n = 4, 6, 8.$$

2.2. Boundary conditions

One point on the top of a panel was fixed in x , y and z directions for compensation of temperature stresses, the second one was fixed in y and z directions, the others were fixed in y direction only.

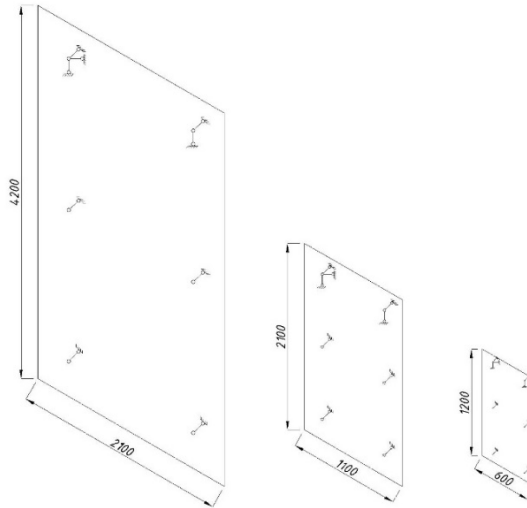


Figure 5. Dimensions of considered panels.

2.3. Applied load

Façade panel was subjected to evenly distributed wind load in accordance with Russian Set of Rules 70.13330.2012 "Load-bearing and separating constructions".

Load value was calculated for the angle zone at the height of +100 m according to Russian Set of Rules 20.13330.2016 "Loads and actions":

$$w_{+(-)} = w_o \cdot k(z_e) \cdot [1 + \xi(z_e)] \cdot c_p \cdot v_{+(-)},$$

where $w_{+(-)}$ is characteristic peak value of positive and negative impact of wind load;

w_o is characteristic value of wind pressure (adopted in accordance with location of construction site):

$$w_o = 0.23 \text{ kPa}$$

z_e is equivalent height ($z_e = 100 \text{ m}$);

$k(z_e)$, $\xi(z_e)$ are coefficients, which take into account change of pressure and wind pulsation at the height z_e respectively:

$$k(100) = 2; \quad \xi(100) = 0.54;$$

$v_{+(-)}$ are correlation coefficients which correspond to positive (+) and negative wind pressure (-) in dependence on the area A , which is subjected to wind load; for panel with dimensions $b \times h = 4200 \times 2100 \text{ mm}$ $v_{+(-)} = 0.82$.

c_p is peak value of aerodynamic coefficients of positive (+) and negative wind pressure (-), defined in Russian Set of Rules 20.13330.2016 "Loads and actions":

For façade structures, which are located in angle zone, $c_p = 2.2$. Therefore, formula of characteristic wind load takes the form of:

$$w_{ny} = 0.23 \cdot 2 \cdot [1 + 0.54] \cdot 2.2 \cdot 0.82 = 1.28 \text{ E}.$$

Design wind load:

$$w_y = w_{ny} \cdot \gamma_f,$$

where γ_f is safety factor.

$$w_y = 1.28 \cdot 1.4 = 1.79 \text{ kPa.}$$

2.4. Ultimate Limit State

In accordance with Ultimate Limit State requirements, which are defined for toughened glass structures in Russian Set of Rules 20.13330.2016 "Loads and actions", design bending strength value of a glass is equal to:

$$R = 120 \text{ MPa.}$$

2.5. Serviceability Limit State

According to Russian Set of Rules 20.13330.2016 "Loads and actions", deflection of flat glass subjected to the most unfavorable combination of factors should not exceed 1/250 of the shortest side of a panel:

$$|w| = \frac{1}{250} a$$

where a is the shortest side of a panel.

For example, for the panel with dimensions 600×1200 mm:

$$a = 600 \text{ mm;}$$

$$|w| = \frac{1}{250} \cdot 600 = 2.4 \text{ mm.}$$

For:

$$a = 1100 \text{ mm} \rightarrow |w| = 4.4 \text{ mm;}$$

$$a = 2100 \text{ mm} \rightarrow |w| = 8.4 \text{ mm.}$$

3. Results

3.1. Load distribution

Percentage load distribution in the panels was derived from the internal efforts obtained in software SCAD.

Figure 9 presents load distribution to point fixtures from [22].

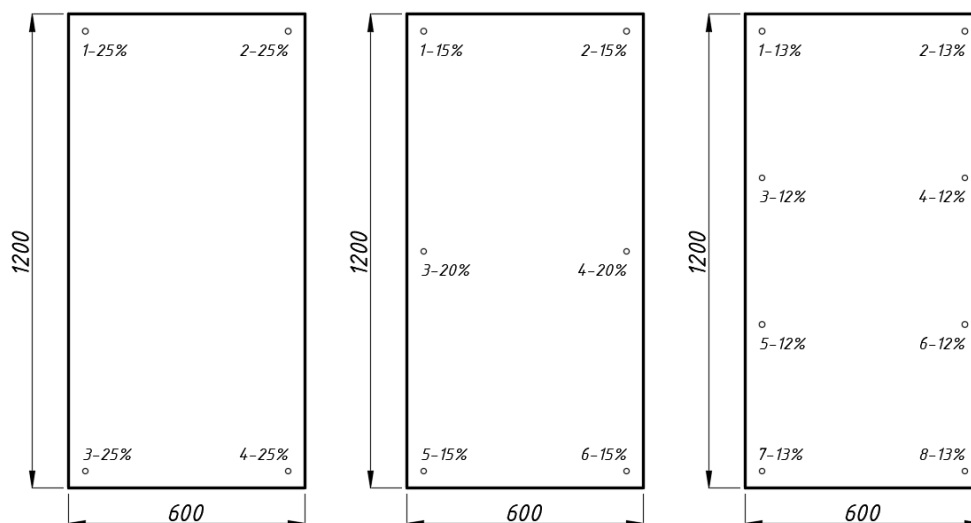


Figure 6. Load distribution to fixtures for the panel 600×1200×10 mm.

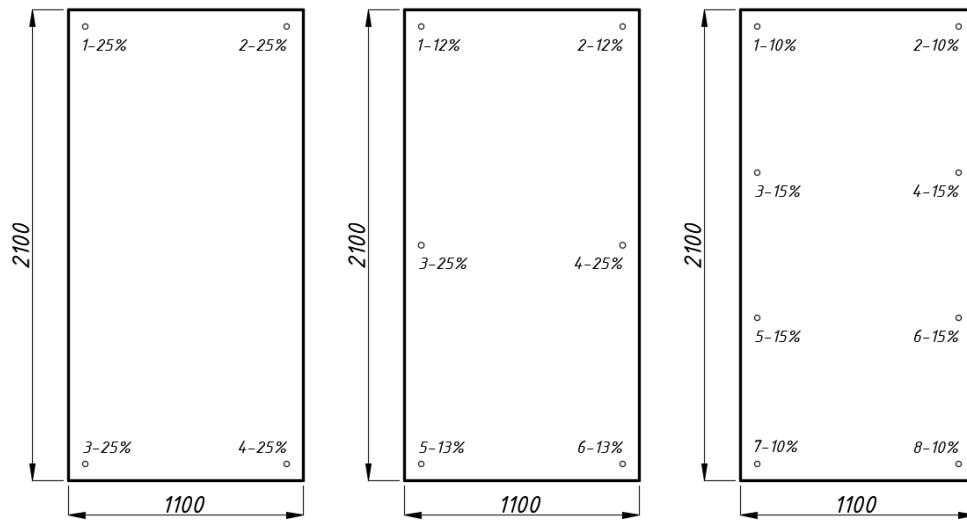


Figure 7. Load distribution to fixtures for the panel 1100x2100x10 mm.

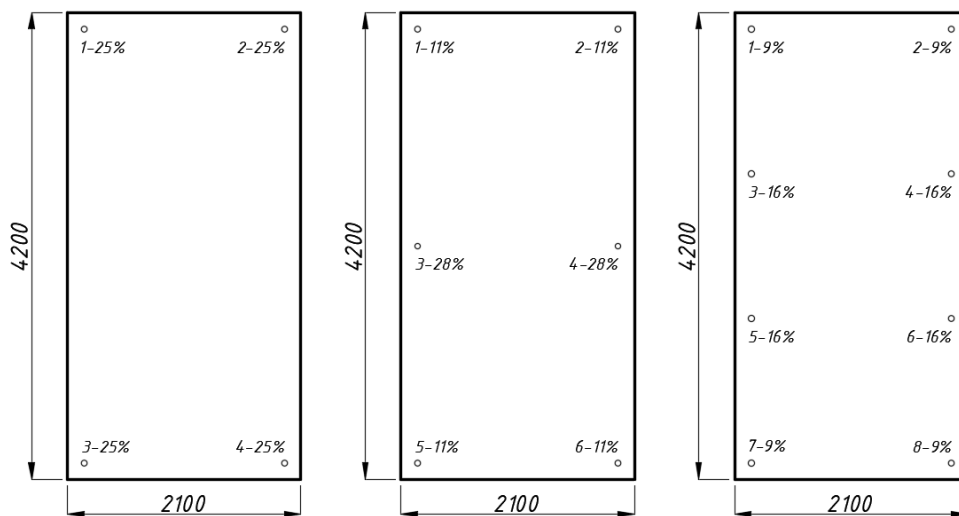


Figure 8. Load distribution to fixtures for the panel 2100x4200x10 mm.

In the panel with 4 fixtures every point bears 25 % of applied load. In the panels with 6 and 8 fixtures the distribution should be checked as it varies depending on dimensions of the panel.

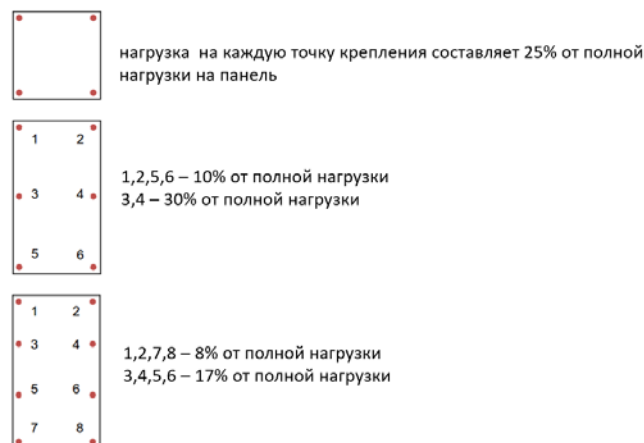


Figure 9. Load distribution to fixtures according to guideline by Dow Corning [22].

Calculation of inaccuracy between values derived from SCAD and Dow Corning guideline:

$$\delta_{0.6 \times 1.2} = \frac{30 - 20}{30} \cdot 100 \% = 33.3 \%$$

$$\delta_{1.1 \times 2.1} = \frac{30 - 25}{30} \cdot 100 \% = 16.7 \%;$$

$$\delta_{2.1 \times 4.2} = \frac{30 - 28}{30} \cdot 100 \% = 6.7 \%.$$

3.2. Modification of the number of point fixtures

The stresses, which arose in the panels with dimensions $b \times h \times t = 2100 \times 4200 \times 10$ mm and different number of fixtures under the action of wind load, are presented below:

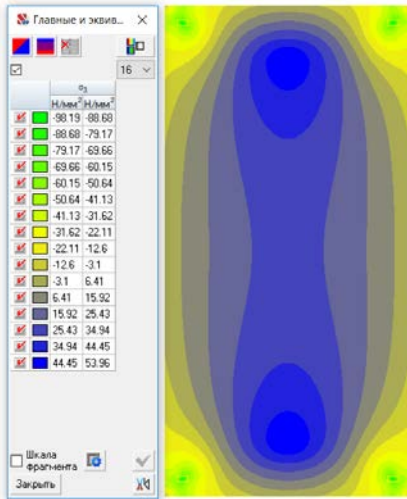


Figure 10. Stresses in panel 2100×4200 mm with 4 point fixtures.

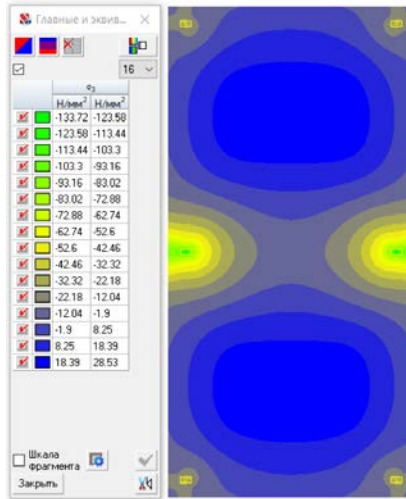


Figure 11. Stresses in panel 2100×4200 mm with 4 point fixtures.

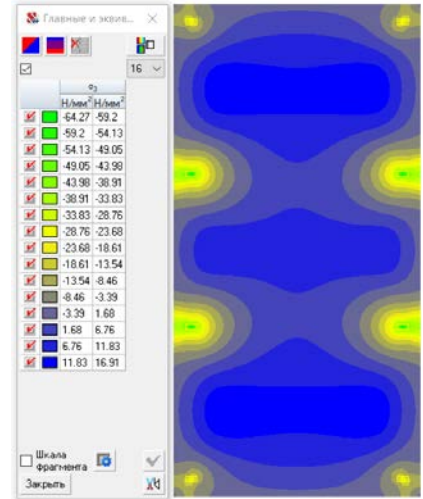


Figure 12. Stresses in panel 2100×4200 mm with 8 point fixtures.

Figure 13 represents graphical dependencies of maximum and average values of stresses on the number of point fixtures.

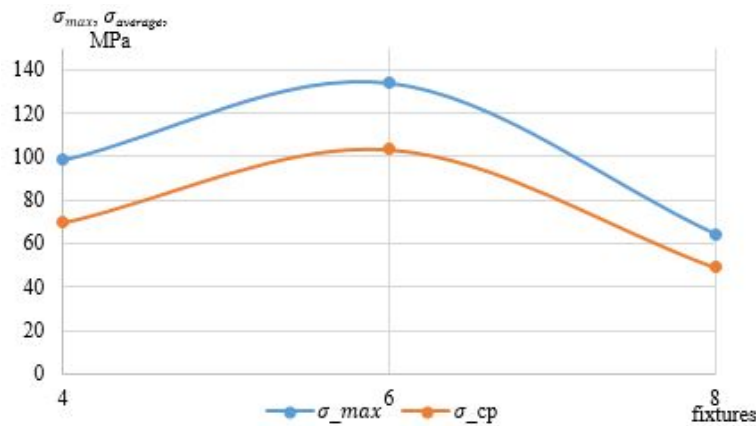


Figure 13. Dependence of maximum and average values of stresses on the number of point fixtures in the panel with dimensions 2100×4200 mm.

3.3. Modification of the thickness of the panel

The deflections in the panels with dimensions $b \times h = 2100 \times 4200$ mm, 6 point fixtures and different values of thickness ($t = 8, 10, 12, 14, 16$ and 18 mm), are presented below:

Figure 20 represents graphical dependencies of maximum deflections on the value of panel thickness.

3.4. Modification of the value of fixture edge distance

The analysis of influence of edge distance was performed on the panel with dimensions $b \times h \times t = 2100 \times 4200 \times 10$ mm while edge distance d was varied for every point fixture.

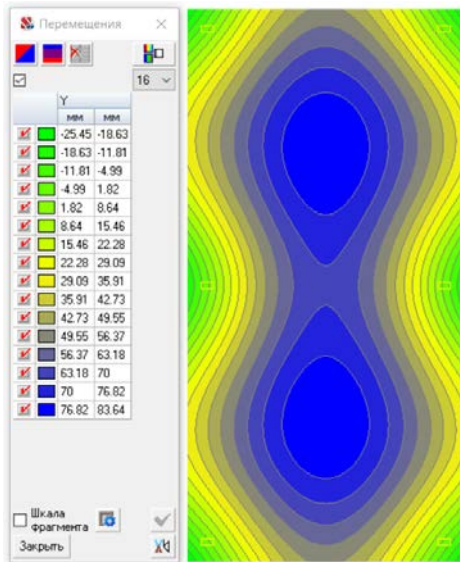


Figure 14. Deflection in panel 2100x4200x8 mm.

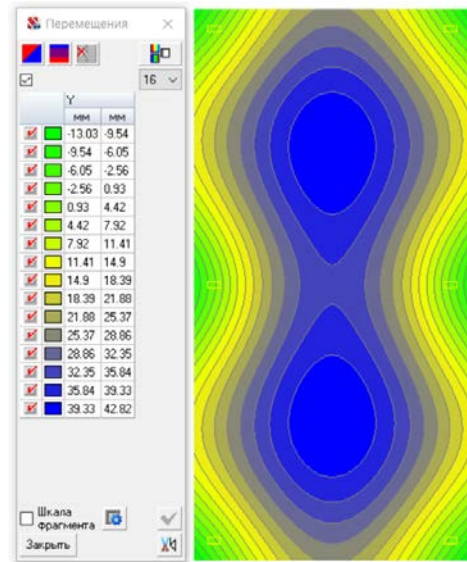


Figure 15. Deflection in panel 2100x4200x10 mm.

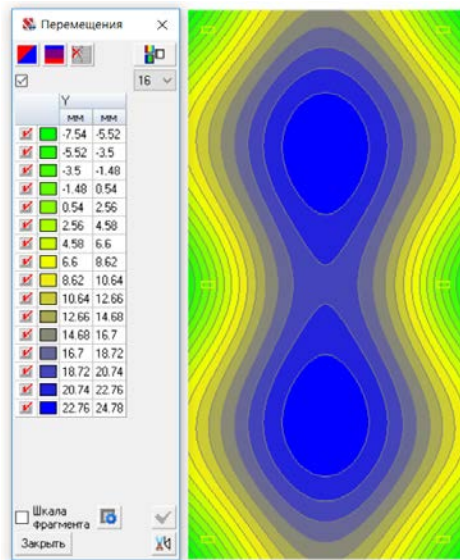


Figure 16. Deflection in panel 2100x4200x12 mm.

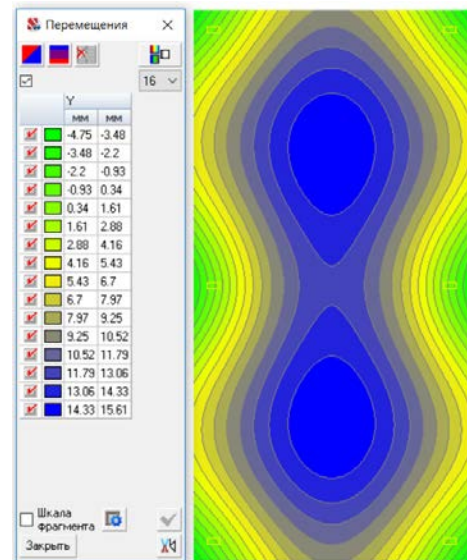


Figure 17. Deflection in panel 2100x4200x14 mm.

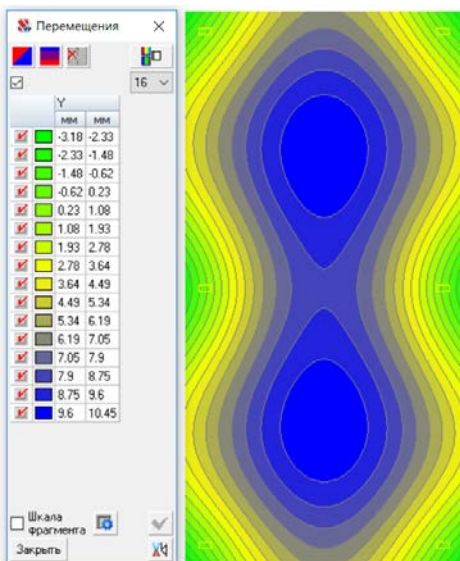


Figure 18. Deflection in panel 2100x4200x16 mm.

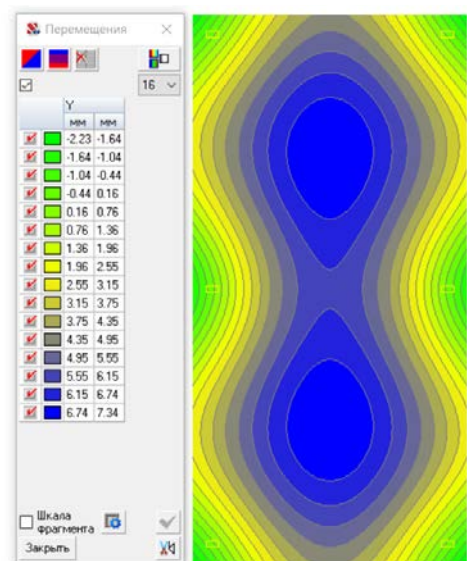


Figure 19. Deflection in panel 2100x4200x18 mm.

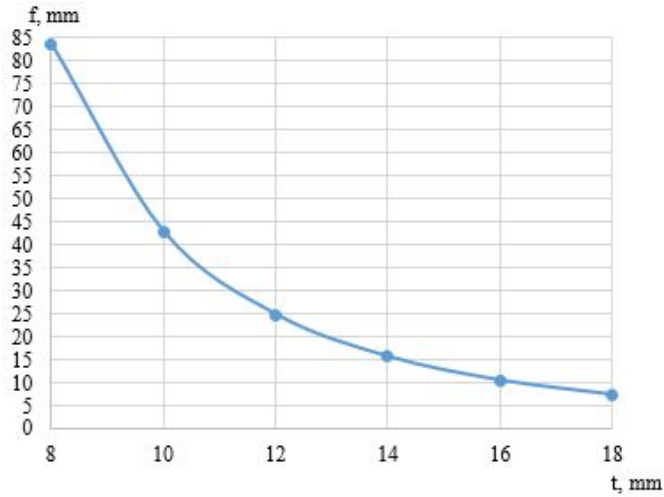


Figure 20. Dependence of maximum values of deflection on the glass thickness in the panel with dimensions 2100×4200 mm.

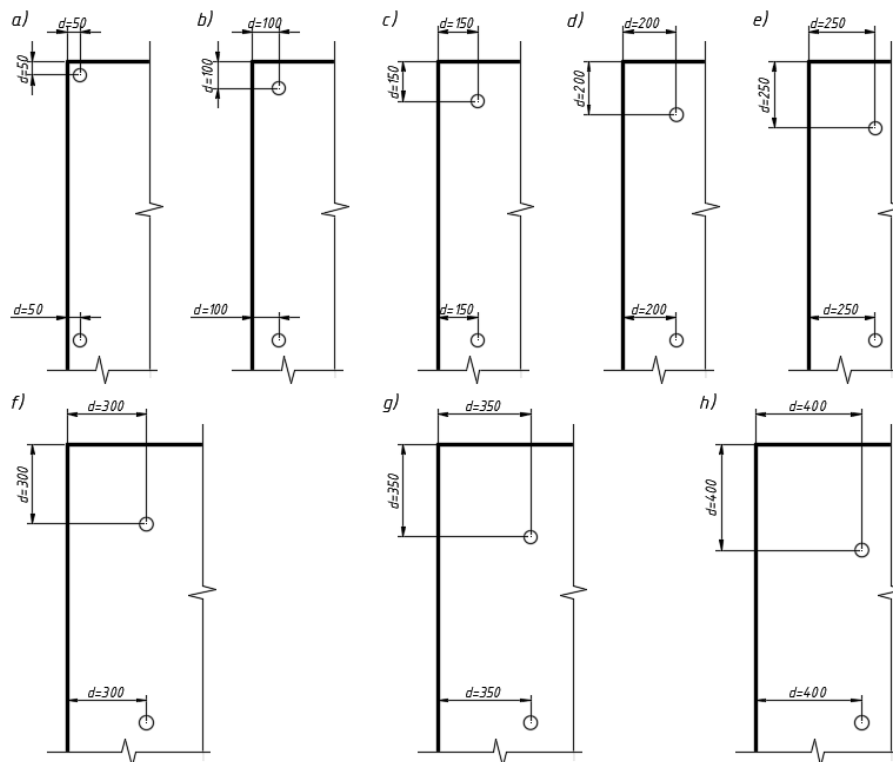


Figure 21. Considered options of point fixture locations relatively panel edge.

As a result, the following diagrams representing stress and deformation distribution in the panels were obtained:

As it can be seen from Figure 38, maximum stresses arose when the edge distance had minimum value. Panels with considered values of edge distance more than 200 mm did not satisfy conditions of Ultimate Limit State.

3.5. Choice of the most optimal structural scheme of façade panel

For the purpose of determination of the most optimal structural scheme, which would satisfy requirements defined by both Ultimate and Serviceability Limit States, a panel with dimensions $b \times h \times t = 2100 \times 4200 \times 16$ mm, 6 point fixtures and edge distance equal to 200 mm was calculated.

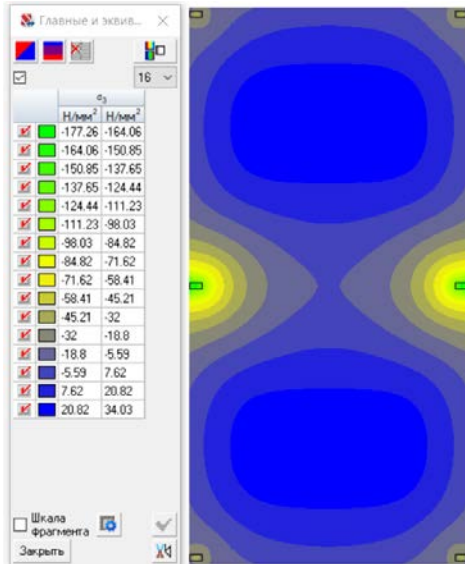


Figure 22. Stresses in the panel with $d = 50$ mm (a)

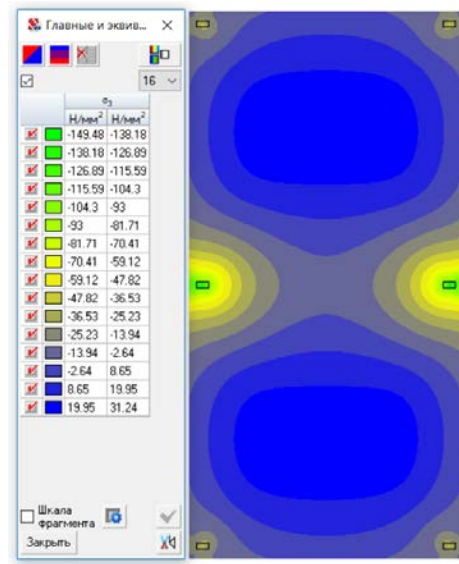


Figure 23. Stresses in the panel with $d = 100$ mm (b)

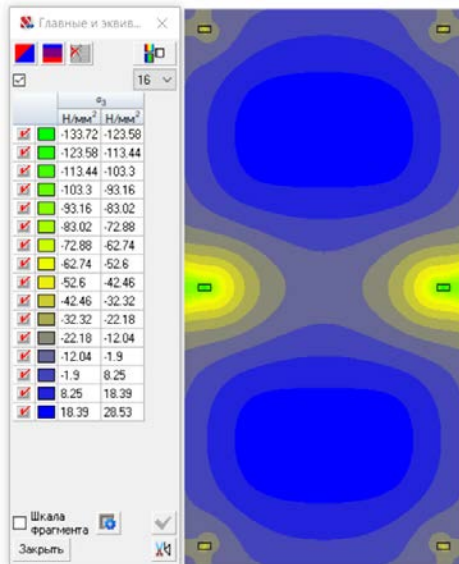


Figure 24. Stresses in the panel with $d = 150$ mm (c)

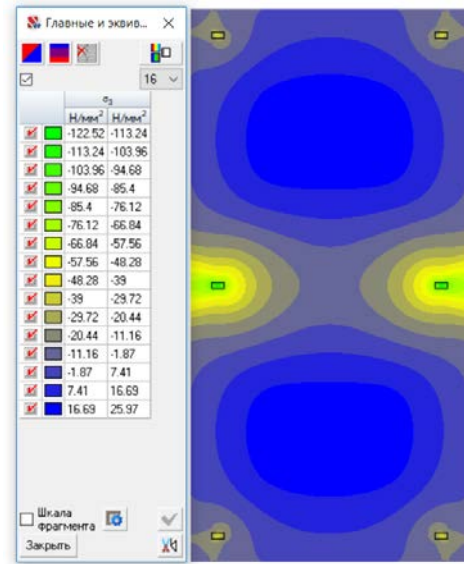


Figure 25. Stresses in the panel with $d = 200$ mm (d)

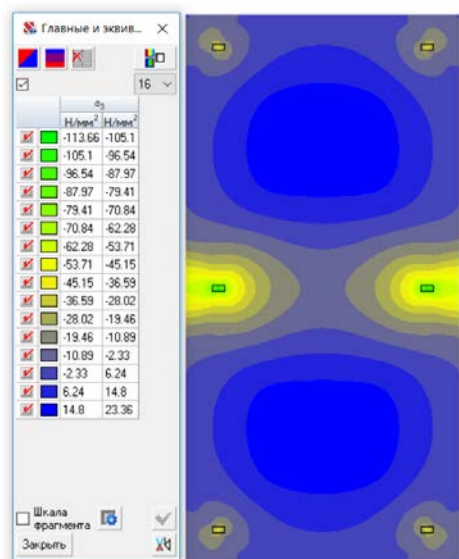


Figure 26. Stresses in the panel with $d = 250$ mm (e).

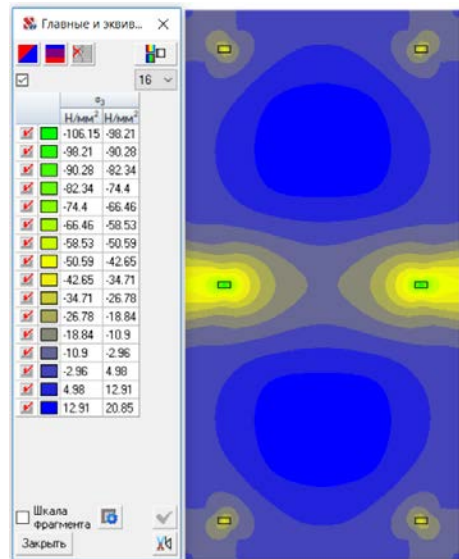


Figure 27. Stresses in the panel with $d = 300$ mm (f).

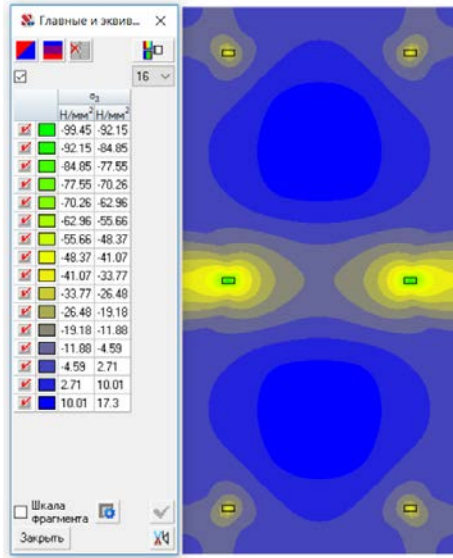


Figure 28. Stresses in the panel with $d = 350$ mm (g).

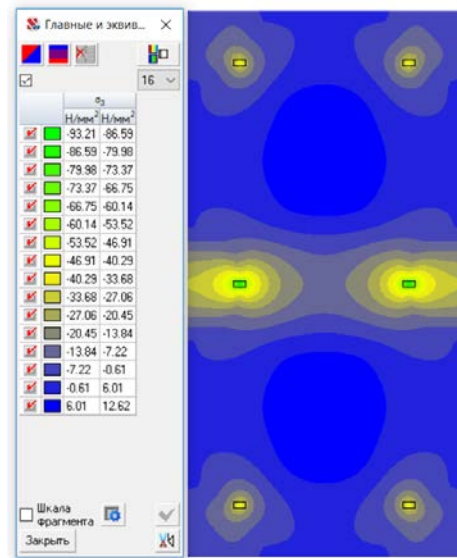


Рисунок 29. Stresses in the panel with $d = 400$ mm (h).

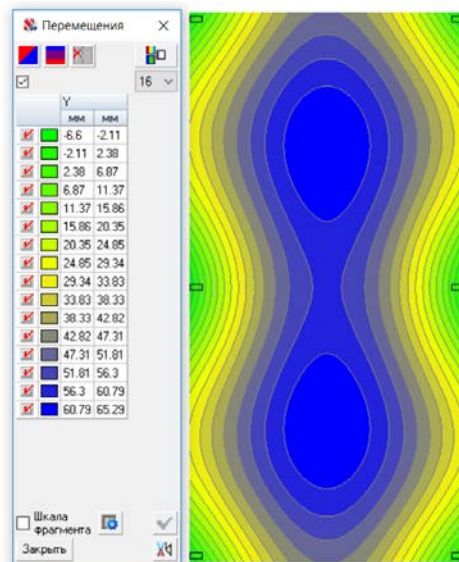


Figure 30. Deformations in the panel with $d = 50$ mm.

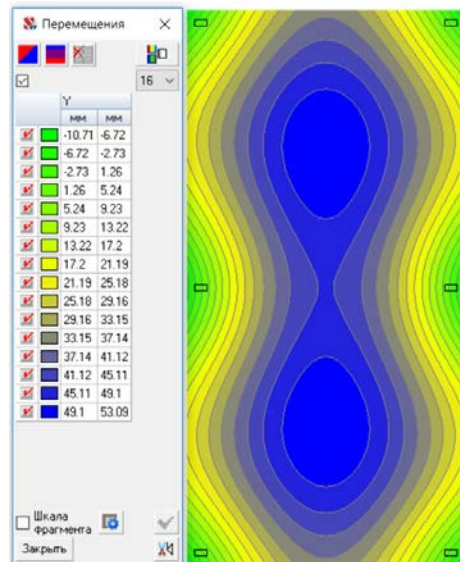


Figure 31. Deformations in the panel with $d = 100$ mm.

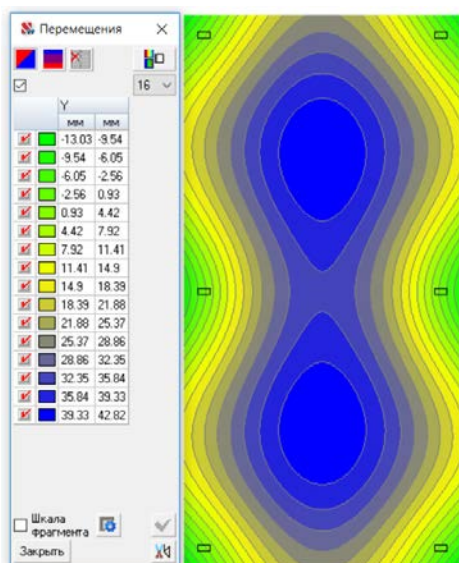


Figure 32. Deformations in the panel with $d = 150$ mm.

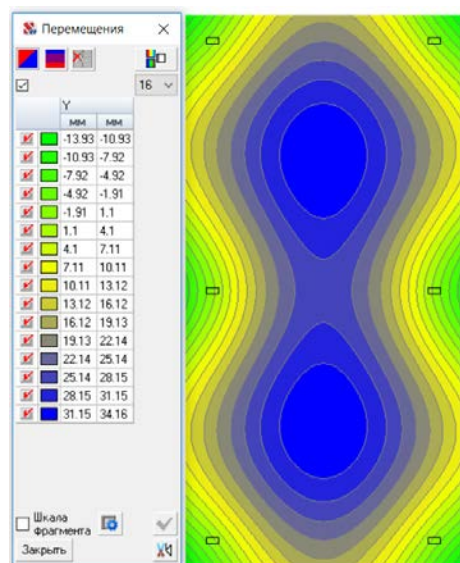


Figure 33. Deformations in the panel with $d = 200$ mm.

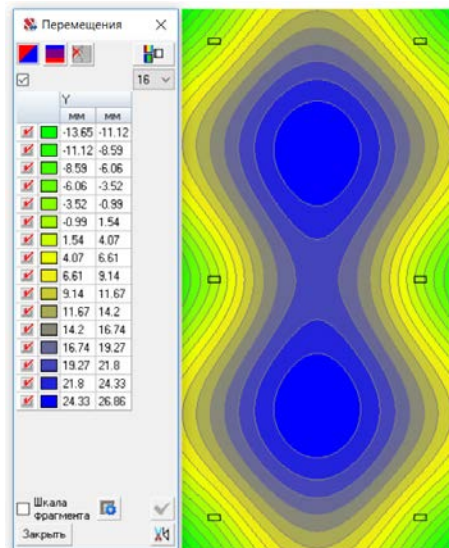


Figure 34. Deformations in the panel with $d = 250$ mm.

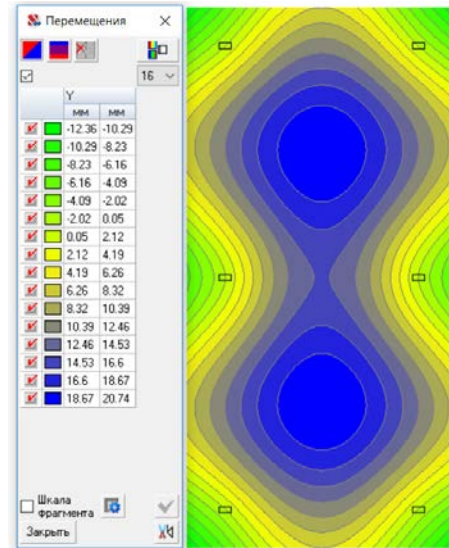


Figure 35. Deformations in the panel with $d = 300$ mm.

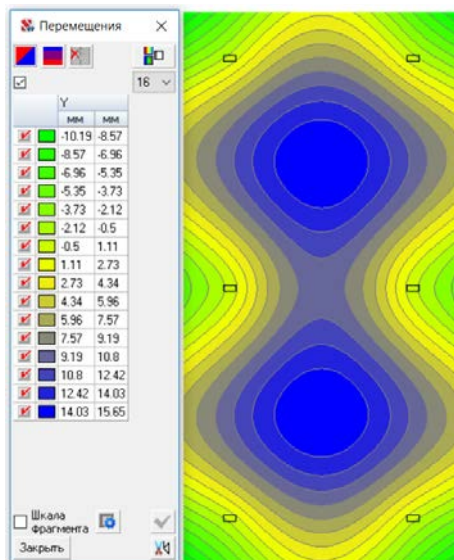


Figure 36. Deformations in the panel with $d = 350$ mm.

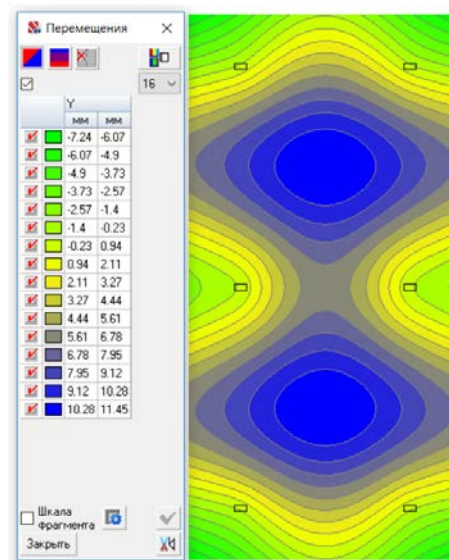


Figure 37. Deformations in the panel with $d = 400$ mm.

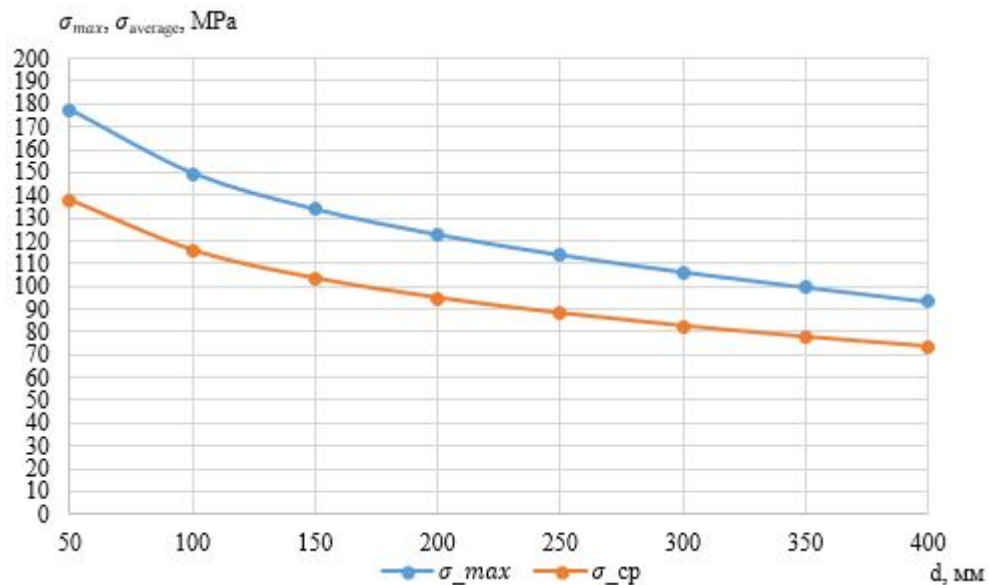


Figure 38. Dependence of maximum and average values of stresses on the fixture edge distance in the panel with dimensions $2100 \times 4200 \times 10$ mm.

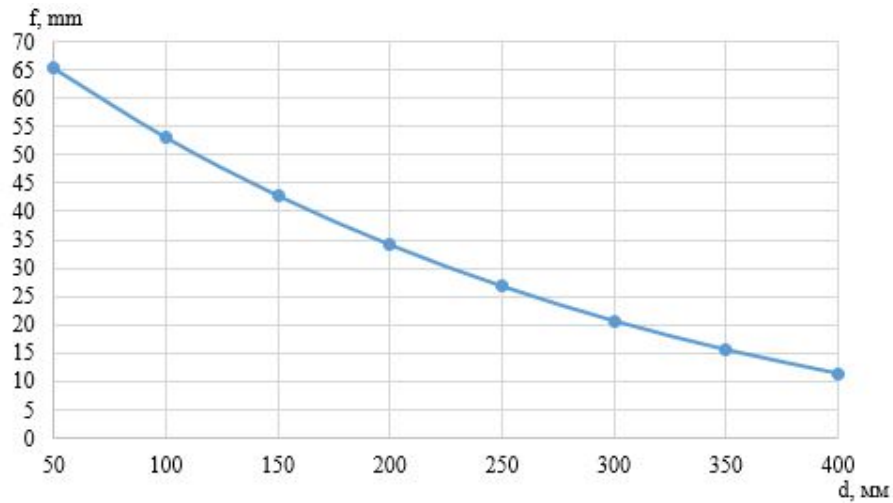


Figure 39. Dependence of maximum values of deformations on the fixture edge distance in the panel with dimensions 2100×4200×10 mm.

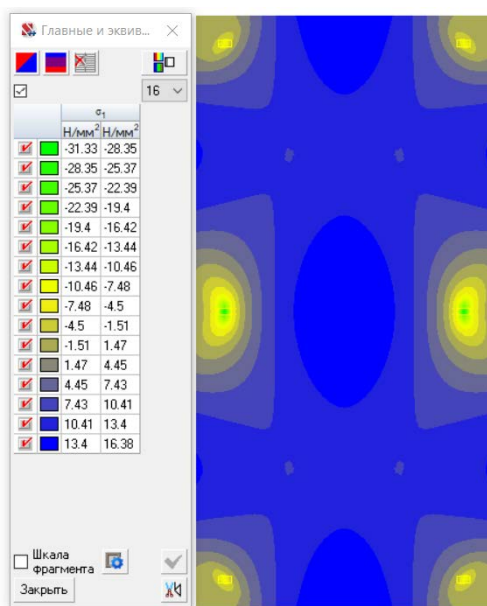


Figure 40. Stress distribution of the panel.

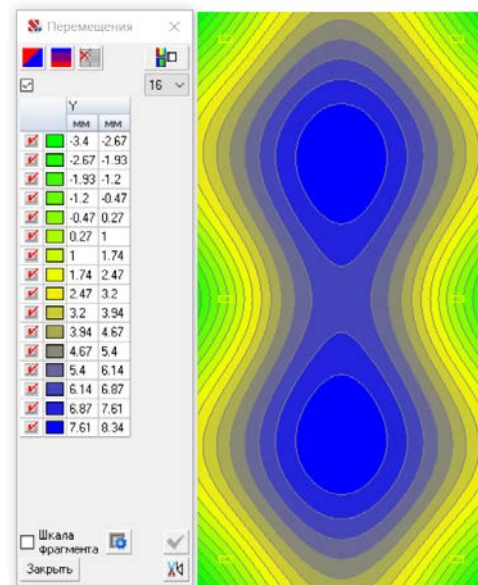


Figure 41. Deformations of panel.

In this scheme the maximum value of the stress which arose on the panel surface σ_{\max} equals to 31.35 MPa. This value is significantly smaller, than maximum allowable strength $R = 120$ MPa.

Maximum deflection f_{\max} equals to 8.34 mm, what does not exceed maximum allowable value for this panel $|w| = 8.4$ mm.

4. Conclusions

The research purpose of this article consisted in calculation of the façade panels under changing parameters such as number of point fixtures, thickness of a panel, value of fixture edge distance and subsequent analysis of their influence on stress-strain state of the panel.

Based on it, the following conclusions were made:

1. Stresses arising in the panel generally decrease with the number of point fixtures increasing. At same time fixture points are concentrators of the stress, and the maximum stress emerge in center fixtures. However, there are exceptional cases (see 4.2)

2. Increase of the number of fixtures does not always lead to increase of its bearing capacity. It can be illustrated on the example of panel with dimensions $b \times h \times t = 2100 \times 4200 \times 10$ mm, which has 6 point fixtures. This panel does not satisfy requirements of ULS, while the same sized panels, but with 4 and 8 fixtures fulfil conditions of Limit State Design. This phenomenon is connected with the fact that in the structural scheme of a continuous beam maximum stress arises in the center support.

3. Increase of the panel thickness leads to decrease of deflections of the panel. Maximum deflections appear in the center of the span between fixtures.

4. Increase of the fixture edge distance leads to decrease of both stresses and deflections of the panel. Maximum stresses and deflections arise when the edge distance is minimum. At the same time, if values of edge distance are increased up to 300–400 mm deflections on the edges become comparable to deflections in the center of the span. If edge distances are greater than 400 mm, deflections on the edges exceed deflections in the center of the span.

5. Percentage distribution of the applied load to the fixtures should be calculated for every design case taking into account edge distances and spans between fixtures.

6. Serviceability Limit state is the defining criteria for the design of glass structures in Russian Federation.

References

- Magay, A.A., Dubynin, N.V. Svetoprozrachnyye fasady vysotnykh mnogofunktionalnykh zdaniy [Translucent facades of high-rise multifunctional buildings]. Vestnik MGSU. 2010. No. 2. Pp. 14–21. (rus)
- Patterson, M.R. Structural glass facades: a unique building technology. Master Thesis, University of Southern California. 2008. 450 p.
- Drass, M., Schneider, J. Constitutive modeling of transparent structural silicone adhesive – TSSA. Proceedings of 14 Darmstädter Kunststofftage – Simulation und Werkstoffmodelle. Darmstadt, 2016.
- Drass, M., Schneider, J. On the mechanical behavior of transparent structural silicone adhesive – TSSA. Mechanics and Computation. 2016. No. 2. Pp. 20–26. DOI: 10.1201/9781315641645-74
- Staudt, Y., Schneider, J., Odenbreit, C. Investigation of the material behavior of bonded connections with silicone. Proceedings of International Conference at glasssec. Dusseldorf, 2014. Pp. 10–20.
- Staudt, Y., Odenbreit, C., Schneider, J. Investigation of Bonded Connections with Silicone under Shear Loading. Proceedings of 4 Conference on Architectural and Structural Applications of Glass. Ghent, 2016. Pp. 3–17.
- Drass, M., Schneider, J., Kolling, S. Damage effects of adhesives in modern glass façades: a micro-mechanically motivated volumetric damage model for poro-hyperelastic materials. International Journal of Mechanics and Materials in Design. 2017. No. 8. Pp. 20–44.
- Pascual, C., Montali, J., Overend, M. Adhesively-bonded GFRP-glass sandwich components for structurally efficient glazing applications. Composite Structures. 2017. No. 160. Pp. 560–573.
- Sitte, S., Brasseur, M.J., Carbary, L.D., Wolf, A.T. Preliminary Evaluation of the Mechanical Properties and Durability of Transparent Structural Silicone Adhesive (TSSA) for Point Fixing in Glazing. Journal of ASTM International. 2011. No. 10. Pp. 4–30.
- Savitskiy, G.A. Vetrovaya nagruzka na sooruzheniya [Wind load applied to buildings]. Moscow: Stroyizdat, 1972. 111 p. (rus)
- Cook, N.J. The designer's guide to wind loading of building structures. Part 2: Static structures. London, 1990. 586 s.
- Nemova, D.V. Navesnyye ventiliruyemye fasady obzor osnovnyye problem [Ventilated facades: an overview of the main problems]. Magazine of Civil Engineering. 2010. No. 5. Pp. 7–11. DOI: 10.18720/MCE.15.3. (rus)
- Gorshkov, A.S., Popov, D.Yu. Konstruktivnoye ispolneniye ventiliruyemogo fasada povyshennoy nadezhnosti [Design of the ventilated facade of the increased reliability]. Magazine of Civil Engineering. 2010. No. 8. Pp. 5–9. (rus)
- Gent, A. Elastic instabilities in rubber. International Journal of Non-Linear Mechanics. 2005. 40(2). Pp. 165–175.
- Dias, V. Development of adhesives constitutive material laws for the assessment of bonded steel to glass partial composite beams. Doctoral Thesis, University of Luxembourg. 2013. 416 p.
- Staudt, Y. Investigation of the material behavior of glued connections with silicone. Master Thesis, Technische Universität Darmstadt. 2013.
- Van Den Bergh, S., Hart, R., Petter, B., Jelle, B.P., Gustavsen, A. Window Spacers and Edge Seals in insulating glass units: a State-of-the-Art Review and Future Perspectives. Energy and Buildings. 2013. No. 58. Pp. 263–280.
- Wolf, A.T. Silicone Sealed Insulating Glass Units. Proceedings of ISAAG – International symposium on the Application of Architectural Glass. Munich, 2004.
- Li, X., Li, S., Zia, Q., Zi, H. Effects of pore sizes of porous silica gels on desorption activation energy of water vapor. Applied Thermal Engineering. 2007. No. 27. Pp. 869–876.
- Baetens, R., Jelle, B.P., Gustavsen, A. Aerogel insulation for building applications: A state-of-the-art review. Energy and Buildings. 2011. No. 43. Pp. 761–769.
- Dow Corning Official website [Online]. URL: https://consumer.dow.com/en-us.html?_ga=2.83410198.1493760776.1527724064-1652577140.1524781935 (reference date: 02.04.18).
- DOWSILTM TSSA/TSSL. Technical Manual. 2018.

Contacts:

Ekaterina Gerasimova, +7(921)9673868; katyageras17@gmail.com

Alexander Galyamichiev, +7(911)8110719; galyamichiev@yandex.ru

Maria Mikhaylova, +7(904)3360888; mmikhaylova@gmail.com

Selcuk Dogru, +905305493259; seltrue@hotmail.com



DOI: 10.18720/MCE.92.11

Напряженно-деформированное состояние панели из стекла с точечным клеевым креплением

Е.Н. Герасимова^а, М.К. Михайлова^б, А.В. Галямичев^а, С. Догру^с

^а Санкт-Петербургский политехнический университет Петра Великого, Санкт-Петербург, Россия

^б НИУПЦ «Межрегиональный институт оконных и фасадных конструкций», Санкт-Петербург, Россия

^с İstanbul Okan Üniversitesi, Стамбул, Турция

* E-mail: katyageras17@gmail.com

Ключевые слова: структурное остекление, силиконовый герметик, точечное крепление, стекло, светопрозрачные конструкции

Аннотация. Статья посвящена исследованию несущей способности конструкции остекления с точечным креплением к несущему основанию. В ней проводится оценка влияния таких факторов, как величина приложенной нагрузки, краевое расстояние, толщина стекла и количество точечных креплений, на напряженно-деформированное состояние панели. Расчет панелей при различных постановках задач проводился методом конечных элементов (МКЭ). Результаты расчета позволяют установить зависимости между рассматриваемыми факторами и напряженно-деформированным состоянием панели, а также определяют возможности использования таких конструкций в соответствии с первой и второй группами предельных состояний.

Литература

1. Магай А.А., Дубынин Н.В. Светопрозрачные фасады высотных многофункциональных зданий // Вестник МГСУ. 2010. № 2. С. 14–21.
2. Patterson M.R. Structural glass facades: a unique building technology. Master Thesis, University of Southern California. 2008. 450 с.
3. Drass M., Schneider J. Constitutive modeling of transparent structural silicone adhesive – TSSA // Proceedings of 14 Darmstädter Kunststofftage – Simulation und Werkstoffmodelle. Darmstadt, 2016.
4. Drass M., Schneider J. On the mechanical behavior of transparent structural silicone adhesive – TSSA // Mechanics and Computation. 2016. No. 2. Pp. 20–26. DOI: 10.1201/9781315641645-74
5. Staudt Y., Schneider J., Odenbreit C. Investigation of the material behavior of bonded connections with silicone // Proceedings of International Conference at glasssec. Dusseldorf, 2014. Pp. 10–20.
6. Staudt Y., Odenbreit C., Schneider J. Investigation of Bonded Connections with Silicone under Shear Loading // Proceedings of 4 Conference on Architectural and Structural Applications of Glass. Ghent, 2016. Pp. 3–17.
7. Drass M., Schneider J., Kolling S. Damage effects of adhesives in modern glass façades: a micro-mechanically motivated volumetric damage model for poro-hyperelastic materials // International Journal of Mechanics and Materials in Design. 2017. No. 8. Pp. 20–44.
8. Pascual C., Montali J., Overend M. Adhesively-bonded GFRP-glass sandwich components for structurally efficient glazing applications // Composite Structures. 2017. No. 160. Pp. 560–573.
9. Sitte S., Brasseur M.J., Carbary L.D., Wolf A.T. Preliminary Evaluation of the Mechanical Properties and Durability of Transparent Structural Silicone Adhesive (TSSA) for Point Fixing in Glazing // Journal of ASTM International. 2011. No. 10. Pp. 4–30.
10. Савицкий Г.А. Ветровая нагрузка на сооружения. М.: Стройиздат, 1972. 111 с.
11. Cook N.J. The designer's guide to wind loading of building structures. Part 2: Static structures. London, 1990. 586 p.
12. Немова Д.В. Навесные вентилируемые фасады обзор основные проблем // Инженерно-строительный журнал. 2010. № 5. С. 7–11. DOI: 10.18720/MCE.15.3.
13. Горшков А.С., Попов Д.Ю. Конструктивное исполнение вентилируемого фасада повышенной надежности // Инженерно-строительный журнал. 2010. № 8. С. 5–9.
14. Gent A. Elastic instabilities in rubber // International Journal of Non-Linear Mechanics. 2005. No. 40(2). Pp. 165–175.
15. Dias V. Development of adhesives constitutive material laws for the assessment of bonded steel to glass partial composite beams. Doctoral Thesis, University of Luxembourg. 2013. 416 p.
16. Staudt Y. Investigation of the material behavior of glued connections with silicone. Master Thesis, Technische Universität Darmstadt. 2013.
17. Van Den Bergh S., Hart R., Petter B., Jelle B.P., Gustavsen A. Window Spacers and Edge Seals in insulating glass units: a State-of-the-Art Review and Future Perspectives // Energy and Buildings. 2013. No. 58. Pp. 263–280.
18. Wolf A.T. Silicone Sealed Insulating Glass Units. Proceedings of ISAAG – International symposium on the Application of Architectural Glass. Munich, 2004.
19. Li X., Li S., Zia Q., Zi H. Effects of pore sizes of porous silica gels on desorption activation energy of water vapor // Applied Thermal Engineering. 2007. No. 27. Pp. 869–876.

20. Baetens R., Jelle B.P., Gustavsen A. Aerogel insulation for building applications: A state-of-the-art review // Energy and Buildings. 2011. No. 43. Pp. 761–769.
21. Dow Corning Official website [Электронный ресурс]. URL: https://consumer.dow.com/en-us.html?_ga=2.83410198.1493760776.1527724064-1652577140.1524781935 (дата обращения: 02.04.18).
22. DOWSILTM TSSA/TSSL. Technical Manual. 2018.

Контактные данные:

Екатерина Николаевна Герасимова, +7(921)9673868; эл. почта: katyageras17@gmail.com

Александр Викторович Галямичев, +7(911)8110719; эл. почта: galyamichev@yandex.ru

Мария Константиновна Михайлова, +7(904)3360888; эл. почта: mmikhaylova@gmail.com

Сельчук Догру, +905305493259; эл. почта: seltrue@hotmail.com

© Герасимова Е.Н., Галямичев А.В., Михайлова М.К., Догру С., 2019



DOI: 10.18720/MCE.92.12

Effects of model-based design and loading on responses of base-isolated structures

A. Dushimimana^{a*}, A.A. Niyonsenga^b, G.J. Decadjevi^a, L.K. Kathumbi^c

^a Ondokuz Mayıs University, Samsun, Turkey

^b Shaoxing University, Shaoxing, China

^c Pan African University, Institute for Basic Science, Technology and Innovation, Nairobi, Kenya

* E-mail: chenkodu432@gmail.com

Keywords: numerical methods, dynamic loads, time of implementation, loading nature, seismically isolated structures, model-based design

Abstract. Numerical studies for a structural dynamic system are performed in Matlab and Simulink environments. Six different earthquakes filtered and corrected using Seismosignal software, are used as seismic loads during implementation. In the first part of this study, the fourth order Runge-Kutta based Matlab code (RK4M) and Simulink Model-Based Design (SMD) are appropriately developed. Both RK4M and SMD are used to solve the governing equations for single storey structure isolated by Lead Core Rubber Bearing (LCRB). The second part compares the developed modelling methods in terms of outputs' accuracy and Time of Implementation (TI). It is shown that both methods agree well in terms of resulting floor accelerations and displacements with slight but justifiable average differences of only 1.3 and 0.98 % respectively; thus, indicating that any of these techniques can be adopted. However, concerning TI, it is observed that SMD is in general quicker to display results as compared to the developed RK4M, which is approximately 58s longer. This leads to suggesting that SMD can be more effective, particularly for earthquakes with long-duration, and most importantly for cases where time is a governing factor during implementation. Besides, long-period and long-duration earthquakes are observed to have particular influence on structural behaviour. This reveals a need for special consideration requirements that are currently not taken into account.

1. Introduction

Simulink provides a block diagram environment that is used as a platform for model-based design. Matlab provides an environment for developing codes relevant to the type of model that is being investigated. The time required to develop the code can be high due to a number of factors, which mainly depend on the type of the structure being modelled. Contrary to Matlab environment, Simulink-model based design can save time of implementation, mainly because of the presence of built-in-blocks that are easy and ready to use. Both Matlab and Simulink environments can be used to solve governing equations of motion of a structural dynamic system, such as active and passive seismically isolated structures.

A significant number of solution methods for differential equations governing a dynamic motion of passive seismically isolated structures have been adopted in the existing literature. For example, a number of researchers have adopted the Wilson Theta method [1, 2], Newmark Beta method [3–6], and Runge-Kutta Methods [3, 4, 7–11]. The latter has been observed to be the most stable, modern and popular method according to most of researchers [3, 4]. However, there is a substantial need to conduct comparative studies on the performance level of methods adopted during implementation. Two of the major performance factors that can be considered are: the accuracy of the results and time required to display desired responses.

Despite a significant number of existing programming software such as Matlab, Python, and Ansys; there is still a substantial need to clarify the easy and fastest software and technique. Such a software and technique can reduce the time required to obtain structural responses during implementation, while providing

Dushimimana, A., Niyonsenga, A.A., Decadjevi, G.J., Kathumbi, L.K. Effects of model-based design and loading on responses of base-isolated structures. Magazine of Civil Engineering. 2019. 92(8). Pp. 142–154. DOI: 10.18720/MCE.92.12

Душимимана А., Ньонсенга А.А., Декаджеви, Г.Дж., Катумби Л.К. Влияние модельно-ориентированного проектирования и нагрузки на отклики конструкции с изолированным фундаментом // Инженерно-строительный журнал. 2019. № 8(92). С. 142–154. DOI: 10.18720/MCE.92.12



accurate results in a short time. Matlab has been significantly reported to possess the ability to perform better compared to other existing programming software used in solving the governing differential equations for dynamic motion of seismic base isolation systems [3, 4, 11]. With this in mind, the use of Matlab and its embedded part (Simulink) to predict the system accuracy and TI can be more reasonable than using other existing programming software. Particularly, when examining a seismic isolation system, significant studies have previously reported Matlab to be effective [7, 12]. Furthermore, studies by use of Simulink have been conducted by a significant number of researchers for solving the governing equations of dynamic motion of seismically isolated structures [12–17]. Specifically, Numerical studies have been conducted on LCRB performance by using both Matlab and Simulink including [7, 8, 12, 18] among others.

The potentiality of adopting Simulink to solve the governing differential equations in seismically isolated structures was reported in [12], where calibration of isolator parameters under long-period motions was mainly targeted. In [19], governing equations of a dynamic system were solved by four different types of methods including Matlab and Simulink environments. It was reported that the latter can be a better technique as it only requires knowledge of blocks' functionality already designed for solving related equations without much knowledge in coding or/and advanced mathematics.

Despite a large number of the existing literature about numerical studies on seismically isolated structures with LCRB, there has been a remarkable gap in searching for the best technique to use during the numerical analysis. Such a technique can be easier, faster and be seen as a prerequisite for practical use, most importantly for projects which prioritize the accuracy of the responses while saving TI. In [20], a numerical algorithm that is based on the finite element model of contact and step-by-step analysis method was used to model a base-structure contact interaction during dynamic loads. It was observed that such a modelling technique can save time compared to the existing well-known iteration algorithm. Similar studies for the sake of developing a modelling method with time-saving, cost-effective, and energy efficient properties were also conducted in [21, 22]. However, these studies were not addressing seismically isolated structures. Therefore, there is a need to develop a modelling technique with the above properties for seismically isolated structures.

With regard to the loading nature, a substantial number of studies have been conducted adopting the normal or short-period earthquakes, as well as short-duration [5, 23–25]. However, a few studies have considered the effect of long-period earthquakes on responses of isolated structures [26–29]. Most notably, the combining effect of long-period and long-duration earthquakes on isolated structures seems to have not been investigated in the existing literature.

In this study, authors aim to compare SMD and RK4M techniques in terms of accuracy of results and TI of resulting responses for a structure that is seismically isolated by LCRB. The accuracy of these techniques is checked based on the resulting outputs, while TI is controlled by carefully recording the elapsed time for each method. Besides, the study aims to examine the effect of earthquake nature on the responses of seismically isolated structures, particularly the long-period and long-duration earthquakes. The main contribution of this work lies in assessing the easiest to use and time-saving technique, which authors believe can mainly be beneficial in reducing the time required during numerical analysis of seismically isolated structures. Besides, the study contributes in revealing the severity of long-period and long-duration earthquakes on seismically isolated structures.

The remainder of this study is structured as follows. Section 2 presents the methodology and description of numerical simulations, and governing differential equations solved in both RK4M and SMD techniques; in Section 3, numerical case study is provided for deep understanding of section 2 and its applicability; in section 4, numerical case study results are discussed; and conclusions are drawn in Section 5.

2. Methods

2.1. Defining Governing Equations

The governing equations for dynamic motion of structures with multiple degrees of freedom, fixed or controlled by LCRB at the base level can be detailed as follow [12, 30]:

The equation of a fixed base structure exposed to seismic load can be expressed as

$$[M_s]\{\ddot{U}_s\} + [C_s]\{\dot{U}_s\} + [K_s]\{U_s\} = -[M_s]\{R\}(\ddot{u}_g). \quad (2.1)$$

A structure isolated by LCRB at its base level can be governed by equations (2.2) and (2.3).

a) The superstructure part is governed by the equation:

$$[M_s]\{\ddot{U}_s\} + [C_s]\{\dot{U}_s\} + [K_s]\{U_s\} = -[M_s]\{R\}(\ddot{u}_g + \ddot{u}_b), \quad (2.2)$$

where $[M_s]$, $[C_s]$ and $[K_s]$ are the mass, damping and stiffness matrices of the superstructure, respectively; $\{U_s\} = \{U_1, U_2, \dots, U_j\}^T$, $\{\dot{U}_s\}$ and $\{\ddot{U}_s\}$ are the unknown floor displacement, velocity and acceleration

vectors respectively; U_j is the lateral displacement of j^{th} floor relative to the base mass; \ddot{u}_b and \ddot{u}_g are the relative acceleration of base mass and earthquake ground acceleration respectively; and $\{R\}$ is the vector of influence coefficients.

b) For the base floor level of the building, the equation of motion can be expressed as:

$$m_b \ddot{u}_b + F_b - k_1 u_1 - c_1 \dot{u}_1 = -m_b \ddot{u}_g, \quad (2.3)$$

where m_b and F_b are base mass and restoring force developed in the isolation system, respectively; k_1 , c_1 , u_1 , and \dot{u}_1 are the stiffness, damping, displacement, and velocity of first storey floor. The value for hysteretic restoring force F_b can be calculated as shown below:

$$F_b = c_b \dot{u}_b + \alpha k_b u_b + (1 - \alpha) f_y Z. \quad (2.4)$$

In equation (2.4), f_y refers to yield force, α stands for the ratio of post-yield to pre-yield stiffness; k_b , c_b , u_b , \dot{u}_b , are stiffness, damping, displacement, and velocity of the bearing, respectively; and Z is a component of Wen's non-linear model shown in (2.5).

$$\dot{Z} = \left[A \dot{u}_b - \beta |\dot{u}_b| |Z| |Z|^{n-1} - \tau \dot{u}_b |Z|^n \right] u_y^{-1}, \quad (2.5)$$

where u_y is yield displacement, and can be calculated for particular structure as described in ASCE 41-13. β , A and τ are dimensionless parameters which are defined based on laboratory experiments. n is a constant value, and this controls the transition from elastic to plastic behavior of the model.

The above equations can be solved by one of the most commonly used techniques such as Runge-Kutta 4th order algorithm, Wilson Theta Method, and Newmark Beta Method, assuming a linear variation over smaller time interval ($dt = 0.001s$). Properties of LCRB such as stiffness (k_b), damping (c_b), damping ratio (ξ_b), yield strength (F_y), normalized yield strength (F_o), and yield displacement (u_y) can be calculated based on following equations [12, 31]:

$$k_b = \left(\frac{2 \cdot \pi}{T_b} \right)^2 \cdot (M_{sup} + m_b), \quad w_b = \frac{2 \cdot \pi}{T_b}; \quad (2.6)$$

$$c_b = 2 \cdot \xi_b \cdot (M_{sup} + m_b) \cdot w_b, \quad g = 9.81; \quad (2.7)$$

$$F_y = F_o \cdot W, \quad u_y = \frac{F_y}{k_b}, \quad \xi_b = 0.15, \quad F_o = 0.0159, \quad W = M \cdot g, \quad (2.8)$$

where m_b , w_b , T_b , g and W are bearing mass, natural frequency, natural period, acceleration of gravity and total weight of structure, respectively. M_{sup} is the total mass of superstructure.

2.2. RK4M Technique

In this research, RK4M is adopted to solve the equations (2.1) to (2.3), as shown by a number of researchers [3, 4, 10, 18]. This algorithm is based on Runge-Kutta 4th order, which is applied in Matlab environment by coding line by line. The equations defining this algorithm are shown in (2.9) to (2.13),

$$y_{k+1} = y_k + \frac{h(f_1 + 2f_2 + 2f_3 + f_4)}{6}, \quad (2.9)$$

where f_1, f_2, f_3, f_4 , are slopes of the given function within a single time step size (h). y_k and y_{k+1} are the previous and current variables for each step size h .

$$f_1 = f(t_k, y_k); \quad (2.10)$$

$$f_2 = f\left(t_k + \frac{h}{2}, y_k + \frac{h}{2} f_1\right); \quad (2.11)$$

$$f_3 = f\left(t_k + \frac{h}{2}, y_k + \frac{h}{2} f_2\right); \quad (2.12)$$

$$f_4 = f(t_k + h, y_k + hf_3). \quad (2.13)$$

The above algorithm will output first order ODEs to be solved by one of the Matlab built-in-function such as ode45, ode23s among others. In this method, preallocation is used wherever possible in order to speed up the code execution time. This process is made through preallocating maximum amount of space required for an array. However, RK4M can only provide displacements and velocities. Therefore, accelerations can be derived from the already obtained velocity values by using one of the existing popular techniques known as numerical derivative. This can be implemented either through forward difference, backward difference, or central difference methods shown in equations (2.14), (2.15), and (2.16) respectively [3, 11].

$$f'(x_k) \approx \frac{f(x_{k+1}) - f(x_k)}{x_{k+1} - x_k}; \quad (2.14)$$

$$f'(x_k) \approx \frac{f(x_k) - f(x_{k-1})}{x_k - x_{k-1}}; \quad (2.15)$$

$$f'(x_k) \approx \frac{f(x_{(k+1)}) - f(x_{(k-1)})}{(x_{(k+1)} - x_{(k-1)})}. \quad (2.16)$$

In this study, forward difference method is adopted and the Matlab built-in function (*diff*) is used to solve equation (2.14). Additionally, input parameters for RK4M (mass of structure $[M_s]$, structure stiffness $[K_s]$) can be generalized as shown in equations (2.17) and (2.18).

$$[M_s] = \begin{bmatrix} m_1 & 0 & 0 & 0 & 0 & 0 \\ 0 & m_2 & 0 & 0 & 0 & 0 \\ 0 & 0 & m_3 & 0 & 0 & 0 \\ 0 & 0 & 0 & \dots & 0 & 0 \\ 0 & 0 & 0 & 0 & \dots & 0 \\ 0 & 0 & 0 & 0 & 0 & m_i \end{bmatrix} \text{ (Kg);} \quad (2.17)$$

$$[K_s] = \begin{bmatrix} k_1 + k_2 & -k_2 & 0 & 0 & 0 & 0 \\ -k_2 & k_2 + k_3 & -k_3 & 0 & 0 & 0 \\ 0 & -k_3 & k_3 + k_4 & -k_3 & 0 & 0 \\ 0 & 0 & \dots & \dots + \dots & \dots & 0 \\ 0 & 0 & 0 & \dots & \dots + \dots & -k_i \\ 0 & 0 & 0 & 0 & -k_i & k_i \end{bmatrix} \text{ (N/m),} \quad (2.18)$$

where i is the number of floors in the investigated structure. In this study, damping matrix $[C_s]$ was derived from $[M_s]$ and $[K_s]$ based on Rayleigh Method [7, 12], which is defined as shown in (2.19).

$$[C_s] = \alpha_0 [M_s] + \alpha_1 [K_s]. \quad (2.19)$$

The coefficients α_0 and α_1 can be obtained by solving equation (2.20)

$$\frac{1}{2} \begin{bmatrix} \frac{1}{w_i} & w_i \\ \frac{1}{w_j} & w_j \end{bmatrix} \begin{Bmatrix} \alpha_0 \\ \alpha_1 \end{Bmatrix} = \begin{Bmatrix} \xi_i \\ \xi_j \end{Bmatrix}, \quad (2.20)$$

where w_i, w_j, ξ_i, ξ_j , are natural frequencies and damping ratios of fixed base structure for i^{th} and j^{th} mode respectively. Damping ratios at i^{th} and j^{th} are assumed to be similar to facilitate the calculation of the concerned coefficients [2, 12].

2.3. SMD Technique

Contrary to the above mentioned RK4M method, SMD is adopted to solve equations (2.1) to (2.3) by logically connecting Simulink built-in blocks. Referring to researchers in [12, 32–37], equations (2.1) to (2.3) can be combined into a single equation (2.21) to represent the structure as a whole, and then transformed into a state-space form of first order equations i.e., a continuous-time state-space model of the system as shown in equations (2.22) and (2.23).

$$[m]\{\ddot{u}(t)\} + [c]\{\dot{u}(t)\} + [k]\{u(t)\} = [d]\{f_{\oplus}(t)\}; \tag{2.21}$$

$$\dot{z}(t) = [A_c]z(t) + [B_c]\{f_{\oplus}(t)\}; \tag{2.22}$$

$$\{y(t)\} = [C]z(t) + [D]\{f_{\oplus}(t)\}. \tag{2.23}$$

The components shown in the above equations are explained in Table 2.1

Table 2.1 Definition of state space model components.

Variant parameter symbol	Definition	Matrix size
z	Space vector	n_1 by 1
\dot{z}	States	n_1 by n_1
f_{\oplus}	Input force vector	r_1 by 1
y	Desired responses vector	m_1 by 1
A_c	Feedback matrix	n_1 by n_1
B_c	Input matrix	n_1 by r_1
$[C]$	Output influence matrix	m_1 by n_1
$[D]$	Direct transmission matrix	m_1 by r_1
$[d]$	Input influence matrix	n_2 by r_1

$n_1 = 2n_2$; n_2 is the number of independent coordinates. r_1 is the number of inputs, m_1 is the number of outputs. $[d]$ characterizes the locations and type of known inputs $f_{\oplus}(t)$ [8, 12, 18, 38, 39].

$$[A_c] = \begin{bmatrix} [0] & [I] \\ -[m]^{-1}[k] & -[m]^{-1}[c] \end{bmatrix}; \tag{2.24}$$

$$[B_c] = \begin{bmatrix} [0] \\ m^{-1}[d] \end{bmatrix}; \tag{2.25}$$

$$\{z(t)\} = \begin{bmatrix} u(t) \\ \dot{u}(t) \end{bmatrix}. \tag{2.26}$$

The sizes of matrices $[C]$ and $[D]$ can be adjusted depending on the desired output [16]. The Simulink-Model Based Design can be constructed as shown below:

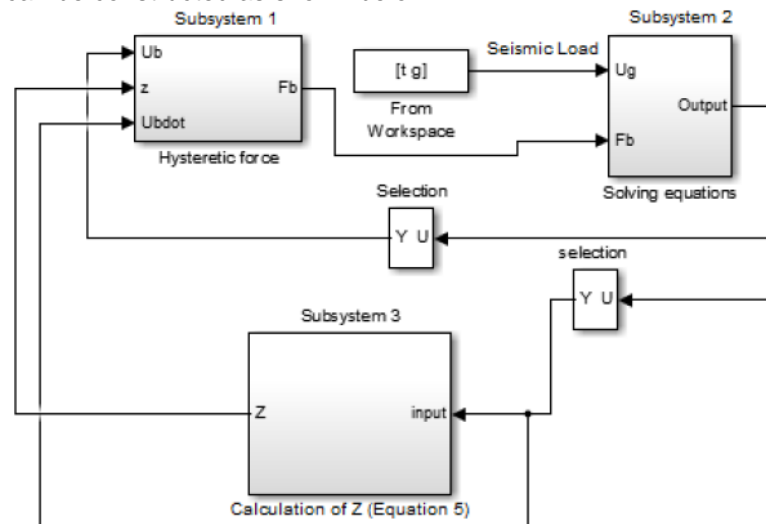


Figure 2.1. Simulink Master Block diagram for modeling isolated structure by LCRB isolator.

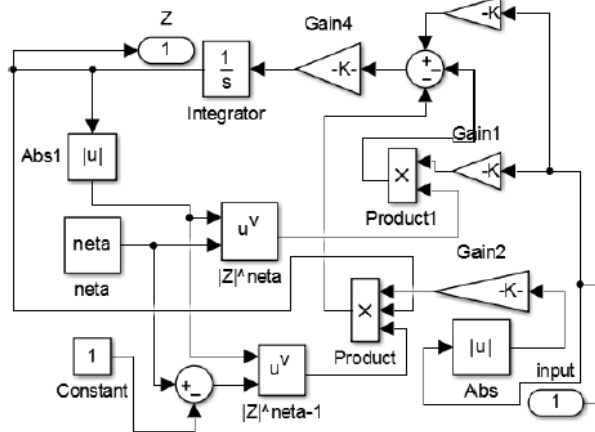


Figure 2.2. Calculation of Z (Subsystem 3).

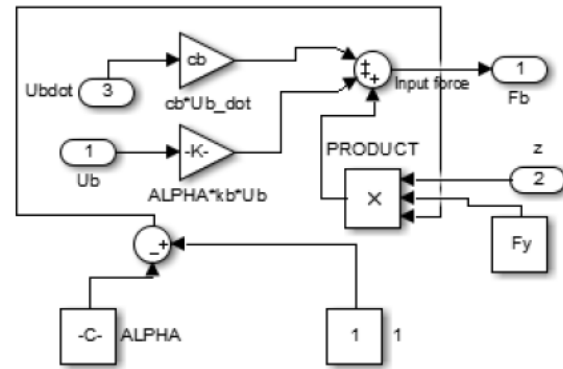


Figure 2.3. Calculation of Fb (Subsystem 1).

Blocks used to form SMD are chosen based on references [3, 12] Model configuration parameters are set based on the recommendations shown in [15] for solving equation of a dynamic system.

2.4. Numerical case study

In this study, the responses of an isolated one storey structure under various earthquakes are investigated. The engineering data for the above structure are as follows: $m_1 = 29\,485\text{ kg}$; $m_b = 6800\text{ kg}$, $k_1 = 11\,912\text{ KN/m}$. The basic dynamic properties of the investigated structure are natural period: $T_{n1} = 0.1\text{ s}$; frequency: $F_{n1} = 10\text{ Hz}$, and damping ratios: $\xi_{n1} = 0.05$. The above characteristics have been previously adopted in [16]. Furthermore, the geometry properties of the considered lead core rubber bearing are: i) diameter = 700 mm, ii) thickness of plates: 56 mm, iii) total thickness of elastomer = 120 mm (each with 4 mm), iv) single steel shim thickness = 3.1 mm. These data have been also adopted in [40]. This structure is exposed to a total of six earthquakes downloaded from PEER strong ground motions [41], filtered and corrected using Seismosignal Software (SS). The characteristics of these earthquakes are summarized in Table 2.2. The results for TI strongly depend on the type of computer being used during implementation. Therefore, the properties of the computers used in this study are as follow: Computer brand: hp ProBook 4540s, Processor: Intel(R) Core(TM) i3-3110M CPU@ 2.40GHz, system type: 64-bit Operating System, and RAM; 4.00GB.

Table 2.2. Characteristics of used earthquakes.

Earthquake Name	PGA (m/s ²)	PGV(m/s)	Duration (s)
Elcentro	3.42	0.32	56.52
Düzce	1.29	0.11	42.29
Chuestsu	2.23	0.23	59.96
Capemembe	1.47	0.42	286.65
Iwate	1.78	0.10	179.97
Kobe	8.18	0.82	49.93

3. Results and Discussions

3.1. Differences Between RK4M and SMD for the Resulting Responses of Structure

Looking at peak values in Table 3.1 and Figure 3.1 to 3.9, it appears that both methods resulted in nearly similar responses with small but justifiable differences. For example, in Table 3.1, based on the results from RK4M under Elcentro earthquake, the maximum responses of BFA, TFA, BFD and TFD were observed to be 3.04 m/s², 3.09 m/s², 0.08 m, 0.08 m, whereas those from SMD were 3.07 m/s², 3.10 m/s², 0.09 m, 0.101 m, respectively. It follows that the average acceleration and displacement differences from both methods were approximately 1 and 1.5 %, respectively. These slight differences may have been caused by from workspace block in SMD, which failed to reproduce the input earthquake acceleration. It can therefore be suggested that this block needs revision for better performance.

Similar interpretations can be done on the results from other earthquakes. For example, a careful analysis on responses from both methods under Duzce, Chuestsu, Capemembe, Iwate and Kobe earthquakes indicates that the average acceleration and displacement differences were: 1 and 1 %, 1.5 and 0 %, 1.5 and 1.4 %, 2 and 1 %, and 1.5 and 1 %, respectively. Similar to Elcentro earthquake, these differences can be attributed to the inefficiency of from workspace block to reproduce the input earthquake acceleration. Overall, the average acceleration differences from both methods under all the earthquakes can be estimated to be 1.3 %, whereas for the displacements the average difference can be estimated to be 0.98 %.

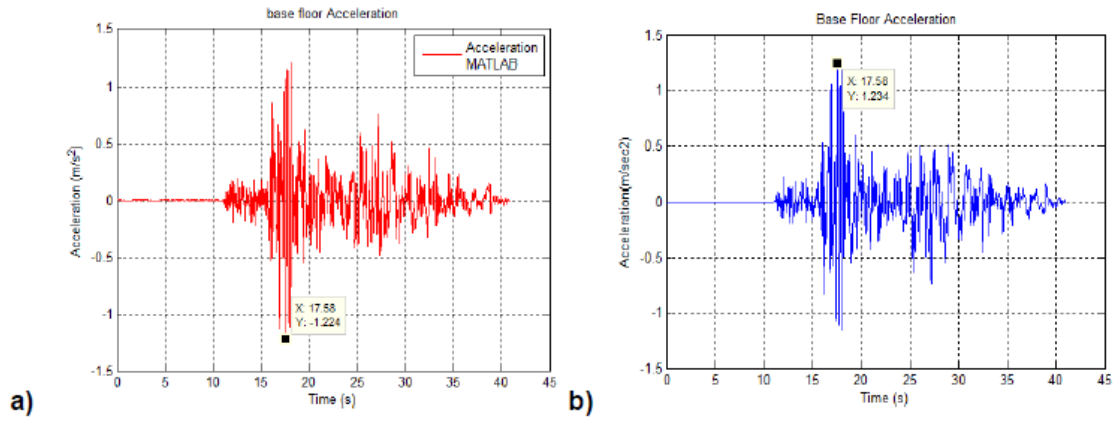


Figure 3.1. Base floor accelerations under Duzce Earthquake: a) RK4M, and b) SMD.

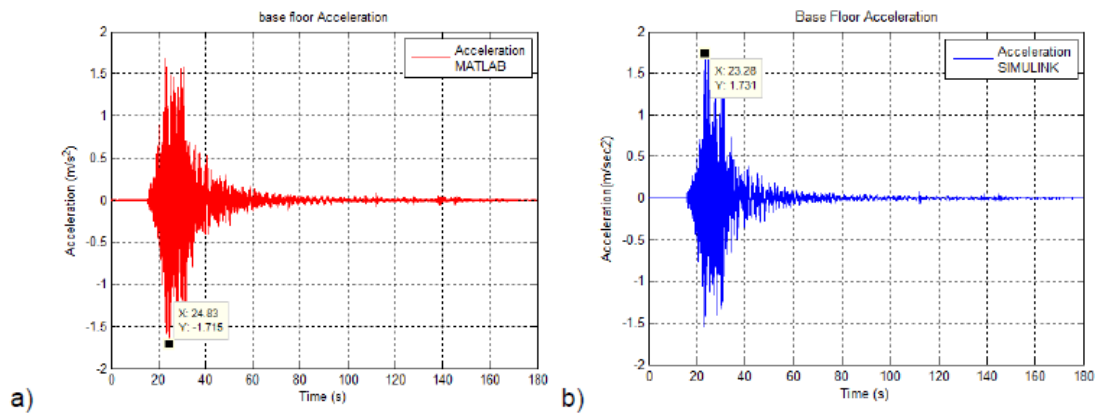


Figure 3.2. Base floor accelerations under Iwate Earthquake: a) RK4M, and b) SMD.

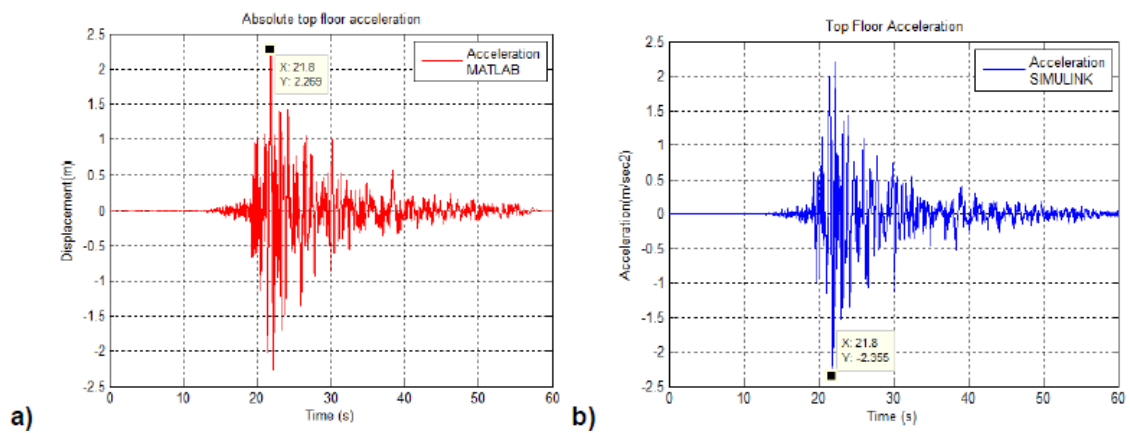


Figure 3.3. Top floor accelerations under Chuestsu Earthquake: a) RK4M, and b) SMD.

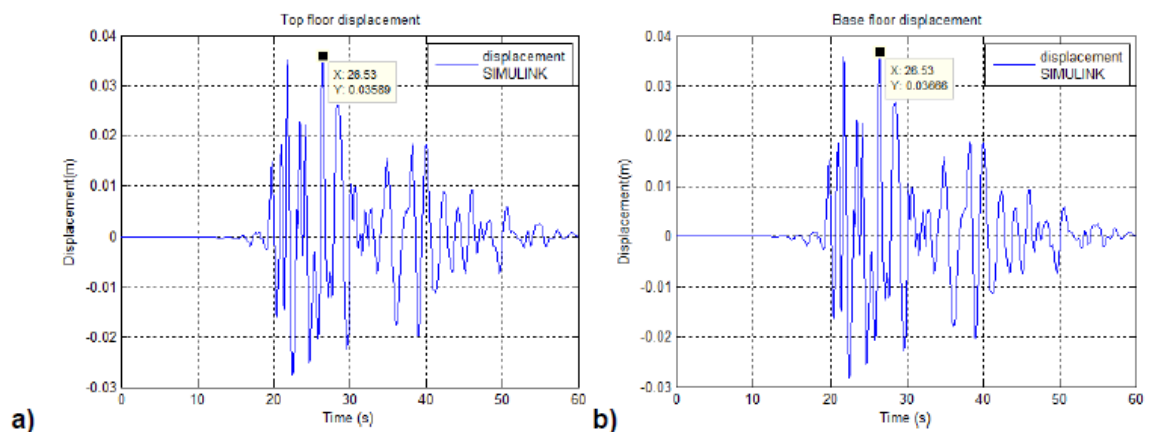


Figure 3.4. a) Top and b) Base floor displacements under Churstsu earthquake for SMD.

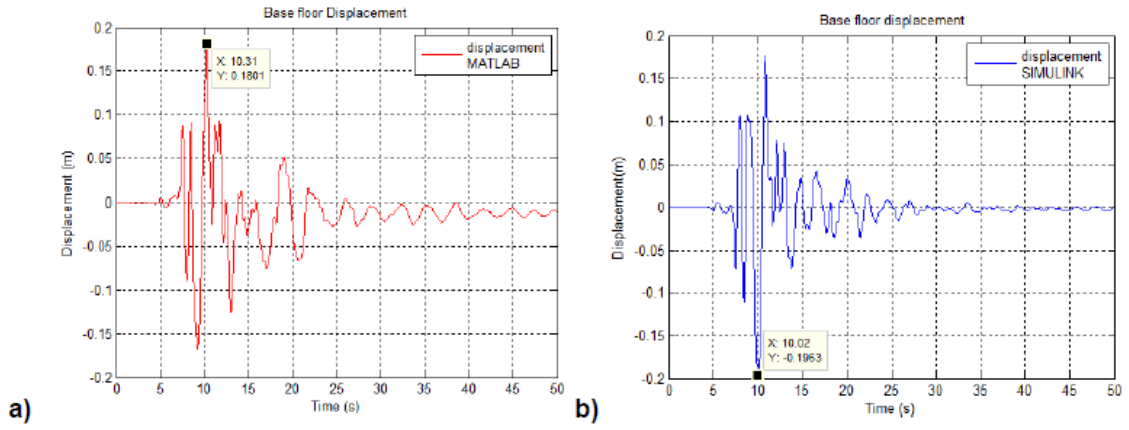


Figure 3.6. Base floor displacements under Kobe Earthquake: a) RK4M, and b) SMD

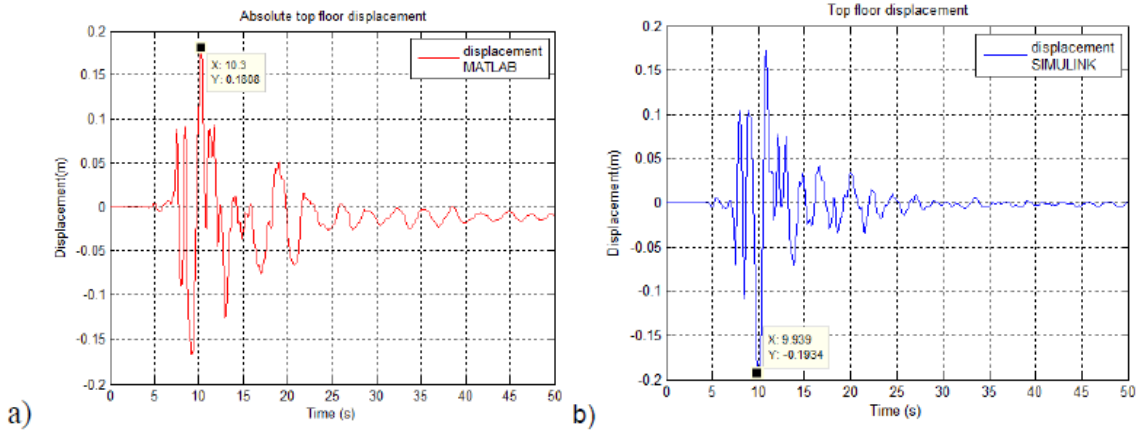


Figure 3.6. Top floor displacements under Kobe Earthquake: a) RK4M, and b) SMD.

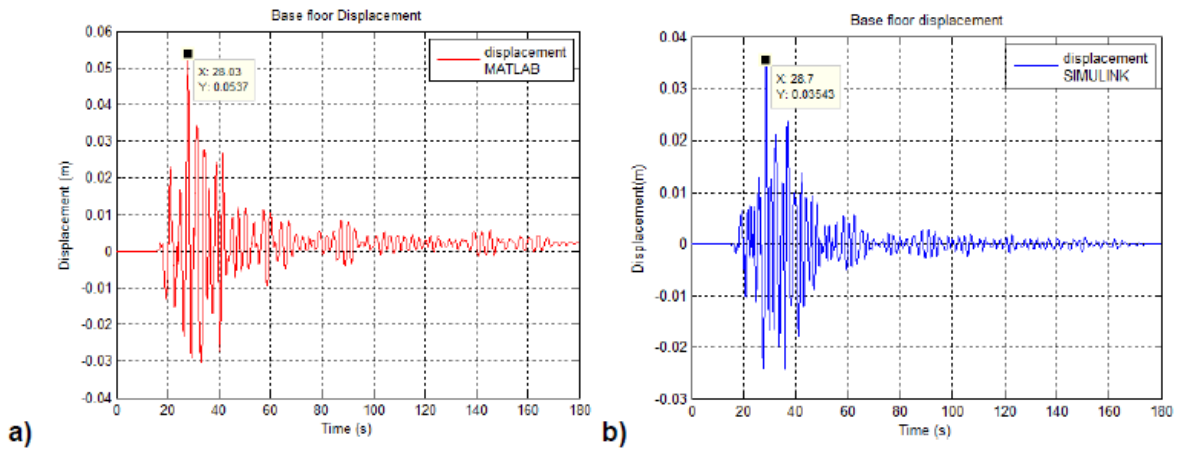


Figure 3.7. Base floor displacements under Iwate Earthquake: a) RK4M, and b) SMD.

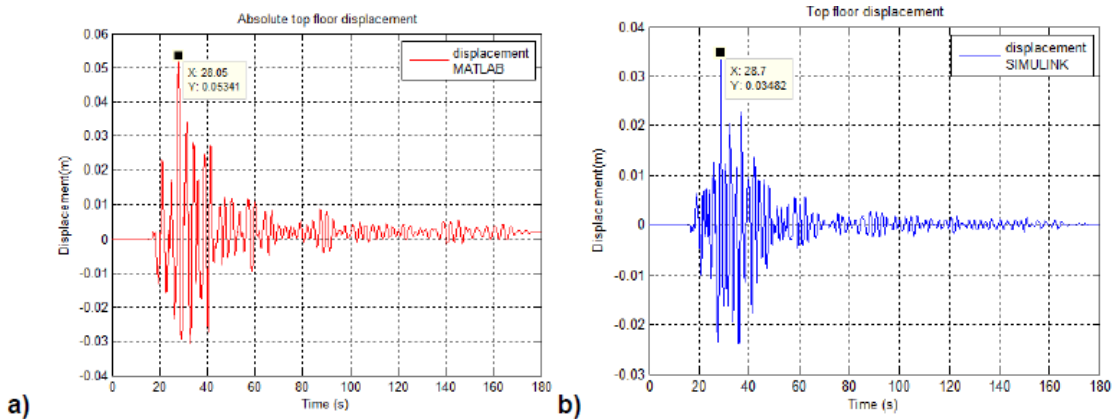


Figure 3.8. Top floor displacements under Iwate Earthquake: a) RK4M, and b) SMD

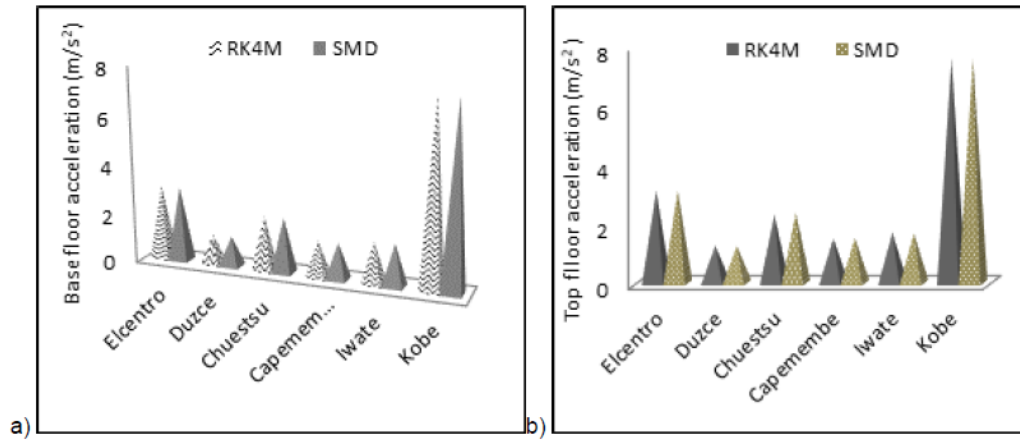


Figure 3.9. Comparison of maximum base and top floor accelerations from RK4M and SMD methods.

Concerning the time instants (t_i) for the occurrence of maximum peak responses, it can be observed from Figure 4.1 to 4.8 that RK4M and SMD methods kept t_i approximately similar for each response. For example, under Duzce earthquake, both methods succeeded in providing maximum base floor acceleration values at exactly similar t_i of 17.58s as shown in Figure 4.1. It follows from this observation that there was a t_i difference of approximately 0s. Under Chuestsu, Kobe and Iwate earthquakes, the t_i for maximum top and base displacements under both methods were nearly 29s, 10s, and 28s, respectively. This uniformity in t_i for top and base floor responses indicates a good agreement between the used methods and high performance of the bearing. This similarity in t_i reveals that both top and base floor displacements of the structure moved with reduced storey drifts. This observation can clearly be seen in Figure 4.4 where maximum displacements were similarly equal, and occurred at exactly t_i of 28.53s for both floors.

Table 3.1. Comparison of RK4M and SMD results for one storey structure.

Earthquake Name/PGA/Direction		Period (Tb)	SR and TI	MATLAB (RK4M)	SIMULINK (SMD)	RK4M&SMD Difference
Elcentro	Direction: NS	3	BFA (m/s ²)	3.04	3.07	0.01
			TFA (m/s ²)	3.09	3.10	0.01
			BFD (m)	0.08	0.09	0.01
			TFD (m)	0.08	0.10	0.02
			TI (s)	17.54	1.51	16.03
Duzce	Direction: NS	3	BFA (m/s ²)	1.22	1.23	0.01
			TFA (m/s ²)	1.25	1.24	0.01
			BFD (m)	0.03	0.02	0.01
			TFD (m)	0.03	0.02	0.01
			TI (s)	14.44	1.56	12.88
Chuestsu	Direction: NS	3	BFA (m/s ²)	2.25	2.27	0.02
			TFA (m/s ²)	2.28	2.27	0.01
			BFD (m)	0.04	0.04	0.00
			TFD (m)	0.04	0.04	0.00
			TI (s)	25.91	1.63	24.28
CAPEMEMBE	Direction: NS	3	BFA (m/s ²)	1.47	1.49	0.02
			TFA (m/s ²)	1.49	1.50	0.01
			BFD (m)	0.31	0.30	0.01
			TFD (m)	0.31	0.29	0.02
			TI (s)	82.29	2.11	80.18
IWATE	Direction: NS	3	BFA (m/s ²)	1.71	1.73	0.02
			TFA (m/s ²)	1.69	1.67	0.02
			BFD (m)	0.05	0.04	0.01
			TFD (m)	0.05	0.04	0.01
			TI (s)	203.98	1.94	202.04
KOBE	Direction: NS	3	BFA (m/s ²)	7.47	7.45	0.02
			TFA (m/s ²)	7.53	7.52	0.01
			BFD (m)	0.18	0.19	0.01
			TFD (m)	0.18	0.19	0.01
			TI (s)	12.75	1.55	11.20

NS: North-South, PGA: Peak ground Acceleration, Tb: Isolation period, SR: Structural responses, TI: Time of Implementation, BFA: Absolute base floor acceleration, TFA: Absolute Top floor acceleration, BFD: Base floor displacement, TFD: Absolute Top floor displacement.

3.2. Differences in TI for RK4M and SMD Methods

On the other hand, the differences in TI were observed to be significantly pronounced between RK4M and SMD methods. TI required for RK4M to display responses were observed to be 17.54, 14.44, 25.91, 82.29, 203.98, and 12.75s under Elcentro, Duzce, Chuestsu, Capemembe, Iwate and Kobe earthquakes, respectively. However, a much more pronounced difference was observed for TI when SMD is adopted. That is, TI for SMD to display responses were observed to be 1.51, 1.56, 1.63, 2.11, 1.94, and 1.55s under Elcentro, Duzce, Chuestsu, Capemembe, Iwate and Kobe earthquakes, respectively. The observations from RK4M and SMD indicate that both methods resulted in differences of 16.03, 12.88, 24.28, 80.18, 202.04, and 11.20s under Elcentro, Duzce, Chuestsu, Capemembe, Iwate and Kobe earthquakes, respectively. In other words, the average TI value required for displaying responses under all earthquakes was approximately 59.50s for RK4M, while that of SMD was approximately 1.72s. It follows from this observation that there was nearly 58s (or 97 %) difference of TI between the used methods when all earthquakes are counted. Particularly, long-duration earthquakes like Capemembe and Iwate were observed to consume much more time for RK4M than for SMD as can be observed in Figure 3.10.

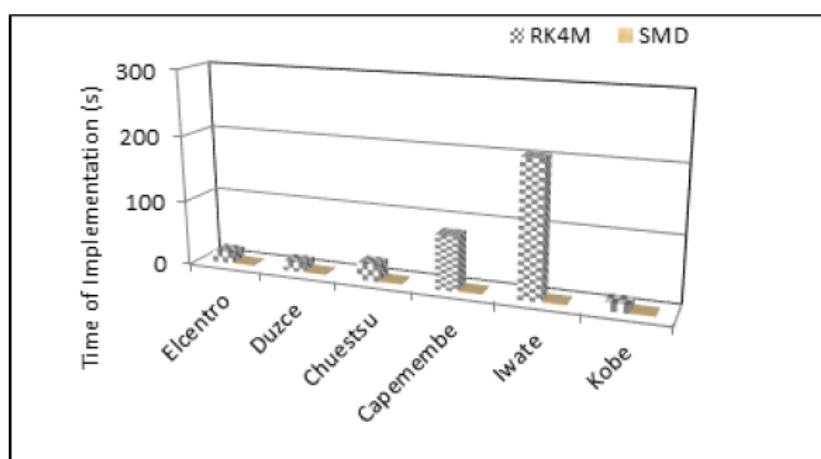


Figure 3.10. Comparison of TI for RK4M and SMD under various earthquakes.

This pronounced difference provided insights about the paramount importance of adopting SMD rather than RK4M for such earthquakes. Overall, the substantial percentage difference in TI under both methods paves the way for suggesting SMD to be more effective than RK4M. The adoption of SMD is reasonable in a way that time is a governing factor in real life. For example, if a project is to take time t for its accomplishment when RK4M adopted, the adoption of SMD can substantially reduce that t . This reduction will result not only from the above mentioned percentage difference in TI, but also from saving time required to develop RK4M code, and sift through lines of the code in order to understand. This will probably result in labor cost-savings through substantial reduction of required working hours.

3.3. Effect of Earthquake Nature on the Resulting Responses

The results in Table 3.1 provide information about the effect of earthquake nature on the responses of the investigated structure. Interestingly, under Capemembe earthquake with PGA of 1.47 m/s^2 , base and top floor displacements were observed to be higher than those resulting from Kobe earthquake with PGA of 8.18 m/s^2 . For example, base and top floor displacements from RK4M under Capemembe earthquake appeared to be similar and equal to 0.31 m, whereas those under Kobe earthquake were similar and equal to 0.18 m. The fact that Capemembe is a long-period and long-duration earthquake in its nature could have been the underlying cause of higher displacements compared to Kobe earthquakes'. Analysis from Seismosignal Software "intensity parameters" indicates that Capemembe earthquake displacement (shown in Figure 3.11) has a predominant period of 3.4s, which makes this earthquake to be of long-period nature. Furthermore, Figure 3.11 shows that this earthquake lasted for nearly 300s, which makes it of long-duration earthquake nature. It is evident from time duration of this earthquake that it possesses many load cycles. Because it had been previously reported that the number of load cycles contributes to bearing damage [42], the presence of many load cycles for this earthquake can dramatically cause severe damage. It can be observed from Table 3.1 and Figure 3.12 that due to the combining effect of long-period and long-duration characteristics of the Capemembe, the maximum displacements of the structure were amplified nearly 10 times the earthquake maximum displacement.

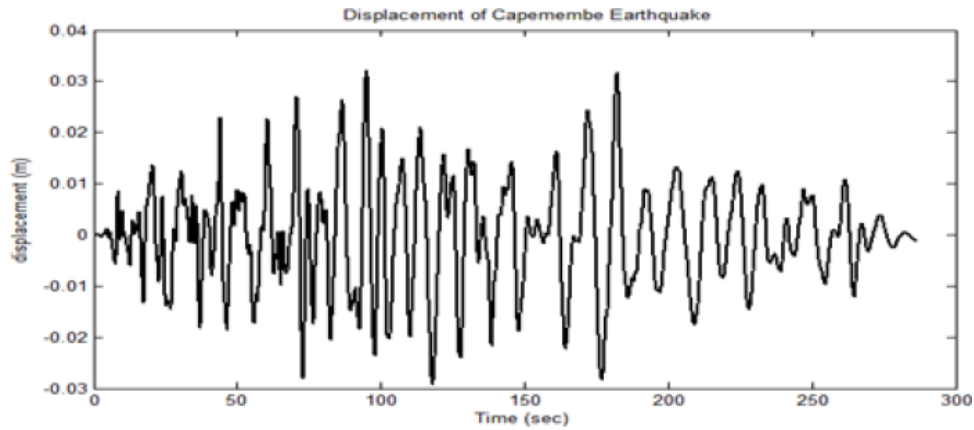


Figure 3.11. Displacement of Capemembe Earthquake.

Another observation from Figure 3.11 is the repetition of peak displacements with almost equal magnitudes (i.e. nearly 0.03 m for each peak) at approximately 72.9, 95.1, 118, 177, and 182.4s. In fact, these peaks occurred in-between 50 and 100 s, 100 and 150s, and 150 and 200s. This shows that earthquake severity on the structure lasted for long, which probably led to development of large isolator strains, and hence large floor displacements. With regard to EN 1337-3 [43], the formula for calculating shear strains (ε_{qE}) due to earthquake-imposed horizontal displacement is $\varepsilon_{qE} = d_{bd} / T_q$, where d_{bd} is the earthquake imposed design displacement and T_q is the total thickness of the elastomer.

Previous studies [40, 44, 45], have reported that large displacements due to strong ground motions can cause the bearing to experience larger shear strains in the elastomer than the allowed strains (100 %) as per EN 1337-3 [43]. This is in agreement with the shear strains obtained from strong Kobe earthquake (i.e.150 %). However, it seems that long-period long-duration earthquakes can also cause excessive shear strains in the bearing regardless of their PGA as shown by Capemembe earthquake which causes shear strains in the elastomer of about 258 %. With regard to previous study conducted by [40], shear strains exceeding 125 % can cause the tensile stresses above $5G$, where G is the shear modulus of the elastomer. However, the code provisions limit tensile stresses in the bearing up to $2G$ in BS EN 15129 [46] and EN 1337-3 [43], up to $2-3G$ in ASHTO [47], and up to $1G$ in JRA [48]. It is, therefore, evident that shear strains from Capemembe earthquake can cause tensile stresses higher than those recommended in the codes. This can lead to development of cracks, buckling, and even rupture during seismic loadings, thus leading to poor performance of isolation system. Therefore, it is of paramount importance to mention that the isolator material properties should be adjusted to avoid such unusual displacements from the aforementioned combining effect of long-period and long-duration earthquakes. This can reduce the cost of damage due to large displacements as had been previously reported by [21], and can result in a sustainable bearing able to last for long period of time.

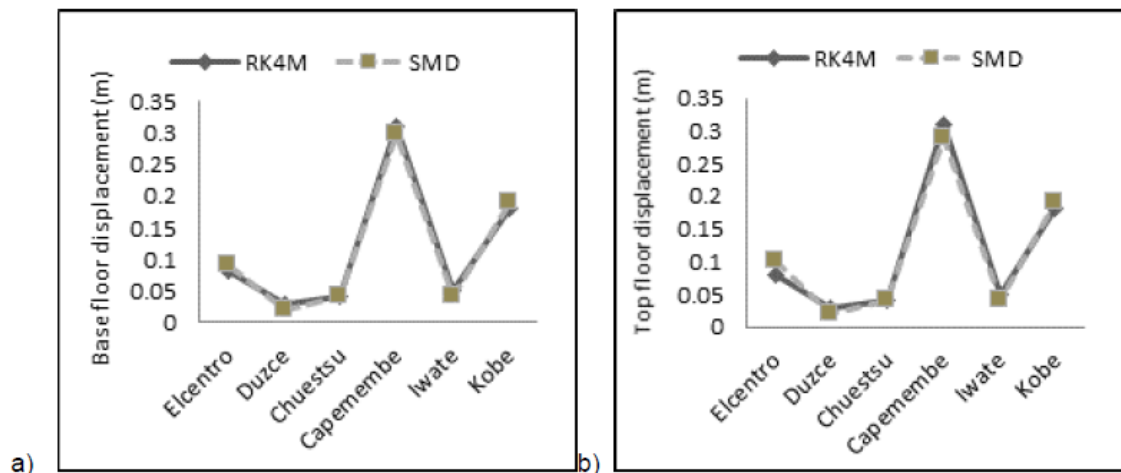


Figure 3.12. Comparison of base and top floor displacements under various earthquakes.

Overall, there was occurrence of nearly similar values of both top and base floor responses under both methods as shown in Figure 3.1 to 3.9. This similarity indicates not only a good agreement between RK4M and SMD methods, but also the effective performance of the bearing. This is because the similarity in top and base responses normally indicates that the structure moves as a rigid body, thus preventing interstorey drifts as well as unwanted cracks during earthquake. However, SMD was observed to be more time-saving than RK4M. On the other hand, the unusual floor displacements observed for long-period and long-duration earthquakes can be an indication that special consideration requirements are necessary. For example, changing the bearing material constituents can be one of possible solutions.

4. Conclusion

In this study, RK4M and SMD methods were adopted for solving differential equations governing a dynamic motion of a structure isolated by LCRB. The resulting responses from both methods were analyzed and compared. For comparison purposes, one storey structure exposed to earthquakes (filtered and corrected using SS) with significant differences in their PGA was investigated. Besides, the combining effect of long-period and long-duration earthquakes on the isolated structures was analyzed. The major findings are listed as shown below:

1. The dynamic responses of the investigated structure were nearly similar under both RK4M and SMD methods. This indicates that there was a good agreement between these methods. However, the developed SMD modelling technique was found to be much easier and faster than RK4M. Therefore, SMD is shown to be a promising method for saving time required during numerical analysis of seismically isolated structures, and can be adopted especially for projects where time is a governing factor.

2. For all earthquakes, the average acceleration difference from both methods was estimated to be 1.3 %, whereas the average displacement difference was estimated to be 0.98 %. The resulting differences are negligible, hence indicating that the accuracy of outputs was comparable.

3. Concerning the TI, it was observed that SMD is more effective in terms of reducing the elapsed time as compared to RK4M. This was demonstrated by TI from RK4M which was approximately 58s longer than that from SMD.

4. SMD was observed to slightly reduce the input earthquake acceleration compared to the acceleration data obtained from SS. This leads to suggesting that "From workspace" block should be revised for better performance.

5. Long-period and long-duration earthquakes need careful and deep investigation, as they showed unusual floor displacements and elastomer shear strains, though their PGAs were small. Therefore, PGA should not necessarily be a good indicator of large floor displacements, unless combined with the earthquake nature. Future studies should deeply investigate the influence of earthquake nature, not only on the responses of the isolated structure but also on the isolator itself such as its material properties.

References

1. Kasimzade, A.A, Tuhta, S. Estimation of Sensitivity and Reliability Base Isolated Building under Earthquake Action. International Symposium on Network and Center-Based Research for Smart Structures Technologies and Earthquake Engineering. Osaka, Japan, 2004. Pp. 407–413.
2. Kasimzade, A.A. Structural Dynamics: Theory and Application to Earthquake Engineering (with CD included for education and dynamic analysis programs). Third Ed. Nobel Publication, 2018. 361 p.
3. Mathews, J.H., Fink, K.D. Numerical Methods Using MATLAB. 4th ed.53(9). Pearson. New Jersey, 2004. 691 p.
4. Gavin, H.P. Numerical Integration in Structural Dynamics. Finite Element Procedures in Engineering Analysis. 2016. Pp. 439–506.
5. Shrimali, M.K., Jangid, R.S. Non-linear seismic response of base-isolated liquid storage tanks to bi directional excitation. Nuclear Engineering and Design. 2002. 217(1–7). Pp. 1–20. DOI: 10.1016/S0029-5493(02)00134-6.
6. Matsagar, V.A., Jangid, R.S. Seismic response of base-isolated structures during impact with adjacent structures. Engineering Structures. 2003. 25(10). Pp.1311–1323. DOI: 10.1016/S0141-0296(03)00081-6.
7. Kasimzade, A.A., Tuhta, S., Atmaca, G. New Structural Seismic Isolation System. Seismic Isolation, Structural Health Monitoring, and Performance Based Seismic Design in Earthquake Engineering: Recent Developments. Springer, 2018. DOI: 10.1007/978-3-319-93157-9
8. Kasimzade, A.A., Dushimimana, A., Tuhta, S., Atmaca, G., Günday, F., Pfidze, K., Abrar, O. A Comparative Study on Effectiveness of Using Horasan Mortar as a Pure Friction Sliding Interface Material. European Journal of Engineering Research and Science. 2019. 4(2). Pp. 64–69. DOI: 10.24018/ejers.2019.4.2.1166.
9. Young, T., Mohlenkamp, M. Introduction to Numerical Math and Matlab Programming. Ohio University, 2009. 193 p.
10. Bangash, M.Y.H. Earthquake Resistant Buildings. Springer. London, 2011. 739 p. DOI: 10.1007/978-3-540-93818-7
11. Smekal, Z. Difference Equations with Forward and Backward Differences and Their Usage in Digital Signal Processor Algorithms. Radioengineering,. 2015. 15(2). Pp. 45–52.
12. Dushimimana, A., Nzamurambaho, F., Shyaka, E., Niyonsenga, A.A. Optimum Performance of Isolation System for Medium Rise Buildings Subject to Long Period Ground Motions. International Journal of Applied Engineering Research. 2018. 13(23). Pp. 16342–16350.
13. Djedoui, N., Ounis, A., Pinelli, J.P., Abdeddaim, M., Mahdi, A., Jean Paul, P. Hybrid Control Systems for Rigid Buildings Structures under Strong Earthquakes. Asian Journal of Civil Engineering. 2017. 18(6). Pp. 893–909.
14. Zhong-ming, X., Xuan, C., Zi-liang, Y. The study of sliding displacement spectrum on sliding base isolation structure. 6th International Conference on Advances in Experimental Structural Engineering, 2015. Pp. 9.
15. Chaturvedi, D.K. Modeling and Simulation of Systems Using MATLAB and Simulink. Taylor & Francis Group 6000. New York, 2010. 734 p.
16. Sina, S. Principal Component and Independent Component Regression for Predicting the Responses of Nonlinear Base Isolated Structures. University of Waterloo, 2008.
17. Nanda, R.P., Agarwal, P., Shrikhande, M. Earthquake Hazard Mitigation for Rural Dwellings by P-F Base Isolation. 14th World Conference on Earthquake Engineering (14WCEE). 11(2)Beijing, China, 2008. Pp. 2–9.
18. Dushimimana, A. The experimental and numerical studies on the effectiveness of aseismic base isolation. Ondokuz Mayıs University. 2019 [Online]. URL: <http://tez.yok.gov.tr/UlusalTezMerkezi/giris.jsp>

19. Mohammadzadeh, A., Valley, G. Solving Nonlinear Governing Equations of Motion Using Matlab and Simulink in First Dynamics Course. American Society for Engineering Education. 2006. 11(2). Pp. 15.
20. Lukashovich, A.A. Modelling of contact interaction of structures with the base under dynamic loading. Magazine of Civil Engineering. 2019. 89(5). Pp. 167–178. DOI: 10.18720/MCE.89.14.
21. Vatin, N.I., Ivanov, A.Y., Rutman, Y.L., Chernogorskiy, S.A., Shvetsov, K. V. Earthquake engineering optimization of structures by economic criterion. Magazine of Civil Engineering. 2017. 76(8). Pp. 67–83. DOI: 10.18720/MCE.76.7.
22. Bayramukov, S.H., Dolaeva, Z.N. Dynamic programming in optimization of comprehensive housing stock modernization. Magazine of Civil Engineering. 2017. 76(8). Pp. 3–19. DOI: 10.18720/MCE.76.1.
23. Jian, F., Xiaohong, L., Yanping, Z. Optimum design of lead-rubber bearing system with uncertainty parameters. Structural Engineering and Mechanics. 2015. 56(6). Pp. 959–982. DOI: 10.12989/sem.2015.56.6.959.
24. Shoaie, P., Tahmasebi, H., Mehdi, S. Seismic reliability-based design of inelastic base-isolated structures with lead-rubber bearing systems. Soil Dynamics and Earthquake Engineering. 2018. 115(June). Pp.589–605. DOI: 10.1016/j.soildyn.2018.09.033.
25. Han, J., Kyu, M., Choi, I. Experimental study on seismic behavior of lead-rubber bearing considering bi-directional horizontal input motions. Engineering Structures. 2019. 198(August). Pp. 109529. DOI: 10.1016/j.engstruct.2019.109529.
26. Yamamoto, Y., Yoshimura, C. Long-Period Ground Motion Simulation of Tokai-Tonankai-Nankai Coupled Earthquake Based on Large-Scale 3D FEM. 15th World Conference on Earthquake Engineering (15WCEE)Lisboa, 2012. Pp. 10.
27. Cheng, X., Jing, W., Li, D. Dynamic response of concrete tanks under far-field, long-period earthquakes. Proceedings of the Institution of Civil Engineers - Structures and Buildings. 2019. Pp. 1–14. DOI: 10.1680/jstbu.18.00024.
28. Hu, R.P., Xu, Y.L. SHM-Based Seismic Performance Assessment of High-Rise Buildings under Long-Period Ground Motion. Journal of Structural Engineering. 2019. 145(6). Pp. 04019038. DOI: 10.1061/(asce)st.1943-541x.0002323.
29. Bai, Y., Guan, S., Lin, X., Mou, B. Seismic collapse analysis of high-rise reinforced concrete frames under long-period ground motions. Structural Design of Tall and Special Buildings. 2019. 28(1). DOI: 10.1002/tal.1566.
30. Rao, P.B., Jangid, R.S. Experimental Study of Base-Isolated Structures. Journal of Earthquake Technology. 2001. 38(1). Pp. 1–15.
31. Tolani, S., Sharma, A. Effectiveness of Base Isolation Technique and Influence of Isolator Characteristics on Response of a Base Isolated Building [Online]. American Journal of Engineering Research (AJER). 2016. (5). Pp. 198–209. URL: www.ajer.org (date of application: 25.10.2019).
32. Friedland, B. Control System Design: An Introduction to State Space Methods. Dover Publications. New York, 1986. 506 p.
33. Butcher, J.C. Numerical Methods for Ordinary Differential Equations. 2nd ed. John Wiley and Sons Ltd, 2003. 484 p.
34. Kang, M.C., Sang-Won, C., Hyung-Jo, J., In-Won, L. Semi-active fuzzy control for seismic response reduction using magnetorheological dampers. Earthquake Engineering and Structural dynamics. 2002. 33. Pp. 723–736. DOI: 10.1002/eqe.372.
35. Nassim, D., Abdelhafid, O., Mahdi, A., Djedoui, N., Ounis, A., Abdeddaim, M. Active Vibration Control for Base-Isolated Structures Using a PID Controller Against Earthquakes. International Journal of Engineering Research in Africa. 2016. 26. Pp. 99–110. DOI: 10.4028/www.scientific.net/JERA.26.99.
36. Dushimimana, A., Gunday, F.. Operational Modal Analysis of Aluminum Model Structures using Earthquake Simulator. International Conference on Innovative Engineering Application (CIEA2018), 2018. Pp. 10.
37. Peter, S., Darina, H. State-Space Model of a Mechanical System in MATLAB/Simulink. Engineering Structures. 2012. 48. Pp. 629–635. DOI: 10.1016/j.proeng.2012.09.563.
38. Kasimzade, A.A., Tuhta, S., Gencay, A. Spherical foundation structural seismic isolation system: development of the new type earthquake resistant structures. 6th international conference on theoretical and applied mechanics (TAM15)Salerno,Italy, 2015.
39. Kasimzade, A.A., Tuhta, S. Stochastic Parametric System Identification Approach for Validation of Finite Element Models : Industrial. 2012. (June 2011). Pp. 41–61.
40. Kalfas, K.N., Mitoulis, S.A., Katakalos, K. Numerical study on the response of steel-laminated elastomeric bearings subjected to variable axial loads and development of local tensile stresses. Engineering Structures. 2017. 134. Pp. 346–357. DOI: 10.1016/j.engstruct.2016.12.015.
41. University of California. Pacific Earthquake Engineering Research Center (PEER) NGA: Ground Motion Database. 2013 [Online]. URL: https://peer.berkeley.edu/peer-strong-ground-motion-databases (date of application: 20.06.2018).
42. Colombo, A., Negro, P. A damage index of generalised applicability. Engineering Structures. 2012. 27. Pp. 1164–1174. DOI: 10.1016/j.engstruct.2005.02.014.
43. EN 1337-3: 2005. Structural bearings – Part 3: elastomeric bearings. Brussels: European Committee for Standardization. 2005.
44. Kumar, M., Whittaker, A.S., Constantinou, M.C. An advanced numerical model of elastomeric seismic isolation bearings. Earthquake Engineering & Structural Dynamics. 2014 [Online]. DOI: 10.1002/eqe.2431. URL: wileyonlinelibrary.com
45. Choun, Y., Park, J., Choi, I. Effects of Mechanical Property Variability in Lead Rubber Bearings on The Response Of Seismic. Nuclear Engineering and Technology. 2014. 46(5). Pp. 605–618. DOI: 10.5516/NET.09.2014.718.
46. BS EN 15129: 2009. Anti-seismic devices. BSI British Standards. 2010.
47. American Association of State Highway and Transportation Officials, AASHTO. Guide Specifications for Seismic Isolation Design. 4th ed. Washington, DC, 2014.
48. Japan Road Association, JRA. Bearing support design for highway bridges. Tokyo, Japan, 2011.

Contacts:

Aloys Dushimimana, +905366560436; chenkodu432@gmail.com

Aude Amandine Niyonsenga, +8617858530159; anaudy92@gmail.com

Gildas Jesuskpedji Decadjevi, +905458418576; gildasdeca@gmail.com

Lilies Kathami Kathumbi, +254780699845; lilieskath@gmail.com



DOI: 10.18720/MCE.92.13

Failure simulation of a RC multi-storey building frame with prestressed girders

V.I. Kolchunov^a, N.V. Fedorova^b, S. Yu. Savin^{b*}, V.V. Kovalev^a, T.A. Iliushchenko^a

^a Southwest State University, Kursk, Russia

^b National Research Moscow State Civil Engineering University, Moscow, Russia

* E-mail: suwin@yandex.ru

Keywords: reinforced concrete, precast and cast-in-place structures, building frame, prestressing, progressive collapse, numerical analysis, accidental actions, Vierendeel truss

Abstract. In recent decades, more and more attention has been paid to studying the mechanisms of resistance to the progressive collapse of various types of buildings and structures. Wherein, one of the most common types of structural systems of multi-storey residential and public buildings is a reinforced concrete frame or reinforced concrete frame-braced system. The scientific literature contains the following mechanisms of resistance of such structural systems to progressive collapse: arch, catenary or Vierendeel truss. However, currently there is not strict correspondence between the type of structural system, the nature of the accidental impact and the resistance mechanisms to progressive collapse. A similar situation exists in the field of developing effective ways to ensure the structural safety of such frames in case of accidental impacts. Therefore, a multi-storey reinforced concrete frame braced structural system with prestressed girders was selected as the object of study in this work. The purpose of the study is thus to establish the resistance mechanism of the reinforced concrete frame with prestressed girders at the failure of an outer column on the ground floor of the building. For the purpose of this study, using the decomposition method, the substructure in the form of two-story two-span reinforced concrete frame has been cut from the 3D model of the structure under consideration and has been performed a nonlinear quasi static analysis of the finite element model of this substructure. As a result of nonlinear numerical analysis, the diagrams of the axial forces and moments and schemes of destruction have been obtained for different values of prestressing in the girders. It has been established that over failed outer column the reinforced concrete frame under consideration transforms to Vierendeel truss. Change of the level of prestressing in the girders of the frame allows varying the stress-strain state and ensures load-bearing capacity of its elements under accidental impacts.

1. Introduction

A large number of investigation on behavior of structures in resisting progressive collapse of building and structures permanently grows especially in the last decades [1]. As a result, an experience accumulated in this field allowed to create and introduce building codes and regulatory documents in design practice. Advanced analysis of these documents is given, for example, in the works [1–3]. However, in a row of cases these regulatory documents do not contain unambiguous and explicit answers for many questions linked with features of design of a protection against progressive collapse and do not take into account the static-dynamic properties of deforming under accidental actions.

A significant number of research articles devoted to assessment resistance of buildings and structures to progressive collapse considers exhaustion of strength of the material as a criterion of failure [4–9]. A significantly less number of investigations deals with the stability problem of compressed and compressed-bent rods of structural systems when some element of the structural system collapsed [10–15].

Analysis of publications on protection of RC frames of buildings and structures against non-proportional failure shows that the resistance mechanism may be different in regard with a number of the floors in the

Kolchunov, V.I., Fedorova, N.V., Savin, S.Yu., Kovalev, V.V., Iliushchenko, T.A. Failure simulation of a RC multi-storey building frame with prestressed girders. Magazine of Civil Engineering. 2019. 92(8). Pp. 155–162. DOI: 10.18720/MCE.92.13

Колчунов В.И., Федорова Н.В., Савин С.Ю., Ковалев В.В., Ильющенко Т.А. Моделирование разрушения железобетонного каркаса многоэтажного здания с предварительно напряженными ригелями // Инженерно-строительный журнал. 2019. № 8(92). С. 155–162. DOI: 10.18720/MCE.92.13



building frame. In particular, the works [16–18] show that the mechanism of alternate load path takes the following forms: arch, catenary or Vierendeel truss. L. Shan, F. Petrone, S. Kunnath, X.H.C. He, W.J. Yi and X.X. Yuan noted that tall building resists to progressive collapse better due to redistribution of power flows. The arch effect may be implemented, if a structural element, for example a column, collapses slowly without dynamic effects. If a number of storeys of a building frame is less than ten ones and first floor column collapses quickly with dynamic effects then resisting mechanism is catenary. However, if a number of storeys is more than ten at the same parameters of accidental impact then behavior of the building frame in resisting to progressive collapse is Vierendeel truss. Similar results were obtained by Y. Li, X. Lu, H. Guan and P. Ren who investigated behavior of the multi-storey RC building frame depending on storey where the column was removed [19].

The works mentioned above deal with investigation of resistance to progressive collapse of cast-in-place multi-storey RC building frames. However, issues on ensuring alternate load path of precast - cast-in-place RC building frames were investigated worse [20–22]. An instrument protecting such a structural system usually is installation of additional links, which redistribute power flows into structural elements at accidental action such as sudden removal of a load bearing element [21].

Therefore this paper is devoted to investigation of behavior of the multi-storey RC building frame made of precast panel-frame elements [22–24]. As additional instrument protecting such a structure against progressive collapse, we proposed applying of continuous pre-stressed reinforcement in girders along the whole length of the building frame or its parts.

2. Methods

Constructive decisions. Load bearing building frame presented in Figure 1 consists of reinforced concrete precast elements (panel-frames) – 1; hollow-core slabs – 2 and continuously prestressed external girders – 3. Here 4 is up and down reinforcement, 5 is a hole for heat insulation and 6 is external multi-layer wall. Steel links between wall panels are marked number 7. The girders of the frame consist of precast and cast-in-place parts the shear resistance of which ensured by transverse reinforcing bars – 8. Conjunction node between column and girder is made of cast-in-place. Outer parts of the reinforcing bars – 9 of the precast hollow-core slabs are involved into cast-in-place part of the girder. Outer parts of the reinforcing bars - 9, 10 jutting from the precast hollow-core slabs and columns are immersed into cast-in-place part of the girder. Steel rods 11 work as anchors. Plugs 12 are installed in holes of hollow-core slabs and separate cast-in-place part of the girder 13. Prestressed reinforcing bars 14 are installed into cast-in-place part of girder along the whole width of the building or its part.

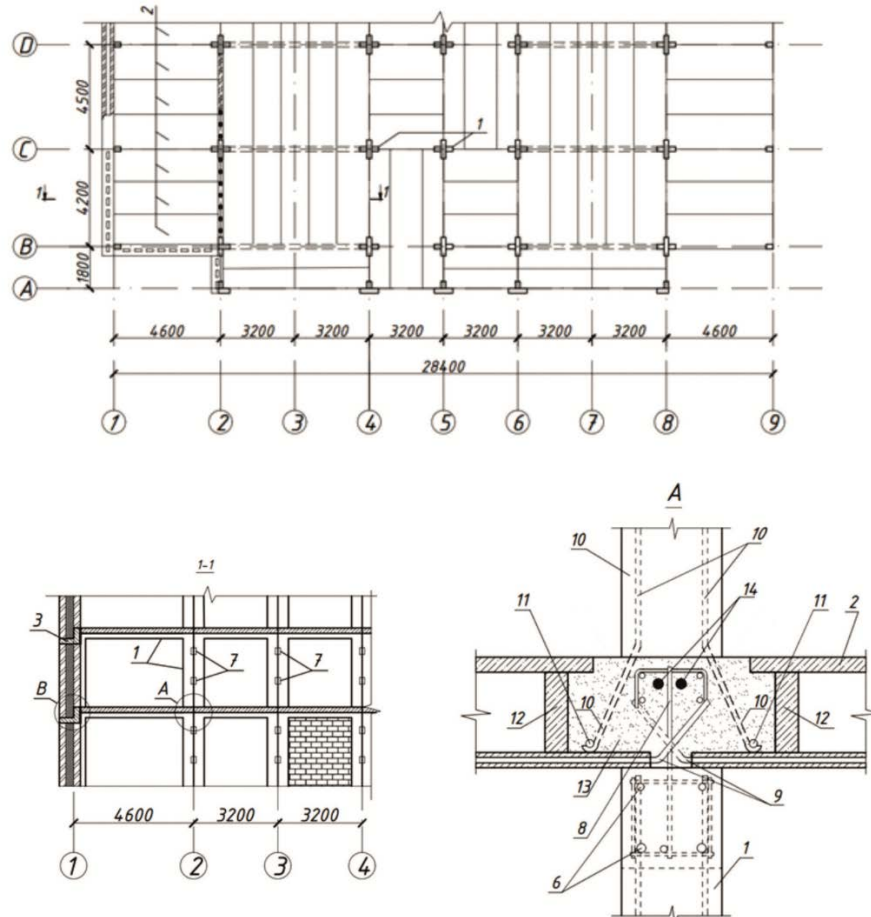


Figure 1. Multi-storey building made of RC panel-frames.

In contrast to earlier constructive decisions of similar building frames [22–24], this one contains prestressed reinforcing bars installed in cast-in-place part of girders along the whole length or width of building or its part. External parts of rebars jutting from the column are introduced into cast-in-place part of the girder. In the upper part of hollow-core slabs, the concrete keys are performed to ensure shear resistance. Moreover, additional steel rods connect slabs with cast-in-place part of girders.

Such decisions provide robustness of building frame both under operational impacts as well as under accidental impact, caused by sudden failure of a column.

Description of model and method. In order to evaluate effectiveness of the suggested protective decisions, we have conducted nonlinear structural analysis of the finite element model cut from the 3D model of building frame using the decomposition method (Figure 2).

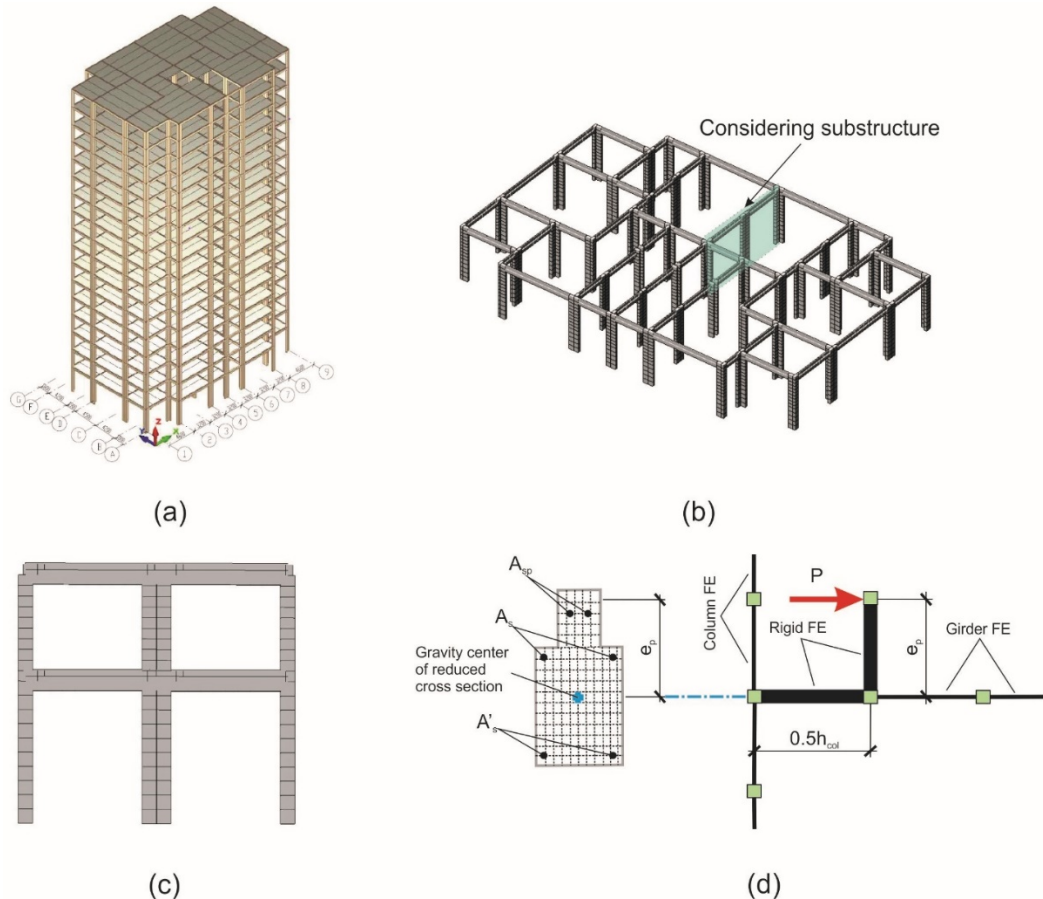


Figure 2. Finite element calculation model of multi-storey RC building frame: first level model (a) second level model (b), substructure for performance simulation (c), scheme for simulating of prestressed girder (d).

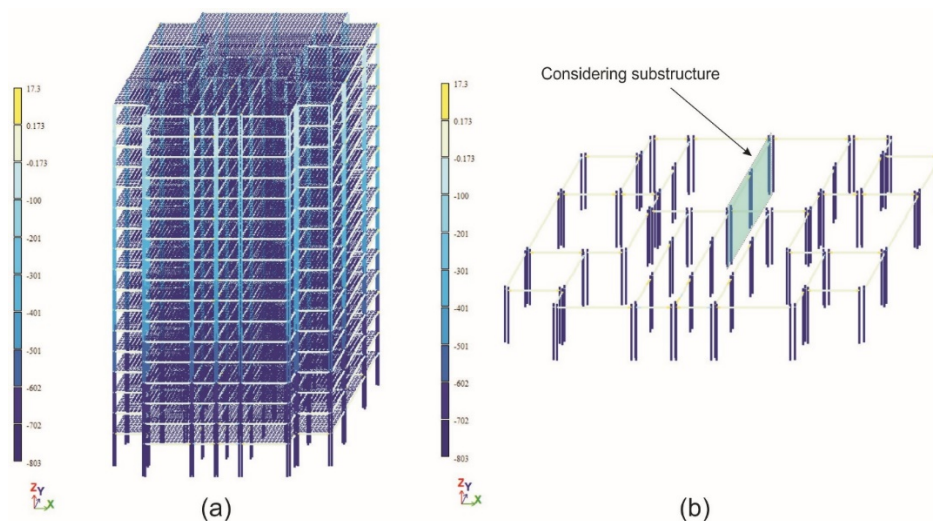


Figure 3. Mosaic of axial forces N (kN) in the structural elements of multi-storey RC building frame (a), mosaic of axial forces N (kN) in the first floor columns of considering building under design combination of loads (b).

At the first stage, we have performed structural analysis of entire reinforced concrete building frame using the finite element method by Lira-CAD program. A calculation scheme of the first level (Figure 2, a) was spatial plate-rod model of whole building, in which elements of frame were simulated by universal rod finite elements (FE), and hollow-core slabs of overlaps are simulated by universal 4-nodes shell elements. Hinge conjunction between girders and hollow-core slabs was simulated using coupled degree of freedom (DOF) X, Y, Z in respective nodes. In order to decrease common laboriousness of calculation and make results clearer from engineering position, we did not take in account non-linear behavior of multi-storey RC building frame at this step. The result of such numerical analysis was diagrams of forces and moments caused by design combination of loads (Figure 3).

In order to provide detailed assessment of stress-strain state of reinforced concrete structural elements of the building frame, we have chosen a substructure (building frame fragment) in the zone of possible local failure of the building frame. Correctness of algorithm suggested here is proved by row of experimental researches, for example, [6, 20], which had established that dynamic effect, caused by sudden structural transformation under accidental action, quickly damping with distance from the place of the local damage.

As example, we have considered the most loaded substructure in the form of two-span two-storey flat frame (Figure 2, b), for which a calculation scheme of the second level have been built (Figure 2, c). Initial data for advanced numerical analysis of behavior of structural elements of this substructure have been obtained from results of numerical analysis for the calculation scheme of the first level. At the same time structural elements of the second level calculation scheme have been simulated by universal physically non-linear rod finite elements with exponential strain - stress dependencies for concrete C60 and steel reinforcement A500.

Slabs of the multi-storey building have been replaced by evenly distributed load in the calculation model of the second level. The stiffness of the building frame part excluded from consideration have been substituted by one-node finite element of elastic spring, which makes the model equivalent to the first level calculation scheme by deformations. In order to take in account prestressing force and its eccentricity e_p , we have introduced rigid rod finite elements (Figure 2, d), in the upper nodes of which prestressing forces P have been attached.

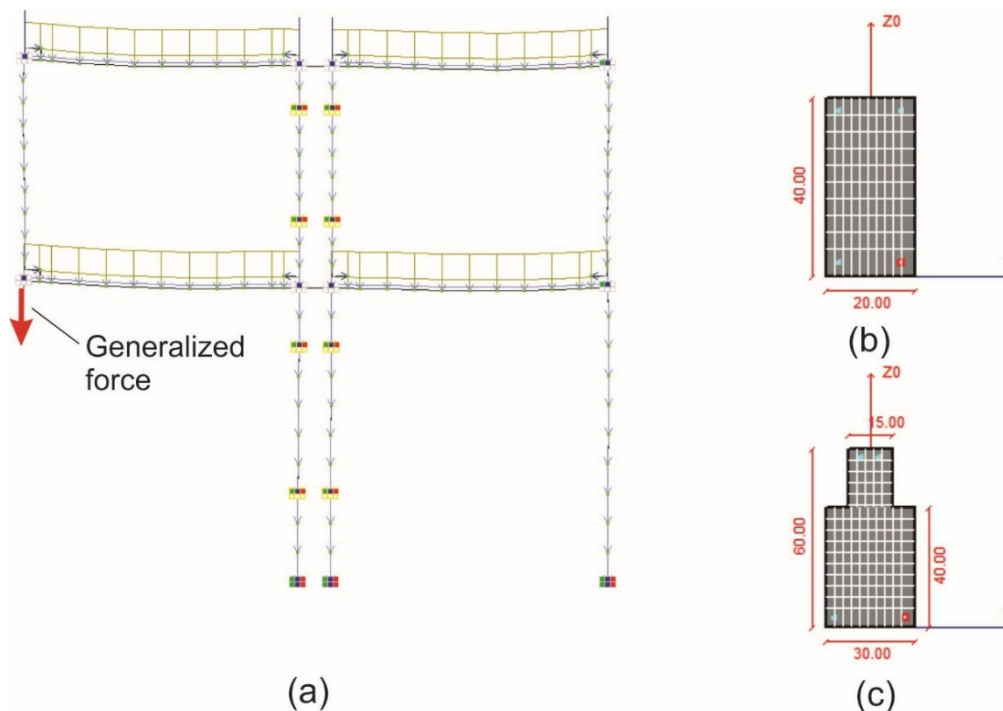


Figure 4. Secondary calculation scheme of second level at the stage of the outer column removal: quasi-static model of substructure in place of local failure (a), calculation cross section of column (b), calculation cross section of girder (c).

Numerical modeling of behavior of the substructure (calculation scheme of the second level) in resisting to progressive collapse have been conducted using step-iterative method. At the same time, we took in account static mode of loading during operational stage and dynamic mode at accidental impact caused by sudden removal of the first floor column. Increment of dynamic force into the secondary second level scheme have been simulated quasi-statically, assuming that removal of the column leads to appearing of the generalized force in the corresponding node of the girder. This force equals to axial force in the collapsed column at the stage of normal operation but change its direction in comparison with operational stage (Figure 4).

3. Results and Discussion

In order to evaluate how prestressing of girders affects to behavior of the substructure under consideration in resisting to progressive collapse, we have performed comparative numerical analysis of robustness for three variants of calculation schemes: without prestressing, when prestressing force equals $0.6 \cdot R_{s,ser} \cdot A_s$ and when prestressing force equals $0.9 \cdot R_{s,ser} \cdot A_s$.

Figure 5 presents results of such calculation in the form of mosaic of bending moments and axial forces and failure schemes. Analysis of results presented in the figure 5 allowed concluding the following.

Installation of prestressed rebars into cast-in-place part of girders of the first floor overlap and connection of these girders with columns of upper floor using steel links provides alternate load paths for redistribution of power flows at accidental impact. Such a decision may serve as a protection against progressive collapse. As a result, structural system under consideration becomes the truss-diaphragm similar to Vierendeel truss. This is consistent with results obtained in the works [16, 17, 19] for cast-in-place reinforced concrete multi-storey building frames.

Thus, we can varies stress-strain state in the zones of a possible local failure of precast-cast-in-place reinforced concrete building frame changing placement of prestressed rebars through the height of girders. It allows us provide bearing capacity of these local zones in accordance with criteria of the special limit state.

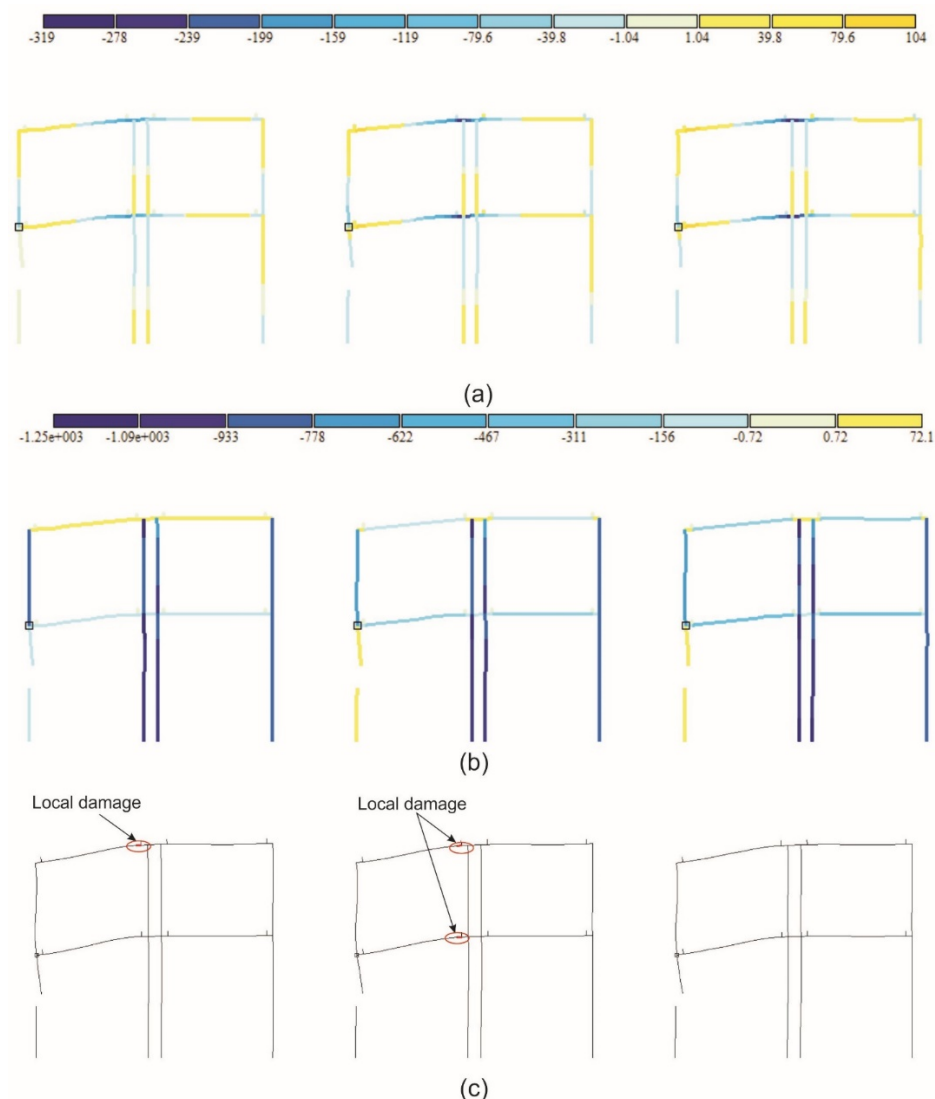


Figure 5. Calculation results for substructure robustness to progressive collapse: moments, kN·m (a), axial forces, kN (b), failure schemes (c). Here accepted: without prestressing (left column), prestressing force equals $0.6 \cdot R_{s,ser} \cdot A_s$ (middle column) and prestressing force equals $0.9 \cdot R_{s,ser} \cdot A_s$ (right column).

At the same time, constructive decision considered above leads to moment increasing into posts. According to this feature, it is necessary to provide additional control of strength and stability of columns as compressed-bent elements [22], as well as carried out reliability control of anchoring of reinforcing bars into connection nodes of posts and girders.

4. Conclusions

1. It is established that reinforced concrete building frame made of precast panel-frame elements with prestressed girders transforms to truss-diaphragm system similar to Vierendeel truss if outer column of the first floor was collapsed.

2. Changing placement of prestressed rebars through the height of girders allows us varying stress-strain state into the danger zones of precast-cast-in-place building frames made of panel-frame elements and provides load bearing capacity of such structures under accidental impacts.

References

- Adam, J.M., Parisi, F., Sagaseta, J., Lu, X. Research and practice on progressive collapse and robustness of building structures in the 21st century. *Engineering Structures*. 2018. 173 (March). Pp. 122–149. doi: 10.1016/j.engstruct.2018.06.082
- Wang, H., Zhang, A., Li, Y., Yan, W. A Review on Progressive Collapse of Building Structures. *The Open Civil Engineering Journal*. 2014. 8(1). Pp. 183–192. doi:10.2174/1874149501408010183
- Androsova, N.B., Vetrova, O.A. the Analysis of Studies and Requirements for the Protection of Buildings and Structures Against Progressive Collapse in Regulatory Documents of Russia and the European Union. *Building and Reconstruction*. 2019. 81(1). Pp. 85–96. doi: 10.33979/2073-7416-2019-81-1-85-96
- Tsai, M.-H. An Approximate Analytical Formulation for the Rise-Time Effect on Dynamic Structural Response Under Column Loss. *International Journal of Structural Stability and Dynamics*. 2018. 18(03). Pp. 1850038. doi:10.1142/S0219455418500384
- Shi, F., Wang, L., Dong, S. Progressive Collapse Assessment of the Steel Moment-frame with Composite Floor Slabs Based on Membrane Action and Energy Equilibrium. *The Open Construction and Building Technology Journal*. 2017. 11(1). Pp. 200–215. doi: 10.2174/1874836801711010200
- Forquin, P., Chen, W. An experimental investigation of the progressive collapse resistance of beam-column RC sub-assemblages. *Construction and Building Materials*. 2017. 152. Pp. 1068–1084. doi: 10.1016/j.conbuildmat.2017.05.179
- Semenov, A.A., Porivaev, I.A., Kuznetsov, D.V., Nguen, T.H., Saitgalina, A.S., Tregubova, E.S. Stress-strain state of high-rise building under wind load and progressive collapse. *Construction of Unique Buildings and Structures*. 2017. 59(8). Pp. 7–26. doi: 10.18720/CUBS.59.1
- Travush, V.I., Fedorova, N.V. Survivability of structural systems of buildings with special effects. *Magazine of Civil Engineering*. 2018. 81(5). Pp. 73–80. doi: 10.18720/MCE.81.8
- Schafer, B.W., Bajpai, P. Stability degradation and redundancy in damaged structures. *Engineering Structures*. 2005. 27. Pp. 1642–1651. doi: 10.1016/j.engstruct.2005.05.012
- McConnell, J.R., Brown, H. Evaluation of progressive collapse alternate load path analyses in designing for blast resistance of steel columns. *Engineering Structures*. 2011. 33(10). Pp. 2899–2909. doi: 10.1016/j.engstruct.2011.06.014
- Szyniszewski, S., Krauthammer, T. Energy flow in progressive collapse of steel framed buildings. *Engineering Structures*. 2012. 42. Pp. 142–153. doi: 10.1016/j.engstruct.2012.04.014
- Gerasimidis, S., Sideri, J. A new partial-distributed damage method for progressive collapse analysis of steel frames. *Journal of Constructional Steel Research*. 2016. 119. Pp. 233–245. doi: 10.1016/j.jcsr.2015.12.012
- Gerasimidis, S., Khorasani, N.E., Garlock, M., Pantidis, P., Glassman, J. Resilience of tall steel moment resisting frame buildings with multi-hazard post-event fire. *Journal of Constructional Steel Research*. 2017. 139. Pp. 202–219. doi: 10.1016/j.jcsr.2017.09.026
- Fedorova, N.V., Savin, S.Y. Ultimate State Evaluating Criteria of RC Structural Systems at Loss of Stability of Bearing Element. *IOP Conference Series: Materials Science and Engineering*. 2018. 463. Pp. 032072. doi:10.1088/1757-899X/463/3/032072
- Kolchunov, V.I., Savin, S.Y. Survivability criteria for reinforced concrete frame at loss of stability. *Magazine of Civil Engineering*. 2018. 80(4). Pp. 73–80. doi: 10.18720/MCE.80.7
- Shan, L., Petrone, F., Kunnath, S., He, X.H.C., Yi, W.J., Yuan, X.X. Robustness of RC buildings to progressive collapse: Influence of building height. *Engineering Structures*. 2019. 183(August 2018). Pp. 690–701. doi: 10.1016/j.engstruct.2019.01.052
- Qiao, H., Yang, Y., Zhang, J. Progressive Collapse Analysis of Multistory Moment Frames with Varying Mechanisms. *Journal of Performance of Constructed Facilities*. 2018. 32(4). Pp. 04018043. doi: 10.1061/(ASCE)CF.1943-5509.0001192
- He, X.-H.-C., Yi, W.-J., Yuan, X.-X. A non-iterative progressive collapse design method for RC structures based on virtual thermal pushdown analysis. *Engineering Structures*. 2019. 189. Pp. 484–496. doi: 10.1016/j.engstruct.2019.03.102
- Li, Y., Lu, X., Guan, H., Ren, P. Numerical investigation of progressive collapse resistance of reinforced concrete frames subject to column removals from different stories. *Advances in Structural Engineering*. 2016. 19(2). Pp. 314–326. doi: 10.1177/1369433215624515
- Guerrero, H., Ji, T., Escobar, J.A., Teran-Gilmore, A. Effects of Buckling-Restrained Braces on reinforced concrete precast models subjected to shaking table excitation. *Engineering Structures*. 2018. 163. Pp. 294–310. doi: 10.1016/j.engstruct.2018.02.055
- Quiel, S.E., Naito, C.J., Fallon, C.T. A non-emulative moment connection for progressive collapse resistance in precast concrete building frames. *Engineering Structures*. 2019. 179. Pp. 174–188. doi: 10.1016/j.engstruct.2018.10.027
- Savin, S.Y., Kolchunov, V.I., Emelianov, S.G. Modelling of resistance to destruction of multi-storey frame-connected buildings at sudden loss of bearing elements stability. *IOP Conference Series: Materials Science and Engineering*. 2018. 456. Pp. 012089. doi: 10.1088/1757-899X/456/1/012089
- Elsanadedy, H.M., Almusallam, T.H., Al-Salloum, Y.A., Abbas, H. Investigation of precast RC beam-column assemblies under column-loss scenario. *Construction and Building Materials*. 2017. 142. Pp. 552–571. doi: 10.1016/j.conbuildmat.2017.03.120
- Nimse, R.B., Joshi, D.D., Patel, P. V. Behavior of wet precast beam column connections under progressive collapse scenario: an experimental study. *International Journal of Advanced Structural Engineering*. 2014. 6(4). Pp. 149–159. doi:10.1007/s40091-014-0072-3

Contacts:

Vitaly Kolchunov, +7(4712)222461; asiorel@mail.ru
 Nataliya Fedorova, +7(960)6971230; fenavit@mail.ru
 Sergey Savin, +7(920)8125909; suwin@yandex.ru
 Vladislav Kovalev, +7(977)8023726; slavutich_1991@mail.ru
 Tatiana Iliushchenko, +7(919)1345907; tatkhalina93@yandex.ru



DOI: 10.18720/MCE.92.13

Моделирование разрушения железобетонного каркаса многоэтажного здания с предварительно напряженными ригелями

В.И. Колчунов^a, Н.В. Федорова^b, С.Ю. Савин^{b*}, В.В. Ковалев^a, Т.А. Ильющенко^a,

^a Юго-Западный государственный университет, г. Курск, Россия

^b Национальный исследовательский Московский государственный строительный университет, Москва, Россия

* E-mail: suwin@yandex.ru

Ключевые слова: моделирование, железобетонный сборно-монолитный каркас, расчетная схема, преднапряжение, аварийные воздействия, численный анализ

Аннотация. В последние десятилетия в области структурного анализа стало все больше внимания уделяться изучению механизмов сопротивления прогрессирующему разрушению различных типов конструктивных систем зданий и сооружений при аварийных воздействиях. Одним из наиболее распространенных типов конструктивных систем многоэтажных жилых и общественных зданий в настоящее время является рамный или рамно-связевой железобетонный каркас. В качестве механизмов его сопротивления прогрессирующему сопротивлению в научной литературе, как правило, выделяются следующие: арочный, вантовый, ферма Виренделя. Однако к настоящему времени не установлено строгого соответствия между типом конструктивной системы, характером аварийного воздействия и механизмами сопротивления прогрессирующему обрушению в зависимости от первых двух факторов. Аналогичная ситуация складывается и в области разработки эффективных способов обеспечения конструктивной безопасности таких каркасов при аварийных воздействиях. Поэтому в качестве объекта исследования в данной работе был выбран многоэтажный железобетонный рамно-связевой каркас с предварительно напряженными ригелями, подверженный аварийному воздействию в виде внезапного удаления колонны крайнего ряда на первом этаже здания. Целью исследования являлось установление механизма сопротивления железобетонного каркаса с предварительно напряженными ригелями при рассматриваемом типе воздействия. Для достижения целей исследования с помощью метода конечных элементов был выполнен нелинейный квазистатический анализ деформирования и разрушения подконструкции в виде двухэтажной двухпролетной рамы, выделенной из каркаса здания методом декомпозиции. По результатам нелинейного численного анализа были получены значения внутренних усилий в элементах подконструкции и схемы ее разрушения в зависимости от величины предварительного напряжения в ригелях. Установлено, что при удалении колонны крайнего ряда в рассматриваемом железобетонном каркасе с предварительно напряженными ригелями над зоной локального разрушения реализуется механизм сопротивления по типу фермы Виренделя. Показано, что изменение уровня усилия предварительного обжатия в ригелях позволяет варьировать НДС статически неопределимой стержневой системы и обеспечивать ее несущую способность при аварийных воздействиях.

Литература

1. Adam J.M., etc. Research and practice on progressive collapse and robustness of building structures in the 21st century // Eng. Struct. 2018. Vol. 173. № March. Pp. 122–149.
2. Wang H., etc. A Review on Progressive Collapse of Building Structures // Open Civ. Eng. J. 2014. Vol. 8. № 1. Pp. 183–192.
3. Андросова Н.Б., Ветрова О.А. Анализ исследований и требований по защите зданий и сооружений от прогрессирующего обрушения в законодательно- нормативных документах России и странах Евросоюза // Строительство и реконструкция. 2019. Т. 81. № 1. С. 85–96.
4. Tsai M.-H. An Approximate Analytical Formulation for the Rise-Time Effect on Dynamic Structural Response Under Column Loss // Int. J. Struct. Stab. Dyn. 2018. Vol. 18. № 03. С. 1850038.
5. Shi F., Wang L., Dong S. Progressive Collapse Assessment of the Steel Moment-frame with Composite Floor Slabs Based on Membrane Action and Energy Equilibrium // Open Constr. Build. Technol. J. 2017. Vol. 11. № 1. С. 200–215.
6. Forquin P., Chen W. An experimental investigation of the progressive collapse resistance of beam-column RC sub-assemblages // Constr. Build. Mater. 2017. Vol. 152. С. 1068–1084.

7. Семенов А.А., Порываев И.А., Кузнецов Д.В., Нгуен Т.Х., Саитгалина А.С., Трегубова Е.С. Напряженно-деформированное состояние высотного здания при ветровом воздействии и прогрессирующем обрушении // Строительство уникальных зданий и сооружений. 2017. № 8(59). С. 7–26.
8. Травуш В.И., Федорова Н.В. Живучесть конструктивных систем сооружений при особых воздействиях // Инженерно-строительный журнал. 2018. № 5(81). С. 73–80.
9. Schafer B.W., Bajpai P. Stability degradation and redundancy in damaged structures // Eng. Struct. 2005. Vol. 27. Pp. 1642–1651.
10. McConnell J.R., Brown H. Evaluation of progressive collapse alternate load path analyses in designing for blast resistance of steel columns // Eng. Struct. 2011. Vol. 33. № 10. Pp. 2899–2909.
11. Szyniszewski S., Krauthammer T. Energy flow in progressive collapse of steel framed buildings // Eng. Struct. 2012. Vol. 42. Pp. 142–153.
12. Gerasimidis S., Sideri J. A new partial-distributed damage method for progressive collapse analysis of steel frames // J. Constr. Steel Res. 2016. Vol. 119. Pp. 233–245.
13. Gerasimidis S., etc. Resilience of tall steel moment resisting frame buildings with multi-hazard post-event fire // J. Constr. Steel Res. 2017. Vol. 139. Pp. 202–219.
14. Fedorova N. V., Savin S.Y. Ultimate State Evaluating Criteria of RC Structural Systems at Loss of Stability of Bearing Element // IOP Conf. Ser. Mater. Sci. Eng. 2018. Vol. 463. 032072.
15. Колчунов В.И., Савин С.Ю. Критерии живучести железобетонной рамы при потере устойчивости // Инженерно-строительный журнал. 2018. № 4(80). С. 73–80.
16. Shan L., etc. Robustness of RC buildings to progressive collapse: Influence of building height // Eng. Struct. 2019. Vol. 183. № August 2018. Pp. 690–701.
17. Qiao H., Yang Y., Zhang J. Progressive Collapse Analysis of Multistory Moment Frames with Varying Mechanisms // J. Perform. Constr. Facil. 2018. Vol. 32. № 4. 04018043.
18. He X.-H.-C., Yi W.-J., Yuan X.-X. A non-iterative progressive collapse design method for RC structures based on virtual thermal pushdown analysis // Eng. Struct. 2019. Vol. 189. Pp. 484–496.
19. Li Y. и др. Numerical investigation of progressive collapse resistance of reinforced concrete frames subject to column removals from different stories // Adv. Struct. Eng. 2016. Vol. 19. № 2. Pp. 314–326.
20. Guerrero H., etc. Effects of Buckling-Restrained Braces on reinforced concrete precast models subjected to shaking table excitation // Eng. Struct. 2018. Vol. 163. Pp. 294–310.
21. Quiel S.E., Naito C.J., Fallon C.T. A non-emulative moment connection for progressive collapse resistance in precast concrete building frames // Eng. Struct. 2019. Vol. 179. Pp. 174–188.
22. Savin S.Y., Kolchunov V.I., Emelianov S.G. Modelling of resistance to destruction of multi-storey frame-connected buildings at sudden loss of bearing elements stability // IOP Conf. Ser. Mater. Sci. Eng. 2018. Vol. 456. 012089.
23. Elsanadedy H.M. и др. Investigation of precast RC beam-column assemblies under column-loss scenario // Constr. Build. Mater. 2017. Vol. 142. Pp. 552–571.
24. Nimse R.B., Joshi D.D., Patel P. V. Behavior of wet precast beam column connections under progressive collapse scenario: an experimental study // Int. J. Adv. Struct. Eng. 2014. Vol. 6. № 4. Pp. 149–159.

Контактные данные:

Виталий Иванович Колчунов, +7(4712)222461; asiorel@mail.ru

Наталья Витальевна Федорова, +7(960)6971230; fenavit@mail.ru

Сергей Юрьевич Савин, +7(920)8125909; suwin@yandex.ru

Владислав Валерьевич Ковалев, +7(977)8023726; slavutich_1991@mail.ru

Татьяна Александровна Ильющенко, +7(919)1345907; tatkhulina93@yandex.ru

© Колчунов В.И., Федорова Н.В., Савин С.Ю., Ковалев В.В., Ильющенко Т.А., 2019



DOI: 10.18720/MCE.92.14

Mechanical and electrical properties of concrete modified by carbon nanoparticles

L.A. Urkhanova^a, S.L. Buyantuev^a, A.A. Urkhanova^a, S.A. Lkhasaranov^a, G.R. Ardashova^a, R.S. Fediuk^{b*}, A.P. Svintsov^c, I.A. Ivanov^a

^a East Siberia State University of Technology and Management, Ulan-Ude, Russia,

^b Far Eastern Federal University, Vladivostok, Russia,

^c Peoples' Friendship University of Russia, Moscow, Russia,

* E-mail: roman44@yandex.ru

Keywords: cements, cement-based composites, binders, concretes, carbon nanoparticles

Abstract. The article presents the study of obtaining electrically conductive concrete using carbon nanoparticles obtained by processing coal in an electric-discharge plasma reactor. An electric-discharge method for producing a sedimentation-resistant and highly dispersed suspension consists in treating coal powder with an electric current in an aqueous medium. Using laser diffraction, it was found that carbon nanoparticles have a particle size in the range from 50 to 500 nm. The microstructure of hardened cement paste was studied using SEM. The compressive strength was tested on cubes with an edge of 100 mm according to EN 12390-6. Determination of the electrical resistance of concrete was carried out on specimens with an edge of 100 mm, placed between two brass plates, through which direct current was passed. The optimum content of carbon nanoparticles (0.01–0.1 % wt.) in the binder is evaluated, which allows to obtain high mechanical properties (30–35 % higher compressive strength compared to a control specimen. It is proved that the mechanism of action of nanoscale modifiers is most manifested in small doses. The dependences of the physicomechanical properties of Portland cement upon the addition of various amounts of carbon nanoparticles are determined. Physicomechanical and exploitation properties of heavyweight electrically conductive concrete are determined. The kinetics of changes in the electrical resistance of concrete at different curing periods is established.

1. Introduction

Cement composites with improved electrical properties in recent years have the potential to be used as deformation sensors for structures, as well as heating elements or anodes in various electrochemical methods [1–5].

Traditionally, the production of such concretes was associated with the addition of conductive particles into the concrete mix, such as multilayer carbon nanotubes [6], soot [7–8], iron oxide nanoparticles [9], nickel powders [10], graphite [11]. The use of electrically conductive aggregates, for example, piezoceramics, also reduces the electrical resistance of the composite [12–13].

The use of these materials allowed expanding the range of cheap electric heaters, especially for extended spaces (floors, walls of garages, parking lots and special structures). In addition, knowledge of electrical parameters is useful for developing accelerated curing processes for concrete mixtures, for example, with electromagnetic heating. The deformation and length of cracks in cement composites are closely related to their electrical resistance, so electrically conductive concrete can be used to monitor structures. Multifunctional smart concrete can be used as a deformation, fire and moisture sensor, acting as a structural material [14–16]. The areas of application of electrically conductive concrete and their required characteristics of electrical resistance are listed in Table 1.

Urkhanova, L.A., Buyantuev, S.L., Urkhanova, A.A., Lkhasaranov, S.A., Ardashova, G.R., Fediuk, R.S., Svintsov, A.P., Ivanov, I.A. Mechanical and electrical properties of concrete modified by carbon nanoparticles. Magazine of Civil Engineering. 2019. 92(8). Pp. 163–172. DOI: 10.18720/MCE.92.14

Урханова Л.А., Буянтуев С.Л., Урханова А.А., Лхасаранов С.А., Ардашова Г.Р., Федюк Р.С., Свинцов А.П., Иванов И.А. Механические и электрические свойства бетона, модифицированного углеродными наночастицами // Инженерно-строительный журнал. 2019. № 8(92). С. 163–172. DOI: 10.18720/MCE.92.14



Table 1. The areas of application of electrically conductive concrete.

Areas of application	Specific electrical resistance, Ohm·cm	References
Anodes	$2 \cdot 10^2 - 8 \cdot 10^3$	[2, 17, 25, 26, 34, 36]
Deformation sensors for structures	$3 \cdot 10^2 - 5 \cdot 10^4$	[5, 6, 9–13, 20, 27]
Anti-icing road surfaces	$7 \cdot 10^4 - 4 \cdot 10^5$	[8, 17, 22, 32, 33]
Heating elements	$2 \cdot 10^6 - 5 \cdot 10^7$	[1, 4, 8, 21, 31, 35, 37]

However, a certain instability of properties associated with increased moisture content, blocking of electrically conductive particles by hydration products, as well as the problems of ensuring a high initial strength and density of such concretes significantly limit their scope [17–21]. It should be noted that the use of electrolyte additives in this case is extremely undesirable.

Shi [22] examined the electrical conductivity of concrete from the perspective of the conductivity of the liquid phase in the pore space. Higher electrical conductivity (lower electrical resistivity) suggests higher porosity. He considered hardened concrete to be a semiconductor or dielectric. The same theory is confirmed by other researchers [23–25].

Velay-Lizankos et al. [26] searched for a connection between the elastic modulus and electrical conductivity, but they did not get a clear dependence. Demirciloglu et al. [27] investigated smart concrete containing brass fibers. Despite the good results, this composition is quite expensive. In addition, the authors were convinced that the temperature and humidity at which it is used are of great importance for the electrical characteristics of concrete.

According to the results of many studies, [28–30] the electrical properties of cement pastes were quite sensitive to minor changes in the microstructure of cement materials.

As a number of authors indicate in their studies, the mechanism of electrical conductivity in composite electrically conductive materials is rather complicated [31–32]. The mechanism of conduction through, for example, dielectrics can be both ionic and electronic in nature. A promising issue is the search for a concrete component with a relatively high electrical conductivity, which will have an effect on the overall electrical conductivity of the composite [33]. Researchers emphasize that electrically conductive components are divided into two groups: metal and carbon [34–36].

Carbon electrically conductive components include soot, graphite and carbon black. They are relatively cheap, available in any region, and have a very low electrical resistivity. Carbon, like metal, has electronic conductivity. However, these materials lower the strength of the composites. So, with a volume content of carbon black above 30 %, a complete loss of the mechanical strength of concrete occurs [37]. One of the solutions to this problem is to reduce the size of low-strength carbon materials. The use of carbon nanoparticles with a high specific surface in this regard to reduce the electrical resistance of concrete is interesting.

In general, it should be noted that the properties of electrically conductive concrete are relatively poorly understood. In world construction practice, there are no standards for the study of the electrical characteristics of concrete. Especially few studies relate to studies of carbon nanoparticles obtained by low-cost methods. The problem of ensuring the sedimentation stability of these particles in suspension has not yet been solved.

The scientific novelty lies in the use of carbon nanoparticles obtained in the processing of coal in a plasma-arc reactor as electrically conductive particles in concrete.

The aim of the article is the development of fine-grained concrete and the study of their physico-mechanical, exploitation, as well as electrical properties. The scope of these concretes is quite extensive – from paving slabs [38] to structures of especially important structures [39].

2. Materials and Methods

To achieve the aim of paper, an electrically conductive concrete composition was developed. It consists of (per 1 m³): Portland cement CEM I 32.5 N (Spasskement, Russia) – 375 kg; quartz-feldspar sand with the fineness modulus 3.84 – 670 kg; granite crushed stone fractions of 5–20 mm – 1160 kg; water – 170 L and carbon nanoparticles (CNP) obtained from coal in a plasma-arc reactor – 0.01–1% by wt. of cement). Moreover, the same proportions were used for the control composition, but without carbon nanoparticles.

Both chemical and mineralogical composition of used Portland cement are listed in Table 2.

Table 2. Chemical and mineralogical composition of Portland cement CEM I 32.5N.

Chemical composition (%)							Mineralogical composition (%)			
CaO	SiO ₂	Al ₂ O ₃	Fe ₂ O ₃	MgO	SO ₃	Na ₂ O	C ₃ S	C ₂ S	C ₃ A	C ₄ AF
65.94	21.70	5.02	4.20	1.25	0.40	0.78	61.0	16.3	6.2	12.8

An electric-discharge method for producing a sedimentation-resistant and highly dispersed suspension from coal at low energy costs and without the use of plasticizers consists in treating a coal powder with a fraction of 200 μm with water by electric current. Under the influence of an electric arc plasma from the material of the electrodes and coal supplied for gasification, synthesis gas ($\text{CO} + \text{H}_2$), activated carbon (sorbent) and carbon nanoparticles — fullerene-containing soot - are formed in one setup. Fullerene-containing soot in this installation is formed along the way, which favorably distinguishes this method of producing carbon nanoparticles in comparison with others. The results of determining the phase composition indicate that the content of fullerene C_{60} in the additive is approximately 1.5–2 %. As a result of the treatment, a sedimentation-stable water-coal suspension (WCS) is obtained.

Figure 1 shows the results of a study of the particle size of CNPs determined by laser diffraction on an SALD-7101 Shimadzu instrument (Japan). The results obtained by laser diffraction show that the carbon nanoparticles lie in the range from 50 to 500 nm.

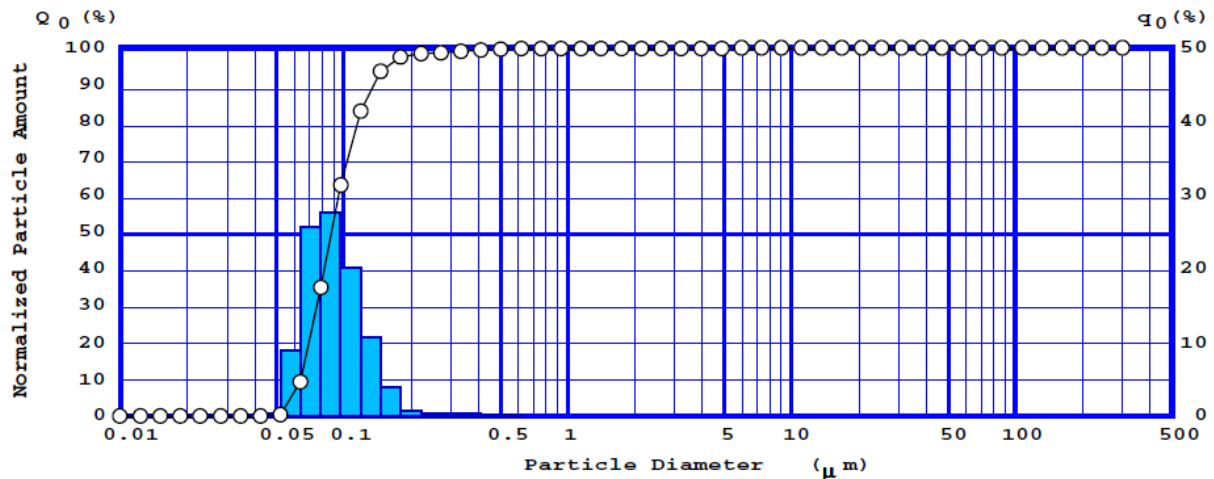


Figure 1. The distribution of CNP particles in the volume of mixing water.

The microstructure of fiber cement compositions was determined using a Jeol JSM 6510 LV scanning electron microscope (Japan) with a magnification of $\times 1000$. The porosity of the hardened cement paste was determined by mercury porosimetry by a Quantachrome PoreMaster 33 instrument.

Concrete cubes of dimensions 100 \times 100 \times 100 mm were prepared for compressive strength test at the age of 2, 7 and 28 days for all mixes. The concrete specimens were unmolded after 24 hours of casting and then immersed in curing tank at room temperature and relative humidity at 65 ± 5 % until the age of testing. This test was carried out using a Shimadzu (Kyoto, Japan) tester machine with a capacity of 200 kN according to EN 12390-3.

Water permeability was determined on cylinder specimens with a diameter of 150 mm, $h = 50$ mm on an Agama-2RM instrument (Russia). Water absorption was determined by weighing the specimens every 24 hours to obtain a constant weight. The study of freeze-thaw resistance was carried out on specimens of 100 \times 100 \times 100 mm. Specimens were immersed in water at first at 1/3 of the height for a day, then at 2/3 of the height also for a day, and then immersed in water completely for two days. Then the specimens were placed in a Polair CV-105S freezer (Russia) at a temperature of -18°C . Each freezing cycle lasted 2.5 hours, the thawing cycle at a temperature of 20°C is 2 hours.

Determination of the electrical resistance of concrete was carried out on specimens with an edge of 10 cm by the following method. A specimen was placed between two 3 mm thick metal brass plates through which direct current was passed. A multimeter was connected to the plates. Ensuring reliable electrical contact between the plates and the specimen was carried out using a press, which was isolated from the plates with rubber gaskets.

3. Results and Discussion

Figure 2 shows the results of a study of the compressive strength of hardened cement paste with different contents of carbon nanoparticles. It was revealed that higher results were obtained with a CNP content in the range of 0.01–0.1 wt. %, at which there was an improvement in strength by 30–35 % compared with the control specimen. With an increase in the content of additives to 1 %, a decrease in the strength of hardened cement paste is observed, while the results are comparable with the control specimen. In our opinion, this is due to the mechanism of action of nanoscale modifiers, which are most manifested in small doses.

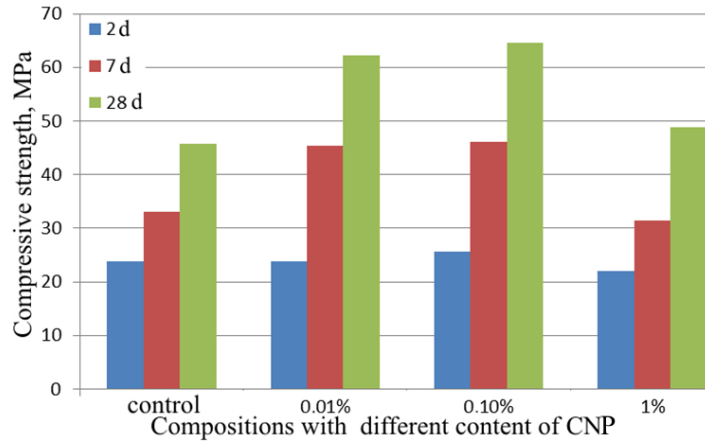
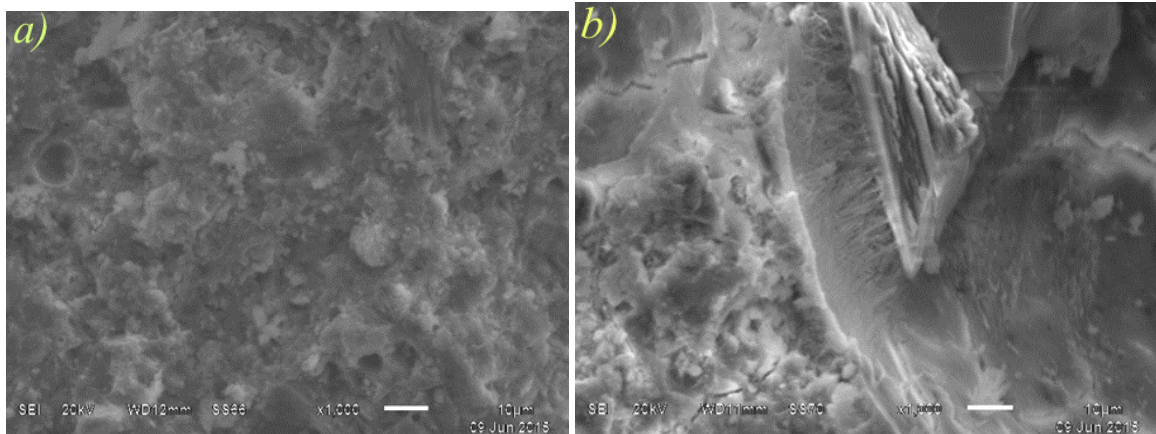


Figure 2. The dependence of the strength of the modified cement paste on the content of CNP.

The microstructure of the specimens using Portland cement (OPC) and CNP is denser compared to the control composition (Figure 3). Carbon nanoparticles act as centers of crystallization of new growths, thereby compacting the microstructure of hardened cement paste. In the control composition, there is a larger amount of pores that are filled with lime crystals of $\text{Ca}(\text{OH})_2$ during the curing process. The addition of CNPs leads to a decrease in capillary porosity, to an increase in the amount of tiny gel pores that are part of the calcium silicate hydrogel. When observing the contact zone of the formed portlandite, there is a dense microreinforcement and its binding to additional calcium hydrosilicates, which leads to an increase in the density and strength of the composite. In the modified composition, the germination and thickening of needle-like spokes-like crystals of calcium hydrosilicates is visible.



**Figure 3. SEM-images of hardened cement paste cleavage (x1000):
a – control composition, b – OPC + CNP 0.01%**

All this favorably affects the change in the compressive strength characteristics of the modified cement paste, as indicated above, in Figure 3.

The increased strength of the modified cement paste occurs not only due to the acceleration of its hydration processes, but also due to a change in the structure and porosity of the hardened cement paste. Using mercury porosimetry, it was found that the addition of CNPs leads to a decrease in the total porosity by 12 % compared to the control composition (Table 3).

Table 3. The porosity of hardened cement paste at the age of 28 days.

Composition	Total porosity, cm^3/g	Pore diameter, μm					
		1–0.1		0.1–0.01		0.01–0.001	
		cm^3/g	%	cm^3/g	%	cm^3/g	%
OPC	0.094	0.02	21.2	0.072	76.4	0.002	2.4
OPC+0.01%	0.083	0.008	9.6	0.073	87.7	0.002	2.7

Table 3 shows the improvement of the capillary-porous structure of hardened cement paste with the addition of CNP in comparison with the structure of hardened cement paste without additives. In concrete technology, there is a generalized idea that micro- and macropores with a radius not exceeding 10^{-4} cm, which should be mostly closed or dead-ends, should prevail in the structure in cement concrete. The pores size distribution in a hardened cement paste with CNP shifts toward an increase in the amount of small pores, the

pore content with a diameter of 1–0.1 μm decreased by 11.6 %, while the pore content in the range 0.1–0.01 μm increased by 11.3 %. A change in the nature of porosity in the direction of increasing the amount of small micropores with the addition of CNPs contributes to the creation of a dense hardened cement paste and the improvement of its physicochemical properties.

The results of differential thermal analysis (Figure 4) of the cement matrix indicate an increase in the intensity of the endoeffect in the temperature range 515–520 $^{\circ}\text{C}$ during the modification of cement with the addition of a coal-water suspension. This indicates an increase in the content of calcium hydroxide, which is associated with an acceleration of cement hydration with the addition of a water-coal suspension. It is worth noting that along with the acceleration of cement hydration with the introduction of the additive, a change in the basicity of the formed calcium hydrosilicates is observed: the endothermic effect in the temperature range 800–840 $^{\circ}\text{C}$ shifts to the right, in the direction of lowering the temperature from 838 to 806 $^{\circ}\text{C}$.

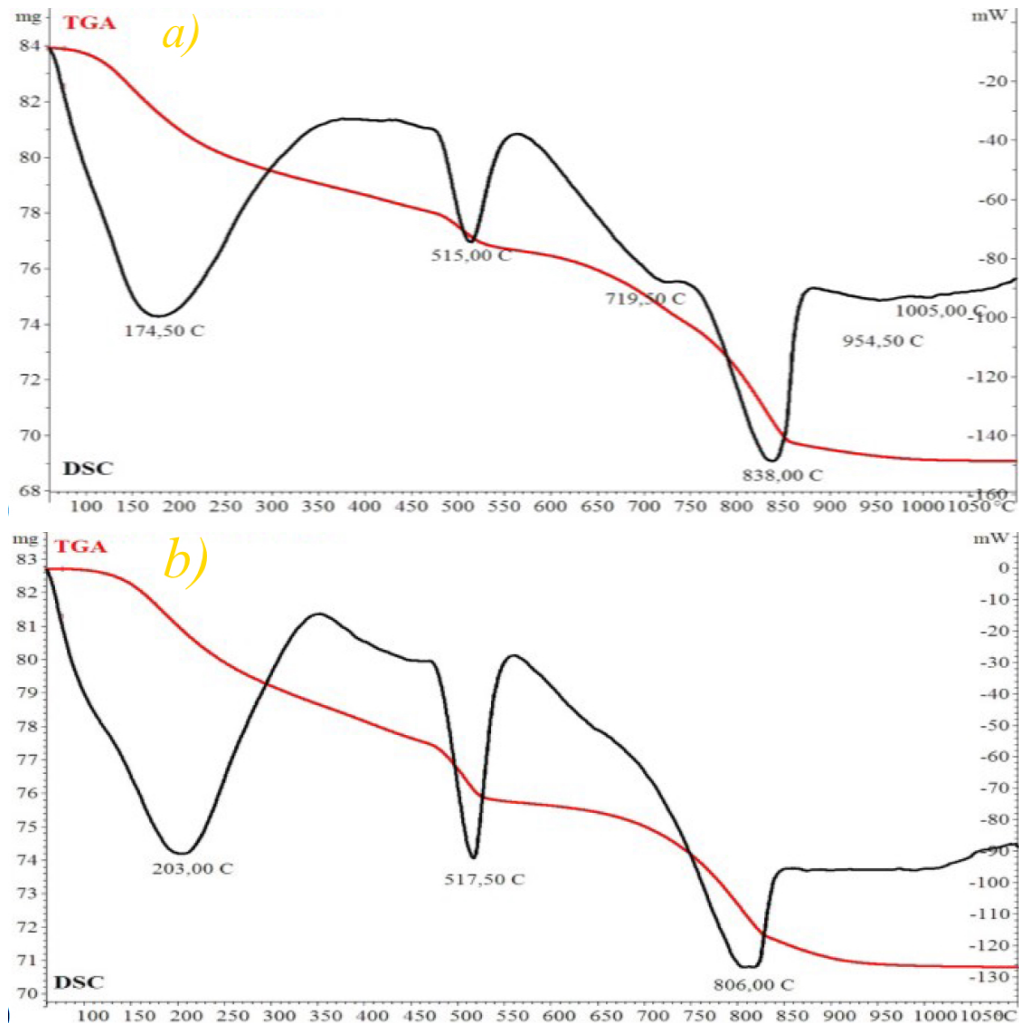


Figure 4. Differential thermal analysis of hardened cement paste: a - OPC, b - OPC + 0.01% CNP

The revealed positive effect of CNP on the properties of hardened cement paste leads to an improvement in the properties of modified concrete. When selecting the composition of modified concrete of class C20, a CNP was used with an optimum concentration of 0.1% by weight of a binder, the consumption of which amounted to 375 kg/m^3 (Table 4).

Table 4. Technological and physicochemical properties of modified concrete.

Properties	Value	
	0% CNP	0.1% CNP
Compressive strength, MPa:		
2 d.	26.5	30.9
7 d.	42.3	43.8
28 d.	51.1	55.0
Water permeability, grade	W12	W18
Water absorption by weight, %	1.4	1.1
Freeze-thaw, cycles	300	300

The addition of CNP increases the compressive strength of concrete by 15-20% compared with the control non-additive composition. The combined effect of CNPs at different stages of concrete curing contributes to the creation of a high-density microstructure, a change in the nature of porosity, and an improvement in the hydrophysical and exploitation characteristics of modified concrete.

Having achieved a certain increase in the physico-mechanical characteristics of the modified concrete, they simultaneously sought to increase its conductive properties. An important technical result in this direction is the creation of a high-density microstructure of hardened cement paste. This will prevent the saturation of concrete with water during exploitation. Thus, the hardened cement paste itself will be a dielectric, while allowing the conductive function to perform carbon nanoparticles. At the same time, it should be noted the use of cement concrete as the electrically conductive composition. As it was proved earlier [3, 7, 12], cement concrete (in comparison with, for example, polymer or polymer cement binders), in addition to high structural and technical and economic indicators, has a fairly good corona resistance and arc resistance.

The second step is the use of carbon nanoparticles as a conductive additive. As shown by experimental results, the electrical resistance of concrete decreased by a factor of two with the addition of CNP in a small amount in comparison with the known electrically conductive additives (Table 4). It is known that carbon conductive components (for example, carbon black or graphite) create continuous conductive chains in electrically conductive concrete, while their concentration is quite high (it reduces strength of concrete). When using carbon nanoparticles, in our opinion, due to the high specific resistance of CNP particles and subject to their uniform distribution in concrete, continuous conductive chains are also created, leading to a decrease in the electrical resistance of the material.

Table 5. Electrical resistance of modified concrete.

Additive type	The amount of additive, % by weight of cement	Specific electrical resistance, Ohm·cm		
		2 d	7 d	28 d
CNP	0.5	$2.0 \cdot 10^6$	$3.0 \cdot 10^6$	$3.4 \cdot 10^6$
	0.1	$1.1 \cdot 10^6$	$3.2 \cdot 10^6$	$4.5 \cdot 10^6$
Carbon black	20	$1.8 \cdot 10^6$	$3.2 \cdot 10^6$	$5.1 \cdot 10^6$
Graphite	20	$1.7 \cdot 10^6$	$3.0 \cdot 10^6$	$8.9 \cdot 10^6$

The decrease in the electrical resistivity of concrete as a result of the use of carbon nanoparticles is explained both by the influence of CNP on the cement hydration process and by the high dispersion of conductive particles. A change in the nature of porosity in the direction of increasing the amount of small micropores with the addition of CNPs contributes to the creation of a dense hardened cement paste and a more uniform distribution of nanosized conductive particles. This creates a homogeneous microstructure of electrically conductive concrete, allowing it to be used for the various applications listed above. In addition, low porosity will prevent the saturation of concrete with water during exploitation, thereby providing more stable electrical characteristics.

4. Conclusion

Based on the results obtained, the following conclusions can be drawn:

- carbon nanoparticles act as centers of crystallization of new growths, thereby compacting the microstructure of hardened cement paste.;
- a change in the nature of porosity in the direction of increasing the amount of small micropores with the addition of CNPs contributes to the creation of a dense structure of hardened cement paste and improve its exploitation properties.
- the electrical resistance of concrete was halved with the addition of CNP in a small amount compared to known electrically conductive additives.
- a small amount of conductive additives compared, for example, with soot and graphite, gives a more durable structure of the concrete matrix.

The relationship between the electrical conductivity of concrete and macroscopic strength correlates with the results of early studies [4, 8, 21].

Prospects for further research can be conducted in two directions:

1. The creation of electrically conductive concrete with low electrical resistivity and the stability of electrical parameters over time under changing exploitation conditions.

2. The study of the electrical properties of existing concrete and the creation of concrete with improved electrical insulation properties: high electrical resistivity, low dielectric loss and permittivity, high electrical strength.

5. Acknowledgements

The article was prepared in the framework of the project part of the state task in the field of scientific activity No. 13.6716.2017 on the topic "Innovative resource- and energy-saving technologies using plasma-energy processes and technologies" ESSTU.

References

- Chang, C., Song, G., Gao, D., Mo, Y.L. Temperature and mixing effects on electrical resistivity of carbon fiber enhanced concrete. *Smart Mater. Struct.* 2013. 22(3). Pp. 1–7.
- Chiarello, M., Zinno, R. Electrical conductivity of self-monitoring CFRC. *Cem. Concr. Compos.* 2005. 27. Pp. 463–469.
- Artamonova, O.V., Slavcheva, G.S., Chernyshov, E.M. Effectiveness of combined nanoadditives for cement systems. *Inorganic Materials*. 2017. Vol. 53. Tshchyu 10. Pp. 1080–1085
- Cwirzen, A., Habermehl-Cwirzen, K., Penttala, V. Surface decoration of carbon nanotubes and mechanical properties of cement/carbon nanotube composites. *Adv. Cem. Res.* 2008. 20. Pp. 65–73.
- Zhang, J., Lu, Y., Lu, Z., Liu, C., Sun, G., Li, Z. A new smart traffic monitoring method using embedded cement-based piezoelectric sensors. *Smart Mater. Struct.* 2015. 24(2). Pp. 1–8.
- Han, B., Yu, X., Kwon, E., Ou, J.P. Effects of CNT concentration level and water/cement ratio on the piezoresistivity of CNT/cement composite. *J. Comp.Mater.* 2012. 46(1). Pp. 19–25.
- Nizina, T.A., Ponomarev, A.N., Balykov, A.S., Pankin, N.A. Fine-grained fibre concretes modified by complexed nanoadditives. *International Journal of Nanotechnology (IJNT)* 2017. Vol. 14. No. 7/8. DOI: 10.1504/IJNT.2017.083441
- Han, B., Zhang, L., Sun, S., Yu, X., Dong, X., Wu, T., Ou, J. Electrostatic self-assembled carbon nanotube/nano carbon black composite fillers reinforced cement-based materials with multifunctionality. *Compos. Part A*. 2015. 79. Pp. 103–115.
- Vipulanandan, C., Mohammed, A. Smart cement modified with iron oxide nanoparticles to enhance the piezoresistive behavior and compressive strength for oil well applications. *Smart Mater. Struct.* 2015. 24(12). Pp. 1–11.
- Han, B., Qiao, G., Jiang, H. Piezoresistive response extraction for smart cement-based composites/sensors. *J. Wuhan Univ. Technol.* 2012. 27(4). Pp. 754–757.
- Chen, M., Gao, P., Geng, F., Zhang, L., Liu, H. Mechanical and smart properties of carbon fiber and graphite conductive concrete for internal damage monitoring of structure. *Constr. Build. Mater.* 2017. 142. Pp. 320–327.
- Siu, S., Ji, Q., Wu, W., Song, G., Ding, Z. Stress wave communication in concrete: I. Characterization of a smart aggregate based concrete channel. *Smart Mater. Struct.* 2014. 23(12). Pp. 1–9.
- Siu, S., Qing, J., Wang, K., Song, G., Ding, Z. Stress wave communication in concrete: II. Evaluation of low voltage concrete stress wave communications utilizing spectrally efficient modulation schemes with PZT transducers. *Smart Mater. Struct.* 2014. 23. Pp. 1–7.
- Klyuev, S.V., Klyuev, A.V., Vatin, N.I. Fiber concrete for the construction industry. *Magazine of Civil Engineering*. 2018. 84(8). Pp. 41–47. doi: 10.18720/MCE.84.4.
- Abirami, T., Loganaganandan, M., Murali G., Fediuk, R., Vickram Sreekrishna, R., Vignesh, T., Janupriya, G., Karthikeyan K. Experimental research on impact response of novel steel fibrous concretes under falling mass impact. *Construction and Building Materials*. 2019. 222. Pp. 447–457.
- Fediuk, R., Smoliakov, A., Muraviov, A. Mechanical Properties of Fiber-Reinforced Concrete Using Composite Binders. *Advances in Materials Science and Engineering*. 2017. No. 2017. Article 2316347. <https://doi.org/10.1155/2017/2316347>.
- Küçük V.A., Çınar, Korucu, H., Simsek, B., Güvenç, A.B., Uygunog'lu, T., Kocakerim, M.M. Thermal, electrical and mechanical properties of filler-doped polymer concrete. *Construction and Building Materials*. 2019. 226. Pp. 188–199.
- Klyuev, S.V., Klyuev, A.V., Khezhev, T.A., Pucharenko Yu.V. Technogenic sands as effective filler for fine-grained fibre concrete. *Journal of Physics: Conference Series*. 2018. 1118. 012020.
- Denisova, Yu.V. Additive technology in construction // *Construction Materials and Products*. 2018. Vol. 1. No. 3. Pp. 33–42.
- Princigallo, A., van Breugel, K., Levita, G. Influence of the aggregate on the electrical conductivity of Portland cement concretes. *Cement and Concrete Research*. 2003. 33. Pp. 1755–1763.
- Rao, R., Wang, H., Wang, H., Tuan, C.Y., Ye, M. Models for estimating the thermal properties of electric heating concrete containing steel fiber and graphite. *Composites Part B: Engineering*, 2019. Vol. 164. Pp. 116–120.
- Shi, S. Effect of mixing proportions of concrete on its electrical conductivity and the rapid chloride permeability test (ASTM C1202 or ASSHTO T277) results. *Cement and Concrete Research* 2004. Vol. 34. Pp. 537–545
- Kozhukhova N.I., Strokova V.V., Kozhukhova M.I., Zhernovsky I.V. Structure formation in alkali activated aluminosilicate binding systems using natural raw materials with different crystallinity degree // *Construction Materials and Products*. 2018. Vol. 1. No. 4. Pp. 38–43.
- Klyuev, S.V., Klyuev, A.V., Vatin, N.I. Fine-grained concrete with combined reinforcement by different types of fibers. *MATEC Web of Conferences*. 2018. No. 245. 03006
- Mesbah, H.A., Yahia, A., Khayat K.H. Electrical conductivity method to assess static stability of self-consolidating concrete. *Cement and Concrete Research*. 2011. Vol. 41. No. 5. Pp. 451–458.
- Velay-Lizancos, M., Azenha, M., Martínez-Lage, I, Vázquez-Burgo, P. Addition of biomass ash in concrete: Effects on E-Modulus, electrical conductivity at early ages and their correlation. *Construction and Building Materials*. 2017. Vol. 157. Pp. 1126–1132.
- Demircillog'lu, E., Teomete, E., Schlangen, E., Javier Baeza, F. Temperature and moisture effects on electrical resistance and strain sensitivity of smart concrete. *Construction and Building Materials*. 2019. Vol. 224. Pp. 420–427.
- Nelyubova, V.V., Babayev, V.B., Alfimova, N.I., Usikov, S.A., Masanin, O.O. Improving the efficiency of fibre concrete production. *Construction Materials and Products*. 2019. Vol. 2. No. 2. Pp. 4–9.

29. Klyuev, S.V., Khezhev, T.A., Pukhareno, Yu.V., Klyuev, A.V. The fiber-reinforced concrete constructions experimental research. Materials Science Forum. 2018. Vol. 931. Pp. 598–602.
30. Fediuk, R.S., Lesovik, V.S., Liseitsev, Yu.L., Timokhin, R.A., Bituyev, A.V., Zaiakhanov, M.Ye., Mochalov, A.V. Composite binders for concretes with improved shock resistance. Magazine of Civil Engineering. 2019. 85(1). Pp. 28–38. DOI: 10.18720/MCE.85.3.
31. Coppio, G.J.L., de Lima, M.G., Lencioni, J.W., Cividanes, L.S. Dyer, P.P.O.L., Silva, S.A. Surface electrical resistivity and compressive strength of concrete with the use of waste foundry sand as aggregate. Construction and Building Materials. 2019. 212. Pp. 514–521.
32. Wang, W., Lu, C., Li, Y., Li, Q. An investigation on thermal conductivity of fly ash concrete after elevated temperature exposure. Construction and Building Materials, 2017. Vol. 148. Pp. 148–154.
33. Liu, K., Cheng, X., Li, J., Gao, X., Cao, Y., Guo, X., Zhuang, J., Zhang, C. Effects of microstructure and pore water on electrical conductivity of cement slurry during early hydration. Composites Part B: Engineering, 2019. 177. 107435.
34. Khajehnouri, Y., Chouteau, M., Rivard, P., Bérubé, C.L. Measuring electrical properties of mortar and concrete samples using the spectral induced polarization method: laboratory set-up. Construction and Building Materials, 2019. 210. Pp. 1–12.
35. Linares-Alemparte, P., Andrade, C., Baza D. Porosity and electrical resistivity-based empirical calculation of the oxygen diffusion coefficient in concrete. Construction and Building Materials. 2019. 198. Pp. 710–717.
36. de Azevedo Basto, P., Savastano Junior, H., de Melo Neto, A.A. Characterization and pozzolanic properties of sewage sludge ashes (SSA) by electrical conductivity. Cement and Concrete Composites. 2019. 104. 103410.
37. Fiala, L., Toman, J., Vodička, J., Ráček, V. Experimental Study on Electrical Properties of Steel-fibre Reinforced Concrete. Procedia Engineering. 2016. 151. Pp. 241–248.
38. Usanova, K., Rybakov, V., Udalova, V., Kovytkov, A. Examination of Quality and Operational Properties of Vibropressed Paving Elements. MATEC Web of Conferences. 2016. 73. 040131.
39. Morozov, V.I., Opbul, E.K., Van Phuc, P. Behaviour of axisymmetric thick plates resting against conical surface. Magazine of Civil Engineering. 2019. 86(2). 2019. Pp. 92–104. doi: 10.18720/MCE.86.9

Contacts:

Larisa Urkhanova, +7(902)1685168; urkhanova@mail.ru

Sergey Buyantuev, +7(950)2817945; buyantuevsl@mail.ru

Ayuna Urkhanova, +7(950)2817945; technosfera@mail.ru

Solbon Lkhasaranov, +7(950)3871856; solbon230187@mail.ru

Galina Ardashova, +7(950)2817945; galya.ardashova1103@mail.ru

Roman Fediuk, +7(950)2817945; roman44@yandex.ru

Alexander Svintsov, +7(905)5826910; svintsovap@rambler.ru

Igor Ivanov, +7(950)2817945; ivanova-2006@mail.ru

© Urkhanova L.A., Buyantuev S.L., Urkhanova A.A., Lkhasaranov S.A., Ardashova G.R., Fediuk R.S., Svintsov A.P., Ivanov I.A., 2019



DOI: 10.18720/MCE.92.14

Механические и электрические свойства бетона, модифицированного углеродными наночастицами

Л.А. Урханова^a, С.Л. Буянтубеев^a, А.А. Урханова^a, С.А. Лхасаранов^a, Г.Р. Ардашова^a, Р.С. Федюк^{b*}, А.П. Свинцов^c, И.А. Иванов^a

^a Восточно-Сибирский государственный университет технологий и управления, г. Улан-Удэ, Россия

^b Дальневосточный Федеральный Университет, г. Владивосток, Россия

^c Российский университет дружбы народов, Москва, Россия

* E-mail: roman44@yandex.ru

Ключевые слова: цементы, цементные композиты, вяжущие, бетоны, углеродные наночастицы

Аннотация. В статье представлены исследования по получению электропроводного бетона с использованием углеродных наночастиц, полученных при переработке угля в электроразрядном плазменном реакторе. Электроразрядный способ получения седиментационно устойчивой и высокодисперсной суспензии заключается в обработке угольного порошка электрическим током в водной среде. С помощью лазерной дифракции было обнаружено, что углеродные наночастицы имеют размер частиц в диапазоне от 50 до 500 нм. Прочность на сжатие была испытана на кубках с ребром 100 мм в соответствии с EN 12390-6. Определение электрического сопротивления бетона проводилось на образцах с ребром 100 мм, размещенных между двумя латунными пластинами, через которые пропусклся постоянный ток. Оценено оптимальное содержание углеродных наночастиц (0,01–0,1 % мас.) в вяжущем, что позволяет получить высокие механические свойства бетона (на 30–35% более высокую прочность на сжатие по сравнению с контрольным образцом). Доказано, что механизм действия наноразмерных модификаторов наиболее выражен в малых дозах. Определены зависимости физико-механических свойств цементного камня при введении различного количества углеродных наночастиц. Исследована микроструктура цементного камня при введении углеродных наночастиц методом растровой микроскопии. Определены физико-механические и эксплуатационные свойства тяжелого электропроводящего бетона. Определена кинетика изменения электрического сопротивления бетона в различные сроки твердения.

Литература

1. Chang C., Song G., Gao D., Mo Y.L. Temperature and mixing effects on electrical resistivity of carbon fiber enhanced concrete. *Smart Mater. Struct.* 2013. № 22(3). Pp. 1–7.
2. Chiarello M., Zinno R. Electrical conductivity of self-monitoring CFRC. *Cem. Concr. Compos.* 2005. № 27. Pp. 463–469.
3. Artamonova O.V., Slavcheva G.S., Chernyshov E.M. Effectiveness of combined nanoadditives for cement systems. *Inorganic Materials.* 2017. Vol. 53. № 10. Pp. 1080–1085.
4. Cwirzen A., Habermehl-Cwirzen K., Penttala V. Surface decoration of carbon nanotubes and mechanical properties of cement/carbon nanotube composites. *Adv. Cem. Res.* 2008. № 20. Pp. 65–73.
5. Zhang J., Lu Y., Lu Z., Liu C., Sun G., Li Z. A new smart traffic monitoring method using embedded cement-based piezoelectric sensors. *Smart Mater. Struct.* 2015. № 24(2). Pp. 1–8.
6. Han B., Yu X., Kwon E., Ou J.P. Effects of CNT concentration level and water/cement ratio on the piezoresistivity of CNT/cement composites. *J. Comp.Mater.* 2012. № 46(1). Pp. 19–25.
7. Nizina T.A., Ponomarev A.N., Balykov A.S., Pankin N.A. Fine-grained fibre concretes modified by complexed nanoadditives. *International Journal of Nanotechnology (IJNT)* 2017. Vol. 14. № 7/8. DOI: 10.1504/IJNT.2017.083441
8. Han B., Zhang L., Sun S., Yu X., Dong X., Wu T., Ou J. Electrostatic self-assembled carbon nanotube/nano carbon black composite fillers reinforced cement-based materials with multifunctionality. *Compos. Part A.* 2015. № 79. Pp. 103–115.
9. Vipulanandan C., Mohammed A. Smart cement modified with iron oxide nanoparticles to enhance the piezoresistive behavior and compressive strength for oil well applications. *Smart Mater. Struct.* 2015. № 24(12). Pp. 1–11.
10. Han B., Qiao G., Jiang H. Piezoresistive response extraction for smart cement-based composites/sensors. *J. Wuhan Univ. Technol.* 2012. № 27(4). Pp. 754–757.
11. Chen M., Gao P., Geng F., Zhang L., Liu H. Mechanical and smart properties of carbon fiber and graphite conductive concrete for internal damage monitoring of structure. *Constr. Build. Mater.* 2017. №142. Pp. 320–327.
12. Siu S., Ji Q., Wu W., Song G., Ding Z. Stress wave communication in concrete: I. Characterization of a smart aggregate based concrete channel. *Smart Mater. Struct.* 2014. № 23(12). Pp. 1–9.
13. Siu S., Qing J., Wang K., Song G., Ding Z. Stress wave communication in concrete: II. Evaluation of low voltage concrete stress wave communications utilizing spectrally efficient modulation schemes with PZT transducers. *Smart Mater. Struct.* 2014. 23. Pp. 1–7.

14. Клюев С.В., Клюев А.В., Ватин Н.И. Фибробетон для строительной индустрии // Инженерно-строительный журнал. 2018. № 8(84). С. 41–47. doi: 10.18720/MCE.84.4
15. Abirami T., Loganaganandan M., Murali G., Fediuk R., Vickhram Sreekrishna R., Vignesh T., Janupriya G., Karthikeyan K. Experimental research on impact response of novel steel fibrous concretes under falling mass impact. Construction and Building Materials. 2019. № 222. Pp. 447–457.
16. Fediuk R., Smoliakov A., Muraviov A. Mechanical Properties of Fiber-Reinforced Concrete Using Composite Binders. Advances in Materials Science and Engineering. 2017. Article 2316347. <https://doi.org/10.1155/2017/2316347>.
17. K  c  k V.A.,   nar, Korucu, H., Simsek, B., G  ven  , A.B., Uygunog  lu, T., Kocakerim, M.M. Thermal, electrical and mechanical properties of filler-doped polymer concrete. Construction and Building Materials. 2019. № 226. Pp. 188–199.
18. Klyuev S.V., Klyuev A.V., Khezhev T.A., Pucharenko Yu.V. Technogenic sands as effective filler for fine-grained fibre concrete. Journal of Physics: Conference Series. 2018. № 1118. 012020.
19. Денисова Ю.В. Аддитивные технологии в строительстве // Строительные материалы и изделия. 2018. Т. 1. № 3. С. 33–42.
20. Princigallo A., van Breugel K., Levita G. Influence of the aggregate on the electrical conductivity of Portland cement concretes. Cement and Concrete Research. 2003. № 33. Pp. 1755–1763.
21. Rao R., Wang H., Wang H., Tuan C.Y., Ye M. Models for estimating the thermal properties of electric heating concrete containing steel fiber and graphite. Composites Part B: Engineering, 2019. Vol. 164. Pp. 116–120.
22. Shi S. Effect of mixing proportions of concrete on its electrical conductivity and the rapid chloride permeability test (ASTM C1202 or ASSHTO T277) results. Cement and Concrete Research 2004. Vol. 34. Pp. 537–545
23. Кожухова Н.И., Строкова В.В., Кожухова М.И., Жерновский И.В. Структурообразование в щелочеактивированных алюмосиликатных системах с использованием природного сырья с различной степенью кристалличности // Строительные материалы и изделия. Т. 1. № 4. С. 38–43.
24. Klyuev S.V., Klyuev A.V., Vatin N.I. Fine-grained concrete with combined reinforcement by different types of fibers. MATEC Web of Conferences. 2018. № 245. 03006
25. Mesbah H.A., Yahia A., Khayat K.H. Electrical conductivity method to assess static stability of self-consolidating concrete. Cement and Concrete Research. 2011. Vol. 41. № 5. Pp. 451–458.
26. Velay-Lizancos M., Azenha M., Mart  nez-Lage I., V  zquez-Burgo P. Addition of biomass ash in concrete: Effects on E-Modulus, electrical conductivity at early ages and their correlation. Construction and Building Materials. 2017. Vol. 157. Pp. 1126–1132.
27. Demircilioǧ  lu E., Teomete E., Schlangen E., Javier Baeza F. Temperature and moisture effects on electrical resistance and strain sensitivity of smart concrete. Construction and Building Materials. 2019. Vol. 224. Pp. 420–427.
28. Нелюбова В.В., Бабаев В.Б., Алфимова Н.И., Усиков С.А., Масанин О.О. Повышение эффективности производства фибробетона. Строительные материалы и изделия. 2019. Т. 2. № 2. С. 4–9.
29. Klyuev S.V., Khezhev T.A., Pukhareno Yu.V., Klyuev A.V. The fiber-reinforced concrete constructions experimental research. Materials Science Forum. 2018. Vol. 931. Pp. 598–602.
30. Федюк Р.С., Лесовик В.С., Лисейцев Ю.Л., Тимохин Р.А., Битуев А.В., Заяханов М.Е., Мочалов А.В. Композиционные вяжущие для бетонов повышенной ударной стойкости // Инженерно-строительный журнал. 2019. № 1(85). С. 28–38. DOI: 10.18720/MCE.85.3.
31. Coppio G.J.L., de Lima M.G., Lencioni J.W., Cividanes L.S. Dyer P.P.O.L., Silva S.A. Surface electrical resistivity and compressive strength of concrete with the use of waste foundry sand as aggregate. Construction and Building Materials. 2019. Vol. 212. Pp. 514–521.
32. Wang W., Lu C., Li Y., Li Q. An investigation on thermal conductivity of fly ash concrete after elevated temperature exposure. Construction and Building Materials. 2017. Vol. 148. Pp. 148–154.
33. Liu K., Cheng X., Li J., Gao X., Cao Y., Guo X., Zhuang J., Zhang C. Effects of microstructure and pore water on electrical conductivity of cement slurry during early hydration. Composites Part B: Engineering. 2019. Vol. 177. 107435.
34. Khajehnouri Y., Chouteau M., Rivard P., B  rub   C.L. Measuring electrical properties of mortar and concrete samples using the spectral induced polarization method: laboratory set-up. Construction and Building Materials. 2019. Vol. 210. Pp. 1–12.
35. Linares-Alemparte P., Andrade C., Baza D. Porosity and electrical resistivity-based empirical calculation of the oxygen diffusion coefficient in concrete. Construction and Building Materials. 2019. Vol. 198. Pp. 710–717.
36. de Azevedo Basto P., Savastano Junior H., de Melo Neto A.A. Characterization and pozzolanic properties of sewage sludge ashes (SSA) by electrical conductivity. Cement and Concrete Composites. 2019. Vol. 104. 103410.
37. Fiala L., Toman J., Vodi  ka J., R   ek V. Experimental Study on Electrical Properties of Steel-fibre Reinforced Concrete. Procedia Engineering, 2016. Vol. 151. Pp. 241–248.
38. Usanova K., Rybakov V., Udalova V., Kovytkov A. Examination of Quality and Operational Properties of Vibropressed Paving Elements. MATEC Web of Conferences. 2016. Vol. 73. 040131.
39. Морозов В.И., Опбул Э., Ван Фук Ф. Работа осесимметричных толстых плит, опертых по конической поверхности // Инженерно-строительный журнал. 2019. № 2(86). С. 92–104. DOI: 10.18720/MCE.86.9

Контактные данные:

Лариса Алексеевна Урханова, +7(902)1685168; urkhanova@mail.ru

Сергей Лубсанович Буянтуев, +7(950)2817945; buyantuevsl@mail.ru

Аюна Алексеевна Урханова, +7(950)2817945; technosfera@mail.ru

Солбон Александрович Лхасаранов, +7(950)3871856; solbon230187@mail.ru

Галина Романовна Ардашова, +7(950)2817945; galya.ardashova1103@mail.ru

Роман Сергеевич Федюк, +7(950)2817945; roman44@yandex.ru

Александр Петрович Свинцов, +7(905)5826910; svintsovap@rambler.ru

Игорь Алексеевич Иванов, +7(950)2817945; ivanova-2006@mail.ru

   Урханова Л.А., Буянтуев С.Л., Урханова А.А., Лхасаранов С.А., Ардашова Г.Р., Федюк Р.С., Свинцов А.П., Иванов И.А., 2019



ПОЛИТЕХ
Санкт-Петербургский
политехнический университет
Петра Великого

Инженерно-строительный институт
Центр дополнительных профессиональных программ

195251, г. Санкт-Петербург, Политехническая ул., 29,
тел/факс: 552-94-60, www.stroikursi.spbstu.ru,
stroikursi@mail.ru

Приглашает специалистов проектных и строительных организаций,
не имеющих базового профильного высшего образования
на курсы профессиональной переподготовки (от 500 часов)
по направлению «Строительство» по программам:

П-01 «Промышленное и гражданское строительство»

Программа включает учебные разделы:

- Основы строительного дела
- Инженерное оборудование зданий и сооружений
- Технология и контроль качества строительства
- Основы проектирования зданий и сооружений
- Автоматизация проектных работ с использованием AutoCAD
- Автоматизация сметного дела в строительстве
- Управление строительной организацией
- Управление инвестиционно-строительными проектами. Выполнение функций технического заказчика

П-02 «Экономика и управление в строительстве»

Программа включает учебные разделы:

- Основы строительного дела
- Инженерное оборудование зданий и сооружений
- Технология и контроль качества строительства
- Управление инвестиционно-строительными проектами. Выполнение функций технического заказчика и генерального подрядчика
- Управление строительной организацией
- Экономика и ценообразование в строительстве
- Управление строительной организацией
- Организация, управление и планирование в строительстве
- Автоматизация сметного дела в строительстве

П-03 «Инженерные системы зданий и сооружений»

Программа включает учебные разделы:

- Основы механики жидкости и газа
- Инженерное оборудование зданий и сооружений
- Проектирование, монтаж и эксплуатация систем вентиляции и кондиционирования
- Проектирование, монтаж и эксплуатация систем отопления и теплоснабжения
- Проектирование, монтаж и эксплуатация систем водоснабжения и водоотведения
- Автоматизация проектных работ с использованием AutoCAD
- Электроснабжение и электрооборудование объектов

П-04 «Проектирование и конструирование зданий и сооружений»

Программа включает учебные разделы:

- Основы сопротивления материалов и механики стержневых систем
- Проектирование и расчет оснований и фундаментов зданий и сооружений
- Проектирование и расчет железобетонных конструкций
- Проектирование и расчет металлических конструкций
- Проектирование зданий и сооружений с использованием AutoCAD
- Расчет строительных конструкций с использованием SCAD Office

П-05 «Контроль качества строительства»

Программа включает учебные разделы:

- Основы строительного дела
- Инженерное оборудование зданий и сооружений
- Технология и контроль качества строительства
- Проектирование и расчет железобетонных конструкций
- Проектирование и расчет металлических конструкций
- Обследование строительных конструкций зданий и сооружений
- Выполнение функций технического заказчика и генерального подрядчика

По окончании курса слушателю выдается диплом о профессиональной переподготовке
установленного образца, дающий право на ведение профессиональной деятельности

